UNIVERSAL POSITION-SENSORLESS CONTROL FOR SWITCHED RELUCTANCE MOTOR DRIVES

UNIVERSAL POSITION-SENSORLESS CONTROL FOR SWITCHED RELUCTANCE MOTOR DRIVES

BY

DIANXUN XIAO, M. Eng.

A THESIS

SUBMITTED TO THE DEPARTMENT OF ELECTRICAL & COMPUTER ENGINEERING

AND THE SCHOOL OF GRADUATE STUDIES

OF MCMASTER UNIVERSITY

IN PARTIAL FULFILMENT OF THE REQUIREMENTS

FOR THE DEGREE OF

DOCTOR OF PHILOSOPHY

Doctor of Philosophy (2021)	McMaster University
(Electrical & Computer Engineering)	Hamilton, Ontario, Canada

TITLE:	Universal Position-Sensorless Control for Switched Reluctance Motor Drives
AUTHOR:	Dianxun Xiao M. Eng., (Electrical Engineering) Harbin Institute of Technology, Harbin, China
SUPERVISOR:	Dr. Ali Emadi
NUMBER OF PAGES:	xxvi, 222

To My Family

Abstract

Switched reluctance motors (SRMs) are promising candidates for electric vehicles due to lower manufacturing costs, higher efficiency, and robustness operation in a harsh environment. For accurate control of the SRM, the real-time rotor position is needed for phase computation. To obtain position information, position-sensorless control techniques have been developed to take the role of position sensors in commercial SRM drives for cost reduction or sensor-fault tolerance capability. Nowadays, the position-sensorless control of SRMs still suffers from a technical problem: the dependence on magnetic characteristics. Existing position estimation algorithms often require time-consuming offline measurement of magnetic parameters, limiting the broad applications due to the low generality. It is therefore of great significance to develop universal position-sensorless control techniques with less magnetic parameter dependence.

Zero- and low-speed position-sensorless control of the SRM needs high-frequency injection into the idle phase to measure the stator inductance. Rotor position is often estimated from the prestored inductance lookup table but is replaced by a new regional phase-locked loop (RPLL) with a self-commissioning process in this thesis. The modeling of the unsaturated stator inductance can be established automatically via the pulse voltage injection at

the initial stage without offline testing. The RPLL embedded with a three-phase heterodyne design can estimate the full-cycle rotor position from the idle-phase inductance based on the unsaturated inductance model. The proposed low-speed position estimator can also realize robust sensorless control in four-quadrant operation and magnetic saturation conditions without complicated magnetic characteristics. Besides, local stability of the position estimator is proved, and an optimized parameter design scheme is given.

Although pulse voltage injection offers accurate position estimation in low-speed operation, the induced pulse current results in additional copper loss and torque ripples. This problem is overcome in the thesis by regulating the magnitude of induced current at a minimal level. The induced current regulator is designed as a terminal sliding-mode controller that adjusts the injection voltage online over the whole idle-phase period. Proper control parameter selection based on the convergence analysis and stability proof ensures robust control performance against parameter uncertainties. The proposed pulse injection scheme combined with the RPLL can guarantee accurate position estimation while reducing copper losses and torque ripples significantly.

Due to the shortened idle-phase duration when the rotor speed increases, pulse injection methods are infeasible for high-speed position estimation. To solve the problem, this thesis proposes a nonlinear observer based on feature position estimation in conduction phases for high-speed sensorless control. A self-commissioning method is adopted to capture a two-dimensional flux linkage curve at a feature position, which avoids offline measurement of the complete three-dimensional characteristics. However, the estimated feature position has low resolution, and its estimation accuracy is degraded by nonideal flux linkage errors. To improve the sensorless control performance, a nonlinear state observer using online Fourier series is then designed to eliminate disturbances in position estimation. Parameter design based on a small-signal analysis is also given to guarantee accurate position and speed estimation.

High-speed position-sensorless control is further simplified using a new quadrature flux estimator without using any flux linkage characteristics. The method requires neither offline measurement nor online self-commissioning. This advantage is realized by adopting a speed-adaptive bandpass filter to extract the fundamental flux linkage. A three-phase phase-locked loop is then used to estimate the rotor position from the orthogonal flux linkage signals without *a priori* knowledge of the SRM magnetic characteristics. The magnetic-parameter-free position estimation can facilitate the application of sensorless control in a general-purpose SRM converter.

A wide-speed range position estimation scheme is realized by combining both the low-speed and high-speed position estimation approaches. Consequently, a universal position-sensorless control scheme is proposed in the thesis, covering the full-speed range and not requiring offline measurement effort.

The proposed position estimation schemes are verified on a 5.5 kW 12/8 SRM test bench.

Acknowledgements

First and foremost, I would like to express my sincerest gratitude to my supervisor, Dr. Ali Emadi. Three years ago, I was a fortunate student receiving the Ph.D. opportunity from him; after three years, I have grown into a young scholar in transportation electrification. Because of his endless encouragement, support, and suggestions, I have the opportunity to conduct research on various topics and achieve fruitful results. It is my most tremendous honor to be his student and study in such a world-leading and professional group at MARC.

I would also like to acknowledge Dr. Mehid Narimani for his kind support in my research on multilevel converters and valuable suggestions on my thesis. I appreciate Dr. Ryan Ahmed, who shared his best knowledge in battery management systems with me and assisted my first journal article in this new field. My gratitude to Dr. Sanjaka Wirasingha for his guidance and inputs in my research related to my Ph.D. thesis. Thank you for Dr. Iqbal Husain for the valuable comments on the thesis.

Special thanks are given to Gaoliang Fang, Zekun Xia, and Xueqing Wang for their knowledge and assistance in experimental setup design. It is my pleasure to work with you. I would also like to thank Dr. Jin Ye for her advice and guidance in my research and publications. Her success in academia as a young professor encourages me to work hard and go forward.

I am grateful to my former project leader, Dr. Shamsuddeen Nalakath, for his efficient research cooperation and numerous insights. I would also like to express my appreciation to my lab colleagues, Silvio Rotilli Filho, Alice Dong, Guanghan Zhao, Yuhang Yang, Giorgio Pietrini, Haomin Li, Jiaqi Yuan, Yihui Li, Zhituo Ni, Xiaoqiang Guo, Rasul Tarvirdilu Asl, Aniket Anand, Jing Zhao, Deqiang Wang, Yue Wang, and Jianbin Liang for your friendship and help in these years.

Words cannot express my gratitude and love to my parents, whose understanding and support are the guarantee of my continuous progress. I also want to thank my girlfriend, Liying Chen, for her love and three-year waiting.

At last, thanks to everyone I met in Canada.

Notation

Symbols

λ	Phase flux linkage
u	Phase voltage
R	Phase resistance
L	Phase self-inductance
i	Phase current
i_{ref}	Reference phase current
N_{r}	Number of rotor poles
θ	Rotor position
$\hat{\theta}$	Estimated rotor position
$\Delta\theta$	Rotor position estimation error
θ_{on}	Phase turn-on angle
θ_{off}	Phase turn-off angle
θ_{a}	Aligned rotor position
θ_{u}	Unaligned rotor position

θ_{ov}	Position at which the stator and rotor poles starting overlap
$\theta_{\mathrm{feature}}$	Feature rotor position
ω	Rotor rotor speed
ω_{ref}	Reference rotor speed
$\hat{\omega}$	Estimated rotor speed
$\Delta\omega$	Rotor speed estimation error
T_{e}	Electromagnetic torque
T_{ref}	Reference electromagnetic torque
T_{L}	Load torque
J	Inertia
B	Friction coefficient
U_{dc}	DC-link voltage
u_{inj}	Amplitude of injected voltages
d	Disturbance
T_{s}	Control frequency/sampling frequency
g	Gate drive signal
$\boldsymbol{F}$	Feature position vector
$\boldsymbol{F}_{\mathrm{h}}$	Harmonic position vector
$\boldsymbol{F}_{\mathrm{f}}$	Fundamental position vector
ε	Input position error signal of the phase-locked loop
λ_{f}	Fundamental flux linkage
λ_{fq}	Quadrature fundamental flux linkage

k_p, k_i	Proportional-integral parameters
ω_0	Central frequency of the SOGI-HPF

Abbreviations

SRM	Switched Reluctance motor
FEA	Finite element analysis
PWM	Pulse-width modulation
RPLL	Reginal phase-locked loop
PLL	Phase-locked loop
NSO	Nonlinear state observer
IM	Induction machine
PMSM	Permanent magnet synchronous motor
SNR	Signal-to-noise ratio
back-EMF	Back electromotive force
SMO	Sliding mode observer
PI	Proportional-integral
KF	Kalman filter
EKF	Extended Kalman filter
LPF	Lowpass filter
HPF	Highpass filter
TSMC	Terminal sliding-mode controller

QFE	Quadrature flux estimator
SOGI	Second-order generalized integrator
SOGI-HPF	Second-order generalized integrator with highpass filter
AC	Alternating current
DC	Direct current
NN	Neural network
MRAS	Model reference adaptive system

Contents

Abstract .... **iv**

Acknowledgements .... **vii**

Notation .... **ix**

Chapter 1 Introduction **1**

1.1 Background and Motivation 1

1.2 Contributions 3

1.3 Outline of the Thesis 4

Chapter 2 Fundamentals of SRM Drives and Literature Review of Position-Sensorless Control **8**

2.1 Fundamentals of SRM Drives 8

2.1.1 Configuration of the Three-Phase SRM Drive 9

2.1.2 Modeling of the SRM 12

2.2 Literature Review of Position-Sensorless Control of SRM Drives 16

2.2.1 Low-Speed Position-Sensorless Control 17

2.2.2 High-Speed Position-Sensorless Control 33

2.2.3 Wide-Speed Range Position-Sensorless Control 53

2.2.4 Discussion 55

2.3 Conclusion 57

Chapter 3 A Regional Phase-Locked Loop Based Low-Speed Position-Sensorless Control Scheme 58

3.1 Introduction..58

3.2 Discussion on Conventional Low-Speed Position Estimation Methods..................60

3.3 Proposed Low-Speed Position Estimation Scheme 62

3.3.1 Overview of the Proposed Method...62

3.3.2 Idle-Phase Inductance Analysis and Self-Commissioning...............................64

3.3.3 Position Estimation from the Idle-Phase Inductance Through an RPLL 66

3.3.4 Analysis of the Approximated Inductance Model..75

3.4 Experimental Verification...79

3.5 Conclusion 91

Chapter 4 Induced Current Reduction Scheme for Low-Speed Position-Sensorless Control 93

4.1 Introduction..93

4.2 Discussion on Conventional Pulse Injection Methods...94

4.3 Proposed Pulse Injection Scheme 96

4.3.1 Design of the Terminal Sliding-Mode Voltage Controller 96

4.3.2 Stability Analysis of the Proposed TSMC 99

4.3.3 Performance Analysis 102

4.3.4 Parameter Design 105

4.3.5 Overall Structure of the Proposed Scheme ... 108

4.4 Experimental Results ... 110

4.5 Conclusions ... 116

Chapter 5 Nonlinear State Position Observer for Position-Sensorless Control at Medium and High Speed ... 118

5.1 Introduction ... 118

5.2 Conventional Feature-Flux-Linkage-Based Position Estimation Method ... 120

5.2.1 Feature Flux Linkage of the SRM ... 120

5.2.2 Position Estimation Based on Feature Flux Linkage: Conventional Method ... 122

5.3 Proposed Position-Sensorless Control Algorithm ... 125

5.3.1 Fourier Series of the Feature Position ... 125

5.3.2 Design of the Proposed NSO ... 127

5.4 Small-Signal Modeling and Parameter Design of the Proposed Observer ... 133

5.4.1 Small-Signal Modeling ... 133

5.4.2 Parameter Design and Stability ... 135

5.5 Experimental Results ... 138

5.6 Conclusion ... 151

Chapter 6 Magnetic-Characteristic-Free Position Observer for High-Speed Position-Sensorless Control ... 153

6.1 Introduction ... 153

6.2 Investigation of Flux Linkage-Based Position Estimation ... 155

6.2.1 Flux Linkage Analysis ... 155

6.2.2 Basic Principle of the Proposed Scheme 156
6.3 Design of the Proposed Position Estimation Scheme Based on QFEs 159
6.3.1 Second-Order Generalized Integrator With A Highpass Filter 159
6.3.2 Overall Design of the Proposed Position Estimator 161
6.3.3 Design of the QFE 162
6.3.4 Design of the Three-Phase PLL 167
6.3.5 Design for Generating Sensorless Operation 169
6.3.6 Design for Negative-Speed Sensorless Operation 171
6.3.7 Selection of Discretization Methods 172
6.4 Experimental Validation 175
6.5 Conclusion 187
Chapter 7 Wide-Speed Range Position-Sensorless Control 189
7.1 Introduction 189
7.2 Wide-Speed Range Sensorless Control Algorithm 190
7.3 Experimental Results 192
7.4 Conclusion 194
Chapter 8 Conclusions and Future Work 196
8.1 Conclusions 196
8.2 Future Work 199
8.3 Publications 201
8.3.1 Accepted Papers 201
8.3.2 Submitted Papers 204

8.3.3 To Be Submitted Papers 204

References 205

List of Tables

2.1 Parameters of the SRM-IM Test Bench 9

2.2 Summary and Comparison of Low-Speed SRM Position-Sensorless Control Strategies 31

2.3 Summary and Comparison of High-Speed SRM Position-Sensorless Control Strategies 52

3.1 Overall Design of the Proposed Regional Heterodyne Operator. 75

6.1 Four Discretization Methods 173

List of Figures

2.1 Three-phase SRM-IM setup. 9

2.2 The schematic of the position-sensorless 12/8 SRM drive. 10

2.3 Switching patterns of the asymmetrical half-bridge converter. (a) Magnetization. (b) Demagnetization. (c) Freewheeling. 11

2.4 Phase voltage and current in the voltage-pulse test. 13

2.5 Flux-linkage characteristic of the SRM. 14

2.6 Co-energy of the SRM at different rotor positions. (a) θ_A. (b) θ_B. 14

2.7 Torque characteristic of the SRM. 15

2.8 Classification of position-sensorless control of SRM drives. (a) Low-speed position-sensorless control. (b) High-speed position-sensorless control. 18

2.9 Overall block diagram of a low-speed position-sensorless SRM drive. 19

2.10 Induced current under pulse voltage injection with varying positions. 21

2.11 General diagram of full-cycle position estimation methods at low speed. 23

2.12 Control diagram of the lookup table-searching method. 26

2.13 Fourier analysis of phase inductance at a given current. 27

2.14 Linear regions in phase inductance profiles of a 12/8 SRM at a given current. 28

2.15 Overall block diagram of a high-speed position-sensorless SRM drive. 33

2.16 Principle of gradient detection methods. 35

2.17 General block diagram of the lookup table-searching method with mutual coupling mitigation. 40

2.18 Control diagram of SRM position observers. 41

2.19 Structure of the PLL-based position observer. 45

2.20 Position estimation using intelligent algorithms. (a) Fuzzy logic. (b) NN. 47

2.21 Position estimation using feature flux linkage. 50

2.22 General control diagram of wide-speed range position-sensorless control. 53

3.1 Pulse-injection-based position estimation methods. (a) Phase current and phase inductance. (b) Current derivative calculation in the conduction period. (c) Current derivative calculation in the idle-phase (injection) period. 61

3.2 Schematic diagram of the proposed position-sensorless control scheme. 63

3.3 Self-commissioning process for parameter identification of L_0 and L_1. 65

3.4 Block diagram of the proposed RPLL-based low-speed position estimation scheme for SRM drives. 67

3.5 Idle-phase inductance in three phases of a 12/8 SRM. (a) θ_{off}-θ_{on}>15°. (b) θ_{off}-θ_{on}=15°. (c) θ_{off}-θ_{on}<15°. 68

3.6 Linearization model of the proposed RPLL. 71

3.7 Nonlinear gain ζ in (3.14) with respect to the position and position error................72

3.8 Bode diagram of the proposed RPLL. 74

3.9 Self-commissioning for the proposed scheme. 80

3.10 Idle-phase inductance, phase current, and position estimation at 100 r/min without load. (a) θ_{on}=0° and θ_{off}=20°. (b) θ_{on}=0° and θ_{off}=15°. (c) θ_{on}=0° and θ_{off}=12°...82
3.11 Position estimation at other speeds without load. (a) 200 r/min. (b) 400 r/min........83
3.12 Experimental position estimation results (in sensor-based control) between the proposed scheme and the conventional phase-inductance vector method at 150 r/min. (a) Proposed scheme under the no-load condition. (b) Proposed scheme under the 30 N·m load condition. (c) Conventional method under the no-load condition. (d) Conventional method under the 30 N·m load condition. 86
3.13 Position-sensorless control at 200 r/min under load changes. 86
3.14 Position-sensorless control at standstill condition with load. 87
3.15 Position-sensorless control under speed variation from 150 r/min to 250 r/min. (a) Ramp speed response. (b) Step speed response..88
3.16 Validation of the speed reversal operation of the proposed sensorless control scheme...89
3.17 Position-sensorless control performance under increasing speed from 150 r/min (15% rated speed) to high speed. 90
3.18 Position estimation results of the proposed RPLL when using different L_1 values. 91
4.1 Illustration of pulse-injection-based position estimation methods. (a) Phase current and phase inductance. (b) Single-period pulse injection method. (c) Double-period pulse injection method. 95

4.2 Injected voltage and induced current of the pulse-injection-based position estimation method. 98

4.3 The control diagram of the proposed TSMC-based pulse injection. 109

4.4 Schematic diagram of the proposed position-sensorless control scheme. 109

4.5 Experimental results of the fixed-amplitude pulse injection method at 200 r/min with 10 N·m load. (a) Injection voltage and phase current. (b) Position estimation. 111

4.6 Experimental results of the proposed pulse injection method at 200 r/min with 10 N·m load. (a) Injection voltage and phase current. (b) Position estimation. 112

4.7 Position estimation results of the proposed pulse injection method at other low speeds with 10 N·m load. (a) 100 r/min. (b) 300 r/min. 113

4.8 The parameter sensitivity test of the proposed scheme at 200 r/min and 10 N·m load. 113

4.9 Comparison of negative torque ripples and copper losses in the idle phase. (a) Fixed-injection-amplitude method. (b) Proposed method. 115

4.10 Position-sensorless control under speed variation from 150 r/min to 250 r/min. (a) Ramp speed response. (b) Step speed response. 116

5.1 Three-phase torque of the SRM. 120

5.2 Feature flux linkage of the SRM at 15°. 122

5.3 Feature position detection: calculated flux linkage, reference flux linkage at 15°, and the estimated feature position. 123

5.4 Limitation of the conventional linear prediction method. 125

5.5 Vector graphs of the feature position. 127

5.6 Block diagram of the NSO for the SRM sensorless control. 127

5.7 The small-signal model of the proposed NSO. 135

5.8 Bode diagram of the position estimation with different pole values. 137

5.9 Schematic diagram of the proposed position-sensorless control. 138

5.10 Feature position detection by flux-linkage estimation at 500 r/min. (a) Calculated flux linkage, reference flux linkage at 15°, and the estimated feature position. (b) Estimated feature position in the mechanical cycle. 140

5.11 Experimental verification of the proposed NSO at 500 r/min. (a) Feature position vector. (b) Estimated harmonic vector. (c) Fundamental vector. (d) Estimated fundamental vector. 142

5.12 Comparative experimental results of the proposed observer and the conventional linear prediction method at 500 r/min. 144

5.13 The comparison of estimation errors between the proposed observer and the conventional linear prediction method at 500 r/min. (a) Position estimation errors. (b) Speed estimation errors. 145

5.14 Position estimation results with different control angles. (a) θ_{on} =0° and θ_{off} =15°. (b) θ_{on} =0° and θ_{off} =23°. 146

5.15 Estimation errors under ramp speed change from 300 r/min to 1000 r/min (rated speed). (a) Actual and estimated speeds. (b) Speed estimation errors. (c) Position estimation errors. 148

5.16 Estimation errors under step speed change from 300 r/min to 1000 r/min (rated speed). (a) Actual and estimated speeds. (b) Speed estimation errors. (c) Position estimation errors. 148

5.17 Comparative tests with the 15 N·m load disturbance at the half-rated speed.........149

5.18 Comparative experimental validation of the conventional linear prediction method, an in-loop-filter-based linear prediction method, and the proposed observer at 500 r/min, with a suddenly added large flux linkage error. (a) Block diagram of the in-loop-filter-based linear prediction method. (b) Position estimation results. 151

6.1 Flux linkage of a three-phase 12/8 SRM at different rotor positions, including |real flux linkage and its model results from (6.2). 156

6.2 The structure of the PLL for position estimation. 158

6.3 The structure of the SOGI-HPF. 159

6.4 Bode diagram of the SOGI-HPF. 161

6.5 Signal processing of the proposed position estimation method based on QFEs.....162

6.6 Design of the proposed QFE. 163

6.7 Illustration of the logic design of the proposed QFE. 164

6.8 Flow chart of the logic design of the QFE in one electrical cycle. 167

6.9 Full-cycle position estimation by combining the three-phase QFE's outputs. 168

6.10 Commutation angle settings of the motoring mode and generating mode. 170

6.11 Illustration of the proposed method in the generating mode. 171

6.12 Flux estimators' phases at ω_0 with different control frequencies when using four discretization schemes (ω_0 =837.76 rad/s, i.e., 133.3 Hz and rated speed). (a) Fundamental flux estimator. (b) Quadrature flux estimator. 174

6.13 The overall control diagram of the proposed position-sensorless control. 176

6.14 Experimental results of three-phase phase current, calculated stator flux, and trigger signals at 500 r/min. 177

6.15 Experimental results of proposed Flux estimation from QFEs at 500 r/min. 178

6.16 Comparative position estimation control results at 500 r/min. (a) Proposed scheme not using magnetic characteristics. (b) Conventional method using magnetic characteristics. 179

6.17 Position-sensorless control performance of the proposed scheme under 15 N·m load change at 800 r/min...180

6.18 Position-sensorless control performance of the proposed scheme under speed changes from 500 r/min to 1000 r/min: (a) Slope speed command. (b) Step speed command. 182

6.19 Position-sensorless control performance at 500 r/min with 15 N·m load. (a) Using fixed commutation angles (θ_{on}=0° and θ_{off}=20°). (b) Using optimized torque sharing function method. 183

6.20 Position-sensorless control result in the generating mode at 500 r/min with -15 N·m load. 184

6.21 Position estimation results when using different voltages for flux linkage calculation at 500 r/min with 15 N·m load. (a) Voltage comparison. (b) Position estimation error comparison. 186

6.22 Position estimation results with current measurement errors around 500 r/min with 15 N·m load. (Condition-I: accurate current measurement, condition-II: 90% gain error, and condition-III: 90% gain error and 2 A offset). (a) Position estimation error and currents. (b) Zoom-in currents. 187

7.1 Wide-speed range position-sensorless control scheme by combining the flux-linkage-based method at high speed and the injection-based estimator at low speed. 191

7.2 Wide-speed range SRM sensorless control by combining the proposed QFE and the pulse-injection-based method. (a) Overall performance. (b) Zoom in position estimation results at a transition point ω=350 r/min. 193

Chapter 1

Introduction

1.1 Background and Motivation

Switched reluctance motors (SRMs) have attracted extensive attention in traction applications [1]. Different from permanent magnet synchronous motors (PMSMs) and induction motors (IMs), the rotor of the SRM is constructed by laminated silicon steels without magnet materials and magnetizing windings. Therefore, the SRM has advantages in lower manufacturing costs, robust mechanical strength, and higher efficiency, making it a potential option for driving systems.

Due to the doubly salient structure of the SRM, the high nonlinearity increases its control complexity. For accurate speed, current and torque control, phase commutation, including turn-on and turn-off angles of the semiconductor switches in the SRM converter, should be determinate [2]. Thus, position sensors such as incremental encoders, resolvers, Hall sensors, and tachometer generators are installed to obtain accurate rotor position. However, the installation of the position sensors has the following drawbacks:

1) Increasing cost and volume. The high price of the position sensor limits the market competitiveness of low-cost and low-power SRM drives. The extra size of the position sensor is unacceptable for specific applications, such as air-conditioning compressors.
2) Reducing the reliability and robustness. The position sensor and its interface circuits would be affected by temperature, humidity, vibration, and other ambient conditions. The working environment dramatically interferes with the regular work of the sensor and reduces its accuracy.

To solve the issues, position-sensorless control of the SRM has been receiving increasing attention in the research community in these twenty years [3]. Due to the doubly salient characteristics, the rotor position can be estimated from the flux linkage or the stator inductance of the SRM via measuring terminal voltages and currents. Numerous position estimation methods have been proposed to obtain the rotor position of the SRM over a wide speed range.

However, the position estimation process is often complicated for the SRM due to its deep magnetic saturation. Flux linkage or stator inductance is a nonlinear function of both the rotor position and phase current. The position estimation from the magnetic characteristics often relies on prestored flux linkage or stator inductance profiles. However, the usage of predefined magnetic characteristics has some drawbacks, such as

1) The acquisition of magnetic features needs knowledge of the motor prototype in the finite element analysis (FEA) or requires time-consuming offline measurement [4].
2) The sensorless control algorithm has low generality and cannot be used for different SRMs if motor characteristics are unknown.

3) The storage of three-dimensional magnetic data requires larger memory, which is not attractive for low-cost applications.
4) The position estimation algorithms are parameter dependent and parameter sensitive.

The purpose of the Ph.D. thesis is to propose universal position-sensorless control schemes for SRM drives without using offline measurement of magnetic characteristics. The rotor position and speed can be estimated via online parameter self-commissioning processes or without using any magnetic characteristics. Wide-speed range position-sensorless control from the standstill to the rated speed are also realized. This work aims to facilitate the position-sensorless control to be a more general-purpose solution for SRMs in various industrial applications.

1.2 Contributions

The author has contributed to several original developments on general-purpose position-sensorless control schemes for SRM drives in a wide-speed range. The contributions are summarized as follows:

1) A low-speed position-sensorless control approach using a regional phase-looked loop (RPLL) for general-purpose SRM drives.
2) A new pulse injection method for low-speed SRM sensorless operation with reduced torque ripples and copper losses.
3) A nonlinear state observer (NSO) for high-speed SRM position-sensorless control using simplified feature flux linkage.
4) A magnetic-characteristic-free high-speed position estimation strategy for SRM drives.

5) Full-speed position-sensorless control with a combination of low-speed and high-speed methods.

1.3 Outline of the Thesis

This thesis develops universal position-sensorless control schemes for SRMs in the full-speed range. Several position estimation strategies are proposed to estimate the rotor position without offline measurement or FEA.

Chapter 2 introduces the fundamentals of SRM drives and a literature review of existing SRM position-sensorless control methods. The test bench of a 5.5-kW 12/8 SRM is first introduced. The SRM modeling including mathematical equations, flux linkage characteristic measurement, and derivation of the nonlinear torque profile are then discussed. After that, the state-of-art research of low-speed and high-speed sensorless control methods are compared and analyzed in the literature review.

Chapter 3 introduces a universal low-speed position estimation scheme based on pulse-voltage injection for SRM drives. In conventional low-speed sensorless control methods, magnetic characteristics are often used for position estimation, but it requires offline measurement and reduces the generality of sensorless control algorithms. To solve the issues, a new position estimator based on an RPLL is designed. The approach utilizes a self-commissioning process to capture the unsaturated inductance adaptively at the initial stage. The RPLL is then adopted to estimate the full-cycle rotor position from the idle-phase inductance during sensorless operation. The speed-reversible sensorless control capability is also realized by a simple heterodyne design. Furthermore, stability analyses and parameter design are given to prove the robust local stability and convergence. Finally, comparative experimental validation is conducted on a 5.5-kW 12/8 SRM setup to verify the proposed method's effectiveness under both no-load and load conditions.

Chapter 4 is an extended work of Chapter 3, where the pulse injection scheme is improved to reduce torque ripples and copper losses caused by high-frequency injection voltages. The high-frequency injection is necessary for low-speed position estimation, but due to the nonlinear inductance profile, the amplitude of induced current increases significantly around the unaligned position. It results in large copper losses and torque ripples in idle phases. To mitigate this problem, this chapters introduces a new pulse injection scheme with magnitude regulation based on terminal sliding-mode control. The amplitude of pulse voltages is adjusted online through a nonlinear control law, and the induced current can be maintained at a minimal level over the whole idle-phase period. Moreover, the adverse impacts of motor parameter uncertainties are eliminated. The position estimation is then realized by the RPLL-based position estimator designed in Chapter 3. As a result, the proposed scheme is able to reduce the torque ripple and power loss significantly without the need of magnetic characteristics. The effectiveness is experimentally validated with comparisons of the conventional method.

Chapter 5 is focused on medium- and high-speed position estimation of SRM drives. The chapter proposes an NSO for robust position-sensorless control of SRM drives over medium- and high-speed range. A classical reference flux linkage method is adopted to capture a feature position of the SRM, which avoids the use of three-dimensional magnetic characteristics and has better universality. However, the estimation accuracy of this method would be easily deteriorated due to flux linkage errors. To ease the problem, the NSO is developed to enhance the robustness against flux linkage distortions for a more accurate position and speed estimation. This observer can reconstruct complete position information from a low-resolution feature position. The adverse impact of flux linkage errors is investigated through a novel small-signal approximation analysis and then suppressed by an augmented state estimator. A parameter design scheme is also given to ensure the stability of the observer and improve the capability in distortion suppression. To baseline the performance, comparative experimental validation between the NSO and a widely used linear prediction method is conducted. The results show that the proposed strategy can improve the overall position-sensorless control performance in both the steady and transient states.

In Chapter 6, the high-speed sensorless control method is further improved, which can estimate the rotor position at high speed without using any magnetic characteristics of SRMs. Although the method proposed in Chapter 5 only uses a simple self-commissioning process to capture feature flux linkage information, the developed strategy in the chapter does not require any offline or online parameter measurement/learning process. Hence, the implementation of the high-speed position-sensorless control would be further simplified. This improvement is achieved by using a novel quadrature flux estimator (QFE) that can extract the fundamental flux and its quadrature from the real-time flux linkage. DC components and flux harmonics caused by the magnetic saturation effect can also be suppressed due to the QFE's adaptive bandpass capability. Therefore, the proposed method can reduce the nonlinearity in SRM flux linkage and derive simple sine-cos position signals. Afterward, the rotor position and speed can be estimated from the fundamental flux signals using a three-phase phase-locked loop (PLL). To baseline the advantages, comparative experimental validation with the conventional method is conducted. The proposed scheme can achieve the same estimation accuracy as the conventional method even though no magnetic characteristics are used.

In Chapter 7, a wide-speed range position-sensorless control design by combining the proposed low-speed methods and high-speed methods is introduced. A speed-related switching function is proposed to determine the operating range of both the low-speed and high-speed position observers. Experimental results are provided to prove the robust and smooth transition in the wide-speed range position-sensorless control.

In the end, Chapter 8 concludes the research contributions in this thesis and discusses future

Chapter 2

Fundamentals of SRM Drives and Literature Review of Position-Sensorless Control

2.1 Fundamentals of SRM Drives

The SRM has a doubly salient structure in rotors and stators, with concentrated windings fully pitched across the stator poles. The torque production of the SRM requires sequential energization on each phase towards a minimum reluctance path, requiring independent phase control capability in an SRM drive [5]. Current regulation is often realized by hysteresis control or pulse-width modulation (PWM), with real-time rotor position feedback to determine the phase commutation instants [2]. In this thesis, a 5.5 kW SRM-induction machine (IM) test bench is built, as shown in Figure 2.1. The parameters of the SRM-IM test bench are given in Table 2.1.

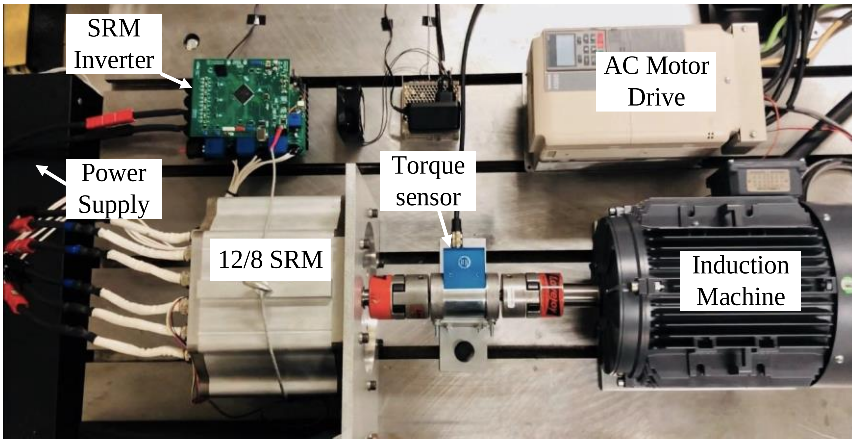

Figure 2.1 Three-phase SRM-IM setup.

Table 2.1 Parameters of the SRM-IM Test Bench

Parameter	Value	Parameter	Value
Number of stator poles	12	Number of rotor poles	8
Rated Power	5.5 kW	Rated Speed	1000 r/min
Rated Voltage	72 V	Phase resistance	18.3 mΩ
Rated Speed (IM)	3530 r/min	Rated Load (IM)	30 N·m
Rated Power (IM)	11 kW	Rated Voltage (IM)	230 V

2.1.1 Configuration of the Three-Phase SRM Drive

The three-phase 12/8 SRM drive is illustrated in Figure 2.2, composed of a three-phase asymmetric half-bridge converter, current sensors, a microcontroller, gate drives, position estimation algorithms, and DC power supplies. Unlike the conventional three-phase full-bridge AC inverter, the asymmetric half-bridge inverter adopts two IGBTs and two fast recovery isolated diodes to configure an asymmetric half-bridge. The converter modulates bipolar phase voltages to generate unipolar phase current as the electromagnetic torque of the SRM is independent of current directions. Each phase in the asymmetric converter can be controlled separately, offering fault-tolerant control capability and flexibility in phase torque control. The gate signals for semiconductor switches are given by gate drives, of which commands are generated in the controller board according to the speed, current or torque reference. The rotor position and speed feedbacks are needed for accurate speed and current control, which are often measured by a position sensor. In position-sensorless drives, the position and speed information are obtained by the position estimation algorithm.

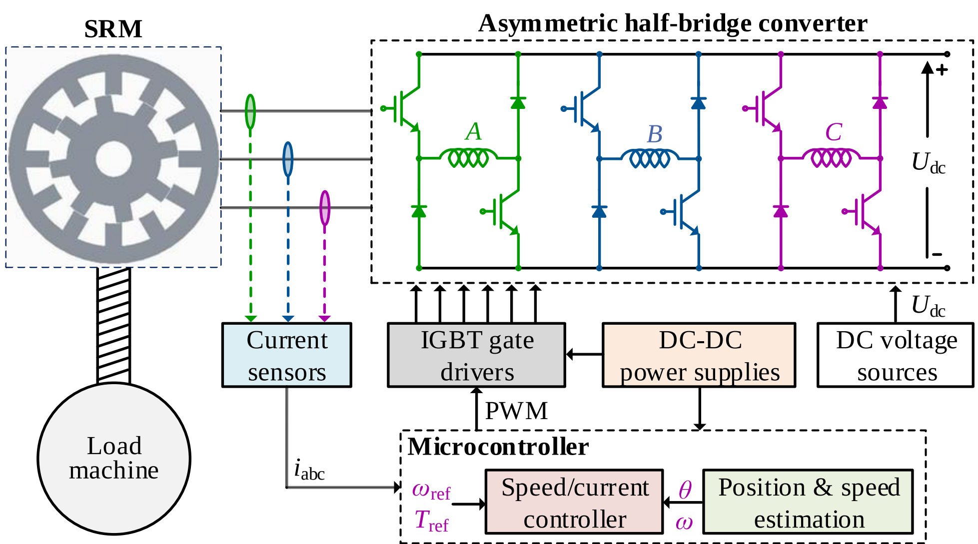

Figure 2.2 The schematic of the position-sensorless 12/8 SRM drive.

The asymmetric half-bridge converter has three switching patterns for one phase, as shown in Figure 2.3. The first switching state happens when the two switches are turned on, as presented in Figure 2.3(a). The DC-link voltage $+U_{dc}$ is added to the stator and increases the stator current, which is a magnetization process. When both the two switches are turned-off, as shown in Figure 2.3(b), the winding is demagnetized under a negative phase voltage of -U_{dc}, forcing the energy stored in the phase windings flows back to the DC bus. The third pattern is freewheeling as shown in Figure 2.3(c), in which one switch is turned off and another one is turned on. In this case, the phase current only flows internally under a zero-phase voltage.

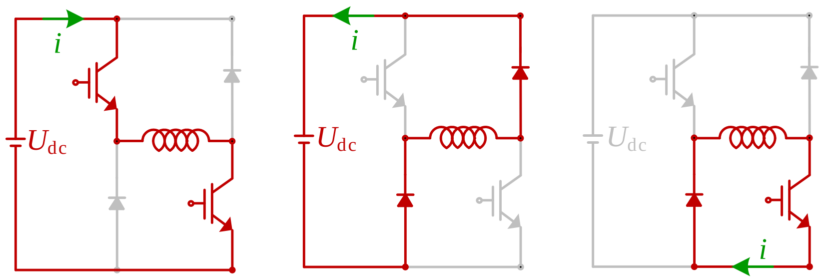

Figure 2.3 Switching patterns of the asymmetrical half-bridge converter. (a) Magnetization. (b) Demagnetization. (c) Freewheeling.

A three-phase asymmetric converter is designed for the 5.5 kW 12/8 SRM test bench. The power converter is rated for 300V/50A. The Infineon 600V/100A IGW10060H3 high-speed IGBT and IDW100E60 fast switching emitter-controlled diode are selected for the SRM inverter. Six isolated 12V to 15V/-9V DC-DC converters are used to supply the six IGBT gate drives (FOD8316). LEM LAH-50P (50-A RMS current sensor) and LEM LV-25P (500-V voltage sensor) are used for the SRM inverter. To guarantee accurate voltage and current measurement, another isolated 12V to ±12V DC-DC converter (PQDE6W-Q24-D12-D) is used to power the sensors and measurement circuits. The isolated power supply can avoid the switching noises from the IGBT, offering accurate current and voltage samplings. By using a 14-bit external analog-digital converter (AD7357) with a differential input structure (by AD8138), the sampling error is less than 5/8192 = 0.06%. In terms of the control board, the DSP TMS320F28335 is employed as the microcontroller, the switching and control frequencies are both set as 20 kHz.

In addition to the inverter, the three-phase 12/8 SRM-IM setup is built. The SRM is served as the test machine, which is powered by the designed three-phase asymmetric-bridge inverter, and an IM is connected as the load, as shown in Figure 2.1. The IM is powered and controlled by a commercial AC motor drive, YASKAWA AC Drive-A1000. Since the rated voltages of the SRM and IM are different, the SRM-IM test bench is not connected in back-to-back. To realize generating operation of either the IM or SRM, a programming load, NHR Model 4700 LXI DC Load, is connected to the DC-link voltage for absorbing the regenerative energy.

2.1.2 Modeling of the SRM

Due to the double saliency, the magnetic characteristic of the SRM is highly nonlinear and presented as a function of phase current and rotor position. The magnetic characteristic can be obtained from the FEA with known parameters of the machine prototype. Alternatively, offline measurement can be performed to derive magnetic characteristics for a commercial SRM. l.

In this thesis, the flux-linkage characteristic is measured experimentally and used to calculate the torque characteristic. The measurement procedure is that by injecting a short-period pulse voltage at different rotor positions, the induced pulse current is measured, and the flux-linkage at a specific position can be calculated by its voltage equation as follows [4]:

$$\lambda(\theta,i)=\int(u-Ri) \tag{2.1}$$

where $\lambda(\theta, i)$ is the flux-linkage, θ is the rotor position, i is the phase current, u is the phase voltage, and R is the stator resistance.

The measurement result at one rotor position is shown in Figure 2.4. As can be seen, with the short-period voltage pulse, the phase current can reach 160 A. By using the equation (2.1), the flux linkage at the position θ with respect to the current ranging from 0 to 160 A can be obtained. Afterward, by repeating the tests for all positions from 0 to 22.5 mechanical degrees (0 to 180 electrical degrees), the flux-linkage characteristic of the SRM can be derived, as shown in Figure 2.5. The other characteristic from 22.5 degrees to 45 degrees can be obtained due to the symmetry. Without specific mention, the rotor position is expressed in mechanical in the thesis. It is worth noting that the rotor of the SRM should be clamped by clamping tools during the tests to avoid the rotor rotating caused by the pulse injection.

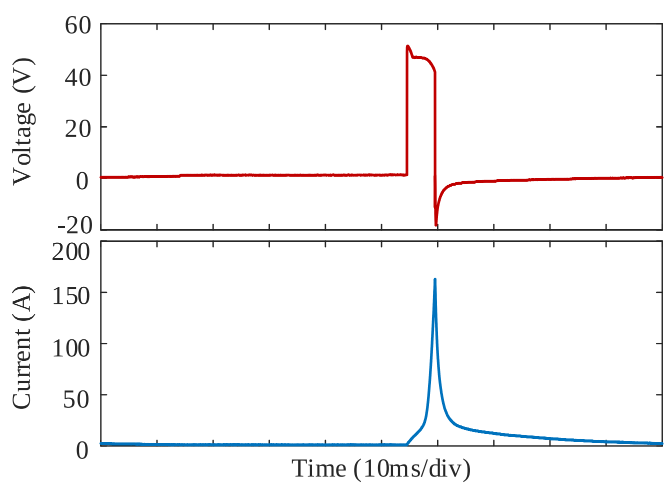

Figure 2.4 Phase voltage and current in the voltage-pulse test.

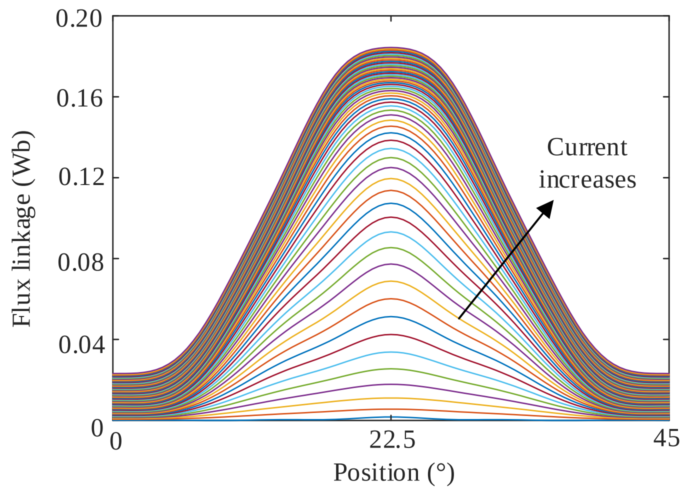

Figure 2.5 Flux-linkage characteristic of the SRM.

After obtaining the flux-linkage characteristic, the torque characteristic can be calculated by the rate of change in magnetic co-energy W with the rotor position θ [6]. The co-energy of the SRM at different rotor positions are illustrated in Figure 2.6. The instantaneous torque derivation at a given phase i_0 is expressed in (2.2).

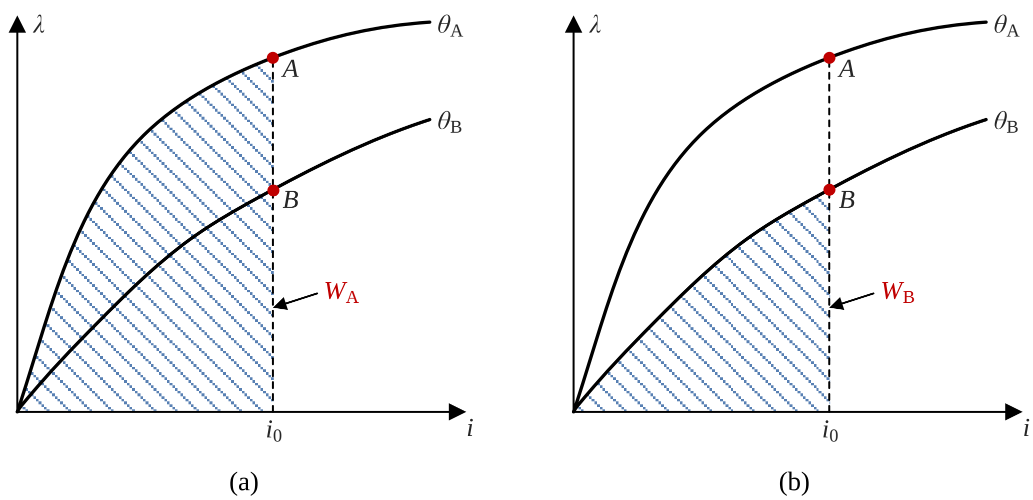

Figure 2.6 Co-energy of the SRM at different rotor positions. (a) θ_A. (b) θ_B.

$$T_e(\theta, i_0) = \frac{W_A - W_B}{\theta_A - \theta_B} = \frac{\int \lambda(\theta_A, i_0) di - \int \lambda(\theta_B, i_0) di}{\theta_A - \theta_B}. \tag{2.2}$$

As long as the position interval between θ_A and θ_B is small enough, the electromagnetic torque at each rotor position and each phase current can be derived accurately based on (2.2). As a result, the derived torque characteristic is shown in Figure 2.7.

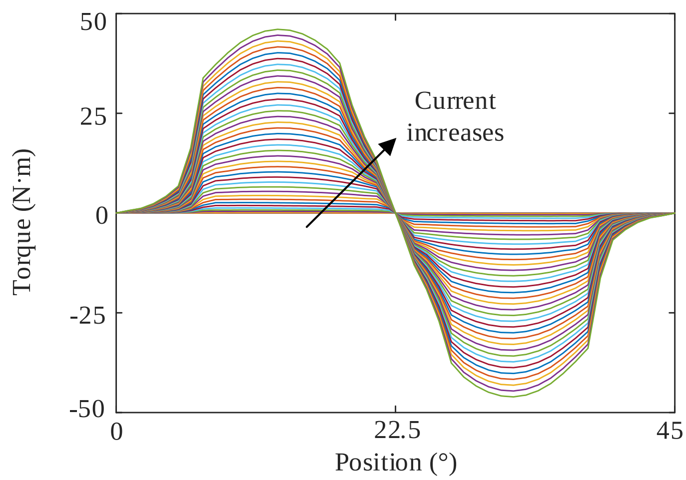

Figure 2.7 Torque characteristic of the SRM.

The mathematic model of the SRM can be formulated using the measured magnetic characteristics. The voltage equation given in (2.3) can be expanded by taking the magnetic saturation and back electromotive force (back-EMF) into account.

$$u = Ri + \frac{d\lambda(\theta, i)}{dt} \tag{2.3}$$

Substituting the relationship between the flux linkage λ and the self-stator inductance L, expressed by

$$\lambda(\theta, i) = L(\theta, i) \cdot i, \tag{2.4}$$

into the voltage equation gives:

$$u = Ri + L_{\mathrm{inc}}\left(\theta, i\right)\frac{di}{dt} + e_{\mathrm{mf}} \tag{2.5}$$

where

$$L_{\mathrm{inc}}\left(\theta, i\right) = L(\theta, i) + i\frac{\partial L(\theta, i)}{\partial i} \tag{2.6}$$

$$e_{\mathrm{mf}} = i\omega\frac{\partial L(\theta, i)}{\partial \theta}, \tag{2.7}$$

the L_{inc} is the incremental inductance, e_{mf} is the back-EMF, and ω is the rotor speed.

With neglection of magnetic saturation, stator inductance is independent of the phase current. Thus, the electromagnetic torque of the SRM can be expressed analytically by

$$T_{\mathrm{e}}(\theta, i) = \frac{1}{2}\frac{dL(\theta)}{d\theta}i^2. \tag{2.8}$$

Considering the magnetic saturation, analytical torque expression is challenging. Instead, the torque characteristic lookup table can be used for torque calculation.

2.2 Literature Review of Position-Sensorless Control of SRM Drives

Position-sensorless control of the SRM drive is a hot spot in academia and industry due to its advantages of low costs and sensor fault-tolerance control capability. The doubly salient structure makes the flux linkage and stator inductance of the SRM being position-related functions. The rotor position can be estimated from the magnetic quantities calculated by terminal voltage and current measurements. In the last decades, tremendous position-sensorless control schemes for SRM drives were proposed, covering standstill operation to high speeds.

According to the available speed region, major position-sensorless control techniques can be roughly categorized into high-speed estimation schemes and low-speed estimation schemes, as presented in Figure 1. High-speed sensorless control is realized by monitoring the motor states during phase excitation periods. Flux linkage or inductance can be obtained from the SRM model during phase conduction periods. The acquisition of magnetic characteristics possesses a high signal-to-noise ratio (SNR) due to the large back electromagnetic force (back-EMF) at high speed, thereby ensuring accurate position estimation. With a decreasing rotor speed, the low back-EMF is not able to guarantee precise flux linkage and inductance calculation in a noisy environment. Alternatively, by means of additional high-frequency pulse voltage injection into idle phases, the magnetic quantities are observable, making the sensorless control feasible at zero and low speeds.

This section aims to present a comprehensive review of the state-of-the-art solutions for position-sensorless control of SRM drives. A schematic overview, performance evaluation, and existing challenges will be analyzed.

2.2.1 Low-Speed Position-Sensorless Control

Low-speed position-sensorless control is realized by injecting high-frequency pulse voltages into the idle-phase stator. Figure 2.9 present a general control diagram of low-speed sensorless control methods of an N-phase SRM. A speed regulator works as an outer loop controller and generates torque reference. A torque control scheme can be adopted to maximize toque output, reduce torque ripples, and give current commands. The torque

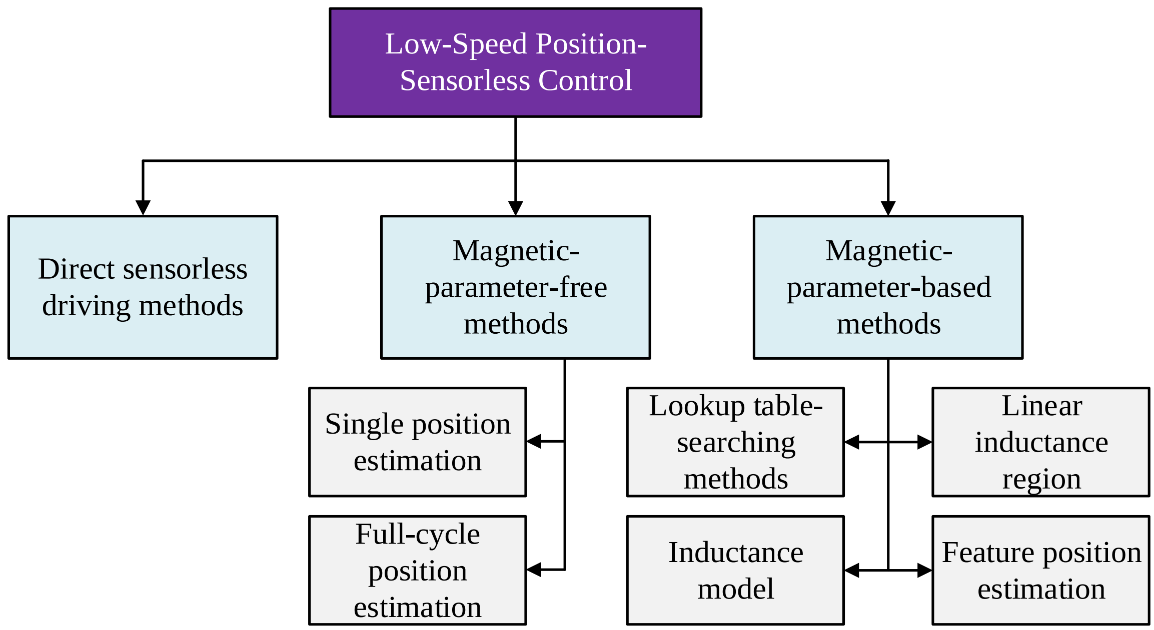

(a)

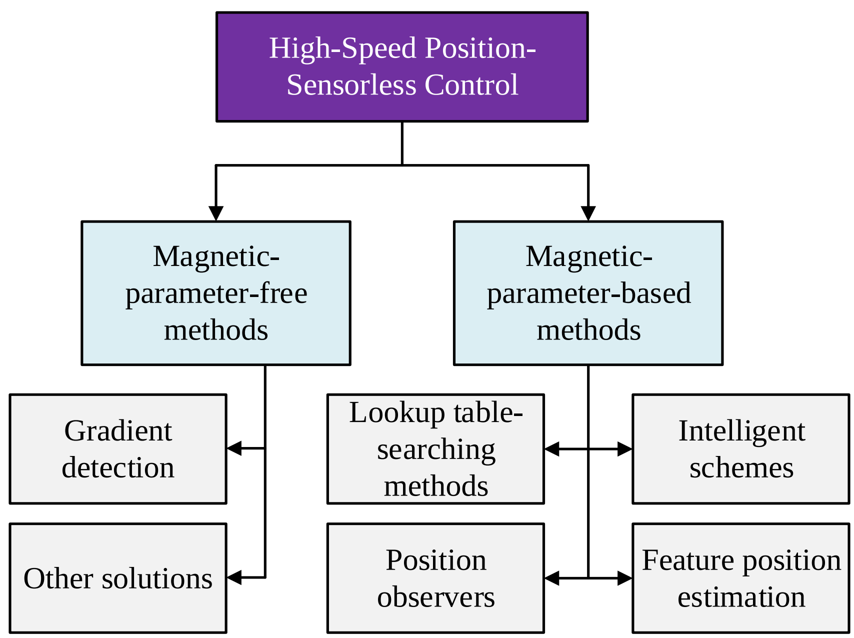

(b)

Figure 2.8 Classification of position-sensorless control of SRM drives. (a) Low-speed position-sensorless control. (b) High-speed position-sensorless control.

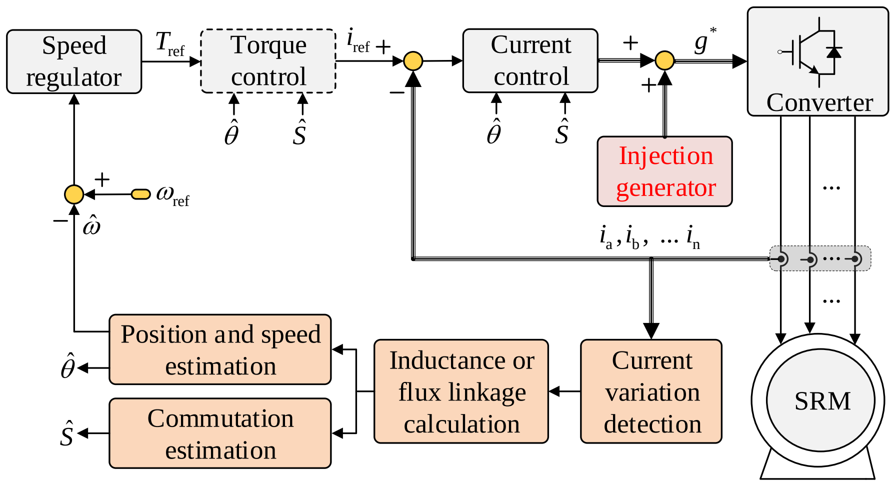

Figure 2.9 Overall block diagram of a low-speed position-sensorless SRM drive.

control is optional but often required for high-performance SRM drives. The reference current is then tracked by the current controllers in all phases. The pulse voltage with adjustable magnitudes and duty cycles is injected into idle phases by modifying the gate command g^* and induces high-frequency currents. The current vibration can be measured for inductance or flux linkage calculation at low speed, including the standstill. The estimated magnetic information can be used for position and speed estimation or predicting the phase commutation instants. With a short period of pulse injection, the induced currents in idle phases is low and can keep the magnetic field unsaturated. Thus, the stator inductance in idle phases are unsaturated and independent of load conditions, facilitating position estimation via inductance detection.

Given the superiority, many research works on low-speed sensorless control have been conducted in literature. This section classifies the low-speed techniques into direct sensorless driving methods, magnetic-parameter-free position estimation methods, and magnetic-parameter-based position estimation methods.

2.2.1.1 Direct Sensorless Driving Methods

For high-speed SRM drive systems, such as compressors and fans, starting stage sensorless control is temporary and does not require high dynamic performance. Direct sensorless driving methods are straightforward for sensorless starting control [7]–[10]. These techniques do not estimate the exact rotor position; instead, the low-speed operation is achieved by selecting the optimal driving phase for torque production and the injection phase for position estimation.

A representative method proposed in [7] injects high-frequency voltage pulses into all phases, and the magnitudes of induced currents are compared. According to the current magnitude order, the phase inductance over one electrical cycle is divided into several sectors. The phase located at the inductance rising region, which gives a positive torque, is selected as the initial driving phase at the standstill. This scheme is feasible for all conventional SRMs, but it cannot support sensorless control in rotating conditions. In [8], a double-current-thresholds solution based on idle-phase pulse injection was analyzed to control the SRM at zero and low speed. As illustrated in Figure 2.10, a low current threshold, located around the aligned position θ_a, is used to determine the idle phases for position sensing, and a high current threshold around the unaligned position θ_u works for conduction phase selection. The approach does not need all-phase pulse injection during normal operation and is able to control the SRM at both zero and low speeds. An alternative direct driving method using one current threshold for the four-quadrant operation was proposed in [9]. The current threshold is predefined by Hall position sensors and is used to determine the phase commutation instant. Furthermore, the threshold-based method was extended to enhance the phase fault-tolerant control capability in [10], adopting a current threshold in idle-phase periods and a flux linkage threshold for conduction phases in phase-fault driving conditions.

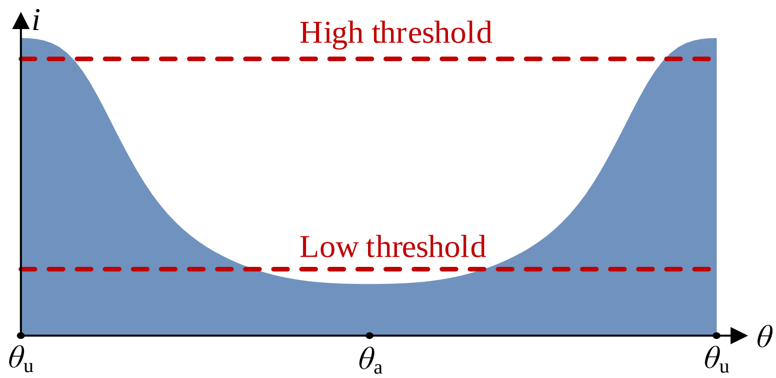

Figure 2.10 Induced current under pulse voltage injection with varying positions.

The direct sensorless control methods are simple for implementation and are motor-parameter-independent, but a common drawback is that these schemes cannot estimate the rotor position. The phase commutation is fixed in various operating conditions. Accurate current and torque control, which requires real-time rotor position feedback, would be infeasible.

2.2.1.2 Magnetic-Parameter-Free Position Estimation

Accurate position estimation is indispensable in high-performance SRM drives to regulate the rotor speed, phase current, and output torque optimally. Stator inductance calculated from the high-frequency induced current carries rotor position information, which can be used for position estimation. With the same advantage as the direct driving methods that do not need machine magnetic characteristics, magnetic-characteristic-free position estimation schemes are potential solutions for low-speed sensorless operation [11]–[18].

A. Single Position Estimation

The first category of model-free position estimation methods was adopted to estimate a single rotor position of the SRM. Initial rotor position estimation belongs to the single position estimation as it is enabled at the starting stage only. Linear regression position estimation methods using quadratic polynomial and Type-V exponent were proposed in [11] and [12] for initial position estimation, respectively. The schemes adopt general inductance models to identify an approximated inductance-position relationship. Injecting voltage pulses in all phases is able to obtain the regression coefficients. In [13], another initial position estimation method using bootstrap circuits was proposed. The inductance is calculated by monitoring the charging time to the peak current value in the bootstrap circuit, and the rotor position can be estimated through a linear inductance model. Note that the linear regression and bootstrap approaches can only estimate an initial position and are unavailable for sensorless control in driving conditions.

To realize position estimation during low-speed operation, the aligned position, reflecting a critical position at which the stator pole and the rotor pole overlap, can be detected with the independence of magnetic characteristics. One approach is to estimate the phase inductance intersection point [14], [15]. The two-phase intersection corresponds to the aligned position or the unaligned position in the remaining phase. Repeating the intersection detection for all phases in sequence, the detected feature positions could be used to estimate full-cycle rotor position over an electrical cycle. Compared to the conventional pulse injection that only calculates the phase inductance in idle phases, the approaches need full-cycle inductance information, which can be obtained from both the idle phase and the conduction phase. A typical way to calculate the conduction-phase inductance is to measure the current ripples caused by the current hysteresis control [14]. However, it causes a limitation that the inductance acquisition is affected by magnetic saturation, which may lead to deviation in aligned position detection under load conditions. Moreover, since the rotor position detection is only available at a critical position, the instants of position estimation are discontinuous. Thus, the inductance intersection detection methods are unavailable at the standstill and require initial position estimation discussed early.

B. Full-Cycle Position Estimation

Different from the single position estimation that obtains limited position information, continuous position estimation methods without SRM magnetic parameters are capable of offering higher estimation accuracy [16]–[18]. A general diagram of the full-cycle position estimation at low speed is presented in Figure 2.11. The core idea of the full-cycle position estimation is to assume a sinusoidal inductance characteristic of the SRM. All-phase inductances calculated from the current variation are transformed by Clark transformation. This coordinate transformation can project the inductor vectors onto an orthogonal coordinate system, which derives sin-cos functions with the rotor position. Afterward, the rotor position can be estimated by arctangent calculation. The idea simplifies the modeling of the SRM, and the position estimation process is as simple as well-known AC machines, i.e., PMSMs.

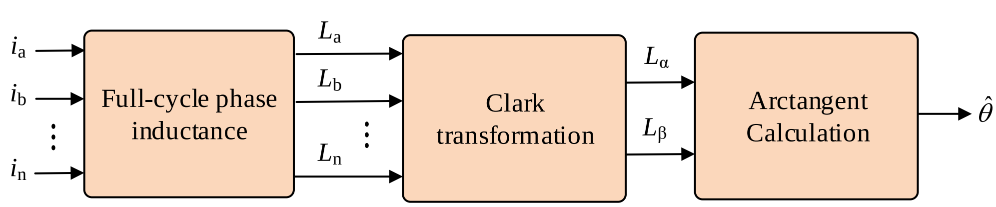

Figure 2.11 General diagram of full-cycle position estimation methods at low speed.

The first attempt of the phase inductance vector method was to estimate the initial position as analyzed in [16]. Same as the aforementioned current magnitude comparison scheme for direct sensorless driving [7], three idle phases are injected by voltage pulses simultaneously to calculate the phase inductance at the standstill. The initial rotor position can then be calculated by coordinate transformation and arctangent functions. Modified research was proposed in [18] for initial position estimation with reduced interference caused by modeling errors. In [17], the phase inductance vector scheme was extended to running conditions. The full-cycle phase inductance derived from both the idle and conduction phases is used for position estimation. Notably, although existing research is focused on a three-phase machine, the phase inductance vector method can be extended to multiphase SRM.

Moreover, the inductance calculation methods proposed in [17] and [18] utilize the current variations under positive and negative injection periods as expressed by (2.9). It cancels the ohmic resistance drop and back-EMF in incremental inductance calculation. A potential benefit is that the available speed range for pulse injection methods can be expanded, facilitating more accessible transition design with high-speed position estimation methods for full-speed sensorless control.

$$L_{\mathrm{inc}}(\theta) = \frac{2u_{\mathrm{inj}}}{di/dt|_{\mathrm{P}} - di/dt|_{\mathrm{N}}} \tag{2.9}$$

where the subscript ‘P’ and ‘N’ denote the positive and negative voltage injection, and u_{inj} is amplitude of injection voltages.

Although the phase inductance vector methods show advantages in continuous position estimation and parameter independence, their accuracy suffers from the magnetic saturation effect since the inductance is assumed to be current independent in these approaches. Therefore, the phase inductance vector schemes in [16]–[18] are suitable for applications with no loads or light loads. Improvements on such schemes can be achieved by involving some *a priori* magnetic characteristic information, which are categorized in the following sections.

2.2.1.3 Magnetic-Parameter-Based Position Estimation

Magnetic-characteristic-based position estimation methods are superior in estimation accuracy at low speeds, which estimate the rotor position based on *a priori* knowledge of the SRM inductance or flux linkage characteristic. Among the existing methods, the usage of magnetic characteristics could be the complete magnetizing data, partial regions, or several feature points. Regardless of the approaches, the magnetic characteristics need to be obtained from either offline/online measurement or the FEA.

A. Lookup Table-Searching Methods

Searching prestored lookup tables of phase inductance is straightforward for position estimation [19]–[24]. A general control diagram is presented in Figure 2.12. The injection phase can be first determined by comparing the magnitude orders of all phases, and then the rotor position is estimated through the inductance-position-current lookup table [19], [20]. The position estimation accuracy is directly associated with the inductance calculation. For more accurate inductance acquisition, the measurement of high-frequency induced current can be improved using a multiple current sampling method with online least-square fitting [21]. In [22], the authors proposed a numerical method to solve the initial position from an optimization problem based on the FEA inductance characteristic. The numerical technique shows robustness to inductance parameter mismatch and thus enhances the estimation accuracy.

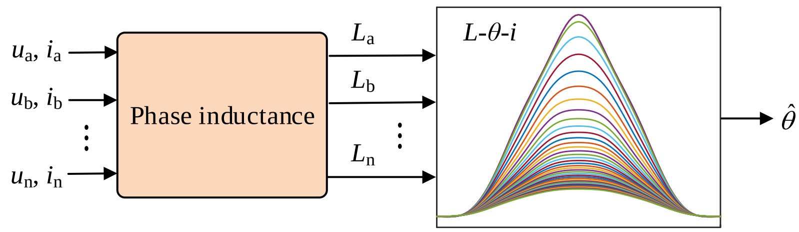

Figure 2.12 Control diagram of the lookup table-searching method.

In aforementioned works, only the motoring conditions and standstill states are considered. According to the defined operating quadrant, two inductance lookup tables in the inductance increasing and decreasing regions can be used for position estimation [23]. Furthermore, an interesting high-frequency voltage injection method inspired by AC machine sensorless control was analyzed in [24]. Instead of injecting voltage pulses into idle phases only as conventional approaches, a pulsating voltage is superimposed on the voltage command uninterruptedly. The resultant high-frequency current is extracted by highpass filters, of which positive or negative current sequences contain rotor position information. The prestored magnetic characteristics are used to adjust the injection amplitude according to load conditions for accurate position estimation. The method in [24] is an attempt to employ mature sensorless control techniques in AC machines for SRM drives. Still, the adverse effect of injected signals on torque ripples would be aggravated.

B. Inductance Model

For a concise sensorless SRM drive, storing complicated magnetic characteristics is not attractive since it occupies large memory and requires more offline effort in parameter measurement. Some research works adopt inductance models for position estimation to save the storage memory [25]–[27]. Since the phase inductance is distributed periodically with respect to the rotor position, a general inductance model can be presented by a Fourier series form, as expressed by:

$$L(\theta,i)=L_0(i)+L_1(i)\sin(N_r\theta+\varphi_1)+\sum_{k=2}^{\infty}L_k(i)\sin(kN_r\theta+\varphi_k)) \tag{2.10}$$

where $L_0(i)$, $L_1(i)$ and $L_k(i)$ represent the DC inductance, the first inductance harmonic's amplitude (also known as the fundamental inductance), and k-th inductance harmonic's amplitude, respectively. φ_k denotes the phase. N_r is the number of rotor poles. The Fourier analysis of phase inductance of a three-phase SRM at a given current is illustrated in Figure 2.13.

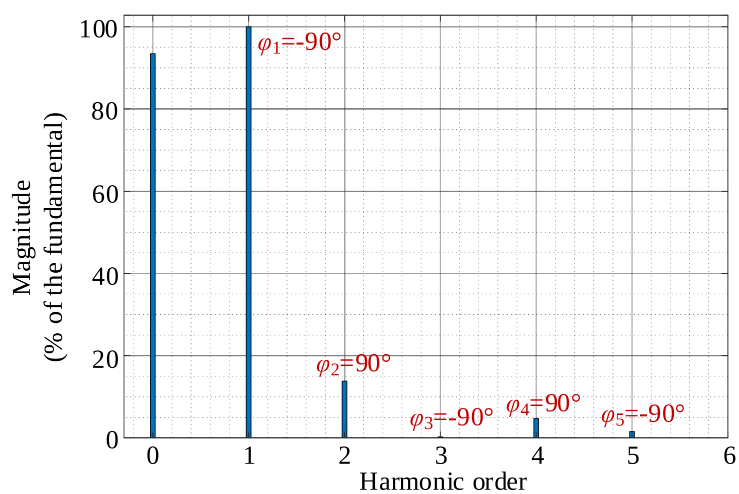

Figure 2.13 Fourier analysis of phase inductance at a given current.

On this basis, a simple inductance Fourier model considering the DC inductance and its first harmonic was used in [25] to estimate the rotor position through an arccosine function. This model ignores other harmonic components and may result in a modeling mismatch. As an upgrade, the second inductance harmonics can be considered in the inductance model, as proposed in [26], of which model coefficients are fitted by polynomial current functions. In [27], the second inductance harmonic model was also employed, while the optimal inductance region was selected for more accurate position estimation. In existing studies of inductance Fourier models, the model with maximum secondary inductance harmonic can offer good estimation accuracy.

C. Linear Inductance Region

Model-based position estimation at low speed can be simplified by using linear inductance characteristics [28]–[32]. The middle region of the phase inductance has a linear relationship with the rotor position in a constant current condition, as illustrated in Figure 2.14.

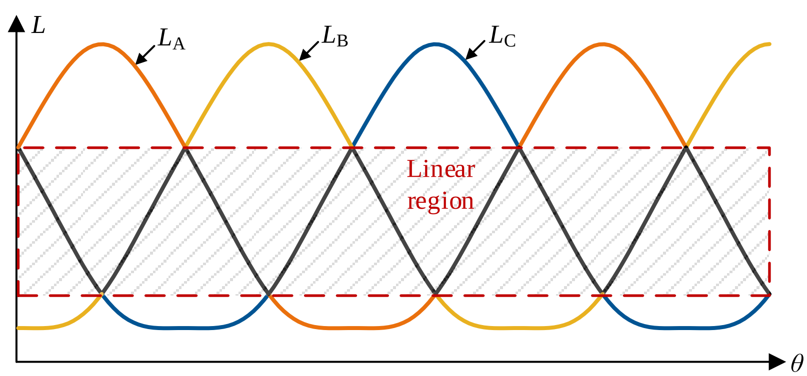

Figure 2.14 Linear regions in phase inductance profiles of a 12/8 SRM at a given current.

Simple offline testing can identify the linear inductance region of a tested machine, and the position estimation is realized via a linear fitting [28]. An improved work proposed in [29] extends the linear region method to a nonideal case with three-phase unbalance inductance, facilitating the method's availability in a more general case. The conventional linear inductance region schemes are more suitable for no-load and light-load conditions, but the position estimation accuracy is distorted when the SRM operates with a heavy load due to the ignorance of magnetic saturation. The literature [30] proposed a modified approach to ease the issue considering the inductance variation with magnetic saturation. The slope of the linear inductance-position relationship changes with the phase current, and the rotor position estimation can be adjusted under various load levels. In [31], the authors analyzed an unsaturated inductance reconstruction method to obtain the unsaturated inductance from the saturated incremental inductance under load conditions. The mapping between the two inductances utilizes the second-order polynomial, which can be manually identified in a commissioning process. The above methods [28]–[31] require full-cycle inductance information in both the idle-phase and the conduction phase. A simplified linear region approach proposed in [32] only considers the idle-phase inductance. The linear region in idle phases can cover the full-cycle rotor position estimation at low speed, simplifying the offline testing effort. The work also analyzes a variable pulse injection scheme to reduce the copper losses and the torque ripples caused by induced currents.

D. Feature Position Estimation

Feature position estimation methods are concise for low-speed position estimation as only partial inductance characteristics at one or several unique positions are used for sensorless control [33]–[37]. These approaches do not require the complete magnetic profiles and large storage memory, suitable for low-cost microcontrollers. A group of special position estimation schemes adopts the same idea as the previous threshold-based direct driving methods, which use several current thresholds to judge the phase commutation instants. In contrast, the rotor position can be estimated simultaneously.

In [33], the high-frequency induced current is extracted using lowpass filters from the sampled currents, and three current thresholds, located at the lower inductance intersection points, are given. When the idle-phase current reaches the preset thresholds, the phase commutation happens, and the rotor position at the intersection point can be recorded. Different from the model-free inductance intersection detection approaches [14], [15], the method in [33] estimates the rotor position only in idle phases, which is possible for sensorless control with the load. In [34], a modified double-current-threshold method, upgraded from the previous work in [8], was proposed. The approach determines phase commutation instants by the two thresholds as the method in [8] and simultaneously estimates the rotor position according to the inductance characteristic at the selected current thresholds. Similar ideas were adopted in single-current-threshold schemes in [35], [36], which can estimate the rotor position and obtain the phase commutation signals by comparing the current threshold and the induced high-frequency current. In addition to the threshold techniques, the research work in [37] utilizes feature flux linkage characteristics at 7.5° and 15°, dividing one electrical cycle into several sectors. The injection phase and the driving phase can be determined by comparing the induced high-frequency flux linkage with the prestored feature flux data. The two feature positions can then be recorded for estimation.

In these feature position estimation methods, only limited position points are detected over one electrical cycle. It causes difficulty in initial position estimation and may require additional motor starting strategies. Another potential problem is the reduced estimation accuracy at an ultra-low speed, in which the undetected rotor position between two feature positions is hard to predict. Whereas, when the rotor speed increases, the speed variation during the short detection interval could be ignored, and a simple linear fitting method is available for continuous position estimation.

2.2.1.4 Comparison of the Low-Speed Position-Sensorless Control Methods

In short, an intuitive review and comparison of existing low-speed position-sensorless control schemes of SRM drives are summarized in Table 2.2.

Table 2.2 Summary and Comparison of Low-Speed SRM Position-Sensorless Control Strategies

Categories	**Sensorless methods**	**Initial sensorless control**	**Low-speed sensorless control**	**Advantages**	**Disadvantages**
Direct sensorless driving	Current magnitude comparison [7]	Yes	No	General-purpose initial driving phase detection	No position estimation & unavailability in driving conditions
	Thresholds based methods [8]–[10]	Yes	Yes	Robustness in driving conditions	No position estimation
Magnetic-parameter-free position estimation	Single position estimation [11]–[15]	Yes [11]–[13]	No [11]–[13]	Computational efficiency	Discontinuous estimation & unavailability with load
		No [14], [15]	Yes [14], [15]		
	Full-cycle position estimation [16]–[18]	Yes	Yes	Continuous estimation	Unavailability with load
Magnetic-parameter-based position estimation	Lookup table-searching [19]–[24]	Yes	Yes	Straightforward solution	Large storage memory
	Inductance model [25]–[27]	Yes	Yes	Less storage memory	Reduced estimation accuracy
	Linear inductance region [28]–[32]	Yes	Yes	Less offline measurement	Increased complexity in saturation cases
	Feature position estimation [33]–[37]	No	Yes	Computational efficiency	Discontinuous estimation

Direct sensorless driving methods have more advantages in terms of generality and simplicity. These schemes do not require magnetic parameters, and the sensorless control is achieved by comparing the current magnitude orders or thresholds. The technique has been the commonly adopted initial driving phase selection method for sensorless starting control. However, the exact position estimation is unavailable in the approaches, thereby no able to adjust the phase commutation instants and realize accurate torque control. Therefore, direct sensorless driving is more suitable for applications not requiring a high-performance low-speed operation.

For low-speed position estimation, magnetic-parameter-free methods are attractive since they are potentially feasible for various SRMs with different ratings and configurations. This advantage is achieved by the general inductance models or feature position detection of the stator pole and the rotor pole. These methods, however, rely on an assumption of magnetic unsaturation. Position estimation accuracy is degraded at load conditions, and even resulting in an unstable sensorless control system. Despite these disadvantages, these solutions are still available for low-power SRM drives with light loads due to the simplicity.

Magnetic-parameter-based position estimation can offer more accurate position estimation during various operating conditions. The rotor position is estimated from the calculated inductance or flux linkage according to the prestored magnetic characteristics. The methods are able to achieve high dynamic performance in sensorless control and combine with other advanced torque control schemes. Although *a priori* knowledge of magnetic profiles is required, which leads to additional offline measurement effort or FEA simulation, this category has good application prospects in commercial products.

2.2.2 High-Speed Position-Sensorless Control

Pulse injection methods for low-speed sensorless control are often infeasible in high-speed operation. The narrower idle-phase period would shorten the injection duration at a higher speed, which leads to inaccurate position estimation in most pulse injection methods. Moreover, the pulse injection causes additional power losses, torque ripples, and acoustic noises, thus not attractive for full-speed sensorless operation. To this end, high-speed position-sensorless control is of interest for SRM drives. A general control diagram of high-speed position-sensorless SRM drive is presented in Figure 2.15.

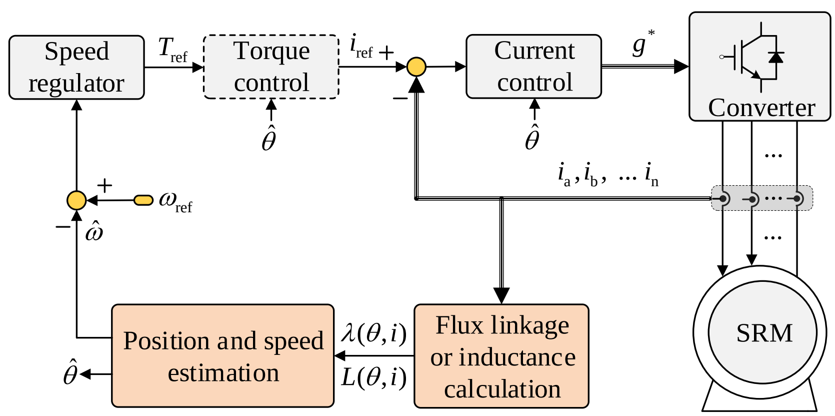

Figure 2.15 Overall block diagram of a high-speed position-sensorless SRM drive.

Through the literature, position estimation at high speed gains more attention than low-speed estimation in the research community. It is due to the fact that the electrical quantities, including flux linkage and stator inductance, become observable under fundamental excitation conditions (i.e., in conduction phases) at high speed. Compared to the low-speed method estimating the position from pulse injection only, more options are available for high-speed position estimation, and direct sensorless driving methods at high speed are not received much attention. This section categories major high-speed position estimation schemes in the literature into magnetic-parameter-free methods and magnetic-parameter-based methods.

2.2.2.1 Magnetic-Parameter-Free Position Estimation Methods

High-speed position estimation independent of magnetic characteristics facilitates a more general-purpose SRM drive. In existing research, gradient-based methods attract much attention. Other approaches proposed recently are also discussed.

A. Gradient Detection

Gradient-based methods utilize geometric features of SRMs for high-speed position-sensorless control. The motoring operation of the SRM overlaps the rotor pole and the stator pole from the unaligned position to the aligned position. The tendency of inductance variation relates to the geometric change and is identical for regular SRMs. Thus, monitoring the geometric location can identify the real-time rotor position. On this basis, two magnetic-characteristic-free methods are proposed, which are current-gradient-based methods [35], [38]–[42] and inductance-gradient-based methods [43]–[47].

Current-gradient detection was proposed in [38] for high-speed sensorless control. The method is suitable for single pulse control, which regulates the phase current by adjusting phase commutation angles under a constant phase voltage. The phase current varies nonlinearly with the relative position between the stator pole and the rotor pole, as shown in Figure 2.16. The current-gradient approach detects the peak phase current over a stroke, and the zero-gradient instant represents the stator pole and the rotor pole starting to overlap [38]. The zero current-gradient instant also denotes the beginning of the positive inductance region, in which a positive torque is generated. Therefore, the current-gradient detection can determine phase commutation for direct sensorless control, as mentioned in [39]. Moreover, the rotor position is estimated by recording the critical position at the zero-current gradient. The stator and rotor pole arcs can be used to calculate the position value without using complicated magnetic characteristics. However, the current gradient detection is inaccurate at the standstill and low speed due to the noisy current differential calculation. In [35], [40], additional low-speed position estimation schemes were combined with the current-gradient-based method for full-speed sensorless operation. Furthermore, another concern of the current gradient detection was raised in [41] that the zero-gradient position varies with the magnetic saturation. Altering the turn-on angle and the rotor speed in single pulse control changes the critical position value at high speed, thereby causing position estimation errors. A solution is to use a prestored compensation lookup table to correct the estimated position [42]. Nevertheless, it involves additional offline measurement.

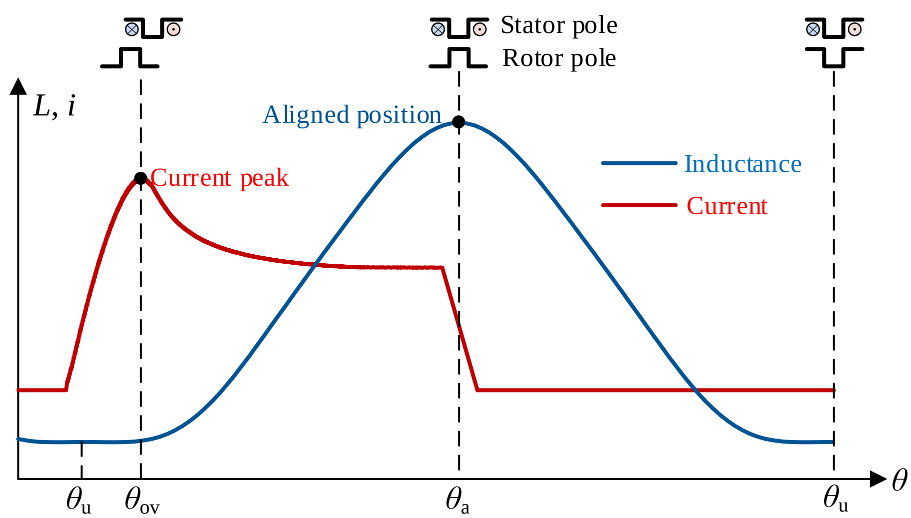

Figure 2.16 Principle of gradient detection methods.

In addition to the current-gradient-based methods, an alternative scheme is to detect the inductance gradient for position estimation [43]–[47], as shown in Figure 2.16. The maximum inductance occurs when the stator pole and the rotor pole are fully aligned, which indicates a feature position at 180° electrical. In [43], the phase inductance was calculated from the flux linkage, and the inductance slope zero-crossing instant was detected for phase commutation. A possible limitation is the fixed commutation angles, thus not able to achieve satisfactory speed and current control performance. The authors in [44] modified the inductance-gradient-based scheme by estimating the rotor position from the aligned position using a linear fitting method. The improved approach can estimate the real-time rotor position and adjust the turn-on and turn-off angles freely. The proposal in [45] further analyzed the erroneous gradient detection at the phase turn-on instant. A joint detection scheme by combining the transformer EMF and the motional EMF was proposed for robust aligned position estimation. Compared with the current-gradient-based method, the modified inductance-gradient technique can reduce the sensitivity to current noises to some extent. Due to the simple implementation and magnetic-characteristic independence, the inductance gradient scheme was applied to other purposes, such as fault-tolerance control [46] and direct torque control [47].

In general, gradient detection-based strategies are excellent in their good universality and are potential candidates for commercial SRM drives. The gradient calculation, however, raises sensitivity issues to current noises. Although improved research has been proposed to mitigate the problem, the current noise issue still needs to be considered seriously. For this reason, gradient detection schemes are more suitable for the single pulse control that regulates smooth phase current. Other current regulation methods, such as pulse-width modulation, current hysteresis control, and model predictive control, cause large current ripples and challenge the position estimation accuracy in variable operating conditions. In addition, gradient-based methods estimate one feature position only, which may reduce the estimation accuracy in speed transient states.

B. Other Solutions

Besides the gradient-based sensorless control, several magnetic-characteristic-free position estimation methods at high speed were proposed in the literature.

In [48], the authors estimated the rotor position by detecting the intersection point of phase inductances in conduction phases. The upper inductance intersection indicates the rotor position at 120° electrical, which can be used for feature position estimation and speed calculation. For an advanced turn-off angle, the upper inductance intersection would disappear. Thus, a direct sensorless driving scheme based on a three-phase inductance comparison can be adopted in this case. The measure is similar to low-speed methods proposed in [14], [15], but the inductance is calculated in conduction phases instead of idle phases. However, they suffer from the same drawback that the estimation accuracy reduces under magnetic saturation conditions.

The above issue can be mitigated using a phase overlapped region method proposed in [49]. The approach assumes a first-order Fourier inductance model composed of a DC bias and a fundamental-frequency inductance. Unknown inductance coefficients, including the DC value and the inductance magnitude, are solved online via two independent inductance equations when two phases overlap. Rotor position information can then be extracted without prestored inductance characteristics. As an improvement, the technique does not require gradient calculation and the assumption of magnetic unsaturation, thereby robust to current ripples and load changes. The analyses on parameter uncertainty validate that the method has less sensitivity to resistance mismatch and uncertain semiconductor conduction voltages. Still, since inductance harmonics are neglected in the proposed inductance model, the remaining impacts on position estimation need to be investigated. Like the previous methods, the sensorless control scheme in [49] also estimates one rotor position in a stroke. Additional assumption of a constant rotor speed over one electrical cycle is required for continuous position estimation by linear polynomial fitting.

2.2.2.2 Magnetic-Parameter-Based Position Estimation Methods

High-speed position-sensorless control based on magnetic characteristics is more straightforward since flux linkage and stator inductance are directly position-related functions. The type of techniques requires *a priori* knowledge of the SRM. In literature, many research works have been conducted in magnetic-parameter-based position estimation due to its excellent control performance.

A. Lookup Table-Searching Methods

Searching prestored magnetic lookup tables is a straightforward solution for position estimation when flux linkage or inductance is known.

A representative work proposed in [50] utilized the calculated flux linkage for position estimation via a prestored three-dimensional position-current-flux lookup table. The rotor position can be found in a one-to-one relationship between the flux linkage and the rotor position at a given current. Since the rate of flux variation with respect to the position change is lower around the unaligned position and the aligned position, searching lookup tables cannot ensure accurate rotor position in these regions. A typical way to guarantee high accuracy over one electrical period is to combine all phases for estimation [51]. The one with the largest slope of the flux linkage is selected as the sensing phase. However, as reported in [50], the flux linkage integration is sensitive to measurement offsets and parameter mismatch. Thus, a new flux linkage calculation method based on the first-switching-harmonic currents and voltages was proposed [52]. The approach avoids pure integration and parameter sensitivity issues, thereby improving the position estimation precision. Besides searching prestored three-dimensional data, the data size can be reduced using an approximate inductance model in which the dimension is reduced to two [53]. The simple implementation of such techniques also facilitates a high-performance sensorless drive system using advanced torque control schemes [54].

In lookup-table-based position estimation methods, mutual couplings between adjacent phases are often neglected. However, when the two phases are excited simultaneously, the mutual quantities are nonnegligible and result in position estimation errors when searching prestored lookup tables, especially in load conditions. Several works were conducted to mitigate the mutual coupling issue in high-speed position estimation. A general block diagram is presented in Figure 2.17.

Early research on mutual couplings in sensorless drives was proposed in [55] and [56]. The methods measure the mutual flux linkage characteristic offline and store it as a compensation block to correct the self-flux linkage calculation. In [57], the proposal calculated the mutual inductance from the induced voltage in an adjacent phase and then

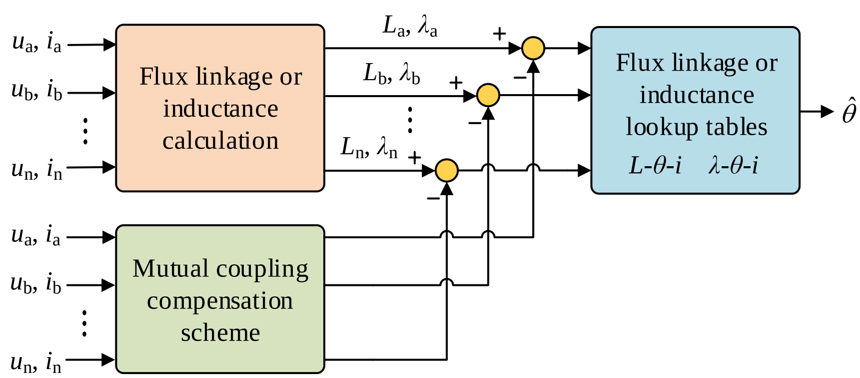

Figure 2.17 General block diagram of the lookup table-searching method with mutual coupling mitigation.

estimated the rotor position from a mutual inductance-position-current lookup table. Although these approaches in [55]–[57] can effectively solve the mutual coupling impact, the additional offline measurement for mutual couplings is required, increasing workload and aggravating parameter sensitivity. To simplify the estimation procedure, improved research has been proposed for position estimation without *a priori* knowledge of mutual couplings [58]–[60]. The literature in [58] analyzed the self-inductance calculation error when two phase conducts. This method divides three operating modes in the current hysteresis control, dependent on current variation polarities in two overlapped phases. The mutual coupling influence does not exist in a particular working mode. On this basis, a variable bandwidth current hysteresis control scheme is proposed to ensure the same working mode during the phase inductance calculation. Follow up [58], a modified solution further considering magnetic saturation was proposed in [59]. Another scheme without using mutual-inductance-information depends on the inductance difference between two overlapped phases for sensorless control [60].

It is worth noting that although mutual coupling characteristics are not required in the schemes [58]–[60], self-inductance or self-flux linkage characteristics are still needed for position estimation.

B. Position Observers

Position observers are turned out to be excellent approaches for sensorless control of AC motor drives [61]–[70] and also attract increasing attention in SRM position estimation. Although the traditional lookup-table-based methods deliver a direct measure for position estimation, several nonideal distortions, such as the current and voltage sampling noises, parameter uncertainty, and eddy current, would harm the estimation accuracy. Being different, state observers estimate the rotor position and speed indirectly and provide desirable filtering capability.

A typical control diagram of position observers is illustrated in Figure 2.18. Most position observers adopt a standard prediction-correction structure. Given a general high-order dynamic system:

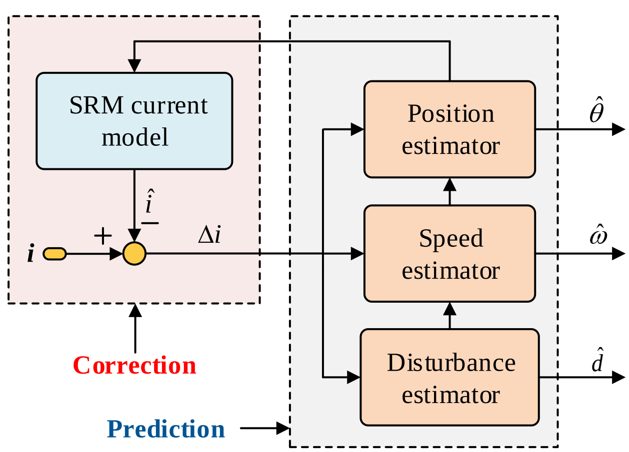

Figure 2.18 Control diagram of SRM position observers.

$$\dot{\boldsymbol{x}} = f(\boldsymbol{x}) + b(\boldsymbol{x})\boldsymbol{u} + \boldsymbol{d} \tag{2.11}$$

where $\boldsymbol{x}$=[x_1, x_2,…, x_n] represents the n-th order system state vector, $f(\boldsymbol{x})$ and $b(\boldsymbol{x})$ are two smooth nonlinear functions of the system state, $\boldsymbol{d}$ denotes uncertain disturbance, and $\boldsymbol{u}$ is the control input.

The state observer can be designed as

$$\dot{\hat{\boldsymbol{x}}} = \underbrace{f(\hat{\boldsymbol{x}}) + b(\hat{\boldsymbol{x}})u}_{\text{Prediction}} + \underbrace{G_n(\Delta x_1)}_{\text{Correction}} \tag{2.12}$$

where $\Delta x_1 = x_1 - \hat{x}_1$ is the prediction error, and $G_n(\cdot)$ is a series of nonlinear estimators.

The state observer estimates the system states $\hat{\boldsymbol{x}}$ by converging a prediction error Δx_1 between a measurable state x_1 and its prediction $\hat{x}_1$. In SRM position estimation, the state x_1 is often selected as the phase current $x_1 = i$. The nonlinear function $f(\boldsymbol{x})$ and $b(\boldsymbol{x})$, as well as control input $\boldsymbol{u}$, can be determined by SRM models. As shown in Figure 2.18, the position observer adopts an SRM current model to predict the current $\hat{i}$, and the estimator converges the current prediction error Δi. Other system states, such as the rotor position $\hat{\theta}$, the rotor speed $\hat{\omega}$, and disturbance $\hat{d}$, can then be estimated. For a reduced order estimator, the disturbance estimation can be removed, and only the rotor position and speed are estimated. The estimator selection determines the observer performance, including filtering capability, parameter adaptation, and dynamics. Existing position observers can be categorized according to the estimator types.

Sliding-mode control is the most popular variable-structure scheme in SRM observer design [71]–[79] due to the remarkable dynamic performance. The sliding-mode observer (SMO) utilizes high-gain nonlinear controllers, often selected as sign functions, to force the estimation error to reach a predefined sliding-mode surface. Finite-time convergence and low steady-state errors of the SMO guarantee accurate position and speed estimation. A typical design of a second-order SMO was analyzed in [71]. The observer adopts a secondary Fourier inverse inductance model as the current predictor. Two correctors using nonlinear sign functions estimate the rotor position and speed based on the mechanical dynamic model. Stability and parameter design conditions are obtained through the Lyapunov stabilization theorem. The parameter tuning of the SMO is a trade-off between filtering capability and transient performance, thereby more robust for sensorless operation in a noisy environment compared with lookup table-based methods. This type of SMO observers was recently applied in broad applications, such as switched reluctance generators [72] and photovoltaic-powered SRM pump systems [73]. In other developed SMOs, the basic structures keep the same, but the selection of the SRM model is various, such as using an analytic nonlinear flux model proposed by Spong in [74] for current prediction [75], [76], or direct searching an inverse inductance lookup table [77]. As a well-known drawback, the SMO leads to chattering problems in estimation due to the nonlinear switching function. Lowpass filters are often required for smooth estimation, but the introduced phase delay limits the dynamic performance significantly. A solution for chattering reduction is to select a smoother switching controller, such as hyperbolic tangent functions in [78]. However, the convergence rate and steady-state errors would be deteriorated and need to be investigated. Notably, although the SMO is robust to noises, the method is still limited to ultra-low speed control since the trade-off parameter design becomes infeasible with significant errors in flux linkage/inductance calculation, as presented in [79].

Linear position observers are alternatives for high-speed position estimation, using linear gains in observer correction [80]–[82]. The linear observer sacrifices the dynamic performance in exchange for a simple structure and easily adjustable parameters. Unless the SMO of which parameter tuning is dependent on operating conditions, the linear observers often adopt a universal parameter design scheme, facilitating a more straightforward implementation. An example linear position observer was discussed in [80]. The observer frame is similar to the SMO, but the tunable linear observer gains replace the nonlinear switching functions. The absence of discontinuous controllers ensures a smoother convergence process, thereby not suffering from the chattering problem. In [81], a linear-gain observer was designed, which obtains the position error signal from the relative change of the phase current with respect to the flux linkage. The linear gains are no longer tunable but calculated from the magnetic characteristics. This approach simplifies the parameter design process, but the fixed gain results in a fixed bandwidth, thus losing the flexibility to adapt to variation in working conditions. Another effective solution of the linear position observer is based on a third-order PLL [82]. The PLL was initially used in grid-connected applications for grid synchronization, but its phase estimation capability coincides with the position estimation. Figure 2.19 presents the control diagram of the PLL-based position observer. The estimation error between the calculated flux linkage and the estimated flux linkage can be converted into a position error signal based on the magnetic characteristics. A third-order PLL then converges the position error and calculates the rotor speed and position. Over other position observers, the PLL-based solution avoids complicated calculation and has a simple parameter design based on pole placement. Many advanced PLL schemes have been proposed in PMSM drives [61]–[63], while the research on the SRM is still limited and has spaces to explore.

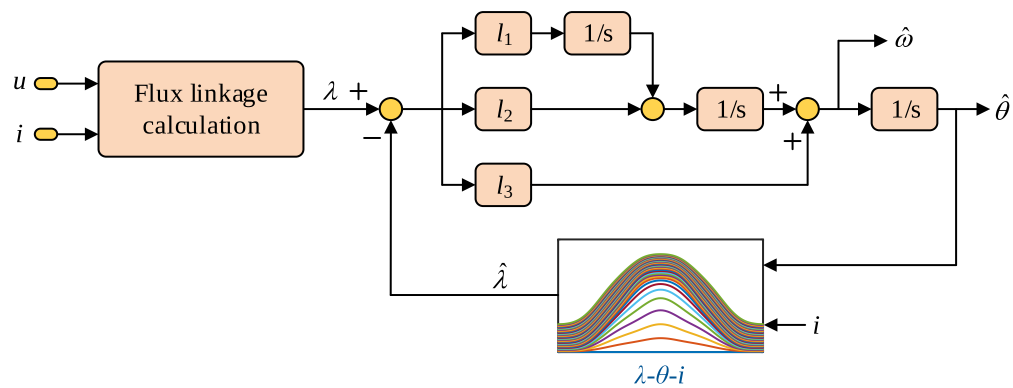

Figure 2.19 Structure of the PLL-based position observer.

Other position observer structures, such as model reference adaptive systems (MRAS) and Kalman filters (KF), were also discussed in the literature [83]–[87]. The MRAS adopts mathematical models of the SRM to compare the existing system. The difference between the measured value and the reference quantity, often set as phase currents, can force the position and speed estimation to converge. MRAS-based position estimators often employ proportional-integral (PI) controllers for error convergence, and successful applications were proposed in [83] and [84] for vector-controlled SRM drives with speed sensorless capability. The convergence performance of the MRAS highly relies on the PI controller design. Due to the presence of SRM modeling nonlinearity, analytical parameter tuning is troublesome in the MRAS schemes. As another dominant observer design tool, KF and its nonlinear version extended Kalman filters (EKF) are known as optimal estimators to eliminate uncertain Gaussian noises. It offers remarkable filtering capability of measurement noises and modeling uncertainties in position estimation. An example of a KF was presented in [85], in which the KF was directly used as a cascaded filter for position and speed estimation. The applications of EKFs can be found in [86] and [87], which adopted the nonlinear voltage model and the mechanical model to construct an EKF estimator for rotor position and speed. The first-order Taylor approximation handles the nonlinearity in mathematic modeling in the EKF. Still, shortcomings of the EKF need to be overcome in practical applications, including the high computational burden, reduced linearization accuracy at ultra-high speeds, and complicated parameter testing.

C. Intelligent Schemes

Magnetic-characteristic-based position estimation methods, such as lookup-table-based methods and position observers, require prestored magnetizing data in the microcontroller. However, a large size of three-dimensional data occupies significant memory storage. Therefore, intelligent fitting algorithms are proposed to redefine the nonlinear magnetic characteristics of the SRM by an input-output relationship. Magnetic characteristic profiles are replaced by the intelligent mechanisms with reduced consumptions of memory resources. Although magnetic data is no longer needed in real-time position estimation, it is usually used as a training data set generator in offline mechanism design. For online mechanism training, a specific SRM needs to be tested multiple times to obtain operational status data. The data acquisition for the intelligent schemes still needs additional measurement effort for a tested machine, which is similar to the offline magnetizing property measurement process for magnetic-characteristic-based techniques. Consequently, this review article categorizes the intelligent schemes as magnetic-parameter-based methods as well. The major intelligent schemes can be divided into fuzzy logic [88]–[90] and neural networks (NN) [91]–[97]. The block diagrams are given in Figure 2.20.

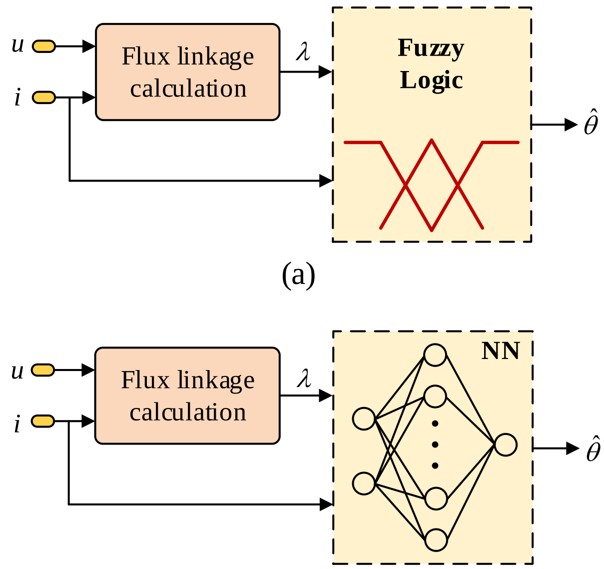

(a)

(b)

Figure 2.20 Position estimation using intelligent algorithms. (a) Fuzzy logic. (b) NN.

An early fuzzy logic-based position estimation method was proposed in [88], aiming to reduce storage memory usage and enhance the robustness to disturbances. Fuzzy rules are trained by static flux linkage curves reflecting the magnetizing characteristics and dynamic terminal voltage and current measurements containing real-time operating conditions. The defined fuzzy logic is adopted to replace the complicated magnetizing profiles, facilitating a compact control system with less storage requirement. The fuzzification is also feasible to simplify a nonlinear flux linkage model since it does not require analytical equations and interpolations [89]. As reported in [90], the fuzzy logic can offer better filtering capability to nonideal distortions, including measurement errors and noises, parameter variation, and integration deviation, over the lookup-table-based methods. Although the fuzzy logic-based approaches achieve several advantages, the main challenge is the complicated design of fuzzy rules in which numerous fuzzy sectors need to be determined for satisfactory estimation performance.

With reduced complexity, NNs have become the mainstream in intelligent algorithm-based position-sensorless control. A back-propagation NN-based estimation method was proposed in [91] to construct an efficient mapping between the electrical input quantities, such as flux linkage and current, and the output mechanical rotor position. The NN was trained by the data set generated from the complete magnetic characteristics offline, but fewer computational resources are required. The research in [92] utilized back-propagation learning rules in a neuro-fuzzy mechanism, validating that the NN is able to simplify the logic design of conventional fuzzification methods. In comparative research [93], Paramasivam *et al*. compared the two position estimators using an adaptive neuro-fuzzy inference system (ANFIS) and NNs. The results validate that the NN consumes less computational resources than the ANFIS. To further simplify the algorithm implementation, more research was focused on the complexity reduction of NNs [94]–[97]. The literature [94] established an NN-based mapping between the saturated inductance and the unsaturated inductance to commutate a switched reluctance generator. A least-mean-square method was embedded in inductance acquisition to reduce the number of neurons and the processing time. In [97], an improved back-propagation-based NN combining a pretreated third input with inductance curve fitting was put forward. Validations show that the method can achieve approximately one-quarter processing reduction compared to conventional NN structures. In [95], a minimal NN without neurons in the hidden layer was analyzed to reduce the computational burden for a specific two-phase SRM. The technique is able to operate in a low-cost microcontroller, but the reduction of hidden layers would affect the estimation accuracy. The research proposed in [96] compared two NNs, back-propagation NN and radial basis function NN, as well as numerical solver selections, in terms of convergence rate and storage memory. The optimal choice of NN structures and numerical solvers can facilitate an accurate estimation system with lower computational burden.

In these studies, intelligent algorithms effectively relieve storage spaces in position estimation and are potential solutions for commercial SRM drives. The estimation accuracy can also be improved due to the robustness of sampling noises and parameter uncertainties. However, intelligent schemes require numerous training sets, including static magnetic characteristics and data acquisition from real-time testing. Consequently, a predesign procedure is inevitable.

D. Feature Position Estimation Methods

Different from the previous position estimation methods that estimate full-cycle rotor position, the feature position estimation method is an alternative solution [98]–[104]. The technique only estimates partial positions in one electrical cycle but requires less flux linkage or inductance profiles. Hence, the feature position estimation has advantages in reducing storage space and offline measurement effort.

The first feature position estimation concept was proposed in [98]. As presented in Figure 2.21, the method sets a flux linkage-current curve at a critical position as the reference. When the real-time calculated flux linkage intersects the reference curve, the particular position can be recorded as a position estimate. Compared with other magnetic-parameter-based methods, this approach only needs the flux linkage information at one position. The research in [99] proposed a similar idea to estimate the critical position by measuring the difference between actual flux and reference flux. Instead of monitoring the curve intersection, the flux linkage difference is converted into a position error and then added to the reference position as a correction term. Recent sensorless control methods discussed in [100] and [101] utilized more feature flux curves at different positions, such as the unaligned position, the aligned position, and the central position. These special flux linkage characteristics can be obtained through an online torque-balancing measurement method proposed in [102] without clamping tools and offline testing. The flux linkage characteristic at arbitrary positions can be deduced with a secondary Fourier model to determine the phase commutation instants. In [103], the feature position estimation method was further developed in a switched reluctance generator. The critical position can be estimated by comparing the current raising time in a chopping period with its reference value. Another method using a linear flux linkage region was proposed in [104], which can be featured by two flux values at endpoints. This method also requires less flux linkage knowledge, and the rotor position can be estimated by linear regression.

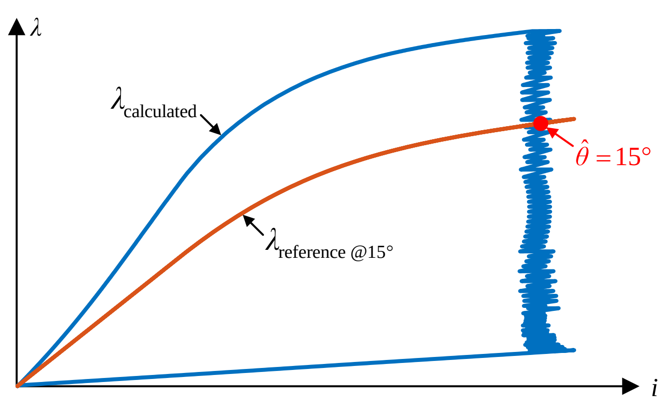

Figure 2.21 Position estimation using feature flux linkage.

Although the above feature position estimation methods do not require complete magnetic characteristics, the position estimation is discontinuous since only one or partial position can be detected in every electrical cycle. The feature position estimation works a discrete Hall position sensor that has limited position detection resolution. The situation is the same as gradient-based methods. The estimation accuracy may be aggravated under fast speed variations or at a lower speed.

2.2.2.3 Comparison of the High-Speed Position-Sensorless Control Methods

For intuitive review, the major high-speed position estimation methods are compared and summarized in Table 2.3.

From the view of universality, magnetic-characteristic-independent methods are preferable since no offline measurement and FEA are needed. Due to the advantage, a potential application is the general-purpose SRM drive in which position-sensorless control is indispensable, as is the case with other commercialized AC motor drives. Among the existing research, gradient detection methods are gained much attention due to the simple implementation. However, the sensitivity to current noises and ripples challenge the method's robustness in industrial applications, which need to be investigated and improved. The inductance intersection detection and the phase overlapped region-based techniques are less sensitive to noises. Notably, the latter one further considers modeling uncertainties in inductance calculation, achieving higher estimation accuracy. As a common drawback, existing magnetic-parameter-free techniques estimate the rotor position discontinuously. One rotor position information is obtained over one electrical cycle. The estimation accuracy may decrease when the rotor speed is low and changes suddenly.

Table 2.3 Summary and Comparison of High-Speed SRM Position-Sensorless Control Strategies

Categories	Sensorless methods	Noise sensitivity	Computational burden	Advantages	Disadvantages
Magnetic-parameter-free position estimation	Gradient detection [29], [32]-[41]	High	Low	Simple implementation	Sensitivity to noises & discontinuous estimation
	Inductance intersection [48]	Medium	Low	Simple implementation	Unavailability with load & discontinuous estimation
	Phase overlapped region [49]	Low	Medium	Robustness to modeling uncertainties	Discontinuous estimation
Magnetic-parameter-based position estimation	Lookup table-searching [50]–[54]	Medium	Low	Straightforward solution	Large storage memory
	Lookup table-searching with mutual coupling elimination [55]–[60]	Medium	Medium	Mutual coupling mitigation	Large storage memory
	Position observers [71]-[87]	Low	Medium	Robustness to noises	Parameter tuning
	Intelligent schemes [88]–[97]	Low	High	Reduced stored data size	Numerous training sets
	Feature position estimation [98]–[104]	Medium	Low	Less storage memory	Discontinuous estimation

High-speed position estimation can be simplified by magnetic characteristics, the same case as the low-speed schemes. Searching prestored magnetizing lookup tables for position estimation is the most straightforward. It also facilitates extended research in eliminating mutual coupling effects on estimation, which are ignored in most methods but cause estimation errors. However, these approaches do not offer the filtering capability. It may challenge the robustness in practical applications, in which the external interference is uncertain. Position observers are good candidates for robust sensorless SRM drives. Feedback control in position observers provide additional trade-off opportunity between noise suppression and dynamic performance, and thus sensorless control can operate in a noisy condition.

The main concern of lookup table techniques and position observers is the demand for large storage memory for magnetizing data, which may limit the implementation in a low-cost microcontroller. In shrinking data usage, intelligent algorithms map the nonlinear characteristics into learning mechanisms with less memory requirement. The methods are also potentially adaptive for various SRMs due to the learning capability, but the training set acquisitions are difficult for industrial SRM drives. Currently, intelligent schemes are limited to a specific machine. The other strategies estimating feature positions are more feasible solutions at high speed. The limitation is the same as magnetic-parameter-free methods, which is the discontinuous position estimation and has reduced accuracy at transient states and lower speeds.

2.2.3 Wide-Speed Range Position-Sensorless Control

Position-sensorless control methods discussed early are feasible for a specific speed region, either low speed or high speed. For wide-speed range sensorless control, several techniques were proposed in the literature by combining both the low-speed method and the high-speed method. A general control diagram is presented in Figure 2.22.

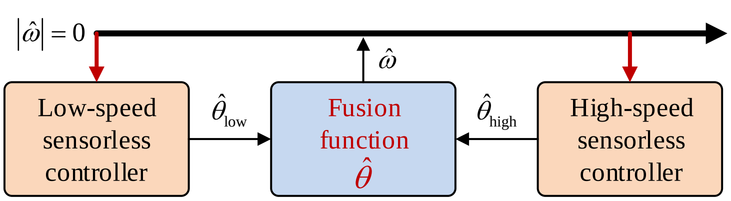

Figure 2.22 General control diagram of wide-speed range position-sensorless control.

A solution for wide-speed range operation is to adopt direct sensorless driving schemes at full speeds, where the phase commutation instants are determined by predefined current threshold and gradient detection [47]. However, the approach does not obtain the rotor position. For full-speed position estimation, the authors in [25] adopted two position estimators in each speed region and designed a hysteresis controller to switch the two schemes. The switching area is selected around a medium speed in which both position estimators offer good accuracy. Since the two approaches estimate the position in different manners, the algorithm fusion of low-speed methods and high-speed methods is easy to realize.

The main challenge of wide-speed range sensorless control is the four-quadrant operation capability. Existing schemes often consider position estimation in the first quadrant, namely in the motoring mode with a positive speed. Under the quadrant change, position estimation logic needs to be modified to adapt the variable phase commutation angles and speed directions [105]. Several techniques were found in the literature regarding the four-quadrant position estimation. The proposal in [79] adjusted the sign of sliding-mode gains in motoring and generating modes to guarantee stability. In [9], a speed reversible operation was achieved using a predefined current threshold. These methods [9], [79] need specific designs for ultra-low operation, but the presented estimation accuracy is limited. Lookup table-based methods are capable of low-speed operation and can be modified in four-quadrant control [23]. The prestored lookup tables need to be adjusted according to the quadrant detection. However, the quadrant determination is challenging around zero speed due to the presence of speed estimation errors. Instability may occur with wrong quadrant detection when the rotor speed changes across zero. For smooth four-quadrant operation, a recent work proposed in [27] considered more criteria based on preset inductance and flux linkage thresholds for quadrant transitions in a wide-speed range. With improved estimation accuracy, the sacrifice of such technique is the increased complexity due to extra auxiliary current chopping control and region adjudgments.

2.2.4 Discussion

Throughout the literature, position-sensorless control of SRM drives has been studied for two decades and can cover a wide-speed range operation. Still, various improvements should be performed in existing methods.

Generally speaking, position estimation of SRMs is more challenging than conventional AC machines due to their nonlinearity caused by doubly salient structures. Existing position-sensorless control strategies often rely on magnetic characteristics for accurate estimation. However, the usage of magnetic parameters requires additional offline measurement or FEA simulation, limiting the algorithm's universality. Although many studies are conducted to realize magnetic-parameter independence, the position-sensorless control still has some limitations, such as reduced estimation accuracy, weak load-carrying capability, and increased complexity. Therefore, it is necessary to develop general position estimation schemes, which can avoid offline measurement, provide higher estimation accuracy, and at the same time have higher calculation efficiency.

Developing new pulse injection methods with fewer side effects on SRM drives is preferable. Conventional pulse injection schemes utilize high-frequency voltage pulses on idle phases for position estimation. However, additional excitation currents cause copper losses and thus challenge the cooling design of both machines and converters. Torque ripples are also generated by pulse signals, degrading the control performance and accelerating mechanical aging. In addition, high-frequency induced currents result in acoustic noises, which should be considered seriously in the applications, such as home appliances and electric vehicles. Consequently, a crucial research direction on low-speed sensorless control is to mitigate these negative influences.

Four-quadrant operation is essential in electric vehicles and needs to be realized in sensorless control. In different speed and torque directions, the SRM working sector changes between the positive torque region and the negative torque region by adjusting phase commutation angles. Most existing methods are only available in a specific quadrant and become unstable when the operating quadrant varies. Several improved works discussed early can realize four-quadrant sensorless operation, but the algorithm complexity increases significantly due to the quadrant determination and switching logic. Moreover, the smooth and fast transition across zero speed is still a challenge. In consequence, it is suggested to develop improved sensorless control schemes for robust and straightforward four-quadrant operation.

To this end, this thesis aims to propose a universal position-sensorless control scheme covering wide-speed range operation and does not require offline magnetic characteristic measurement. It can improve the algorithm’s adaptation capability to various SRM types and facilitate broad applications of position-sensorless control in a commercially general-purpose SRM drive.

2.3 Conclusion

This chapter introduces the fundamentals of the SRM drive, with testing setup design and magnetic characteristic measurement. An overview of major position-sensorless control strategies of SRM drives is also presented. In the literature review, existing sensorless control strategies are categorized into low-speed methods and high-speed methods. First, low-speed sensorless control methods using pulse injection are discussed. Direct driving methods, magnetic-perimeter-free methods, and magnetic-parameter-based methods are summarized with highlighting the merits and shortcomings. Then, high-speed position estimation schemes are categorized according to the usage of magnetic characteristics, and a comparison among the main features of existing research is given. Full-speed sensorless control schemes combing both low-speed methods and high-speed methods are also analyzed. Finally, the chapter discusses the current challenges in SRM sensorless control.

Chapter 3

A Regional Phase-Locked Loop Based Low-Speed Position-Sensorless Control Scheme

3.1 Introduction

Low-speed position-sensorless control of the SRM drive can be realized by injecting high-frequency pulse voltages into the idle phase. The magnitude of the induced high-frequency current is measured to obtain the stator inductance, which is then used for position estimation. However, obtaining the stator inductance characteristics is not an easy task, and time-consuming offline measurement is required. Although some advanced schemes can estimate the rotor position without using the prestored magnetic characteristics [11]–[18], as mentioned in the literature review, the methods ignore the magnetic saturation effect, thus not able to support sensorless operation at heavy load conditions.

To realize position estimation under load conditions without using *a priori* knowledge of magnetic parameters, this chapter proposes a new position estimator with a novel RPLL (regional phase-locked loop) for SRM drives. Firstly, a self-commissioning process is designed to self-learn the parameters of an idle-phase inductance model at the initial stage without manual involvement. Then, the idle-phase inductance is normalized by the self-acquired parameters and used for position estimation. Since the derived inductance in each idle phase is discontinuous over one electrical cycle, all idle-phase inductances are considered simultaneously, and a new heterodyne approach in different inductance regions is proposed in the RPLL to obtain the rotor position in the whole electrical cycle.

Compared to existing low-speed position estimation methods, the proposed position estimation approach has several advantages:

1) It does not require time-consuming offline measurement of magnetic characteristics. Instead, a simple self-commissioning method is proposed to improve the generality of the sensorless control scheme.
2) The proposed approach can guarantee accurate position estimation under both no-load and load conditions due to the eliminated magnetic saturation effect.
3) The RPLL can achieve smooth speed reversal in sensorless operation without using complicated quadrant judgments.
4) The position estimator offers filtering capability to noises and model uncertainties, thus improving the robustness and enhancing the stability.

Finally, experimental validation is carried out on a 12/8 SRM setup to verify the proposed position estimation strategy.

3.2 Discussion on Conventional Low-Speed Position Estimation Methods

Figure 3.1(a) illustrates the implementation of high-frequency pulse voltage for low-speed position estimation, where the phase current and phase inductance of the SRM are presented. The current hysteresis control with the soft chopping mode [2] is used to regulate the current when the phase conducts, and the zoom-in current is presented in Figure 3.1(b). The soft chopping involves a magnetization process with the positive DC-linkage voltage U_{dc}, and a slow demagnetization process with zero voltage. The high-frequency injection containing a pair of positive (P) and negative (N) voltage pulses, as shown in Figure 3.1(c), is enabled during the idle-phase period. The injection amplitude is set as the DC-link voltage U_{dc}. The current sampling period is defined as T_s. To assure the induced current i decaying to zero before the next positive voltage pulse starts, additional period for a negative voltage pulse is added.

In the idle phase, magnetic saturation can be neglected due to the low induced current when the injection period is short. The SRM model with the positive injection can be written as:

$$U_{\mathrm{dc}} = Ri + L(\theta, i)\left.\frac{di}{dt}\right|_{\mathrm{P}} + i\omega\frac{\partial L(\theta, i)}{\partial \theta} \tag{3.1}$$

The subscript ‘P’ denotes the positive injection. The voltage drops of switches and diodes in the asymmetric half-bridge converter are ignored in the SRM model in comparison with the large DC-link voltage.

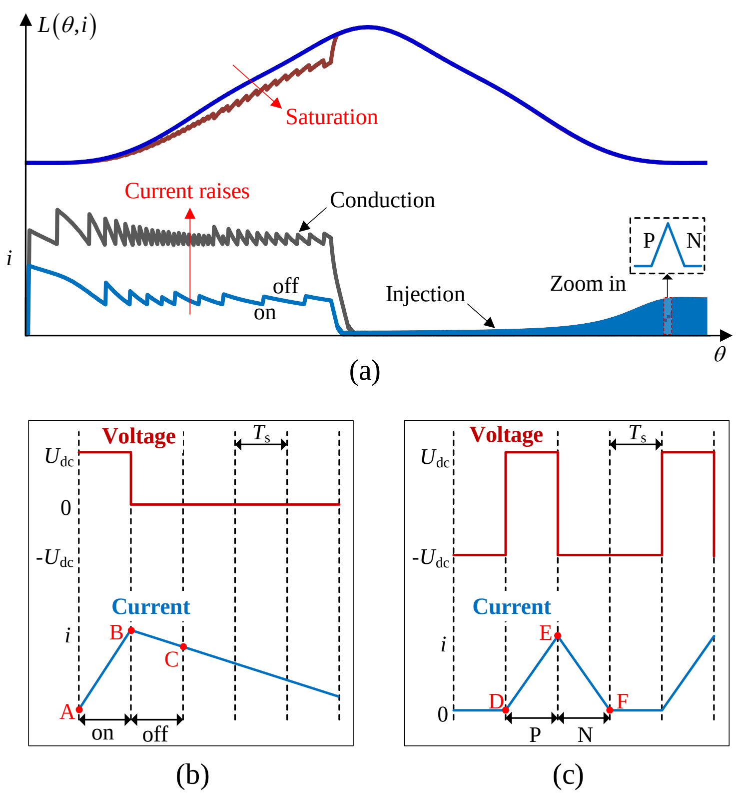

Figure 3.1 Pulse-injection-based position estimation methods. (a) Phase current and phase inductance. (b) Current derivative calculation in the conduction period. (c) Current derivative calculation in the idle-phase (injection) period.

Similarly, the SRM model with the negative injection can be expressed as

$$-U_{\mathrm{dc}} = Ri + L(\theta,i)\left.\frac{di}{dt}\right|_{\mathrm{N}} + i\omega\frac{\partial L(\theta,i)}{\partial\theta} \tag{3.2}$$

where the subscript ‘N’ denotes the negative injection.

The changes of the ohmic voltage drop and back-EMF are small during the short injection periods at low speed. According to Figure 3.1(c), the phase inductance can then be calculated by combining (3.1) and (3.2):

$$L(\theta,i)\big|_{\mathrm{idle}} = \frac{2U_{\mathrm{dc}}}{di/dt|_{\mathrm{P}} - di/dt|_{\mathrm{N}}} = \frac{2U_{\mathrm{dc}}T_{\mathrm{s}}}{2i_{\mathrm{E}} - i_{\mathrm{D}} - i_{\mathrm{F}}}. \tag{3.3}$$

Some injection-based methods also use the inductance in the phase conduction period for position estimation. When the phase conducts, current ripples caused by the hysteresis control can be used to calculate the phase inductance by detecting the current changing rate. According to Figure 3.1(b), the phase inductance in hysteresis control is calculated by

$$L(\theta,i)\big|_{\text{conduction}} = \frac{U_{\text{dc}}}{di/dt\big|_{\text{on}} - di/dt\big|_{\text{off}}} = \frac{U_{\text{dc}}T_{\text{s}}}{2i_{\text{B}} - i_{\text{A}} - i_{\text{C}}}. \tag{3.4}$$

where the subscripts "on" and "off" represent the on-state and off-state in the soft chopping hysteresis control mode, and the phase voltages are U_{dc} and zero, respectively.

As shown in Figure 3.1, when the phase current increases due to the load, the conduction-phase inductance decreases nonlinearly with the increased current. Hence, the conventional methods [11]–[18] cannot ensure accurate position estimation under load conditions unless using prestored nonlinear magnetic lookup tables. Since the approach needs offline measurement of SRM's magnetic characteristics, the control algorithm's generality would be limited due to the increasing complexity and additional manual workload.

To make the low-speed position estimation simpler, this chapter aims to design a new scheme that does not need offline testing while achieving good robustness to load variation.

3.3 Proposed Low-Speed Position Estimation Scheme

3.3.1 Overview of the Proposed Method

As analyzed before, the magnetic saturation in conduction phases makes the position estimation complicated under load conditions. To avoid using magnetic characteristics, the rotor position can be estimated from the idle-phase inductance only. Since the idle-phase inductance is unsaturated and load independent, the same estimation accuracy can be ensured under both no-load and load conditions.

Figure 3.2 shows the overall control structure of the proposed low-speed sensorless control scheme. The outer loop consists of a speed PI controller, and the current hysteresis controller is used to regulate the phase current in the inner loop. The high-frequency pulse voltage is injected in idle phases by modifying the gate signal, and the induced high-frequency current is used for position estimation. In sensorless operation, the estimated position and speed are used as feedbacks for speed and current control. A simple online self-commissioning scheme is also designed in the proposed position estimation scheme, which avoids the offline measurement used in conventional methods.

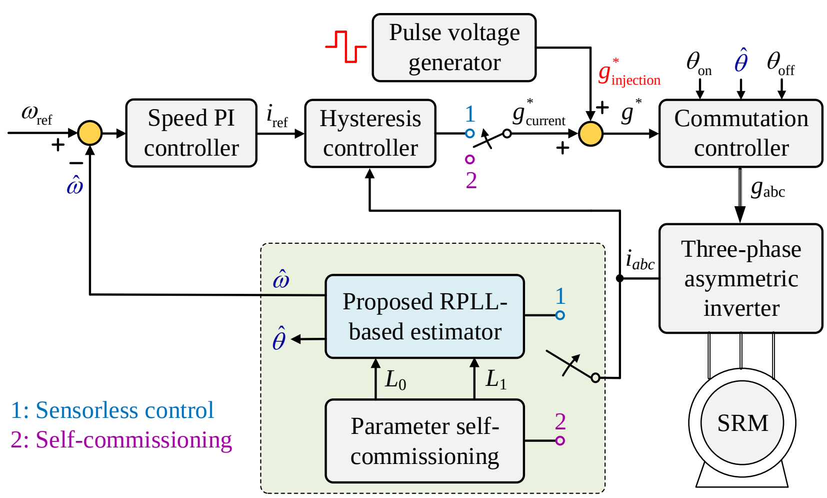

Figure 3.2 Schematic diagram of the proposed position-sensorless control scheme.

In this section, the self-commissioning will be introduced first. Then, a new RPLL-based position estimator will be proposed to estimate the full-cycle position.

3.3.2 Idle-Phase Inductance Analysis and Self-Commissioning

With a short injection period, the induced current in the idle phase is low, and thus the calculated inductance through the pulse injection is the unsaturated inductance. The inductance model of the unsaturated inductance can be approximately expressed by the DC inductance L_0 and the fundamental component L_1:

$$\begin{cases} L_{\mathrm{A}} = L_0 - L_1 \cos\left(N_{\mathrm{r}}\theta\right) \\ L_{\mathrm{B}} = L_0 - L_1 \cos\left(N_{\mathrm{r}}\theta - 2\pi/3\right) \\ L_{\mathrm{C}} = L_0 - L_1 \cos\left(N_{\mathrm{r}}\theta + 2\pi/3\right) \end{cases} \tag{3.5}$$

where the high-order inductance harmonics are ignored in the approximated model. The effects of the approximation are limited on position estimation, which will be discussed later.

As can be observed from (3.5), the idle-phase inductance is a function of the rotor position. If the two parameters, L_0 and L_1, are known, the rotor position can be estimated. On this basis, a simple self-commissioning process is introduced in this chapter to obtain the L_0 and L_1.

As illustrated previously in the overall diagram shown in Figure 3.2, by disabling the current controller during the self-commissioning, three phases of the SRM are turned off simultaneously. In this case, the SRM is not controlled and does not rotate, and all phases are idle. Then, injecting high-frequency pulse voltages into the three phases, and the three-phase inductances (3.5) can be calculated by detecting the current variation as expressed in (3.3). To reduce the noise and improve the steady-state accuracy of inductance identification, lowpass filters (LPFs) can be added in the inductance calculation, as shown in Figure 3.3. It is notable that the LPF is only used for the self-commissioning process.

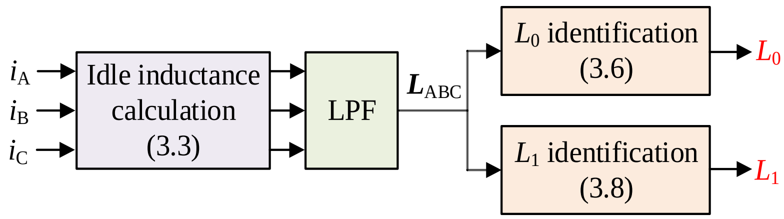

Figure 3.3 Self-commissioning process for parameter identification of L_0 and L_1.

Afterward, the DC inductance value L_0 can be calculated by summing the three-phase inductance, as follows:

$$L_0 = \left(L_A + L_B + L_C\right)/3 . \tag{3.6}$$

To obtain the amplitude of the fundamental inductance, the inductance (3.5) in the abc-frame is transformed into the αβ-frame, which derives

$$\begin{cases} L_\alpha = \dfrac{2}{3}\left(L_A - \dfrac{1}{2}L_B - \dfrac{1}{2}L_C\right) = -L_1\cos\left(N_r\theta\right) \\ L_\beta = \dfrac{\sqrt{3}}{3}\left(L_B - L_C\right) = -L_1\sin\left(N_r\theta\right) \end{cases} . \tag{3.7}$$

Then, the estimated magnitude L_1 can be derived by normalization calculation, as:

$$L_1 = \sqrt{{L_\alpha}^2 + {L_\beta}^2} . \tag{3.8}$$

Since the idle-phase inductance is independent of the load level, the L_0 and L_1 are unchanged during operation. Therefore, the proposed self-commissioning process only needs to be run once for the same SRM, and the L_0 and L_1 obtained by (3.6) and (3.8) can be stored as constant values for position estimation. Compared to the offline measurement in conventional methods, the self-commissioning is simpler since it does not require any manual operation and can run automatically.

Afterward, the self-commissioning is disabled, and the speed and current controllers are enabled to control the SRM under rotating conditions. The uncertain parameters in the derived idle-phase inductance can be eliminated by using the stored parameters from the self-commissioning, which results in

$$\begin{cases} L_{\mathrm{An}} = \left(L_{\mathrm{A}} - L_0\right)/L_1 = -\cos\left(N_{\mathrm{r}}\theta\right) \\ L_{\mathrm{Bn}} = \left(L_{\mathrm{B}} - L_0\right)/L_1 = -\cos\left(N_{\mathrm{r}}\theta - 2\pi/3\right) \\ L_{\mathrm{Cn}} = \left(L_{\mathrm{C}} - L_0\right)/L_1 = -\cos\left(N_{\mathrm{r}}\theta + 2\pi/3\right) \end{cases} \tag{3.9}$$

where L_{An}, L_{Bn}, and L_{Cn}, denote the normalized idle-phase inductance.

Therefore, the normalized idle-phase inductance is only a position function, which can be used for position estimation.

3.3.3 Position Estimation from the Idle-Phase Inductance Through an RPLL

Based on the normalized inductance in (3.9), a conventional solution to estimate the rotor position is using inverse trigonometric calculation [16]–[18]. However, this method cannot distinguish the quadrants of the rotor position. For example, if an anti-cosine calculation is used for (3.9), it can only calculate the position ranging from 0 to π, i.e., in the first and second quadrants. Additional quadrant judgment strategies are required to derive the full-cycle rotor position, such as adding a position offset by comparing phase inductance values [17]. Whereas the compensation logic would be more complicated for solving the position from (3.9) when considering the speed reversal (i.e., four-quadrant) operation of an SRM. Also, the anti-trigonometric calculation does not offer noise suppression capability.

To address the problems, this section proposes a new position estimator based on an RPLL, of which schematic diagram is shown in Figure 3.4. The normalized idle-phase inductance is derived through (3.9) from the idle-phase inductance. A regional heterodyne operator is then adopted to extract the position error information ε from the normalized three idle-phase inductances. Afterward, a PLL is used to converge the position error ε to zero and estimate the mechanical speed and the mechanical position. The proposed scheme does not need to distinguish the quadrants and is robust to inductance calculation noises.

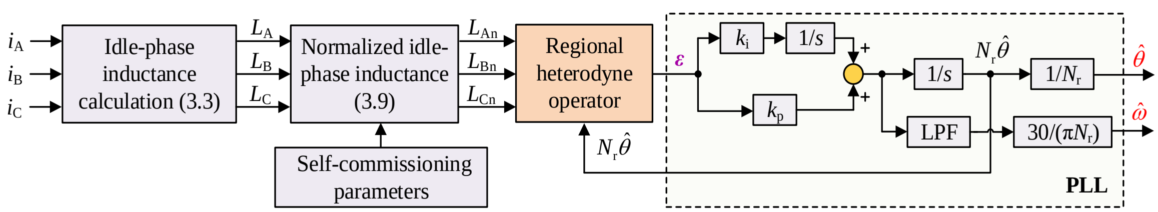

Figure 3.4 Block diagram of the proposed RPLL-based low-speed position estimation scheme for SRM drives.

3.3.3.1 Regional Heterodyne Operator in One Phase

The design of a one-phase regional heterodyne operator for position information extraction is introduced first. Figure 3.5 shows the idle-phase inductance in three phases of a 12/8 SRM. For the sake of brevity, the inductance is set as zero when the phase conducts. Due to the rotating operation of the three-phase SRM conducting at most two phases simultaneously, at least one-phase inductance can be detected through the idle-phase high-frequency injection. Thus, the full-cycle position estimation from idle-phase inductance is available.

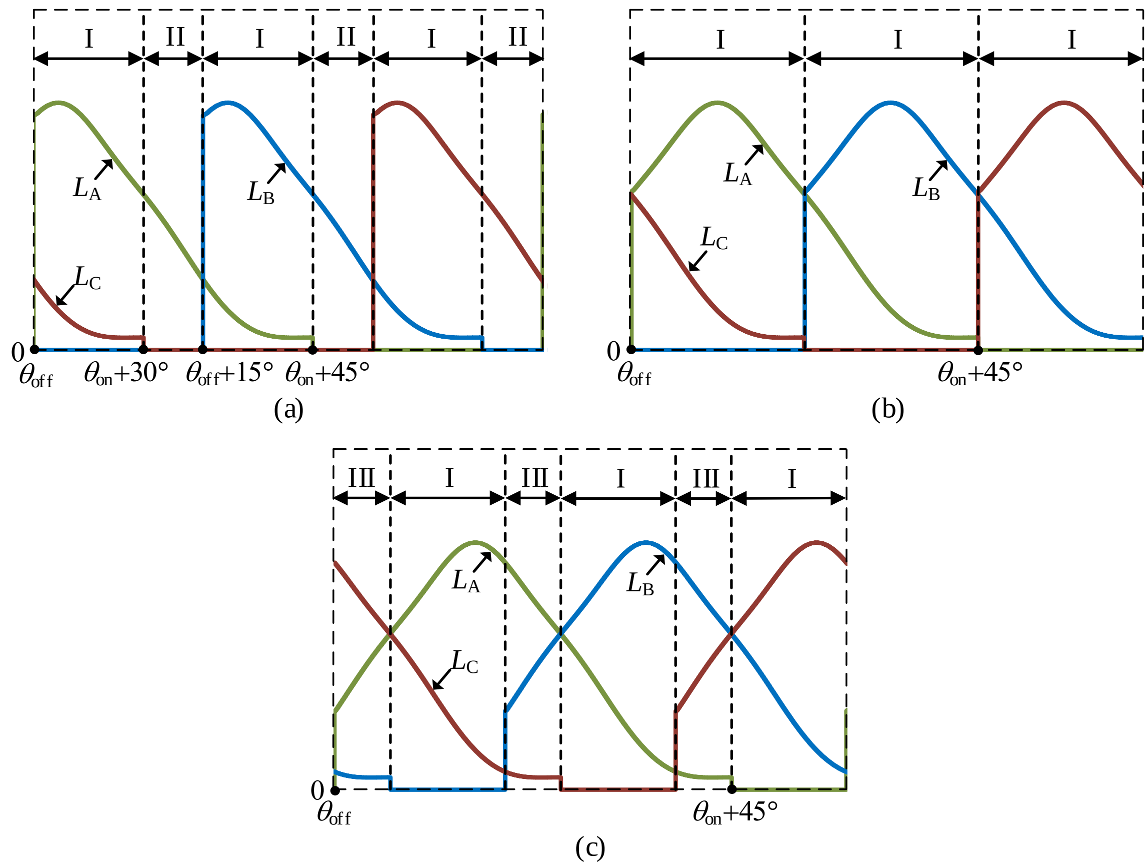

Figure 3.5 Idle-phase inductance in three phases of a 12/8 SRM. (a) θ_{off}-θ_{on}>15°. (b) θ_{off}-θ_{on}=15°. (c) θ_{off}-θ_{on}<15°.

To analyze comprehensively, three operating cases with different turn-on and turn-off angles are considered. Figure 3.5(a) shows the idle-phase inductance when the turn-on angle and turn-off angle satisfies θ_{off}-θ_{on}>15°. In region-I, the phase-A and phase-C inductances are obtained, both of which can be used to extract the position information through a double-phase heterodyne calculation. According to (3.9), the input signal ε_I of the PLL in region-I can be derived by

$$\begin{aligned}\varepsilon_{\mathrm{I}} &= \frac{2}{\sqrt{3}}\left[-L_{\mathrm{An}}\cos\left(N_{\mathrm{r}}\hat{\theta}+2\pi/3\right)+L_{\mathrm{Cn}}\cos\left(N_{\mathrm{r}}\hat{\theta}\right)\right] \\ &= \sin\left(N_{\mathrm{r}}\theta-N_{\mathrm{r}}\hat{\theta}\right)\approx N_{\mathrm{r}}\left(\theta-\hat{\theta}\right)=N_{\mathrm{r}}\Delta\theta\end{aligned} \tag{3.10}$$

where the position estimation error $\Delta\theta$ is defined as the difference between the actual and the estimated positions.

As observed from (3.10), the heterodyne calculation derives a position error information. If the position error $\varepsilon_{\mathrm{I}} \approx N_{\mathrm{r}}\Delta\theta$ is controlled to zero, the estimated position will converge to the actual position. This convergence can be guaranteed by adopting a PLL after the heterodyne operator, which will be discussed later.

Different from region-I, there is only one idle-phase inductance in region-II, as shown in Figure 3.5(a). For the 12/8 SRM, region-II is located at the range of [θ_{on}+30°, θ_{off}+15°], and the conduction range satisfies θ_{off}-θ_{on}>15°. To obtain the position error signal $\Delta\theta$ like (3.10), a single-phase heterodyne method is designed for the phase-A inductance as

$$\varepsilon_{\mathrm{II}} = \frac{L_{An} + \cos\left(N_{\mathrm{r}}\hat{\theta}\right)}{\sin\left(N_{\mathrm{r}}\hat{\theta}\right)} = \varepsilon_{\mathrm{II\text{-}amp}} \cdot 2\sin\frac{N_{\mathrm{r}}\Delta\theta}{2} \approx \varepsilon_{\mathrm{II\text{-}amp}} \cdot N_{\mathrm{r}}\Delta\theta \tag{3.11}$$

where $\varepsilon_{\mathrm{II\text{-}amp}}$ is the amplitude of the $\varepsilon_{\mathrm{II}}$, given as

$$\varepsilon_{\mathrm{II\text{-}amp}} = \frac{\sin\left[N_{\mathrm{r}}\left(\theta - \Delta\theta/2\right)\right]}{\sin\left[N_{\mathrm{r}}\left(\theta - \Delta\theta\right)\right]}. \tag{3.12}$$

As shown, the amplitude $\varepsilon_{\mathrm{II\text{-}amp}}$ is unity when the $\Delta\theta$ is equal to zero. With $\varepsilon_{\mathrm{II\text{-}amp}}$=1, the expression of (3.11) will be the same as (3.10), i.e., $\varepsilon_{\mathrm{II}} \approx N_{\mathrm{r}}\Delta\theta$.

Besides the case shown in Figure 3.5(a), there may be other combinations of turn-on and turn-off angles in SRM control. The conduction range of the SRM could be θ_{off}-θ_{on}=15° or θ_{off}-θ_{on}<15°, as shown in Figure 3.5(b) and Figure 3.5(c), respectively. In Figure 3.5(b), there is no overlap among all phases, and two-phase inductance can always be detected.

Therefore, the position estimation in this case is simple as only the double-phase heterodyne calculation of (3.10) is used. If the conduction range is narrower as shown in Figure 3.5(c), either the double-phase inductance or the three-phase inductance (marked as region-III) can be detected in the idle phases. For the sake of simplicity, the double-phase heterodyne method can still be used for region-III, which utilizes two of three idle-phase inductances to obtain the position information., namely:

$$\varepsilon_{\mathrm{III}} = \varepsilon_{\mathrm{I}} . \tag{3.13}$$

Notably, the cases in Figure 3.5(b) and 3.5(c) are seldomly used in the SRM control since the conduction range is often set to be larger than 15° to reduce the torque ripple.

As a result, the heterodyne operators in the three regions are designed to extract the position error information from the idle-phase inductance.

3.3.3.2 PLL Design and Stability Analysis

After the regional heterodyne operator, a classic PLL [106] is modified in the proposed RPLL to converge the position estimation error $\Delta\theta$ and then estimate the rotor speed and position. Being different, since the heterodyne calculation is nonlinear, the stability of the RPLL is further analyzed.

According to (3.10) and (3.11), a linearization model of the proposed RPLL can be derived and shown in Figure 3.6. Due to the presence of $\varepsilon_{\text{II-amp}}$ in (3.11), a nonlinear gain ζ is introduced in the feedforward path, which can be expressed as (3.14).

$$\zeta = \begin{cases} 1 & \text{, in region-I or -III} \\ \dfrac{\sin\left[N_{\mathrm{r}}\left(\theta - \Delta\theta/2\right)\right]}{\sin\left[N_{\mathrm{r}}\left(\theta - \Delta\theta\right)\right]} & \text{, in region-II} \end{cases} \tag{3.14}$$

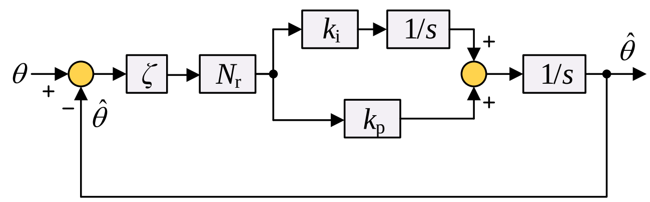

Figure 3.6 Linearization model of the proposed RPLL.

The transfer function of the proposed RPLL can be written according to its linearization model, as

$$G(s)=\frac{\hat{\theta}(s)}{\theta(s)}=\frac{\zeta N_{\mathrm{r}}\left(k_{\mathrm{p}}s+k_{\mathrm{i}}\right)}{s^2+\zeta N_{\mathrm{r}}\left(k_{\mathrm{p}}s+k_{\mathrm{i}}\right)} \tag{3.15}$$

where the nonlinear gain ζ is regarded as a constant coefficient for the sake of simplification.

The prerequisite for convergence of the position error $\Delta\theta$ is to ensure the RPLL's stability. Through the transfer function, the stability criteria can be derived based on the Routh–Hurwitz stability criterion:

$$\begin{cases}\zeta N_{\mathrm{r}}k_{\mathrm{p}}>0\\ \zeta N_{\mathrm{r}}k_{\mathrm{i}}>0\end{cases}. \tag{3.16}$$

If the PI parameters, k_p and k_i, are designed as positive values, the stability criterion becomes:

$$\zeta>0. \tag{3.17}$$

Obviously, the stability criterion is satisfied in region-I and region-III where ζ=1. However, the stability condition is unclear in region-II due to the nonlinear gain, as expressed in (3.14).

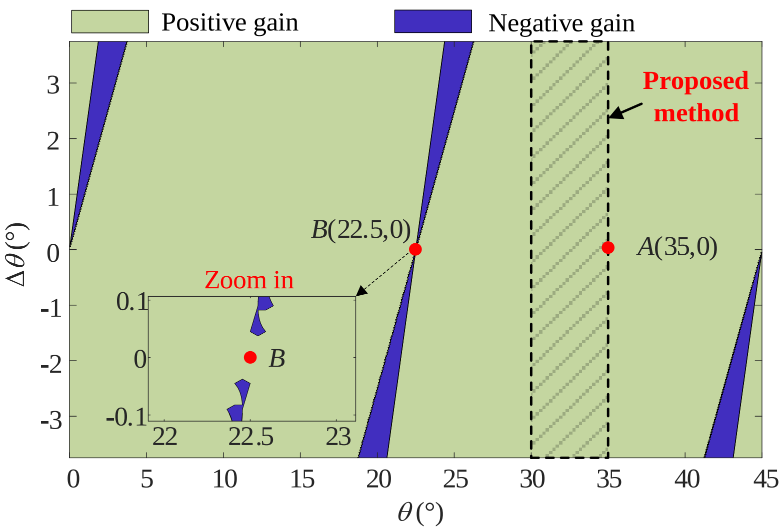

Figure 3.7 Nonlinear gain ζ in (3.14) with respect to the position and position error.

To analyze the stability of the RPLL in region-II, the nonlinear gain in (3.14) with respect to the rotor position and position error is drawn in Figure 3.7. As observed, the nonlinear gain is positive in most regions, in which the local stability can be guaranteed. However, negative gains can be found around θ=0° and θ=22.5° and would result in instability according to the criteria condition given in (3.17). To better illustrate the stability conditions, two example points are given in the figure. For an equilibrated point *A*(35, 0), where the position is 35° and the position error is zero, it is in the positive-gain region and far away from the unstable area. Therefore, point *A* would have a considerable stability margin against position error variation, which ensures the robust local stability of the RPLL. For point *B*(22.5,0), although the positive gain can be satisfied within a neighborhood, as shown in the zoom-in figure, the stability margin is significantly narrower than point *A*. Hence, even though the position error at point *B* is zero, the RPLL is sensitive to a small perturbance and may diverge to an unstable point when the position error varies. In consequence, the local stability of the RPLL with the nonlinear gain will be robust if the operating point of the SRM is within the positive-gain region and away from the unstable area.

According to the local stability analysis, the single-phase heterodyne operator with a nonlinear gain cannot be used for the whole position range. However, it is suitable for position estimation of the proposed RPLL. As analyzed earlier, the single-phase heterodyne calculation is only used for region-II within [θ_{on}+30°, θ_{off}+15°]. The turn-on angle θ_{on} is often around the unaligned position (0°) to improve the current tracking rate of the SRM, and the turn-off angle θ_{off} is set advanced to the aligned position (22.5°) to avoid negative torque. Therefore, the nonlinear gain used in the proposed RPLL is only located in a narrow region. To illustrate clearly, region-II [θ_{on}+30°, θ_{off}+15°] with θ_{on}=0° and θ_{off}=20° is drawn in Figure 3.7 as an example. As can be seen, region-II is encompassed by the positive-gain region. The local stability against robust against large position error variation can be ensured in the proposed RPLL.

Based on the robust stability in all the three regions, the convergence of position estimation can be guaranteed. As can be found from the transfer function (3.15), the proposed RPLL is a type-II system that has a zero-tracking error of a step or ramp signal, such as the rotor position $\theta(s)=\omega_0/s^2$ that is a ramp signal at a constant speed ω_0 in the steady state. Therefore, the steady-state position error $\Delta\theta_{ss}$ is zero according to the final value theorem, expressed as follows:

$$\Delta\theta_{ss} = \lim_{s\to 0} s\cdot\theta(s)\cdot\left[1-G(s)\right] = \lim_{s\to 0}\frac{\omega_0 s}{s^2+\zeta N_r\left(k_p s+k_i\right)} = 0\,. \tag{3.18}$$

Accordingly, the RPLL can converge the position error derived by the proposed regional heterodyne operator. Then, the rotor speed and position can be estimated.

To configure the RPLL's parameters, the characteristic equation of the transfer function is written with a double pole:

$$s^2 + \zeta N_\mathrm{r}\left(k_\mathrm{p}s + k_\mathrm{i}\right) = \left(s + \rho\right)^2 \tag{3.19}$$

which gives the parameter design scheme:

$$k_\mathrm{p} = 2\rho/N_\mathrm{r} \text{ and } k_\mathrm{i} = \rho^2/N_\mathrm{r} \tag{3.20}$$

where ρ is the absolute value of the RPLL's double pole, and the nonlinear gain ζ is regarded as unity due to the convergence.

The tuning of the double pole ρ is a trade-off between the response rate and noise suppression capability. Figure 3.8 shows the Bode diagram of the proposed observer with different pole values. The RPLL has a lowpass-frequency characteristic, which can suppress the measurement noises and harmonic disturbance.

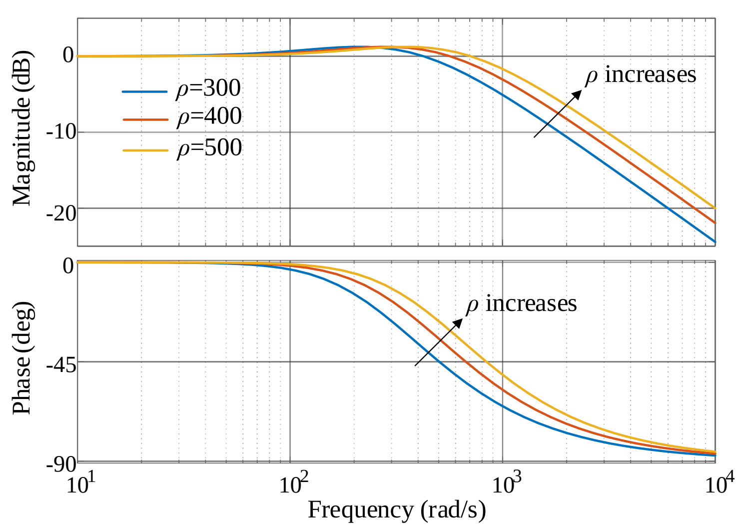

Figure 3.8 Bode diagram of the proposed RPLL.

3.3.3.3 Overall Design of the Regional Heterodyne Operator

In the previous analysis, the design of the phase-A regional heterodyne operator is introduced as an example. Other phases' design is similar by considering the 2π/3 phase shift. The overall design scheme is summarized in Table 3.1.

Table 3.1 Overall Design of the Proposed Regional Heterodyne Operator.

Idle phases	$\varepsilon =$
Phase-A	$\left[L_{\mathrm{An}}+\cos\left(N_{\mathrm{r}}\hat{\theta}\right)\right]\Big/\sin\left(N_{\mathrm{r}}\hat{\theta}\right)$
Phase-B	$\left[L_{\mathrm{Bn}}+\cos\left(N_{\mathrm{r}}\hat{\theta}-2\pi/3\right)\right]\Big/\sin\left(N_{\mathrm{r}}\hat{\theta}-2\pi/3\right)$
Phase-C	$\left[L_{\mathrm{Cn}}+\cos\left(N_{\mathrm{r}}\hat{\theta}+2\pi/3\right)\right]\Big/\sin\left(N_{\mathrm{r}}\hat{\theta}+2\pi/3\right)$
Phase-A and -C	$\frac{2}{\sqrt{3}}\left[-L_{\mathrm{An}}\cos\left(N_{\mathrm{r}}\hat{\theta}+2\pi/3\right)+L_{\mathrm{Cn}}\cos\left(N_{\mathrm{r}}\hat{\theta}\right)\right]$
Phase-A and -B	$\frac{2}{\sqrt{3}}\left[L_{\mathrm{An}}\cos\left(N_{\mathrm{r}}\hat{\theta}-2\pi/3\right)-L_{\mathrm{Bn}}\cos\left(N_{\mathrm{r}}\hat{\theta}\right)\right]$
Phase-B and -C	$\frac{2}{\sqrt{3}}\left[L_{\mathrm{Bn}}\cos\left(N_{\mathrm{r}}\hat{\theta}+2\pi/3\right)-L_{\mathrm{Cn}}\cos\left(N_{\mathrm{r}}\hat{\theta}-2\pi/3\right)\right]$
Phase-A, -B and -C	$\frac{2}{\sqrt{3}}\left[-L_{\mathrm{An}}\cos\left(N_{\mathrm{r}}\hat{\theta}+2\pi/3\right)+L_{\mathrm{Cn}}\cos\left(N_{\mathrm{r}}\hat{\theta}\right)\right]$

3.3.4 Analysis of the Approximated Inductance Model

This chapter adopts an approximate inductance model in (3.5) that ignores other inductance harmonics, while it would result in modeling errors. In this subsection, the effects of the modeling error on the self-commissioning and position estimation are analyzed.

For a more accurate inductance model of the SRM, the inductance harmonics need to be considered. Particularly, the second harmonic is most dominant among other high-order harmonic components. Thus, a modified inductance model can be established by considering the second harmonic:

$$\begin{cases} L'_{\mathrm{A}} = L_0 - L_1 \cos\left(N_{\mathrm{r}}\theta\right) - L_2 \cos\left(2N_{\mathrm{r}}\theta\right) \\ L'_{\mathrm{B}} = L_0 - L_1 \cos\left(N_{\mathrm{r}}\theta - 2\pi/3\right) - L_2 \cos\left(2N_{\mathrm{r}}\theta - 4\pi/3\right) \\ L'_{\mathrm{C}} = L_0 - L_1 \cos\left(N_{\mathrm{r}}\theta + 2\pi/3\right) - L_2 \cos\left(2N_{\mathrm{r}}\theta + 4\pi/3\right) \end{cases} \tag{3.21}$$

where L_2 is the magnitude of second inductance harmonic. For the sake of distinction, the superscript ′ represents the variable when considering the inductance harmonic. The modified model in (3.21) is accurate to the SRM inductance characteristic, of which accuracy is proved in the literature [101].

The self-commissioning process expressed in (3.6)-(3.8) can be rewritten by considering the effect of second inductance harmonics, as follows:

$$\hat{L}_0 = \left(L'_{\mathrm{A}} + L'_{\mathrm{B}} + L'_{\mathrm{C}}\right)/3 = L_0 \tag{3.22}$$

$$\begin{cases} L'_{\alpha} = \dfrac{2}{3}\left(L'_{\mathrm{A}} - \dfrac{1}{2}L'_{\mathrm{B}} - \dfrac{1}{2}L'_{\mathrm{C}}\right) \\ L'_{\beta} = \dfrac{\sqrt{3}}{3}\left(L'_{\mathrm{B}} - L'_{\mathrm{C}}\right) \end{cases} \tag{3.23}$$

$$\hat{L}_1 = \sqrt{L'^2_{\alpha} + L'^2_{\beta}} = \sqrt{L_1{}^2 + L_2{}^2 + 2L_1L_2\cos(3N_{\mathrm{r}}\theta)} \neq L_1 . \tag{3.24}$$

As can be seen from (3.22) and (3.24), the inductance harmonic does not affect the estimation accuracy of L_0, but the L_1 estimation contains additional bias and varies with different initial positions. Hence, the approximation inductance model (3.5) used for the self-commissioning results in inaccurate estimation of the magnitude L_1.

Then, the L_0 and L_1 estimation obtained in (3.22) and (3.24) are used to normalize the idle-phase inductance:

$$\begin{cases} L'_{\mathrm{An}} = \left(L'_{\mathrm{A}} - \hat{L}_0\right)\Big/\hat{L}_1 = -k_{\mathrm{err}}\cos\left(N_{\mathrm{r}}\theta\right) + \Delta L_{\mathrm{A}} \\ L'_{\mathrm{Bn}} = \left(L'_{\mathrm{B}} - \hat{L}_0\right)\Big/\hat{L}_1 = -k_{\mathrm{err}}\cos\left(N_{\mathrm{r}}\theta - 2\pi/3\right) + \Delta L_{\mathrm{B}} \\ L'_{\mathrm{Cn}} = \left(L'_{\mathrm{C}} - \hat{L}_0\right)\Big/\hat{L}_1 = -k_{\mathrm{err}}\cos\left(N_{\mathrm{r}}\theta + 2\pi/3\right) + \Delta L_{\mathrm{C}} \end{cases} \tag{3.25}$$

where

$$k_{\mathrm{err}} = L_1\big/\hat{L}_1 \tag{3.26}$$

is the gain error due to the inaccurate L_1 estimation, and

$$\begin{cases} \Delta L_{\mathrm{A}} = -L_2\cos\left(2N_{\mathrm{r}}\theta\right)\big/\hat{L}_1 \\ \Delta L_{\mathrm{B}} = -L_2\cos\left(2N_{\mathrm{r}}\theta - 4\pi/3\right)\big/\hat{L}_1 \\ \Delta L_{\mathrm{C}} = -L_2\cos\left(2N_{\mathrm{r}}\theta + 4\pi/3\right)\big/\hat{L}_1 \end{cases} \tag{3.27}$$

are the second inductance harmonics after normalization.

Afterward, the proposed regional heterodyne operator is used to obtain the input error signal ε of the PLL. Here, the effect of the inductance harmonic is analyzed in the region-I as an example. Other regions can be analyzed in the same way.

According to (3.10), the input error signal in the region-I can be expressed as (3.28) when considering the inductance harmonic:

$$\begin{aligned} \varepsilon'_{\mathrm{I}} &= \frac{2}{\sqrt{3}}\left[-L'_{\mathrm{An}}\cos\left(N_{\mathrm{r}}\hat{\theta} + 2\pi/3\right) + L'_{\mathrm{Cn}}\cos\left(N_{\mathrm{r}}\hat{\theta}\right)\right] \\ &\approx k_{\mathrm{err}}N_{\mathrm{r}}\Delta\theta - L_2\sin\left(3N_{\mathrm{r}}\theta - N_{\mathrm{r}}\Delta\theta\right)\big/\hat{L}_1 \end{aligned}. \tag{3.28}$$

Compared to the case (3.10) ignoring the inductance harmonic, the actual input signal $\varepsilon'_{\mathrm{I}}$ of the PLL has a gain error and a third harmonic distortion.

The third harmonic distortion caused by the modeling error is smaller since $\hat{L}_1$ is larger than L_2. Besides, the harmonic distortion can be further mitigated by the RPLL due to the lowpass-frequency characteristic, as shown in Figure 3.8.

For the gain error, the transfer function of the RPLL in the region-I can be modified as (3.29) when considering the gain error:

$$G(s)=\frac{\hat{\theta}(s)}{\theta(s)}=\frac{k_{\mathrm{err}}N_{\mathrm{r}}\left(k_{\mathrm{p}}s+k_{\mathrm{i}}\right)}{s^2+k_{\mathrm{err}}N_{\mathrm{r}}\left(k_{\mathrm{p}}s+k_{\mathrm{i}}\right)} \tag{3.29}$$

To analyze the effect of on position estimation, the convergence of the position estimation error can be derived from the transfer function (3.29) according to the final value theorem:

$$\Delta\theta_{\mathrm{ss}}=\lim_{s\to 0}s\cdot\theta(s)\cdot\left[1-G(s)\right]=\lim_{s\to 0}\frac{k_{\mathrm{err}}\omega_0 s}{s^2+k_{\mathrm{err}}N_{\mathrm{r}}\left(k_{\mathrm{p}}s+k_{\mathrm{i}}\right)}=0\,. \tag{3.30}$$

It can be found that the gain error k_{err} caused by the inaccurate L_1 estimation does not affect the proposed method since the estimation error $\Delta\theta_{\mathrm{ss}}$ can still converge to zero. The estimated rotor position can track the actual rotor position when the L_1 estimation contains errors. The analysis will be validated experimentally.

In summary, although the approximation inductance model contains modeling errors, the adverse impact is mitigated in the proposed method. A more accurate model can improve the estimation accuracy theoretically, but the enhancement may be limited in practical applications. Due to the presence of current sampling errors, mutual couplings, and external disturbances, the ignored high-order harmonics are not the primary error sources. Moreover, the approximation model can offer simpler implementation since no time-consuming offline measurement is needed.

3.4 Experimental Verification

In this section, the proposed position estimation method is validated by experiments on a 5.5-kW three-phase 12/8 SRM test bench. Since the rated torque of the IM is 30 N·m, the maximum load that can be applied is 30 N·m in the setup. A torque transducer (NCTE Series 3000) is installed to measure the shaft torque, and the sampling rate of the torque transducer is 100 Hz. The DC-link voltage and injection voltage are set as 72 V. The injection frequency could be selected higher to avoid much delay in inductance calculation of (3.3), and the injection duty can be set as high as possible to increase the SNR of the induced current measurement. According to Figure 3.1, the injection frequency is 6.67 kHz, and the duty cycle is full. The cut-off frequency of the LPF in the parameter self-commissioning process is 5 Hz to ensure accurate initial parameter estimation. Note that the LPF is not used during SRM sensorless control, and thus it does not affect the control performance. The tunable parameter of the proposed RPLL is set as ρ=320. Experimental results are recorded in a Tektronix® MDO3024 oscilloscope and plotted in MATLAB. The actual position is measured by a resolver to calculate estimation errors.

The experimental result given in Figure 3.9 shows the proposed self-commissioning process for learning the DC inductance and the magnitude of the idle-phase inductance. The current controller is disabled in the self-commissioning, and pulse voltages are injected into the three phases to calculate the inductance value by (3.3). Since the injection period is short, the torque caused by the injection voltages is negligible, and the SRM can keep standstill during the three-phase injection. From the self-learning result, after injecting pulse voltages in all phases, the three-phase inductance values are obtained, which are around L_A=2.054 mH, L_B=2.728 mH, and L_C=0.361 mH. Therefore, the DC bias L_0 and the magnitude of the phase inductance L_1 can be calculated based on (3.6) and (3.8), which are L_0=1.714 mH and L_1=1.408 mH. The two idle-phase inductance parameters will be used for position estimation during the SRM operation. Compared to conventional sensorless control methods that need the offline measurement of magnetic characteristics, the proposed self-commissioning is automatic and more straightforward. The self-commissioning algorithm is just adopted once for the same motor.

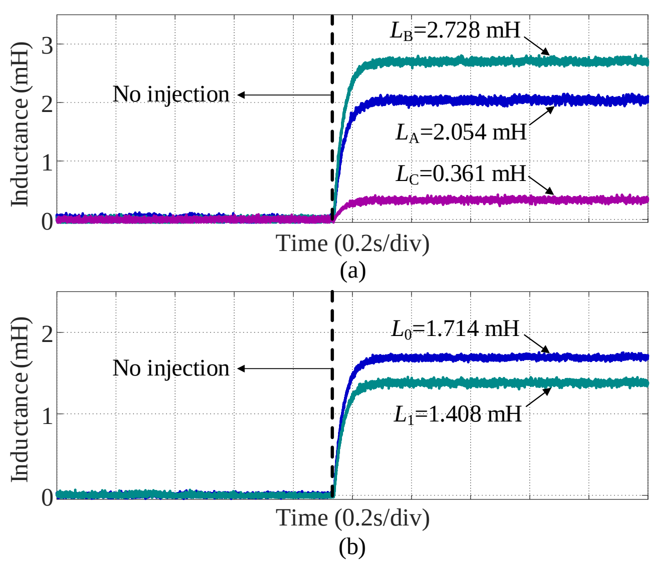

Figure 3.9 Self-commissioning for the proposed scheme.

After the self-commissioning, the speed and current controllers are enabled for the normal operation of the SRM. Figure 3.10 shows the idle-phase inductance, phase current, and position estimation results. The SRM is operated at 100 r/min and no load. Without losing generality, three cases with different turn-on/off angles are given. As depicted in Figure 3.10(a), in which the turn-on and turn-off angles are θ_{on}=0° and θ_{off}=20°, high-frequency pulse voltages are injected into the idle-phase to calculate the phase inductance, while the inductance values are set to zero when the phase is turned on. Due to the low inductance around the unsaturated position (0°), the phase current has larger ripples when the hysteresis control is used during the phase turns on. Still, it does not affect the position estimation because only the idle-phase inductance is used in the proposed sensorless control scheme. Since the LPFs for inductance calculation are not used when the motor rotates, the derived inductance contains spikes. According to the analysis in Figure 3.5, two-phase inductance is obtained simultaneously in region-I, and the proposed RPLL can estimate the rotor position with the double-phase heterodyne calculation. When only one-phase inductance is detected by the injection signal, i.e., in region-II, the proposed single-phase heterodyne method can be used according to Table 3.1. As shown from the experimental result in Figure 3.10(a), the estimated rotor position can match the actual position by the proposed RPLL even though no magnetic characteristics are used for estimation. Although region-I and region-II employ different heterodyne calculation, the position estimation between the regions is smooth and stable. Afterward, Figure 3.10(b) and Figure 3.10(c) show the results in narrower conduction ranges of [θ_{on}=0°, θ_{off}=15°] and [θ_{on}=0°, θ_{off}=12°] at 100 r/min. Only the double-phase heterodyne calculation is used in the two cases since either double-phase or three-phase inductance is obtained during the operation. As shown, the proposed approach can still estimate the rotor position accurately, which proves the method’s effectiveness with different turn-on and turn-off angles.

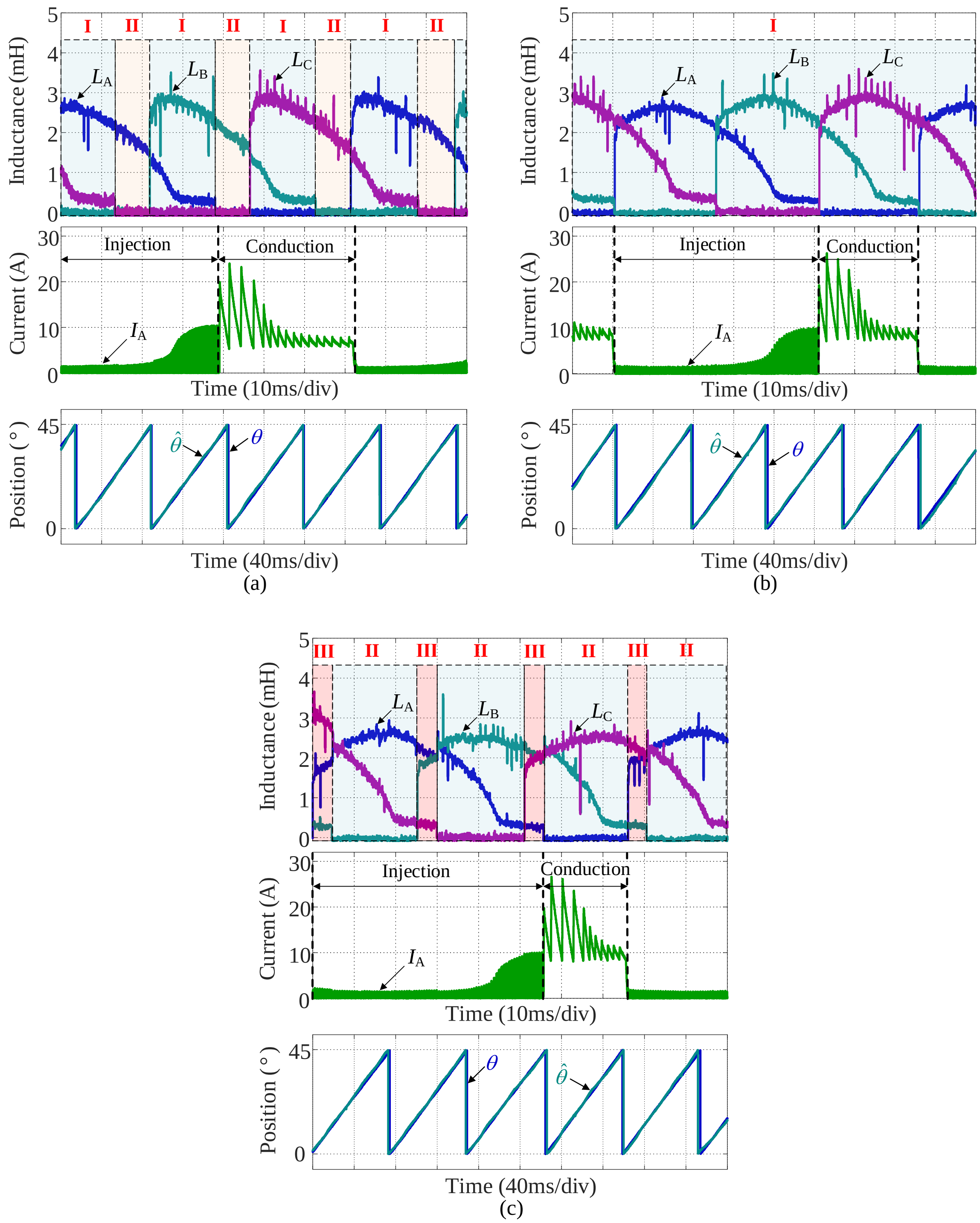

Figure 3.10 Idle-phase inductance, phase current, and position estimation at 100 r/min without load. (a) θ_{on}=0° and θ_{off}=20°. (b) θ_{on}=0° and θ_{off}=15°. (c) θ_{on}=0° and θ_{off}=12°.

The position estimation results at other operating speeds with no load are given in Figure 3.11. It is notable that since the phase conduction range of a 12/8 SRM often lags behind 15° to reduce the torque ripple, the control angles used in the rest of the chapter are kept as θ_{on}=0° and θ_{off}=20° for brevity. The actual position and estimated position under 200 r/min and 400 r/min are given in Figure 3.11(a) and Figure 3.11(b), respectively. Similar to the estimation result at 100 r/min, the proposed method can achieve accurate position estimation at a medium speed. It benefits combining the proposed low-speed method with other high-speed position estimation schemes for full-speed sensorless control.

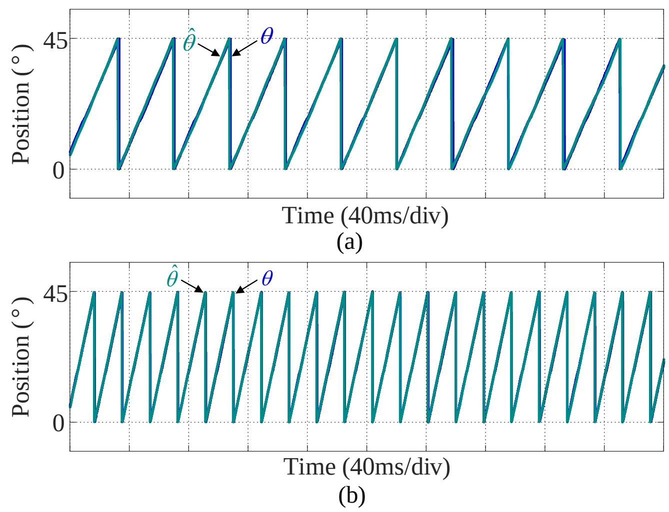

Figure 3.11 Position estimation at other speeds without load. (a) 200 r/min. (b) 400 r/min.

To verify the improvement compared to the conventional method, the proposed position estimation scheme is compared with the phase-inductance vector method proposed in [17]. In the traditional method, it estimates the full-cycle position from the inductance detected in both the idle-phase period (3.3) and the conduction period (3.4). This scheme does not require any offline measurement of magnetic characteristics, but it cannot support accurate estimation under load conditions. To illustrate the limitation in the conventional scheme, Figure 3.12 compares the position estimation results with a 30 N·m load (100% torque that the IM can apply) at 150 r/min. As shown, when the SRM runs under no-load conditions, both the proposed method (Figure 3.12(a)) and the conventional scheme (Figure 3.12(c)) can achieve accurate position estimation. When the load increases to 30 N·m, the SRM becomes saturated. From Figure 3.12(b), the proposed scheme is not affected by the saturation effect since only the idle-phase inductance is used, and therefore, the rotor position can still be estimated well under the load condition. However, the conventional method has distorted position estimation in Figure 3.12(d) since it does not consider the saturation effect on position estimation. The large position error cannot support sensorless control, so the comparative tests are implemented using the actual position feedback for clear illustration. In consequence, the proposed scheme inherits the advantage of the conventional method [17] that does not require any offline measurement effort for magnetic characteristics and further realizes the accurate estimation under load conditions.

Due to the improved operation capability under load conditions, the proposed scheme can achieve good estimation accuracy with the load variation. Figure 3.13 depicts experimental results under a load disturbance given by the IM where the actual speed, the estimated speed, the position estimation error, and the shaft torque measured by torque transducer are shown. The SRM first runs at the no-load condition at 200 r/min, and then a 30 N·m load is added on the motor shaft. Since the speed is controlled by SRM, the rotor speed decreases at the load-added instant while can fast converge to 200 r/min. After the load is removed, the motor speed temporally increases and then comes back to 200 r/min.

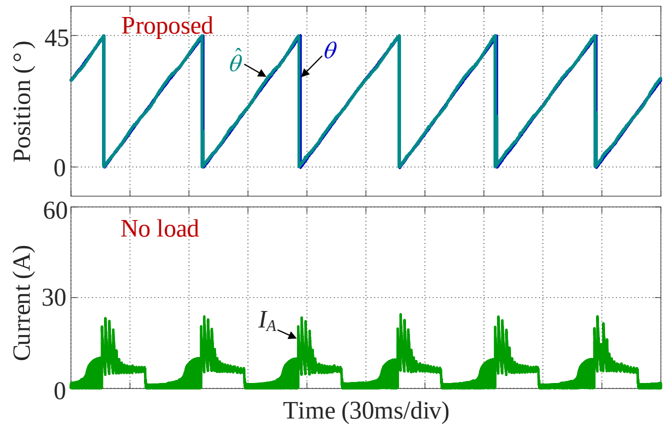
Proposed
45
0
Position (°)
$\hat{\theta}$
θ
60
30
0
Current (A)
No load
I_A
Time (30ms/div)

(a)

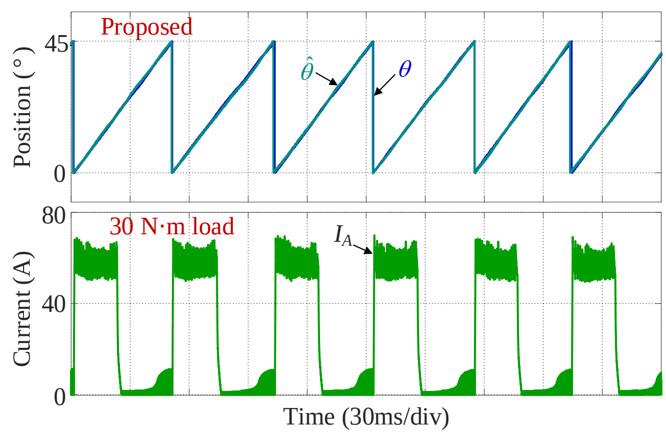
Proposed
45
0
Position (°)
$\hat{\theta}$
θ
80
40
0
Current (A)
30 N·m load
I_A
Time (30ms/div)

(b)

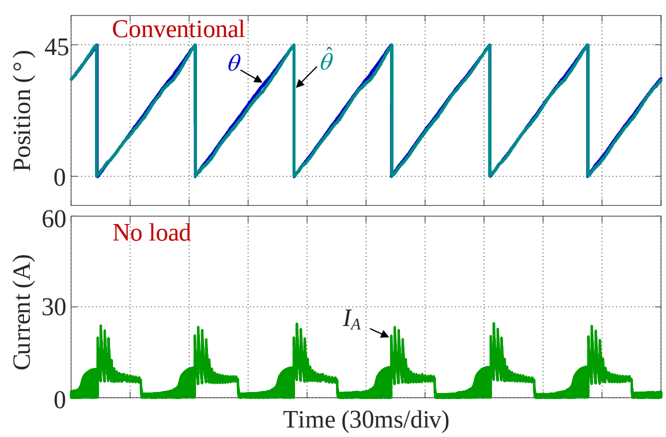
Conventional
45
0
Position (°)
θ
$\hat{\theta}$
60
30
0
Current (A)
No load
I_A
Time (30ms/div)

(c)

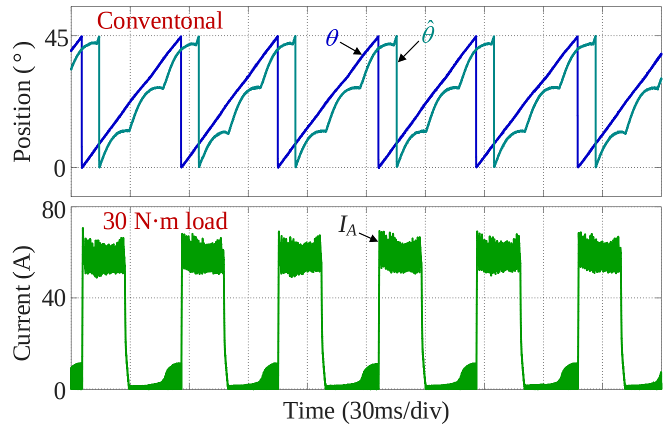

(d)

Figure 3.12 Experimental position estimation results (in sensor-based control) between the proposed scheme and the conventional phase-inductance vector method at 150 r/min. (a) Proposed scheme under the no-load condition. (b) Proposed scheme under the 30 N·m load condition. (c) Conventional method under the no-load condition. (d) Conventional method under the 30 N·m load condition.

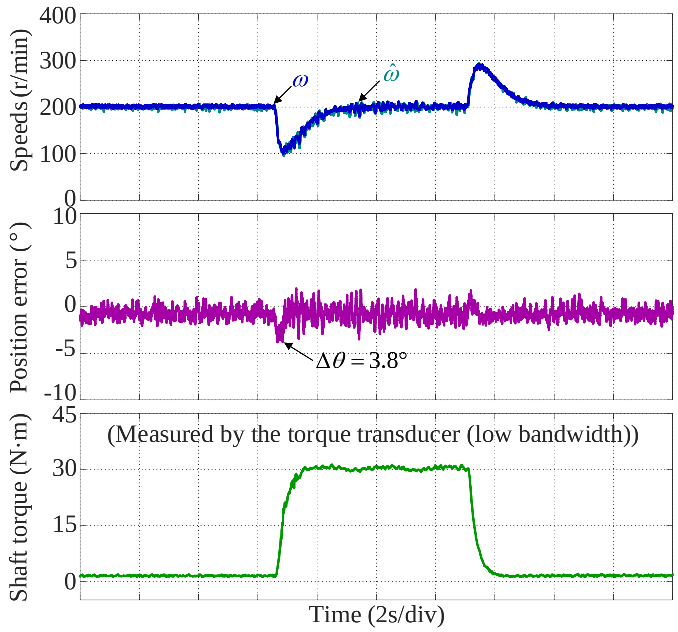

Figure 3.13 Position-sensorless control at 200 r/min under load changes.

During the load change, the speed estimation from the proposed RPLL can track the speed variation. The transient position estimation errors at the load disturbance instant is

3.8°. Hence, the experimental test validates that the robust sensorless control under load conditions can be achieved without using any offline obtained magnetic characteristics. It is notable that since the sampling rate of the torque transducer is only 100 Hz, so high-frequency torque ripples may not be captured by this torque transducer.

The position and speed estimation accuracy are also validated at standstill (zero speed) with 30 N·m load, as shown in Figure 3.14. As can be found, the estimated rotor speed can track the actual speed around zero, and the maximum position error is 1.7° under the 30 N·m load. Besides, the rotor speed of the SRM can be well controlled under the zero-speed condition with load by using the proposed position-sensorless control scheme.

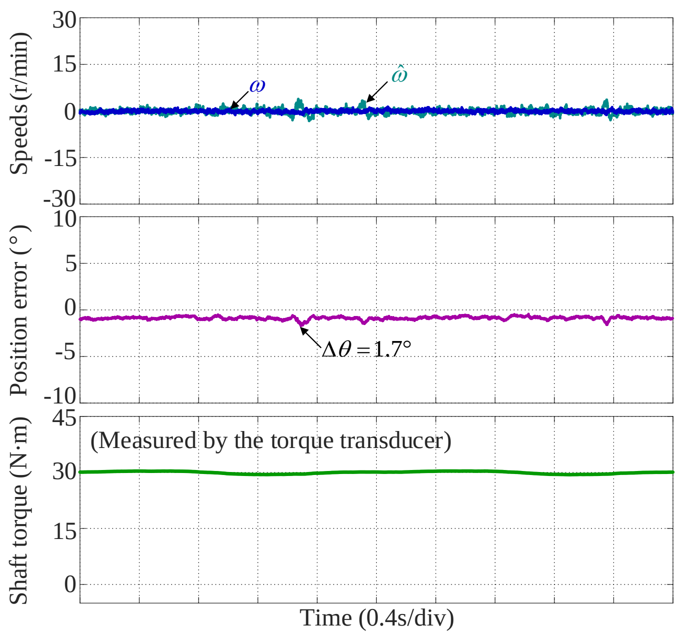

Figure 3.14 Position-sensorless control at standstill condition with load.

Furthermore, the speed transient performance of the proposed method is verified by experiments. Figure 3.15 shows the position and speed estimation under a ramp speed response and a step speed response, respectively. The rotor speed is controlled in the sensorless model from 150 r/min to 250 r/min. As can be found, the SRM can well track both the slowly varying and fast varying speed responses. The overall position estimation error is around zero, and the maximum transient position error is 2.4° in the ramp speed test and 2.3° in the step speed test.

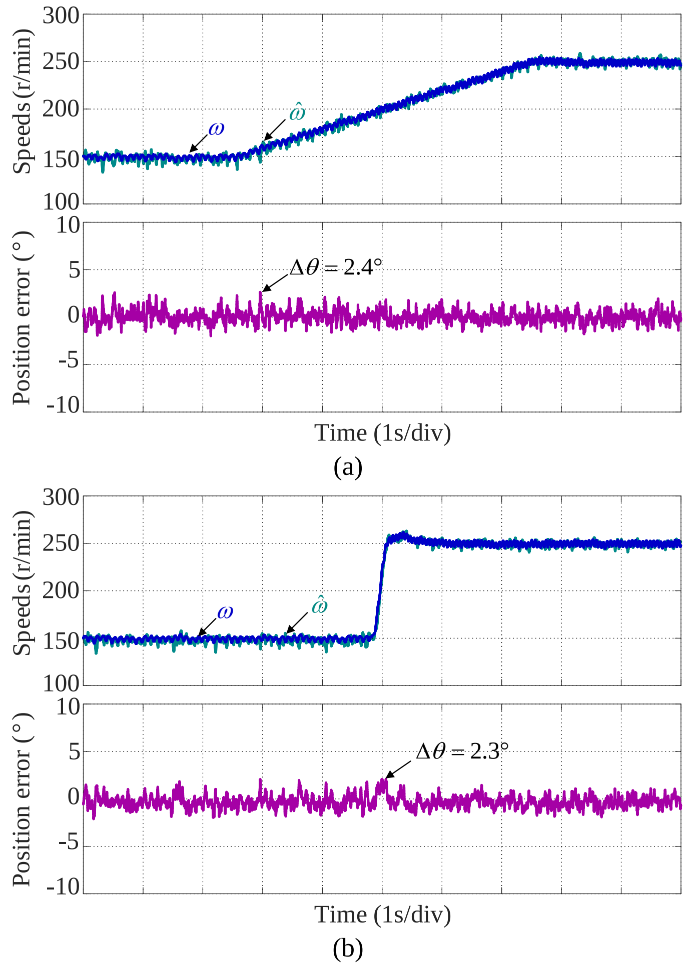

Figure 3.15 Position-sensorless control under speed variation from 150 r/min to 250 r/min. (a) Ramp speed response. (b) Step speed response.

As another improvement, the proposed position-sensorless control can achieve speed reversal operation without additional quadrant judgment. In Figure 3.16, position and speed estimation results under a speed reversal test between 150 r/min and -150 r/min are shown.

During the speed reversal, the negative torque will be required when the rotor speed decreases or is negative. The negative torque is realized by changing the turn-on angle and turn-off angle from (0° and 20°) to (25° and 45°) in this test. As can be observed from the results, the estimated speed has a good agreement to the actual value when the rotor speed changes in opposite directions. The maximum position estimation error during the speed transition is around 3°, and the average position error is almost around zero. Therefore, the proposed sensorless control scheme can easily realize the speed reversal operation without using additional judgement scheme.

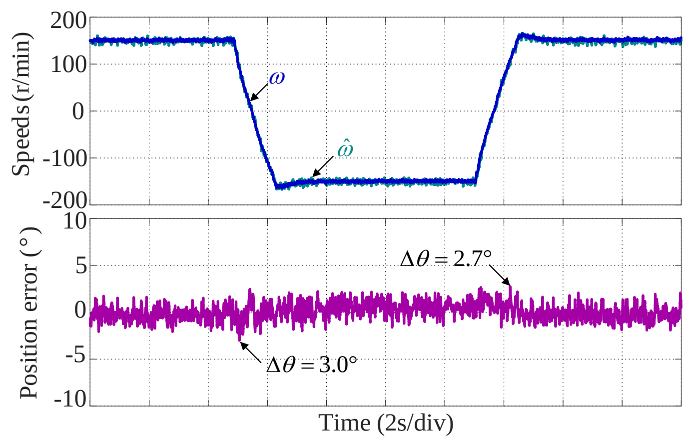

Figure 3.16 Validation of the speed reversal operation of the proposed sensorless control scheme.

It is also notable that the proposed approach cannot support very high speed sensorless control since the large back-EMF would narrow the idle-phase region for pulse injection. Figure 3.17 shows the experimental result under a speed rise starting from 150 r/min (15% rated speed). At low speed, the speed and position can be well estimated. However, when the speed raises, the position estimation error gradually increases. The rotor speed even starts decreasing around 750 r/min (75% rated speed) since negative torque is generated when the position estimation error is too large. Afterward, the sensorless control becomes unstable, and the inverter is shut down. Note that, this is the common feature of the pulse-injection-based methods. High-speed sensorless control can be done by combining a model-based method.

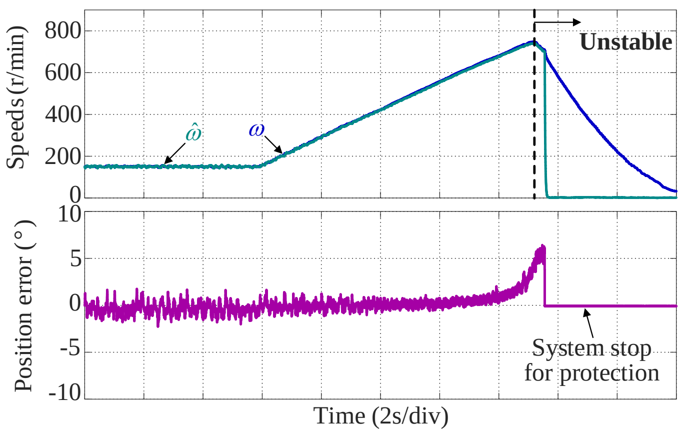

Figure 3.17 Position-sensorless control performance under increasing speed from 150 r/min (15% rated speed) to high speed.

The chapter adopts a simplified inductance model (3.5) for position estimation, and the effects of modeling errors are discussed early. To validate the analysis, experimental results of position estimation by using different L_1 values in the proposed method are shown in Figure 3.18. The motor runs at 200 r/min in sensorless control, and the L_1 value is changed from 1.408 mH (obtained from the self-commissioning) to 2.112 mH (adding a 50% error). As shown, the position errors are the same before and after increasing the L_1 value, which validates that the accuracy of L_1 does not affect the proposed RPLL. Even though the approximate inductance model would cause inaccurate estimation of L_1 since the second inductance harmonic is nonnegligible, accurate position estimation can still be guaranteed by the RPLL.

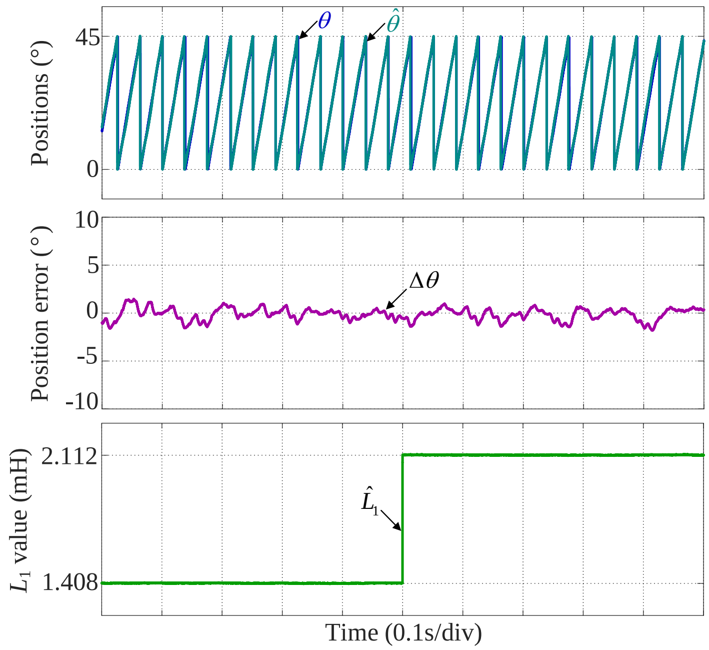

Figure 3.18 Position estimation results of the proposed RPLL when using different L_1 values.

3.5 Conclusion

This chapter proposes a general-purpose low-speed position-sensorless control scheme for SRM drives with enhanced generality. The approach adopts a new position estimator based on an RPLL with a self-commissioning process to estimate the rotor position without using *a priori* knowledge of magnetic characteristics. Compared to existing low-speed position estimation methods, the proposed scheme is independent of motor parameters and does not require offline measurement. Hence, it improves the position estimation algorithm's universality and facilitates practical implementation. Moreover, the proposed approach can support robust sensorless operation at both no-load and load conditions due to the eliminated saturation effect. Speed reversal sensorless control can also be realized by the proposed RPLL through a simple heterodyne design. Experimental results validate that the proposed position estimator has good estimation accuracy in different operating conditions even though not using the offline measured magnetic characteristics.

Chapter 4

Induced Current Reduction Scheme for Low-Speed Position-Sensorless Control

4.1 Introduction

Pulse injection methods are effective for low-speed position estimation of SRM drives. The RPLL proposed in the previous chapter can realize stable position-sensorless control without using prestored magnetic characteristics. However, additional copper losses and torque ripples are common issues for pulse-injection-based schemes, including the RPLL-based approach. Typically, the magnitude of injected pulse voltages is constant and set as the DC-link voltage. Since the stator inductance varies with the rotor position, induced current is distributed nonlinearly in the idle phase, which has a lowest magnitude at the aligned position and has a largest magnitude at the unaligned position. Lower induced current leads to low SNR in inductance calculation, while the larger induced current causes significantly copper losses and torque ripples. The trade-off makes the implementation complicated and cannot achieve satisfactory performance in the sensorless SRM drive.

This chapter aims to mitigate the issue by proposing a new pulse injection scheme for low-speed position estimation with the reduced induced current, whilst keeping the same estimation accuracy. The injection amplitude of pulse voltages is no longer constant; instead, it can be adjusted online through a terminal sliding-mode controller (TSMC) to keep a minimal induced current's magnitude in the whole idle-phase period. The minimal induced current is able to guarantee sufficient SNR for accurate position estimation, while torque ripples and copper losses can be reduced a lot compared to the previous pulse injection method. Besides, due to the insensitivity to model errors and system parameter variations, the proposed TSMC is independent of the exact magnetic characteristics of an SRM and does not require offline measurement effort. The controller design and performance analyses are discussed in detail in the chapter. Experimental results on a three-phase 12/8 SRM setup validate the proposed method's effectiveness.

4.2 Discussion on Conventional Pulse Injection Methods

The conventional pulse injection method for low-speed position-sensorless control is illustrated in Figure 4.1. Figure 4.1(a) shows the phase current and phase inductance of the SRM. The hysteresis control with the soft chopping mode is used to regulate the current when the phase conducts. The high-frequency pulse voltages are injected into the idle phase for position estimation. The injection amplitude is set as the DC-link voltage U_{dc}, which is the maximum voltage that can apply on the phase, as shown in Figure 4.1 (b) and (c).

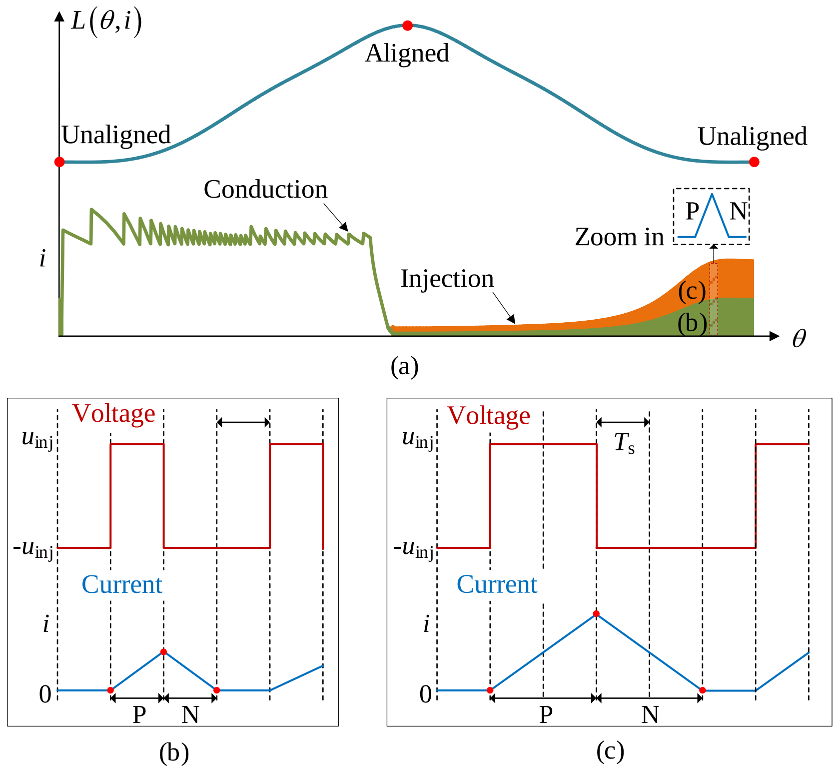

Figure 4.1 Illustration of pulse-injection-based position estimation methods. (a) Phase current and phase inductance. (b) Single-period pulse injection method. (c) Double-period pulse injection method.

As discussed in Chapter 3, the pulse injection method often adopts a pair of positive (P) and negative (N) voltage pulses during the idle-phase period, as presented in Figure 4.1(b). To assure the induced current i decaying to zero before the next positive voltage pulse starts, additional one-period negative voltage pulse is added. This injection scheme is named as the single-period pulse injection method. Since the phase inductance around the aligned position is largest and becomes lowest around the unaligned position, the magnitude of the induced current in the idle phase varies with the rotor position. For example, the induced current has lower magnitude around the aligned position, while it increases when approaching the unaligned position. This uneven distribution of the induced current raises some issues:

1) The SNR of position estimation is related to the current measurement accuracy around the aligned position due to the lowest current magnitude.
2) Large copper losses and torque ripples are caused due to the significant induced current when the inductance is lower.

In position-sensorless control, position estimation accuracy should be guaranteed for reliable operation. The magnitude of induced current can be increased by either using a larger injection magnitude (maximum equal to the DC-link voltage) or adopting a lower-frequency pulse injection, as presented in Figure 4.1(c). The two ways can increase the SNR of current measurement, thus improving the inductance calculation accuracy for position estimation. However, the current around the unaligned position increases dramatically with the larger injection amplitude or lower injection frequency. The improved accuracy of position estimation also aggravates power losses and torque ripples.

To reduce the negative impact of pulse injection and keep the same position estimation accuracy, the induced current around the unaligned position needs to be reduced.

4.3 Proposed Pulse Injection Scheme

4.3.1 Design of the Terminal Sliding-Mode Voltage Controller

The proposed pulse injection approach adopts a TSMC to reduce the idle-phase induced current by adaptively adjusting the injection amplitude. The terminal sliding-mode control is chattering-free and superior in global convergence rate and parameter insensitivity [107]. It is feasible for handling a nonlinear control problem, such as the above issue of large induced current caused by the nonlinear inductance.

To avoid time-consuming offline measurement of the phase inductance, the proposed scheme does not use the SRM inductance characteristics for induced current regulation. Regarding all parameter uncertainties as a voltage disturbance Δu, the voltage equation in the idle phase can be expressed as

$$u = L_{\mathrm{c}} \dot{i}_{\mathrm{h}} + \Delta u \tag{4.1}$$

where L_c is a constant inductance value, which is an approximation of the phase inductance. i_h represents the high-frequency induced current in the idle phase.

The voltage disturbance Δu consists of the ohmic voltage drop Ri_h, the back-EMF $i_h\omega\cdot(\partial L/\partial\theta)$, and the dominant disturbance caused by the inductance parameter mismatch $\tilde{L} = L - L_{\mathrm{c}}$:

$$\Delta u = \tilde{L}\dot{i}_{\mathrm{h}} + Ri_{\mathrm{h}} + i_{\mathrm{h}}\omega\cdot\left(\partial L/\partial\theta\right). \tag{4.2}$$

The proposed TSMC aims to regulate the induced current to a minimal level. The high-frequency current peak can be detected at the Point B or Point E in each injection period, as illustrated in Figure 4.2. In this chapter, the double-period pulse injection is used as an example to analyze the proposed method. Other injection frequency is also available.

The current peak is related to the injection voltage u_{inj}, so the high-frequency current can be minimized by adjusting the injection voltage in the idle-phase period. Define the high-frequency current at the Point B as the high-frequency current peak i_{peak}, the voltage equation at this instant can be expressed as

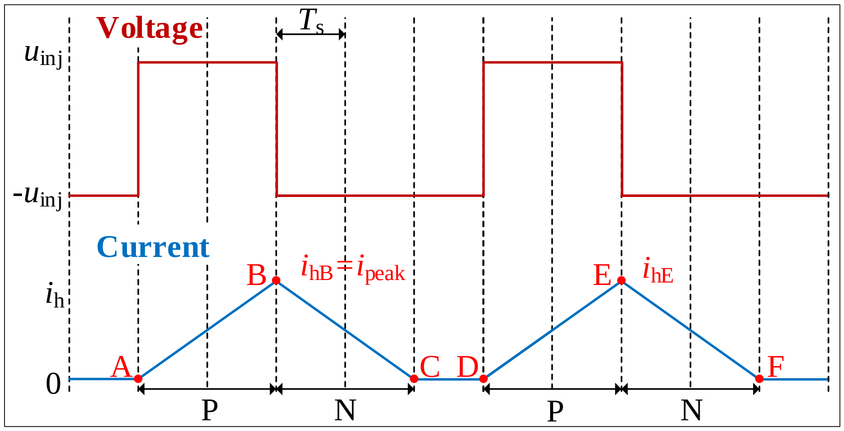

Figure 4.2 Injected voltage and induced current of the pulse-injection-based position estimation method.

$$u_{inj} = L_c \dot{i}_{peak} + \Delta u \,. \tag{4.3}$$

A reference current magnitude of the high-frequency induced current is given as a constant value i_{HFref}. The voltage equation can be rewritten as:

$$u_{inj} = L_c \left(\dot{i}_{peak} - \dot{i}_{HFref} \right) + \Delta u \,. \tag{4.4}$$

Define the current tracking error as $e=i_{peak}-i_{HFref}$, which gives

$$u_{inj} = L_c \dot{e} + \Delta u \,. \tag{4.5}$$

Then, we can obtain the dynamic model of the induced current tracking error, as follows:

$$\dot{e} = u_{inj}/L_c - \Delta u/L_c \,. \tag{4.6}$$

According to the terminal sliding-mode theory [107], a terminal sliding-mode surface can be selected as

$$s = \dot{e} + \alpha \mathrm{sgn}(e)|e|^{0.5} \tag{4.7}$$

where α>0 is a constant.

Theorem: For the system error dynamics (4.6), it will reach and converge along with the terminal sliding-mode surface s=0 in a finite time, if the control low (i.e., injection amplitude) u_{inj} is designed as

$$\begin{cases} u_{\mathrm{inj}} = L_{\mathrm{c}}\left(u_{\mathrm{a}} + u_{\mathrm{b}}\right) \\ u_{\mathrm{a}} = -\alpha \operatorname{sgn}(e)\left|e\right|^{0.5} \\ \dot{u}_{\mathrm{b}} + \beta u_{\mathrm{b}} = -m \cdot \operatorname{sgn}(s) \end{cases} \tag{4.8}$$

with a parameter design scheme:

$$m = \beta u_{\mathrm{b}} + \zeta / L_{\mathrm{c}} \tag{4.9}$$

where β>0 and ζ>0 are constants.

As s=0 reaches, e=0 will be satisfied, and the peak of the induced current can be maintained and minimized as the reference value $i_{\mathrm{peak}}=i_{\mathrm{HFref}}$ in the idle phase.

4.3.2 Stability Analysis of the Proposed TSMC

4.3.2.1 Neglecting Modeling Errors

The stability of the proposed voltage control low expressed in (4.8) is first proved in this section by neglecting modeling errors in (4.1). In this case, the stator inductance used in the voltage control is assumed to be accurate $L_{\mathrm{c}}=L$, and the ohmic voltage drop and back-EMF are ignored. The voltage equation is therefore simplified to an ideal model as

$$u = L\dot{i}\,. \tag{4.10}$$

Considering a Lyapunov function candidate $V=s^2/2$, its time-derivative can be expressed as

$$\dot{V} = s\dot{s} \tag{4.11}$$

The terminal sliding-mode surface can be rewritten by substituting (4.6) into (4.7) with L_c=L and Δu=0:

$$s = u_{\text{inj}} / L + \alpha \text{sgn}(e)|e|^{0.5}. \tag{4.12}$$

Further substituting u_{inj} of (4.8) into (4.12) gives

$$s = u_{\text{b}}. \tag{4.13}$$

Then, the time-derivative of s can be obtained by using $\dot{u}_{\text{b}}$ expressed in (4.8), as follows:

$$\dot{s} = \dot{u}_{\text{b}} = -\beta u_{\text{b}} - m \cdot \text{sgn}(s). \tag{4.14}$$

Hence, we can obtain $\dot{V}$ via substituting (4.14) into (4.11):

$$\begin{aligned} \dot{V} &= s\dot{s} = -s\beta u_{\text{b}} - sm \cdot \text{sgn}(s) \\ &= -s\beta u_{\text{b}} - m \cdot |s|. \end{aligned} \tag{4.15}$$

Given the parameter design scheme in (4.9), $\dot{V}$ can be rewritten as

$$\begin{aligned} \dot{V} &= -\zeta |s| / L + (-\beta u_{\text{b}} \cdot s - \beta u_{\text{b}} \cdot |s|) \\ &\le -\zeta |s| / L < 0 \end{aligned} \tag{4.16}$$

According to the Lyapunov stability criterion, the system can reach the terminal sliding-mode surface in a finite time.

4.3.2.2 Considering the Modeling Errors

The TSMC-based injection voltage control is asymptotically stable when neglecting the modeling errors, as proved before. However, the exact stator inductance needs to be measured offline, and in the disturbance Δu, the back-EMF term often causes additional modeling errors when the rotor speed increases. To avoid time-consuming offline measurement and improve the robustness at varies operating conditions, the stability conditions of the proposed scheme need to be reconsidered when the modeling errors are neglected.

Using the same Lyapunov function candidate as defined above, the terminal sliding-mode surface can be expressed by substituting (4.6) into (4.7), in which the stator inductance is a constant and the disturbance is unknown but considered:

$$s = u_{\text{inj}}/L_{\text{c}} - \Delta u/L_{\text{c}} + \alpha \operatorname{sgn}(e)|e|^{0.5}. \tag{4.17}$$

Substituting u_{inj} of (4.8) into (4.17) results in

$$s = -\Delta u/L_{\text{c}} + u_{\text{b}}. \tag{4.18}$$

Then, the time-derivative of s can be obtained as:

$$\dot{s} = -\Delta\dot{u}/L_{\text{c}} + \dot{u}_{\text{b}} = -\Delta\dot{u}/L_{\text{c}} - \beta u_{\text{b}} - m \cdot \operatorname{sgn}(s). \tag{4.19}$$

The derivative of the Lyapunov function candidate $\dot{V}$ can be expressed via substituting (4.19) into (4.11):

$$\begin{aligned} \dot{V} &= s\dot{s} = -s\,\Delta\dot{u}/L_{\text{c}} - s\beta u_{\text{b}} - sm \cdot \operatorname{sgn}(s) \\ &= -s\,\Delta\dot{u}/L_{\text{c}} - s\beta u_{\text{b}} - m \cdot |s|. \end{aligned} \tag{4.20}$$

Using the parameter design scheme given in (4.9), $\dot{V}$ can be expressed by

$$\begin{aligned} \dot{V} &= \left(-s\Delta\dot{u} - \zeta|s|\right)/L_{\text{c}} + (-\beta u_{\text{b}} \cdot s - \beta u_{\text{b}} \cdot |s|) \\ &\le \left(-s\Delta\dot{u} - \zeta|s|\right)/L_{\text{c}}. \end{aligned} \tag{4.21}$$

Compared to the previous result neglecting the modeling errors in (4.16), the dynamics of the disturbance Δu has influence on the stability of the proposed TSMC. To ensure the condition $\dot{V} < 0$ being always held, the tunable parameter should satisfy

$$\zeta > \left|\Delta\dot{u}\right|, \tag{4.22}$$

namely ζ being larger than the bounded value of the parameter uncertainty variation.

The proof is completed.

Remark: According to (4.21), the proposed scheme is insensitive to the parameter uncertainty since the resultant disturbance Δu, which are caused by the inductance uncertainty, ohmic voltage drop, and the back-EMF, has no effects on convergence to the surface s=0, if the tunable parameter ζ is selected to be a large value as (4.22).

This benefits that although a constant inductance value L_c is preset in the controller, its exact value does not need to be known. For example, suppose the induced current is not well regulated to the reference due to the parameter mismatch between the preset value L_c and the actual inductance. In that case, the desired control performance can be achieved by increasing ζ. Moreover, the robustness against the resistance changes and speed variation can also be enhanced by mitigating the effects of the overall disturbance Δu. Consequently, the proposed method does not require exact magnetic characteristics and parameters of the SRM, which simplifies the practical implementation since no extra offline measurement effort is needed, thereby improving the algorithm's generality.

4.3.3 Performance Analysis

4.3.3.1 Convergence Analysis

The Lyapunov stability theorem is satisfied by proper parameter design in (4.22), and therefore the system dynamics can converge to the terminal sliding-mode surface s=0. According to the system dynamic designed in (4.7), the time-domain dynamic function of the proposed controller can be expressed by

$$s = \dot{e} + \alpha \operatorname{sgn}(e)\left|e\right|^{0.5} = 0\,. \tag{4.23}$$

The convergence rate can be solved from the dynamic equation. When the initial error condition is positive $e(0)>0$, the dynamic error e keeps positive before reaching the terminal sliding-mode surface. Therefore, the dynamic function can be expressed as

$$\dot{e} + \alpha e^{0.5} = 0\,. \tag{4.24}$$

Rewriting it in time-derivative form gives

$$\frac{de}{dt} = -\alpha e^{0.5}\,. \tag{4.25}$$

Separating the variables and integrating both sides gives

$$\int \frac{de}{e^{0.5}} = \int \left(-\alpha\right) dt\,. \tag{4.26}$$

Then the solve of the error dynamic function can be deduced as

$$e = \frac{1}{4}\left[-\alpha t^2 + 2\sqrt{e(0)}\right]. \tag{4.27}$$

Therefore, the convergence time of the system error can be solved as

$$t_{s=0} = \frac{2\sqrt{e(0)}}{\alpha}\,. \tag{4.28}$$

Similarly, the convergence time when the initial error condition is negative $e(0)<0$ can be obtained as

$$t_{s=0} = \frac{2\sqrt{-e(0)}}{\alpha}\,. \tag{4.29}$$

Thus, the convergence time of the proposed method is summarized as follows:

$$t_{s=0} = \frac{2\sqrt{|e(0)|}}{\alpha}. \tag{4.30}$$

As can be observed, the proposed controller can converge the system error, namely the error between the reference current peak i_{HFref} and the actual high-frequency current peak i_{peak} within a finite time. The convergence rate can be accelerated when selecting a large tunable parameter α or reducing the initial current magnitude error.

4.3.3.2 Chattering Analysis

The common drawback of sliding-mode control is the chattering problem. This issue can be suppressed by the proposed TSMC.

To analyze the chattering phenomenon, the designed voltage control law in (4.8) is repeated here and submitting the s derived from (4.7):

$$\begin{cases} u_{inj} = L_c\left(u_a + u_b\right) \\ u_a = -\alpha \mathrm{sgn}(e)|e|^{0.5} \\ \dot{u}_b + \beta u_b = -m \cdot \mathrm{sgn}(s) = -m \cdot \mathrm{sgn}\left[\dot{e} + \alpha \mathrm{sgn}(e)|e|^{0.5}\right] \end{cases}. \tag{4.31}$$

Two chattering sources exist in the proposed control law, which are u_a and u_b that contain the switching functions. Comparing the two chattering sources, the switching function in u_b has dominant chattering around the sliding-mode surface due to the derivative of the system error $\dot{e}$. For the u_a, the $|e|^{0.5}$ in u_a can suppress the chattering problem when the sliding-mode surface is approaching. Thus, if the tunable parameter α is not sufficient large, the chattering in u_a could be neglected.

For the sub-control law u_b, although the switching function $-m \cdot \mathrm{sgn}(s)$ contains large chattering, the transfer function between the sub-control law u_b and $-m \cdot \mathrm{sgn}(s)$ presents a lowpass frequency characteristic:

$$u_{\mathrm{b}} = \frac{1}{s_{\mathrm{L}} + \beta} \cdot \left[-m \cdot \mathrm{sgn}(s) \right] \tag{4.32}$$

where s_L represents the Laplace operator in this transfer function, and β is the cutoff frequency. As observed, the chattering problem from the switching function can be filtered out by the LPF, and a smooth control law u_b can be derived.

In consequence, the proposed TSMC does not suffer from the conventional sliding chattering problem.

4.3.4 Parameter Design

In the proposed TSMC-based controller, the reference current i_{HFref} needs to be first determined for copper loss and torque ripple reduction. The constant inductance approximation L_c used in the control law can also be set together with i_{HFref}. Three control parameters α, β, and ζ will be designed to achieve satisfactory control performance.

4.3.4.1 Selection of the Reference Current Magnitude and L_c

The reference magnitude i_{HFref} of the induced current determines the torque ripple and the copper loss of the pulse injection method. For accurate position sensing, the selection of the reference magnitude should ensure sufficient SNR for inductance calculation. In SRM drives, various nonideal factors would distort the inductance calculation from the induced current. First, the mutual inductance would cause self-inductance calculation errors when two phases overlap. Second, the DC-link voltage ripples lead to additional inductance calculation error when the phase commutates since the DC-link voltage u_{dc} is often assumed to be constant in estimation (3.3). These errors often occur around the aligned position at which the induced current is the lowest, thereby resulting large estimation errors. To mitigate the problem, the magnitude of the induced current needs to be set as larger as possible.

Since the stator inductance reaches the maximum at the aligned position, as shown in Figure 4.1, the maximum appliable value of a constant current magnitude i_{HFref} is

$$i_{\text{HFref (max)}} = \frac{\Delta T \cdot U_{\text{dc}}}{L_{\text{aligned}}} = \frac{2T_{\text{s}} \cdot U_{\text{dc}}}{L_{\text{aligned}}} \tag{4.33}$$

where $L_{aligned}$ is the aligned inductance of the SRM.

Then, through the proposed TSMC, the magnitude induced current can be controlled as the reference value given in (4.33) in the whole idle phase.

It is notable that the calculation of the reference current does not require the prestored magnetic characteristic. According to the minimum reluctance principle of the SRM, when only one phase is excited and other phases are turned off, the rotor will move to the aligned position where the reluctance is minimum. After that, by injecting the pulse voltage, the magnitude of the induced current at the aligned position is the selected reference magnitude given in (4.33).

The constant inductance approximation value L_c used in the control law can also be set as the aligned inductance obtained by the above self-testing, namely L_c=$L_{aligned}$ for simplicity. This approximation does not affect the estimation accuracy according to the Lyapunov-based proof given in (4.22).

4.3.4.2 Design of α

The parameter design of α relates to the convergence rate of the proposed method. From (4.30), the convergence time is inverse to α for a certain initial error $e(0)$. For faster convergence performance, a large α is suggested. However, the parameter has some influence on chattering of the sub-control law u_a as expressed in (4.31). Although the adverse impact is suppressed by the error term $|e|^{0.5}$, the selection of α is still considerable.

To simplify the parameter design of α, the convergence performance can be first improved by reducing the initial tracking error $e=i_{peak}-i_{HFref}$, according to (4.30). For normal SRM control, the idle phase starts around the aligned position, at which the stator inductance approaches the maximum, and then ends around the unaligned position, at which the stator inductance reaches the minimum. Hence, to keep a minimal induced current in the whole idle-phase period, the injection amplitude u_{inj} needs to be higher around the aligned position and then gradually decrease when approaching the unaligned position. Therefore, the initial values of the control law in each injection cycle could be preset to the largest values, such as U_{dc}, to accelerate the convergence process:

$$\begin{cases} u_a = 0 \\ u_b = U_{dc}/L_c \end{cases} \tag{4.34}$$

which gives

$$u_{inj} = L_c\left(u_a + u_b\right) = U_{dc}\,. \tag{4.35}$$

With the initial voltage value given to the TSMC, the initial tracking error e can be minimized, and the convergence time can be reduced. The parameter α can be therefore selected more flexibly in a wide range due to the simpler trade-off between the convergence rate and the chattering level. In this chapter, α is selected to be 2000, which gives the convergence time of 1 ms when the initial error $e(0)$ is equal to 1. When the reference magnitude is selected as (4.33), the initial error is almost zero, and thus the convergence time could reduce to microsecond, which is fast enough for the proposed control.

4.3.4.3 Design of β

As analyzed in (4.32), the parameter β determines the cutoff frequency of the LPF in the control law for chattering reduction. Since the convergence rate is enhanced by presetting the initial values to be U_{dc}, as expressed in (4.35), the cutoff frequency can be given to a lower value to suppress the chattering phenomenon. In this method, the cutoff frequency is chosen as the maximum rotor frequency at which the pulse injection method is enabled for low-speed sensorless control. Here β=251.2 rad/s (40 Hz, 300 r/min).

4.3.4.4 Design of ζ

The tunable parameter ζ is crucial for the proposed scheme to guarantee the asymptotic stability and robustness to parameter mismatch. According to the stability condition derived in (4.22), the parameter needs to larger than the bounded value of the disturbance variation during SRM operation. As expressed in (4.2), the disturbance variation is fast due to the high-frequency induced current. Therefore, a larger ζ =12000 is selected in the chapter to ensure the stability of the proposed method.

4.3.5 Overall Structure of the Proposed Scheme

According to the design, the control diagram of the TSMC to adjust the injection voltage for current reduction is summarized in Figure 4.3.

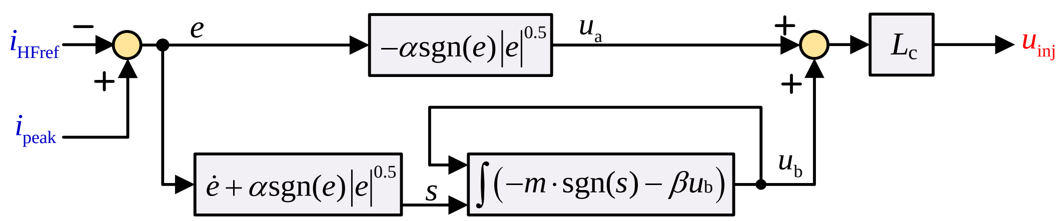

Figure 4.3 The control diagram of the proposed TSMC-based pulse injection.

The proposed sensorless control scheme with reduced induced current is illustrated in Figure 4.4. The sensorless SRM drive is controlled in speed-current dual loops. The low-speed position estimation scheme is the same as the previous RPLL-based estimator, which can estimate the rotor position and speed from the calculated inductance without using offline measured magnetic characteristics. As an improvement, the proposed TSMC can control the induced current to be a minimal level for copper loss and torque ripple reduction by adjusting the injection voltage u_{inj}. The injection voltage is regulated according to the reference high-frequency current i_{HFref}.

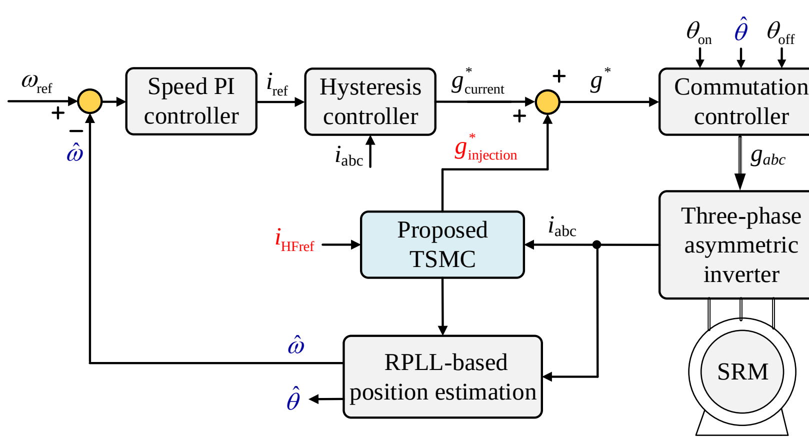

Figure 4.4 Schematic diagram of the proposed position-sensorless control scheme.

4.4 Experimental Results

The proposed pulse injection approach based on the TSMC for induced current reduction is verified on the 5.5 kW SRM test bench. The control parameters of the position estimator RPLL, speed and current controllers, and sampling frequencies are the same as the ones mentioned in Chapter 3. All experimental results are measured in the position-sensorless control mode.

Figure 4.5 shows the injection amplitude, phase-A current, and position estimation results of the pulse injection method proposed in Chapter 3 with the fixed injection amplitude at 200 r/min at 10 N·m. In this method, the injection voltage is set as a constant value of the DC-link voltage, and the induced current in the idle phase is nonlinearly distributed due to the stator inductance variation. The current is much lower when the injection starts (around the aligned position 22.5°) and then becomes significant at the end of injection (unaligned position 0°). Although the rotor position can be accurately estimated, the large induced current around the unaligned position would cause additional copper losses and torque ripples.

In comparison, the proposed scheme in this chapter can reduce the idle-phase induced current, as presented in Figure 4.6. The injection amplitude u_{inj} is adjusted online by the proposed TSMC to keep the current's magnitude constant and track the reference value i_{HFref}=2 A. The injection amplitude of the proposed scheme is gradually decreased when the rotor position approaches the unaligned position 0° to reduce the induced current. In addition, the proposed scheme can achieve a similar position estimation accuracy to the fixed-injection-amplitude method, while generating much less current in the idle phase.

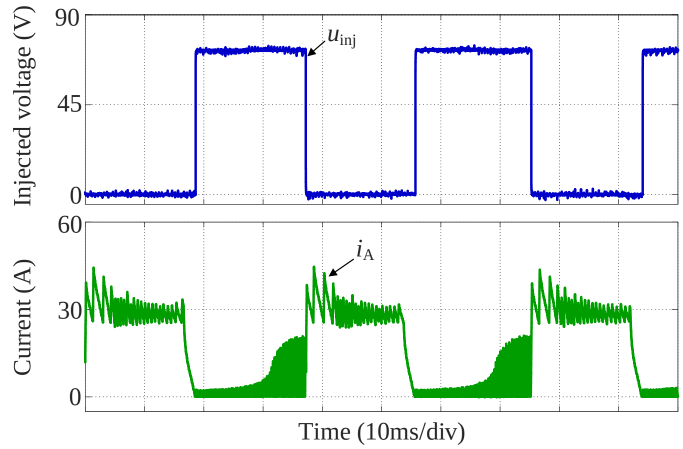

(a)

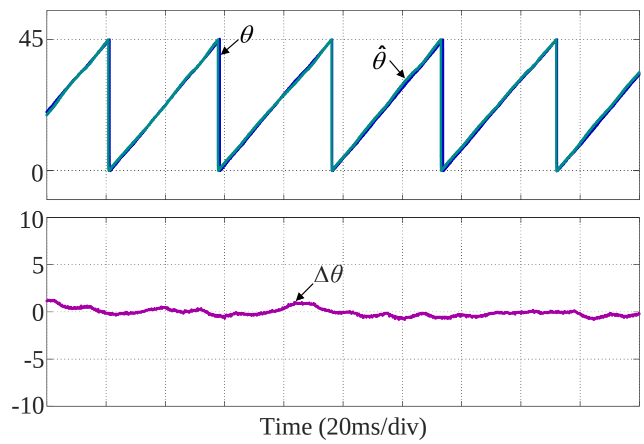

(b)

Figure 4.5 Experimental results of the fixed-amplitude pulse injection method at 200 r/min with 10 N·m load. (a) Injection voltage and phase current. (b) Position estimation.

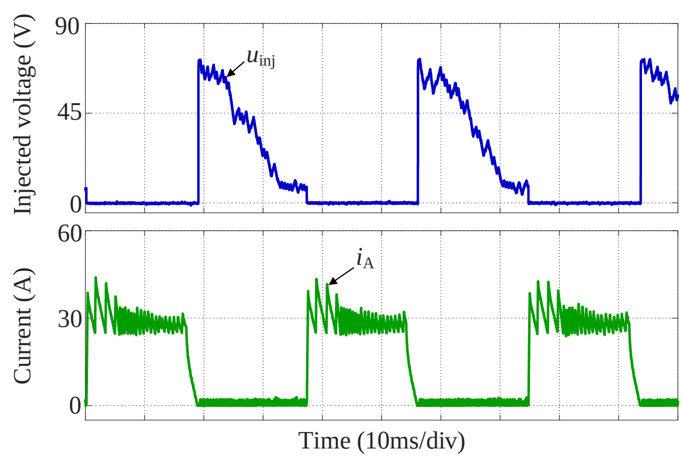

(a)

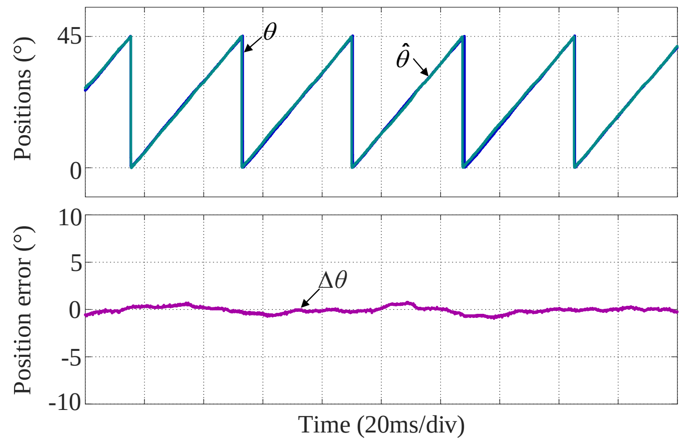

(b)

Figure 4.6 Experimental results of the proposed pulse injection method at 200 r/min with 10 N·m load. (a) Injection voltage and phase current. (b) Position estimation.

The position estimation accuracy of the proposed method is also validated at other rotor speeds of 100 r/min and 300 r/min with a 10 N·m load, as shown in Figure 4.7. Due to the robustness to the disturbance including the back-EMF, the position estimation accuracy and current control performance can be maintained at different speeds. As observed from the results, both the rotor position at 100 r/min and 300 r/min can be estimated well.

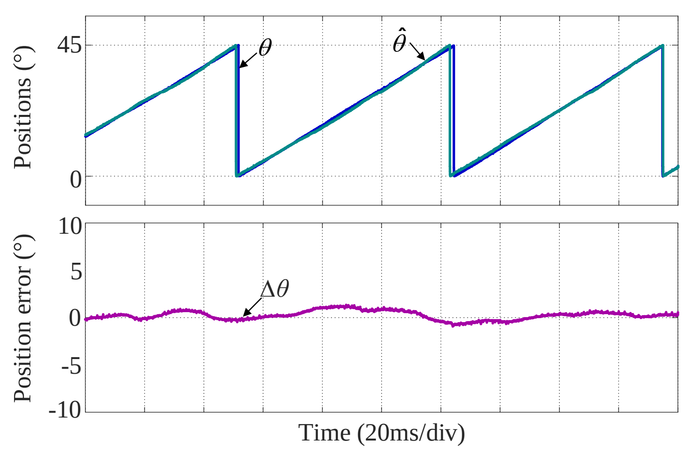

(a)

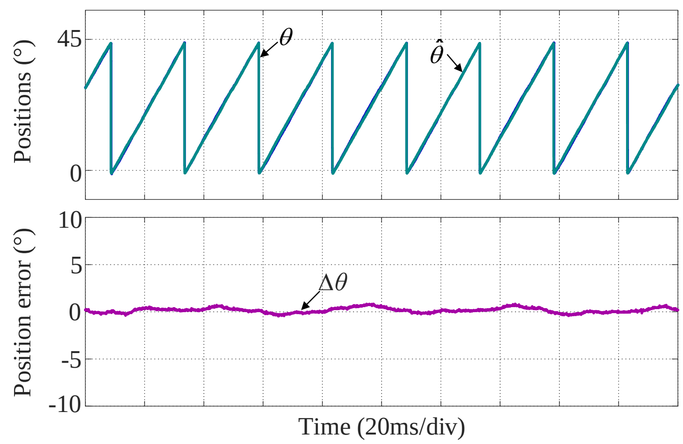

(b)

Figure 4.7 Position estimation results of the proposed pulse injection method at other low speeds with 10 N·m load. (a) 100 r/min. (b) 300 r/min.

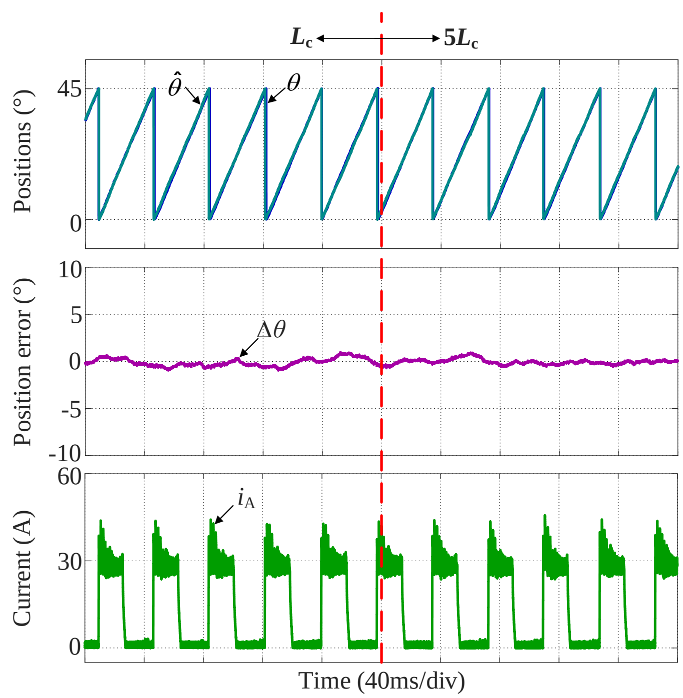

Figure 4.8 The parameter sensitivity test of the proposed scheme at 200 r/min and 10 N·m load.

As analyzed before, the proposed TSMC-based pulse injection method is insensitive to the parameter mismatch. This feature is validated experimentally at 200 r/min and 10 N·m load, as demonstrated in Figure 4.8. The preset inductance value used in the TSMC is L_c=3 mH, which is obtained by injecting a pair of pulse voltages at the standstill and at the aligned position. The preset constant inductance is apparently inaccurate since the actual inductance varies with the rotor position nonlinearly. Still, the proposed method can achieve desirable control performance with the inductance mismatch. Furthermore, by dramatically increasing the inductance to $5L_c$, the induced current can also be regulated as a constant well, and there is almost no difference in position estimation accuracy. It verifies the good robustness to parameter uncertainties of the proposed scheme. Therefore, no inductance characteristic measured offline is needed for induced current reduction.

Due to the reduced idle-phase current, torque ripples and copper losses caused by pulse voltages in the whole idle phase can be reduced, as indicated in Figure 4.9. The torque is calculated using the torque characteristic for better accuracy, instead of torque transducer measurement. The peak negative torque ripple is reduced from -1.3 N·m to -0.1 N·m (92.3% reduction), which could be neglected for the SRM torque control. For the copper loss reduction, it is related to the resistance value of the SRM, so this experimental test shows the percentage copper loss reduction for a general illustration. The RMS current in the idle phase is reduced from 5.47 A to 1.11 A by the proposed scheme. Since the copper loss is proportional to the square of the RMS current, the percentage of the copper loss reduction is 95.9% in the idle phase. As a consequence, the adverse impact of the conventional pulse injection method on the SRM drive can be mitigated by the proposed approach.

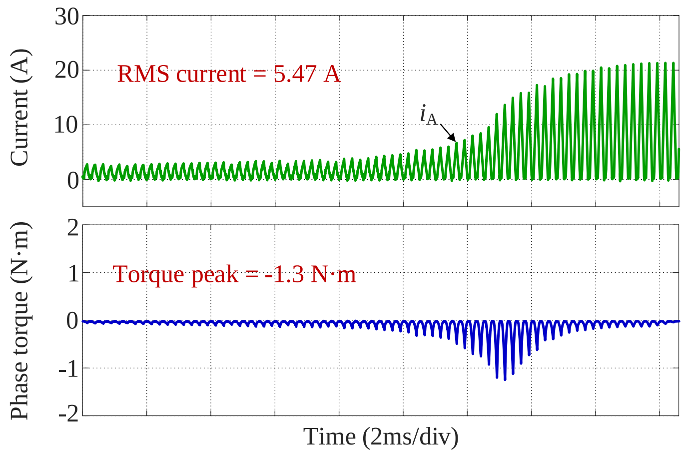

(a)

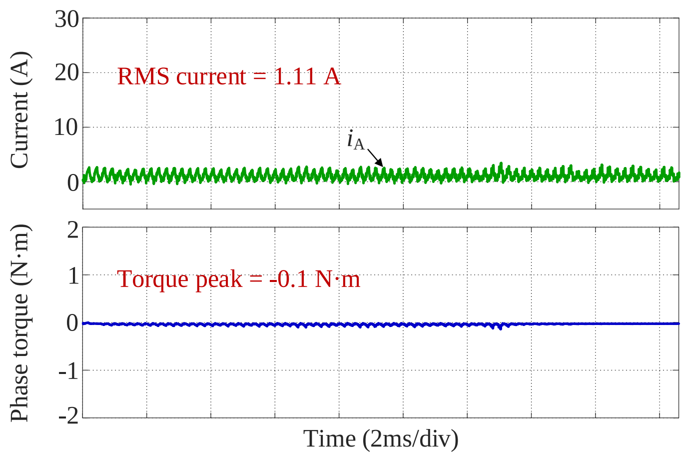

(b)

Figure 4.9 Comparison of negative torque ripples and copper losses in the idle phase. (a) Fixed-injection-amplitude method. (b) Proposed method.

After that, the dynamic performance of the proposed pulse injection scheme is also validated. Figure 4.10 shows the speed transient performance of the proposed scheme from 150 r/min to 250 r/min at no load conditions. The actual speed, estimated speed, and the position estimation error are presented. In Figure 4.10(a), the rotor speed command is a ramp signal, and the SRM can operate well in sensorless control, and the estimated speed can track the actual one in the transient state. Figure 4.10(b) presents the estimation results when a step speed command is given. As observed, accurate position estimation can also be achieved by the proposed scheme, in which the maximum transient position error is 2.6°.

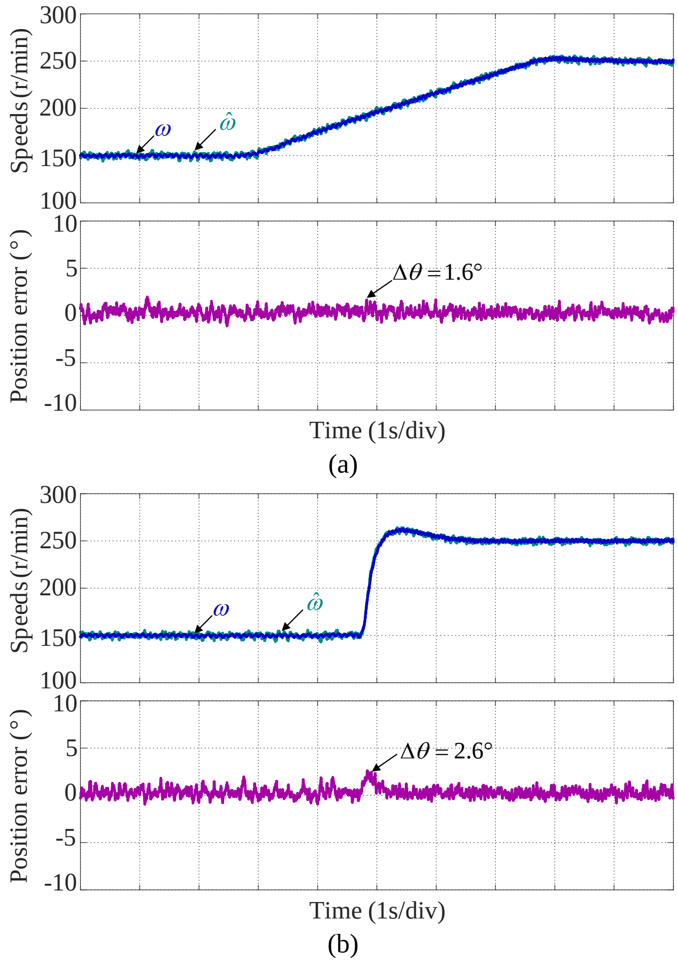

Figure 4.10 Position-sensorless control under speed variation from 150 r/min to 250 r/min. (a) Ramp speed response. (b) Step speed response.

4.5 Conclusions

This chapter presents a new pulse injection method for SRM position-sensorless control with the reduced induced current. The induced current's magnitude is regulated to a selected minimal level by adjusting the injection amplitude online. A TSMC with a nonlinear control law is designed to achieve the desired current regulation performance. Convergence and robustness to parameter uncertainties are theoretically proved. Experimental results of a three-phase 12/8 SRM validate that the induced current can be significantly reduced. 92.3% torque ripple reduction and 95.9% copper loss reduction in the idle phase are achieved by the proposed approach compared to the constant-amplitude pulse injection method, while keeping the similar position estimation accuracy.

Chapter 5

Nonlinear State Position Observer for Position-Sensorless Control at Medium and High Speed

5.1 Introduction

Pulse injection for low-speed position estimation is infeasible for high-speed operation since the idle-phase duration becomes narrow and cannot support full-cycle position estimation by the RPLL. Due to the large back-EMF, flux linkage calculation in conduction phases possesses good accuracy and can be used for high-speed position estimation. Therefore, pulse injection is not necessary and can be removed when the speed raises. A typical approach for position estimation is to search a prestored flux linkage lookup table. However, the measurement process is time-consuming and not available for a general-purpose SRM inverter.

In this chapter, a feature-position-based position estimation strategy with an NSO (nonlinear state observer) is proposed for SRM medium- and high-speed sensorless operation. A feature position at 15 degree is captured by a reference flux linkage curve. The feature flux linkage can be obtained online through a self-commissioning process, avoiding offline measurement. Since the derived feature position is discontinuous, the NSO is designed to estimate the full-cycle position. In detail, the proposed observer adopts an effective Fourier series method [108], which is used for Hall signals, to acquire the inherent frequency characteristic of the discrete feature position. Then, two online Fourier estimators are proposed to eliminate primary position harmonics and derive a continuous rotor position. Besides, this chapter further develops the conventional Fourier series method by revealing the adverse effect of flux linkage errors on position estimation through a novel small-signal linearization approach. The derived small-signal model indicates that the flux linkage error can result in high-order position harmonics in the feedforward path of the position observer. On this basis, an augmented state estimator considering the nonideal flux distortion is discussed. A parameter design scheme based on the small-signal analysis is also given to achieve better distortion rejection capability and guarantee the observer's stability. To baseline the advantage of the proposed method over conventional SRM position estimation methods, the contributions of the proposed observer over existing schemes are summarized as follows:

1) Compared to existing feature-position-based methods [98]–[104], the proposed observer abandons the conventional linear prediction method. Higher estimation accuracy can be achieved by enhancing the robustness against flux linkage errors.

2) Compared to conventional state observers [71]-[87], the proposed observer does not require three-dimensional magnetic characteristics. Thus, the technique has simpler implementation and is potential for broader applications.

Finally, the effectiveness of the proposed control strategy is validated on a 12/8 SRM setup with comparative experimental tests with existing methods.

5.2 Conventional Feature-Flux-Linkage-Based Position Estimation Method

5.2.1 Feature Flux Linkage of the SRM

Instead of using the full flux linkage characteristic, the feature flux linkage at a specific position, for example 15°, can be easily measured in the self-commissioning process by a phase torque balancing method proposed in [102]. Figure 5.1 shows the three-phase torque of the SRM.

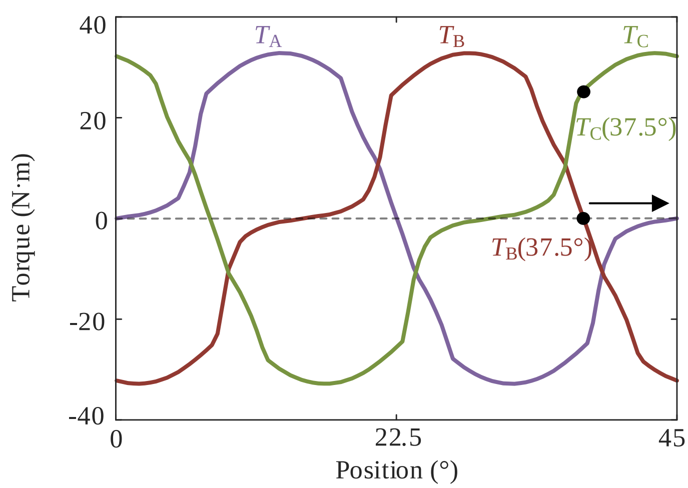

Figure 5.1 Three-phase torque of the SRM.

The torque relationship among the three phases can be expressed by (5.1):

$$\begin{cases} T_{\mathrm{A}}(\theta) = T_{\mathrm{A}}(\theta+15°)=T_{\mathrm{B}}(\theta-30°) \\ T_{\mathrm{A}}(\theta) = T_{\mathrm{C}}(\theta+30°)=T_{\mathrm{C}}(\theta-15°) \\ T_{\mathrm{A}}(\theta) = -T_{\mathrm{A}}(45°-\theta) \end{cases} \tag{5.1}$$

Similarly, the flux linkage relationship among the three phases can be expressed as:

$$\begin{cases} \lambda_{\mathrm{A}}(\theta) = \lambda_{\mathrm{A}}(\theta+15°)=\lambda_{\mathrm{B}}(\theta-30°) \\ \lambda_{\mathrm{A}}(\theta) = \lambda_{\mathrm{C}}(\theta+30°)=\lambda_{\mathrm{C}}(\theta-15°) \\ \lambda_{\mathrm{A}}(\theta) = \lambda_{\mathrm{A}}(45°-\theta) \end{cases} \tag{5.2}$$

To measure the flux linkage at 15°, phase B should be excited first. When only phase B is turned on, the rotor will rotate at the aligned position of phase B, namely 37.5°. As shown in Figure 5.1, the electromagnetic torques of phase B and phase C are illustrated. Since the phase B is at the aligned position, the torque $T_{\mathrm{B}}(37.5°)$ is zero, and the $T_{\mathrm{C}}(37.5°)$ is positive. Then, if phase B and phase C are simultaneously excited by the same voltage, due to the $T_{\mathrm{C}}(37.5°) > T_{\mathrm{B}}(37.5°)$, the overall torque is positive, and the rotor will continue rotating until reach the position at 0°. At 0°, the total torque can be calculated based on (5.1) as:

$$\begin{cases} T_{\mathrm{B}}(0°) = T_{\mathrm{A}}(30°) \\ T_{\mathrm{C}}(0°) = T_{\mathrm{A}}(15°) \\ T_{\mathrm{A}}(30°) = -T_{\mathrm{A}}(15°) \end{cases} . \tag{5.3}$$

As can be seen, the $T_{\mathrm{B}}(0°) = -T_{\mathrm{C}}(0°)$, and hence the rotor will keep at 0°.

Afterward, according to (5.2), the three-phase flux linkage can be obtained as

$$\begin{cases} \lambda_{\mathrm{B}}(0°) = \lambda_{\mathrm{A}}(30°) \\ \lambda_{\mathrm{C}}(0°) = \lambda_{\mathrm{A}}(15°) \\ \lambda_{\mathrm{A}}(15°) = \lambda_{\mathrm{A}}(30°) \end{cases} . \tag{5.4}$$

From (5.4), the flux linkage at 15° is the same as the phase-B and phase-C flux linkage at 0°. By injecting a low-frequency and low-amplitude pulse into phase B and phase C together, the total torque still remains at zero, and the flux linkage at 15° $\lambda_A(15°) = \lambda_B(0°) = \lambda_C(0°)$ can then be calculated based on the voltage equation (2.1).

The derived feature flux linkage at 15° is shown in Figure 5.2. Compared to the offline measurement, the feature flux linkage can be measured online, so that it can be used in the general-purpose SRM inverter.

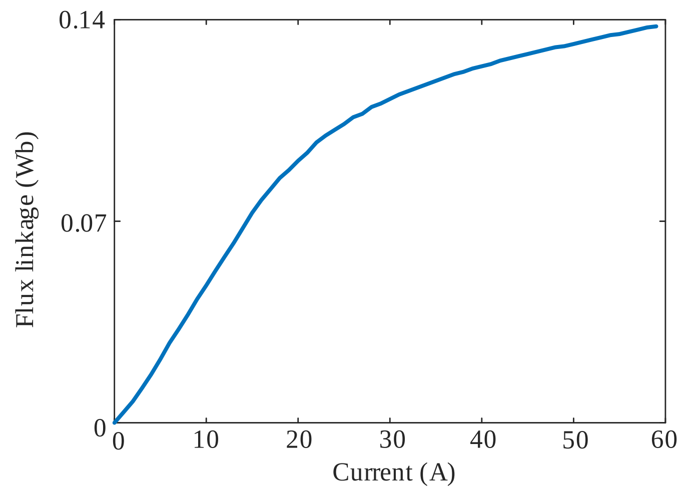

Figure 5.2 Feature flux linkage of the SRM at 15°.

5.2.2 Position Estimation Based on Feature Flux Linkage: Conventional Method

The rotor position can be estimated using one feature flux linkage curve, instead of the complete magnetic characteristic, as shown in Figure 5.3. The real-time flux linkage is calculated by the voltage equation (2.1), and the reference flux linkage is the feature curve measured in the self-commissioning stage. When the intersection between the calculated flux linkage and the reference flux linkage is detected, the rotor position stepping by 15°

can be measured. As can be seen from Figure 5.3, there are only three position points over one electrical cycle; therefore, the position estimation resolution is limited. It is notable that regardless of the current control methods, such as current hysteresis control, PWM control or single pulse control, the intersection point of two flux linkage exists, and the feature position can be estimated.

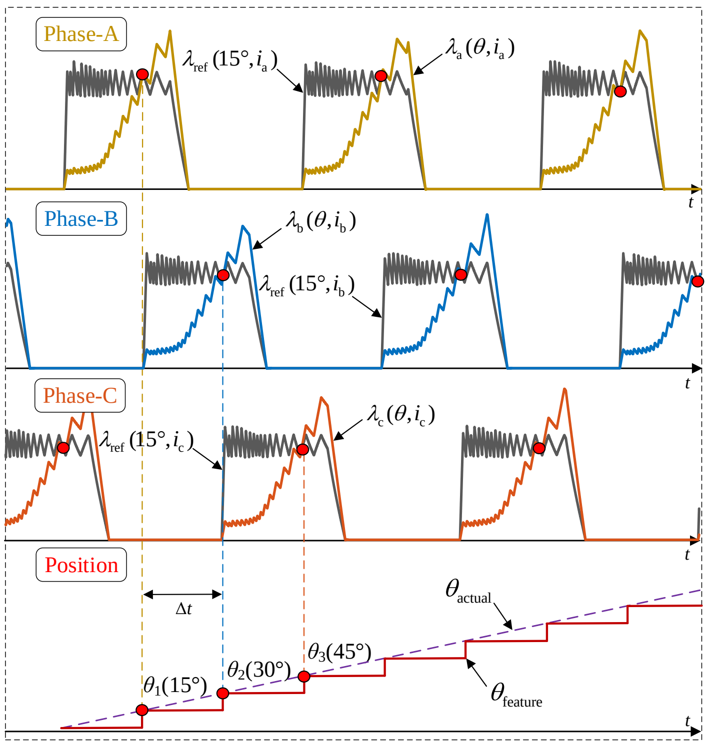

Figure 5.3 Feature position detection: calculated flux linkage, reference flux linkage at 15°, and the estimated feature position.

To estimate the continuous rotor position and speed, the linear prediction method is often applied in the literature [2]-[4], which can be expressed as

$$\begin{cases} \bar{\omega} = \dfrac{\theta_2 - \theta_1}{\Delta t} = \dfrac{15°}{\Delta t} \\ \hat{\theta} = \theta_2 + \bar{\omega} \cdot t \end{cases} \tag{5.5}$$

where θ_1 and θ_2 are two successive feature positions, $\bar{\omega}$ is the average rotor speed between θ_1 and θ_2, and Δt is the time interval between two feature positions. As observed, by assuming the rotor speed keeping constant over 15°, the unknown position between θ_2 and θ_3 can be predicted by the average speed $\bar{\omega}$. When the feature position at θ_3 is detected, the rotor speed will be updated by (5.5) again and then used to predict the unknown position in the next interval.

However, the conventional linear prediction is sensitive to the flux-linkage errors and often has low estimation accuracy. As illustrated in (5.6), voltage and current sampling errors, stator resistance mismatch, and mutual couplings are inevitable in the SRM drive, which can cause the flux-linkage error $\Delta\lambda$:

$$\lambda'(\theta,i)=\underbrace{\int\left(u-Ri\right)dt}_{\lambda(\theta,i)}+\underbrace{\int\left(\Delta u-\Delta R\Delta i\right)dt+\lambda_{\text{mutual}}}_{\Delta\lambda} \tag{5.6}$$

where the superscript $'$ denotes the variables considering the non-ideal errors, the subscript "0" represents the ideal flux linkage without any distortions, and λ_{mutual} is the mutual flux linkage caused by the overlap of two conduction phases. When monitoring the intersection of the reference and calculated flux linkage curves, the $\Delta\lambda$ would lead to a detection error Δf in the feature position and reduce the speed estimation accuracy, expressed as:

$$\begin{cases}\bar{\omega}'=\dfrac{\theta_2-\theta_1+\Delta f}{\Delta t}=\dfrac{15^\circ+\Delta f}{\Delta t}=\bar{\omega}+\Delta\omega \\ \hat{\theta}'=\theta_2+\bar{\omega}'\cdot t=\hat{\theta}+\Delta\omega\cdot t\end{cases}. \tag{5.7}$$

Compared with the ideal case in (5.5), the speed ripple $\Delta\omega$ is introduced, and its adverse effect will be further amplified in the estimated rotor position due to the presence of the integrator $\Delta\omega\cdot t$. To illustrate clearly, Figure 5.4 shows the estimated position from the conventional linear prediction method. As shown, the detected feature position often has deviations compared to the actual position due to the flux-linkage error. However, a more significant position error can be found in the estimated position, which still leads to discontinuous position estimation. As a result, the robustness to flux linkage errors should be enhanced to improve the estimation accuracy.

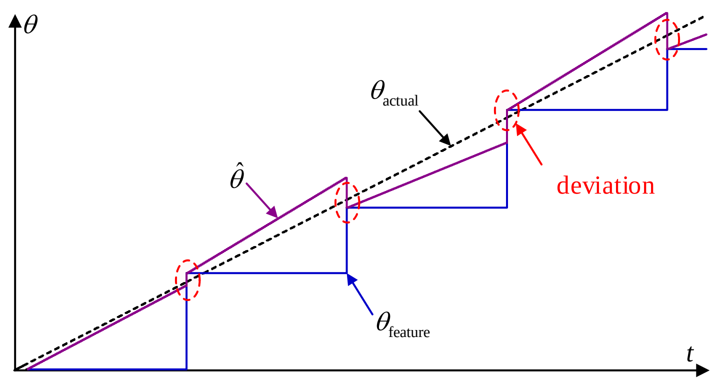

Figure 5.4 Limitation of the conventional linear prediction method.

5.3 Proposed Position-Sensorless Control Algorithm

5.3.1 Fourier Series of the Feature Position

As the detected feature position is discontinuous, it is necessary to investigate its inherent frequency characteristic. The rotor position of the SRM is repeated every 360°, so it can be rewritten into a vector form for Fourier analysis:

$$\boldsymbol{F} = \cos\left(\theta_{\text{feature}}\right) + j\sin\left(\theta_{\text{feature}}\right) \tag{5.8}$$

where $\boldsymbol{F}$ denotes the feature position vector and j is the imaginary index.

To derive complete rotor position information from θ_{feature}, Fourier series is adopted to analyze the frequency characteristic of $\boldsymbol{F}$ [108]. The Fourier series expansion of a function $\boldsymbol{F}(\theta)$ can be expressed by

$$\boldsymbol{F}\left(\theta\right)=\sum_{k=-\infty}^{\infty}a_{\text{k}}e^{jk\theta} \tag{5.9}$$

$$a_{\text{k}}=\frac{1}{2\pi}\int_{-\pi}^{\pi}\boldsymbol{F}\left(\theta\right)e^{-jk\theta}d\theta \tag{5.10}$$

By applying the Fourier series to (5.8), $\boldsymbol{F}$ can be decomposed into a fundamental vector $\boldsymbol{F}_{\text{f}}$ and a set of harmonic vectors $\boldsymbol{F}_{\text{h}}$, as follows:

$$\boldsymbol{F}=\boldsymbol{F}_{\text{f}}+\boldsymbol{F}_{\text{h}} \tag{5.11}$$

where

$$\boldsymbol{F}_{\text{f}}=e^{j(\theta-\varphi)},$$

$$\boldsymbol{F}_{\text{h}}=\sum_{k=1}^{\infty}\left[-\frac{1}{kN-1}e^{-j\left[(kN-1)\theta+\varphi\right]}+\frac{1}{kN+1}e^{j\left[(kN+1)\theta-\varphi\right]}\right].$$

In (5.11), N is the number of “steps” in the step-manner feature position over one mechanical cycle, and $\varphi=\pi/N$ is the phase of the fundamental vector. For a 12/8 SRM, N and φ are equal to 24 and $\pi/24$, respectively.

As shown in (5.11), the fundamental vector $\boldsymbol{F}_{\text{f}}$ contains the rotor position θ with a phase shift φ, while high-order harmonics exist in $\boldsymbol{F}_{\text{h}}$. To illustrate clearly, the diagram of the three vectors $\boldsymbol{F}$, $\boldsymbol{F}_{\text{f}}$, and $\boldsymbol{F}_{\text{h}}$ are drawn in Figure 5.5. Since the feature position is detected by every 15°, the vector graph of $\boldsymbol{F}$ is a polygon with twenty-four sides. The polygon can be decomposed by the Fourier series into a unit circle $\boldsymbol{F}_{\text{f}}$ and harmonic vector $\boldsymbol{F}_{\text{h}}$. If the harmonics in $\boldsymbol{F}_{\text{h}}$ can be eliminated, an accurate rotor position will be obtained from $\boldsymbol{F}_{\text{f}}$.

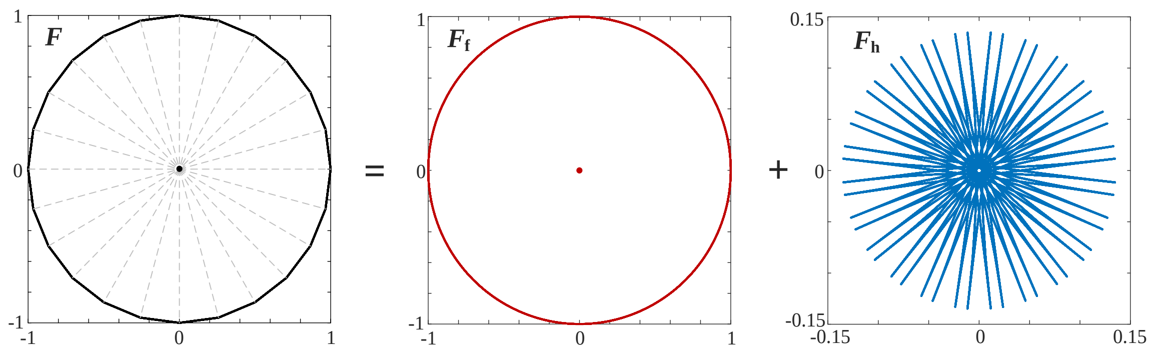

Figure 5.5 Vector graphs of the feature position.

5.3.2 Design of the Proposed NSO

As the harmonic vector $\boldsymbol{F}_{\mathrm{h}}$ in (5.11) is presented as a function of rotor position θ, a position observer has to be designed to eliminate the $\boldsymbol{F}_{\mathrm{h}}$. Figure 5.6 shows the overall block diagram of the proposed NSO.

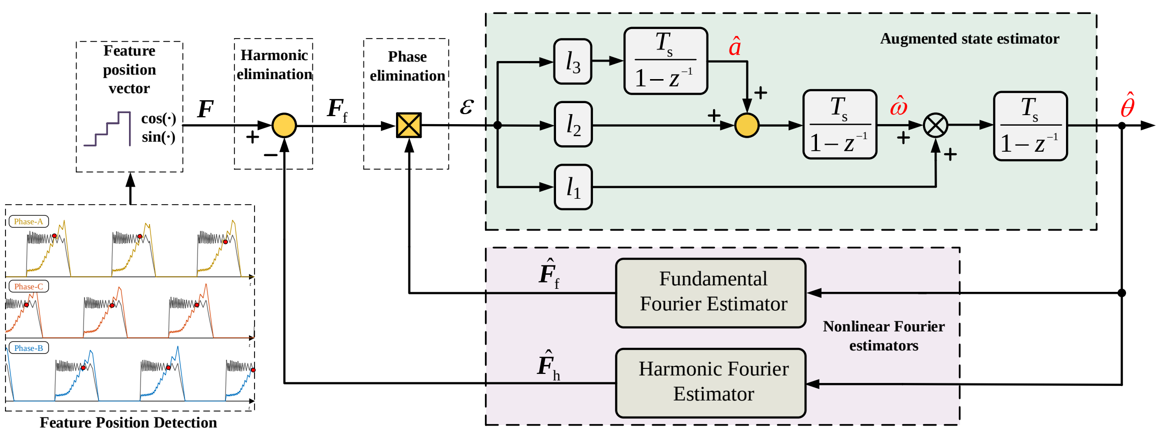

Figure 5.6 Block diagram of the NSO for the SRM sensorless control.

The feature position detected from the flux-linkage comparison method is mechanical position and ranges from 0° to 360°. This discontinuous position is set as the observer input and rewritten as a vector $\boldsymbol{F}$ through (5.8). Two nonlinear Fourier estimators are designed to estimate the fundamental and harmonic vectors. An augmented state estimator is then employed to estimate the rotor position and speed. Here, the structure of the proposed observer is expressed in the discrete form in order for digital implementation.

As the core of the NSO, the design of the nonlinear Fourier estimators and the augmented state estimator will be concentrated in this section.

5.3.2.1 Nonlinear Fourier Estimators

The nonlinear Fourier estimators in the observer feedback path are expected to estimate the fundamental vector $\boldsymbol{F}_\mathrm{f}$ and harmonic vector $\boldsymbol{F}_\mathrm{h}$ based on the estimated rotor position. According to the Fourier expansion, the fundamental and harmonic vectors can be obtained if the rotor position is estimated, as

$$\hat{\boldsymbol{F}}_\mathrm{f} = e^{j\left(\hat{\theta}-\varphi\right)}, \tag{5.12}$$

$$\hat{\boldsymbol{F}}_\mathrm{h} = \sum_{k=1}^{\infty}\left[-\frac{1}{kN-1}e^{-j\left[(kN-1)\hat{\theta}+\varphi\right]}+\frac{1}{kN+1}e^{j\left[(kN+1)\hat{\theta}-\varphi\right]}\right] \tag{5.13}$$

where the circumflex ^ denotes the estimated value.

To obtain the $\boldsymbol{F}_\mathrm{f}$ that contains accurate position information, the harmonic vector $\hat{\boldsymbol{F}}_\mathrm{h}$ has to be eliminated from the feature position vector $\boldsymbol{F}$. According to (5.11), the $\boldsymbol{F}_\mathrm{f}$ can be derived by subtracting $\hat{\boldsymbol{F}}_\mathrm{h}$ from $\boldsymbol{F}$:

$$\boldsymbol{F}_\mathrm{f} = \boldsymbol{F} - \boldsymbol{F}_\mathrm{h} \approx \boldsymbol{F} - \hat{\boldsymbol{F}}_\mathrm{h} \tag{5.14}$$

where the $\hat{\boldsymbol{F}} \approx \boldsymbol{F}_\mathrm{h}$ is satisfied when the estimated position converges to the actual position. In that case, all harmonic components in the vector $\boldsymbol{F}$ can be removed.

Afterward, a heterodyne method is applied to the actual and estimated fundamental vectors, namely $\boldsymbol{F}_{\mathrm{f}}$ and $\hat{\boldsymbol{F}}_{\mathrm{f}}$, to cancel out the phase shift φ. An equivalent position estimation error ε can then be obtained as

$$\varepsilon = \hat{\boldsymbol{F}}_{\mathrm{f}} \times \boldsymbol{F}_{\mathrm{f}} = \sin\left(\theta - \hat{\theta}\right) \approx \Delta\theta \tag{5.15}$$

where $\Delta\theta = \theta - \hat{\theta}$ is the position estimation error. If the error is small enough, the approximation in (5.15) holds.

Therefore, the harmonics in the feature position vector $\boldsymbol{F}$ are eliminated by adopting the proposed nonlinear Fourier estimators, thereby deriving the fundamental vector $\boldsymbol{F}_{\mathrm{f}}$ that contains complete position information. The equivalent position estimation error ε in (5.15) can be generated without any distortions. If $\varepsilon \approx \Delta\theta$ converges to zero, a continuous and accurate rotor position will be estimated even though only the feature position is detected.

5.3.2.2 Augmented State Estimator

As the previous nonlinear Fourier estimators obtain the equivalent position estimation error only, a state estimator can be used for position and speed estimation. In this section, an augmented state estimator is adopted and assembled in the NSO to estimate the rotor speed and position by converging the position error derived in (5.15). Its capability in suppressing the flux linkage errors on estimation is analyzed as well, and the parameter design scheme will be given.

Due to the rotor speed and position both representing the dynamic states of the SRM, the state estimator can be designed based on the mechanical dynamic equation of the SRM, as follows:

$$\begin{cases} \dot{\theta} = \omega + \Delta f_1 \\ \dot{\omega} = a + \Delta f_2 = \left[\left(T_{\mathrm{e}} - T_{\mathrm{L}} \right) / J - B\omega \right] + \Delta f_2 \\ \dot{a} = \delta + \Delta f_3 \end{cases} \tag{5.16}$$

where T_e is the electromagnetic torque, T_L is the load, J is the inertia, B is the viscous friction coefficient, and a is the motor acceleration, and δ is a constant. The time derivative of the acceleration a exists and is bounded by δ, but unknown. Δf_1, Δf_2, and Δf_3 denote the disturbance and noise. In the SRM sensorless control, these disturbances are caused by the flux-linkage error, such as mutual coupling, parameter mismatch, etc.

The rotor position error is the only known variable after adopting the nonlinear Fourier estimators, but the electromagnetic torque T_e, the load torque T_L, parameters J and B, boundary value δ, and disturbance $\Delta f_{1,2,3}$ cannot be directly obtained unless using the three-dimensional torque-current-position characteristic, external torque transducers, or offline measurement. However, the additional effort would complicate the control algorithm and reduces the generality. The large memory for magnetizing data storage is not available for a low-cost SRM drive. It is the main difference in observer design compared with AC motor drives [108], [109], of which electromagnetic toque can be easily obtained analytically, and the load torque can be estimated with the known electromagnetic torque through an observer.

In order to estimate the rotor speed and position of the SRM with robustness against the distortions, as well as not using any motor-specific parameters, an augmented state estimator is adopted based on the position estimation error derived in (5.15) and also considering the motor dynamics, as follows:

$$\begin{cases} \dot{\hat{\theta}} = \hat{\omega} + l_1\left(\theta - \hat{\theta}\right) \\ \dot{\hat{\omega}} = \hat{a} + l_2\left(\theta - \hat{\theta}\right) \\ \dot{\hat{a}} = l_3\left(\theta - \hat{\theta}\right) \end{cases} \tag{5.17}$$

where l_k (k=1,2,3) are the observer gains.

Compared to (5.16), all disturbances from the flux-linkage error and uncertainties can be estimated by the linear controllers. Although the electromagnetic torque information, the load value, and inertia are unknown, taking these uncertainties as a unified acceleration can simplify the observer design, since it does not require time-consuming measurement of torque characteristic and inertia. Also, no motor-specific parameters are used in the proposed estimator, which avoids the parameter sensitivity issue and enhances its robustness. Hence, it would be practical for the low-cost SRM sensorless drive.

When the position estimation error in (5.17) converges, all the unknown perturbations in the estimation will eventually be zero. The undesired disturbances $\Delta f_{1,2,3}$ caused by the flux-linkage error can be therefore suppressed by the state estimator.

Besides the rotor position and speed required for SRM control, the state estimator extends the estimation to the motor acceleration by a linear controller with a gain l_3. This augmented design can help the sensorless control fast track the speed variation of the SRM and enhance the transient estimation accuracy, even though the torque information is not used.

To illustrate the advantage of the proposed observer, the dynamic transfer function of position and speed estimation errors can be derived from (5.17):

$$\Delta\theta(s) = \frac{s^3}{s^3 + l_1 s^2 + l_2 s + l_3}\theta(s) \tag{5.18}$$

$$\Delta\omega(s) = \frac{s^3 + l_1 s^2}{s^3 + l_1 s^2 + l_2 s + l_3}\omega(s)\ . \tag{5.19}$$

As shown in the error transfer function, the proposed position estimation and speed estimation are the type-III and type-II systems, respectively. Giving the final value theorem of the linear control system, as expressed in (5.20):

$$err_{\mathrm{ss}} = \lim_{s\to 0}\left[sG_{\mathrm{err}}(s)u(s)\right] \tag{5.20}$$

where err_{ss} is the steady-state error, G_{err} is the error transfer function, and u is the input.

The steady-state position and speed estimation errors, $\Delta\theta_{\mathrm{ss}}$ and $\Delta\omega_{\mathrm{ss}}$, under a step speed response ($\omega(s)=1/s$ & $\theta(s)=1/s^2$) and a ramp speed response ($\omega(s)=1/s^2$ & $\theta(s)=1/s^3$), can be obtained as:

$$\Delta\omega_{\mathrm{ss}} = \lim_{s\to 0} s\frac{s^3 + l_1 s^2}{s^3 + l_1 s^2 + l_2 s + l_3}\cdot\left(\frac{1}{s}\ \text{or}\ \frac{1}{s^2}\right) = 0 \tag{5.21}$$

$$\Delta\theta_{\mathrm{ss}} = \lim_{s\to 0} s\frac{s^3}{s^3 + l_1 s^2 + l_2 s + l_3}\left(\frac{1}{s^2}\ \text{or}\ \frac{1}{s^3}\right) = 0\ . \tag{5.22}$$

Therefore, the proposed observer can estimate the rotor speed and position of the SRM with zero steady-state errors during the step and ramp speed responses.

Compared to the conventional linear prediction method for position estimation that is sensitive to flux linkage errors, the proposed observer considers the non-ideal influence of the flux-linkage error and establishes an augmented state estimator to improve the transient performance. Higher accuracy of the rotor position and speed estimation can be achieved.

5.4 Small-Signal Modeling and Parameter Design of the Proposed Observer

5.4.1 Small-Signal Modeling

In the proposed NSO, three control gains l_k (k=1,2,3) determine the estimation performance and should be specified designed. However, the high nonlinearity of the observer makes the parameter design complicated. In this section, a novel small-signal linearization model of the nonlinear observer is proposed for optimal parameter design.

Due to the presence of flux-linkage errors, the feature position contains deviations compared to the actual position, leading to perturbations $\Delta f_{1,2,3}$ in all estimation. Hence, the small-signal model is established by considering the estimation error in the proposed observer. The fundamental vector extracted by (5.14) can be rewritten as

$$\boldsymbol{F}_{\mathrm{f}}' = \boldsymbol{F} - \hat{\boldsymbol{F}}_{\mathrm{h}} = \boldsymbol{F}_{\mathrm{f}} + \underbrace{\boldsymbol{F}_{\mathrm{h}} - \hat{\boldsymbol{F}}_{\mathrm{h}}}_{\Delta \boldsymbol{F}_{\mathrm{h}}} \tag{5.23}$$

where the error term $\Delta\boldsymbol{F}_{\mathrm{h}}$ in (5.23) represents the estimation error of the harmonic vector. It can be expressed according to the Fourier series, which gives

$$\begin{aligned} \Delta \boldsymbol{F}_{\mathrm{h}} = &\sum_{k=1}^{\infty}\left[-\frac{1}{kN-1}e^{-j\left[(kN-1)\theta+\varphi\right]}+\frac{1}{kN+1}e^{j\left[(kN+1)\theta-\varphi\right]}\right] \\ &-\sum_{k=1}^{\infty}\left[-\frac{1}{kN-1}e^{-j\left[(kN-1)\hat{\theta}+\varphi\right]}+\frac{1}{kN+1}e^{j\left[(kN+1)\hat{\theta}-\varphi\right]}\right]. \end{aligned} \tag{5.24}$$

Under a quasi-locked condition $(\theta-\hat{\theta}\to 0)$, (5.24) can be simplified to an approximation model as

$$\Delta \boldsymbol{F}_{\mathrm{h}} \approx \Delta\theta \times \sum_{k=1}^{\infty}\left[e^{-j\left[(kN-1)\theta+\varphi-0.5\pi\right]}+e^{j\left[(kN+1)\theta-\varphi+0.5\pi\right]}\right]. \tag{5.25}$$

Accordingly, the fundamental vector derived by (5.23) can be expressed by

$$\begin{aligned}\boldsymbol{F}_{\mathrm{f}}' &= \boldsymbol{F}_{\mathrm{f}} + \Delta \boldsymbol{F}_{\mathrm{h}} \\ &\approx e^{j(\theta-\varphi)} + \Delta\theta \times \sum_{k=1}^{\infty}\left[e^{-j\left[(kN-1)\theta+\varphi-0.5\pi\right]}+e^{j\left[(kN+1)\theta-\varphi+0.5\pi\right]}\right].\end{aligned} \tag{5.26}$$

It reveals that the fundamental vector extracted by the nonlinear estimators contains the undesired harmonics $\Delta \boldsymbol{F}_{\mathrm{h}}$. These distortions are presented in high orders, i.e., ($kN\pm1$)th, and proportional to the position estimation error $\Delta\theta$.

By adopting the heterodyne method presented in (5.15), the equivalent position error ε, which is the input of the augmented state estimator, can be obtained as:

$$\varepsilon = \hat{\boldsymbol{F}}_{\mathrm{f}} \times \boldsymbol{F}_{\mathrm{f}}' \approx \Delta\theta + \Delta\theta \times \sum_{k=1}^{\infty}\left[2\cos\left(kN\theta\right)\right]. \tag{5.27}$$

As observed, the $(kN\pm1)^{\text{th}}$ harmonics in the $\boldsymbol{F}_{\mathrm{f}}'$ can generate the $(kN)^{\text{th}}$ position error in ε.

According to Figure 5.6 and (5.27), the overall small-signal model of the proposed observer is drawn in Figure 5.7. The approximate model shows the inherent relationship between the actual and estimated rotor positions. The nonlinear feedback path is eliminated and replaced by the unit feedback path. Position harmonics are expressed by a compact form given in (5.27). The augmented state estimator, which can converge the position error ε, is still embedded in the model since it has been expressed in a linear form. As shown, the proposed small-signal model presents a more straightforward structure than the exact model. The linear approximated model can be used to further analyze the observer stability and design the parameters.

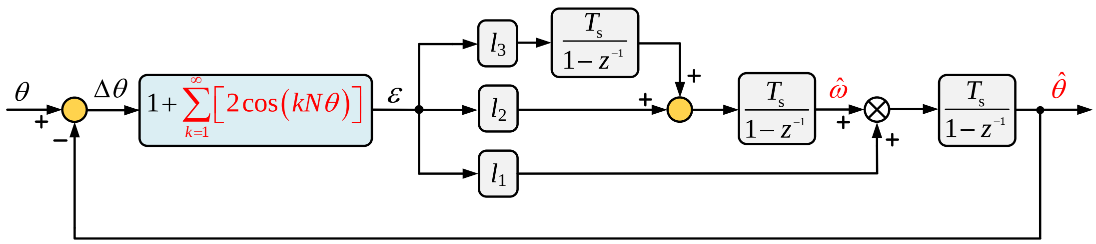

Figure 5.7 The small-signal model of the proposed NSO.

5.4.2 Parameter Design and Stability

Due to the nonlinear estimators in the feedback path, most harmonics in the feature position can be physically eliminated before entering the augmented state estimator. Therefore, it offers the possibility to design a high-bandwidth observer. Whereas, from the view of the small-signal model, there are still several high-order position harmonics in the feedforward path, as shown in Figure 5.7. The extra harmonics indicate how the perturbations $\Delta f_{1,2,3}$ from the flux-linkage error increase the estimation error. Still, these distortions can be eliminated by optimizing the parameter design of the augmented state estimator.

According to the transfer function given in (5.18), the proposed observer is a third-order system, and an effective way to configure all linear gains is to set a triple-negative pole on the real axis. On this basis, the characteristic equation of the transfer function (5.18) can be transferred to the form with a triple root:

$$s^3 + l_1 s^2 + l_2 s + l_3 = (s + p)^3 = 0 \tag{5.28}$$

where $p \in \mathbb{R}^+$, and the triple poles of the observer are $s_{1,2,3} = -p$. This pole placement gives a critically damped observer, which is always stable since all poles are in the negative real axis. The stability can therefore guarantee the convergence of all state estimation errors.

The observer's stability can be analyzed through the characteristic equation given in (5.28). According to the Routh stability criterion, a system is stable when all coefficients in the characteristic equation are positive, which gives the stability criterion of the proposed observer as

$$l_1 > 0,\ l_2 > 0,\ l_3 > 0\,. \tag{5.29}$$

The above criterion should be always satisfied in order to estimate the accurate rotor position without perturbance caused by the flux linkage error.

Comparing both sides in equation (5.28) gives a design scheme of the linear gains:

$$l_1 = 3p,\ l_2 = 3p^2,\ l_3 = p^3\,. \tag{5.30}$$

According to the stability criterion (5.29), it is easy to find that when the observer's triple pole -*p* is located in the negative real axis, i.e., *p*>0, the proposed observer will be stable. By selecting different *p* values, the Bode diagram of the position estimation is shown in Figure 5.8. Intuitively, the position estimation possesses as a lowpass position observer, and its phase margin is always positive, which ensures the stability. The lowpass characteristic can reject high-order position harmonics and distortions caused by the flux linkage error, thereby improving the estimation accuracy. With a large *p*, the bandwidth of the position estimation increases, which gives a faster response rate but reduces the harmonic-filtering capability. Therefore, the tuning of the observer parameter can be done by considering the frequency of the primary harmonic in the estimated position.

As analyzed earlier in the small-signal model in (5.27), the position harmonic exists in the equivalent position error ε and needs to be eliminated by selecting a proper observer bandwidth. The observer bandwidth can be defined as the frequency when the magnitude is -3 dB, which yields:

$$\omega_{\text{bandwidth}} \approx 3.9p \,. \tag{5.31}$$

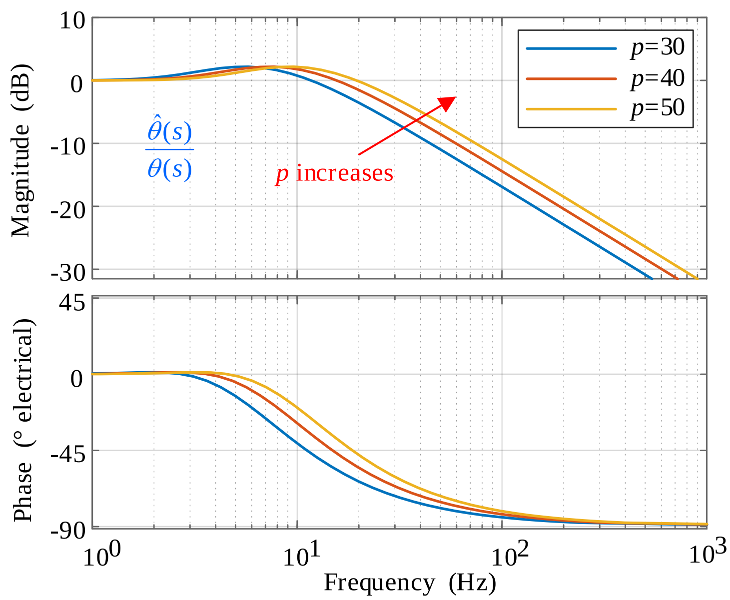

Figure 5.8 Bode diagram of the position estimation with different pole values.

Since the harmonic components in the model are in high-order, i.e., kN^{th}, k=1, 2, …, the observer bandwidth can be set higher to achieve fast-dynamic performance as long as the dominant position harmonics can be filtered. Therefore, the optimal bandwidth of the proposed observer is set to be smaller than the dominant harmonic frequency when k=1, namely:

$$\omega_{\text{bandwidth}} \approx 3.9p < \omega_{\text{h\_dominant}} = N\omega_{\text{m\_enable}} \tag{5.32}$$

where ω_{m_enable} is the lowest rotor frequency (in mechanical) when the proposed position estimation method is enabled. Below that frequency, the model-based estimation is well-known disabled, and pulse-injection-based techniques can be used for starting stage and low-speed sensorless operation.

5.5 Experimental Results

The proposed position estimation scheme based on NSO is verified on the 12/8 SRM setup. Figure 5.9 shows the schematic diagram of the proposed SRM sensorless control.

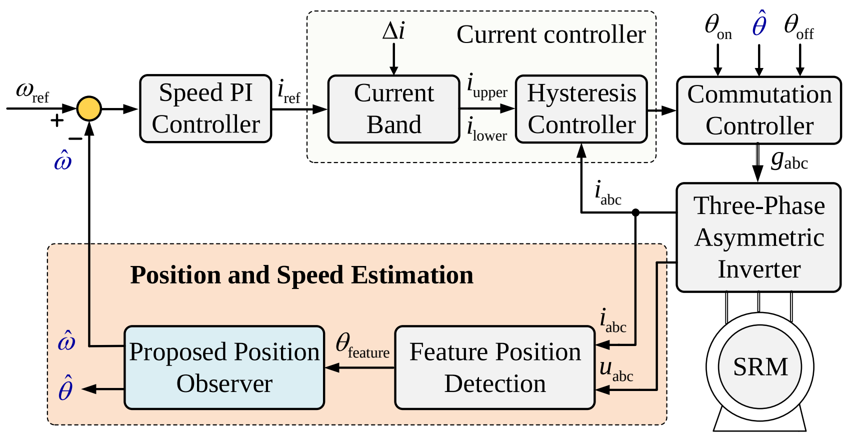

Figure 5.9 Schematic diagram of the proposed position-sensorless control.

The high-speed controller uses the same structure as the low speed. A speed PI controller is used to track the reference speed ω_{ref} and generate the reference phase current i_{ref}. The current hysteresis controller is used in the current loop, in which the upper current reference i_{upper} and lower current reference i_{lower} are calculated according to a preset bandwidth Δi. Afterward, the commutation of each phase is controlled according to the comparison between the estimated rotor position and turn-on and turn-off angles, θ_{on} and

θ_{off}. Without specific mention, the commutation angles are set as θ_{on} =0° and θ_{off} =20°. For position-sensorless control, the rotor speed and position used in the speed and current controllers are estimated from the proposed observer, instead of the position sensor.

Since the proposed scheme is based on the flux linkage estimation, it is used for medium- and high-speed position estimation. The speed threshold to enable the proposed observer is set to around 300 r/min (the rated speed of the SRM is 1000 r/min). According to the parameter design in (5.32), the observer bandwidth is set to be 120 rad/s and the p is equal to 30. When the rotor speed is lower than 300 r/min, high-frequency pulse injection can be used for position estimation. The following experimental tests validate the advantage of the proposed observer compared to the conventional linear prediction method. All experimental results are recorded in the position-sensorless control mode by using the proposed method.

The feature position at 15° is first detected by the flux-linkage estimation method. Figure 5.10 shows the experimental results of the flux estimation in three phases at 500 r/min. The real-time stator flux linkage is calculated through the SRM voltage equation. The reference flux-linkage curve at 15° is learned by self-commissioning process as analyzed before, which does not require the offline measurement and FEA simulation. As shown in Figure 5.10(a), when the intersection of the real-time calculated flux linkage and the reference curve is detected in the three phases, the rotor position stepped by 15° is recorded as the feature position. It is worth noting that the feature position shown in Figure 5.10(a) is used for controlling the phase A, and the feature position for other phases can be obtained by shifting the phase-A position by 15°. Compared to the actual position derived by a

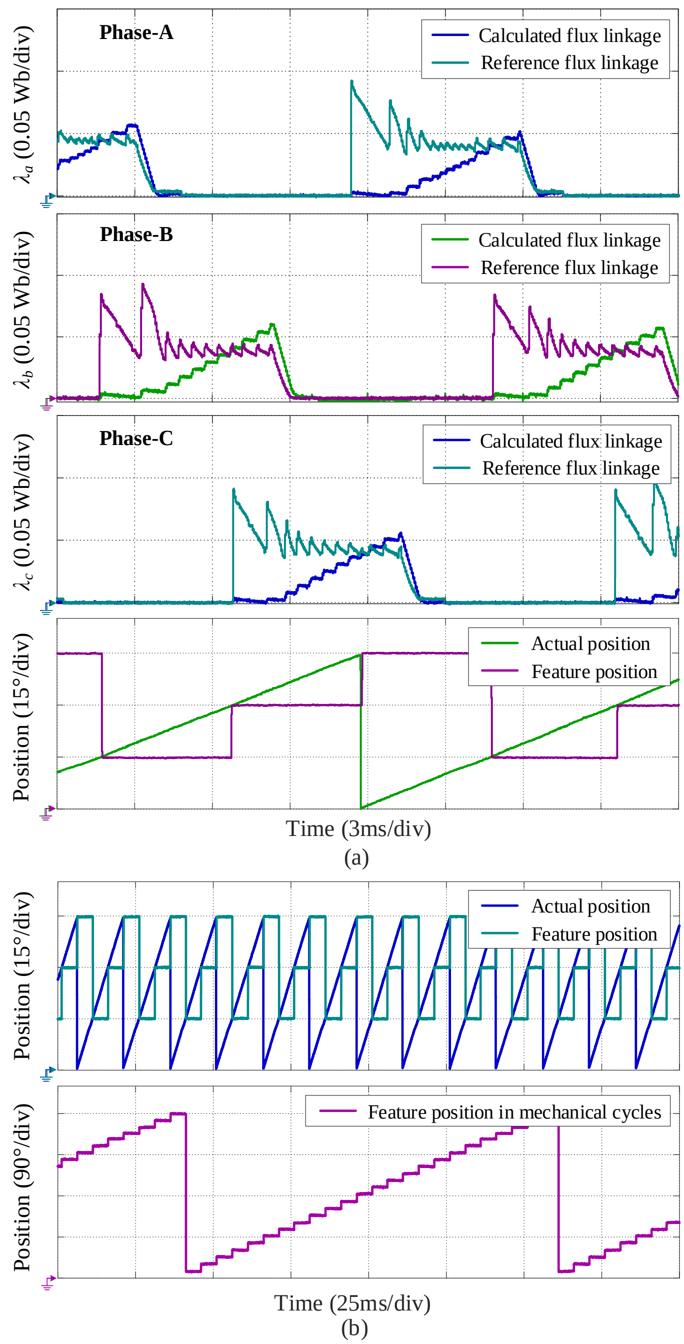

Figure 5.10 Feature position detection by flux-linkage estimation at 500 r/min. (a) Calculated flux linkage, reference flux linkage at 15°, and the estimated feature position. (b) Estimated feature position in the mechanical cycle.

resolver, the feature position is step-manner and inaccurate, which cannot be used for SRM control. In order to improve the estimation accuracy by using the proposed NSO, the feature position ranges from 0° to 45° is transferred to a complete mechanical cycle, i.e., being scaled by 360° as shown in Figure 5.10(b). Thereby, the feature position can be further written in the vector form of the proposed observer, as indicated in (5.8).

To illustrate the effectiveness of the proposed scheme, the intermediate variables of the NSO are shown in Figure 5.11. The feature position shown in Figure 5.11(b) is rewritten in the vector form by (5.8), where the waveform of the orthogonal vector $\boldsymbol{F}$ is depicted in Figure 5.11(a). Due to the limited resolution of the feature position, the feature position vector $\boldsymbol{F}$ is discrete and contains large harmonics. To eliminate the harmonic vectors in $\boldsymbol{F}$, the harmonic Fourier estimator is built based on Fourier series expansion to estimate the harmonic vector $\hat{\boldsymbol{F}}_{\mathrm{h}}$, as depicted in Figure 5.11(b). By subtracting the harmonic vector $\hat{\boldsymbol{F}}_{\mathrm{h}}$ from the discontinuous vector $\boldsymbol{F}$, the fundamental vector $\boldsymbol{F}_{\mathrm{f}}$ that is more continuous can be extracted, as shown in Figure 5.11(c). It should be noted that the harmonics cannot be entirely eliminated in $\boldsymbol{F}_{\mathrm{f}}$, since high-order position harmonics are still in presence in the forward path, which has been analyzed in the small-signal model. Whereas, the higher-order harmonics can be further reduced by the proposed observer by selecting the optimal linear gains by (5.30). Thus, these harmonic disturbance in $\boldsymbol{F}_{\mathrm{f}}$ would not affect the position estimation accuracy. As a result, the estimated fundamental vector $\hat{\boldsymbol{F}}_{\mathrm{f}}$, which is calculated from the estimated rotor position, has fewer harmonics, as shown in Figure 5.11(d). Compared to the feature position vector $\boldsymbol{F}$, the harmonics in the discrete position vector can be fully eliminated. Particularly, no phase delays are introduced by the proposed observer, which has been proved in (5.22). Therefore, the position information lost in the feature position can be completely reconstructed by the proposed method.

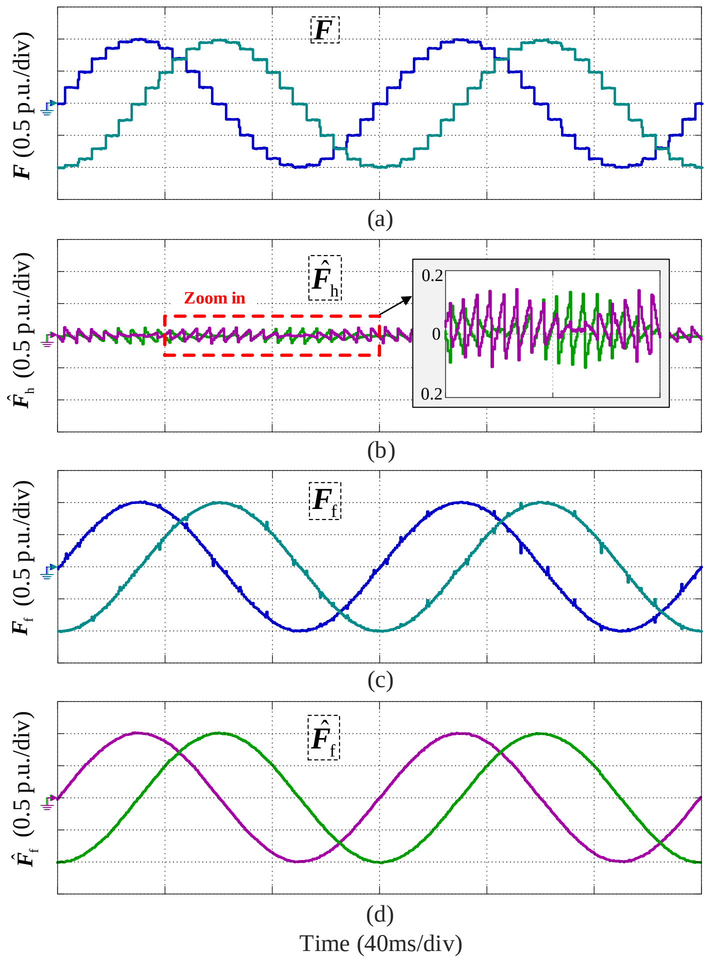

Figure 5.11 Experimental verification of the proposed NSO at 500 r/min. (a) Feature position vector. (b) Estimated harmonic vector. (c) Fundamental vector. (d) Estimated fundamental vector.

The position estimation results at 500 r/min of the proposed observer, as well as the conventional linear prediction method for comparison purpose, are shown in Figure 5.12. As analyzed previously, voltage distortions, current measurement errors, parameter mismatch, and mutual flux linkage can result in inevitable flux linkage errors. Therefore, the feature position cannot be detected exactly when comparing the real-time flux linkage and the reference curve. It would cause small deviations in the estimated feature position compared to the actual position, which is shown in Figure 5.12. When the conventional linear prediction method is used, the unknown position within the next interval of two feature position points is predicted based on the previous average speed. However, due to the deviation in the feature position, the calculated average speed is inaccurate, and the estimated rotor position from the linear prediction method is still discontinuous. The large position error would limit sensorless control performance, especially under the load condition. In contrast, the proposed observer takes these flux linkage errors into account and treats them as a perturbance in position estimation. Three linear controllers are designed based on the mechanical dynamic equation to eliminate these perturbances by converging the position estimation error to zero. Through the small-signal linearization, the perturbance from flux linkage errors can be regarded as high-frequency noises in the feedforward path of the position estimator. Due to the lowpass characteristic and zero-tracking errors of the proposed observer, the nonideal distortions can be rejected by properly designing the observer's bandwidth, and meanwhile the stability can also be guaranteed. Moreover, the low-resolution issue of the feature position can be solved by using the nonlinear Fourier estimators. Most of the harmonics in the input feature position can be removed before entering the augmented state observer. Therefore, the bandwidth of the estimator can be set higher, and fast dynamic performance and good perturbance suppression capability can be achieved at the same time. As a result, compared with the conventional linear prediction method, the estimated position of the proposed scheme is in better agreement with the actual position.

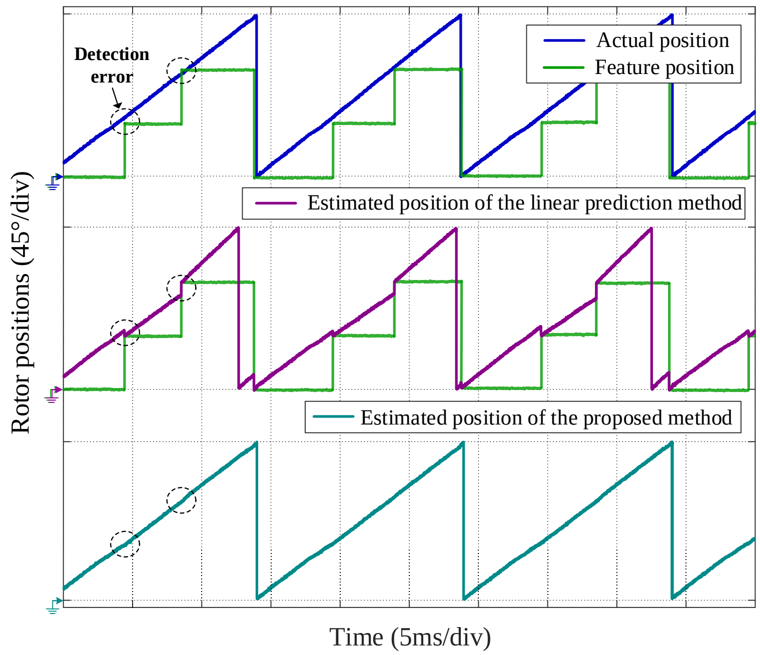

Figure 5.12 Comparative experimental results of the proposed observer and the conventional linear prediction method at 500 r/min.

To baseline the improvement on estimation accuracy, Figure 5.13 compares the position and speed estimation errors of the proposed observer and the conventional linear prediction method at 500 r/min. Due to the flux linkage errors, the linear prediction method causes large ripples in the estimated rotor position, and the maximum absolute position error is 5.2° as shown in Figure 5.13(a). Besides, from the result in Figure 5.13(b), the deviation of the feature position has a more serious impact on speed estimation, where the maximum absolute speed error reaches to 139.8 r/min. Although the linear prediction method can theoretically offer accurate estimation if no flux linkage errors exist, this criterion is ideal and cannot be guaranteed in practical applications. Using lowpass filters could be a solution to remove the estimation ripples in the conventional method, but it would bring a DC drift in position estimation and cause large speed-tracking error during the speed-transient state. As a result, the conventional linear feature-position-based method would have large speed and position estimation errors and result in a vulnerable sensorless control. In comparison, the proposed observer can well estimate the rotor position and speed with much fewer errors. The maximum position error can be reduced to 1.8°, and the speed estimation error always keeps within 18.2 r/min. The average position and speed estimation error are both around zero. Moreover, the significant estimation ripples are reduced by the proposed observer, which thereby ensures more stable and smoother speed and current control.

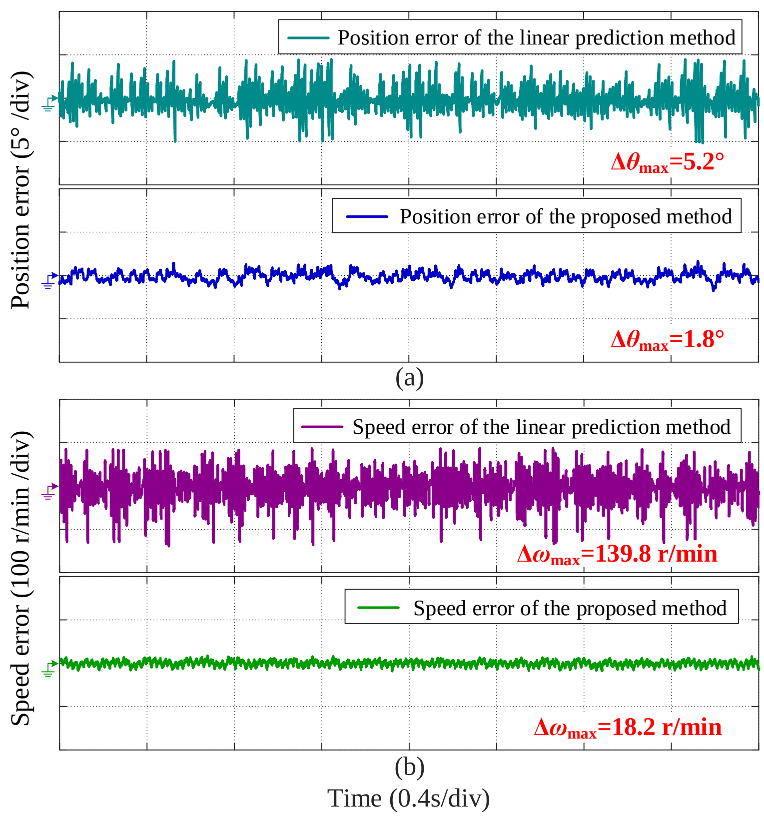

Figure 5.13 The comparison of estimation errors between the proposed observer and the conventional linear prediction method at 500 r/min. (a) Position estimation errors. (b) Speed estimation errors.

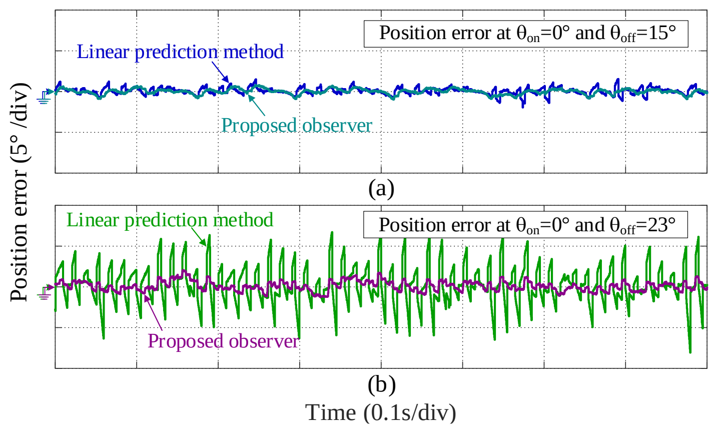

Figure 5.14 Position estimation results with different control angles. (a) θ_{on} =0° and θ_{off} =15°. (b) θ_{on} =0° and θ_{off} =23°.

The position estimation with other control angles are further validated experimentally, as shown in Figure 5.14. One of the main sources of flux linkage errors is the mutual coupling effect, which cannot be ignored when two phases have an overlapping region and the phase current is large. A comparative test is conducted by using different control angles. Figure 5.14(a) is the position estimation error at the control angles θ_{on}=0° and θ_{off}=15°, in which the mutual crossing effect is small and can be neglected. In Figure 5.14(b), the wider control angles of (θ_{on}=0°, θ_{off}=23°) are used for comparison, and other conditions are kept the same. In this case, the two adjacent phases have a wider overlap region, and the mutual flux linkage effect would be larger. As can be seen from Figure 5.14(a), when turn-on region of each phase is small (0°-15°), the position estimation results of the proposed observer and the conventional linear prediction method are similar since the flux linkage error is small. However, when the overlap region becomes larger due to the lag turn-off angle of 23°, as illustrated in Figure 5.14(b), significant position errors can be found in the conventional linear prediction method. In comparison, the proposed observer shows better robustness against the flux linkage error, and the position error is slightly increased when the turn-on angle is lag but still much smaller than the conventional method.

Moreover, the speed transient performance and the estimation accuracy at other speeds are also validated, as shown in Figure 5.15 and Figure 5.16. The SRM runs in the sensorless control mode with the proposed observer at no load. In the test, the SRM first operates at 300 r/min and then accelerates to 1000 r/min (rated speed). In Figure 5.15, a ramp reference speed is given, and Figure 5.15(a) depicts both the actual speed and the speed estimation results of the linear prediction and the proposed observer. As can be observed, although the conventional scheme can track the speed variation, the linear prediction is quite sensitive to the feature position detection error, and the speed and position errors are significant, as shown in Figure 5.15(b) and (c), respectively. As an improvement, the proposed observer can track well the speed change, and the overall estimation errors are much lower than the conventional method. Furthermore, Figure 5.16 shows the estimation results under a step speed reference from 300 r/min to 1000 r/min. It can be found that the proposed method can still offer higher estimation accuracy of both the rotor speed and position compared to the conventional linear prediction method. Besides, due to the more accurate estimation, the SRM can be well controlled in the sensorless control mode with a fast speed transient response.

Figure 5.17 indicates the dynamic performance of the sensorless control with load disturbance. The speed is kept as 500 r/min, and the IM is served as the load machine to generate a 15 N·m load torque in the inverse direction. The load is added at 6 seconds and then removed at 14 seconds. As can be seen from Figure 5.17(a), due to the load change

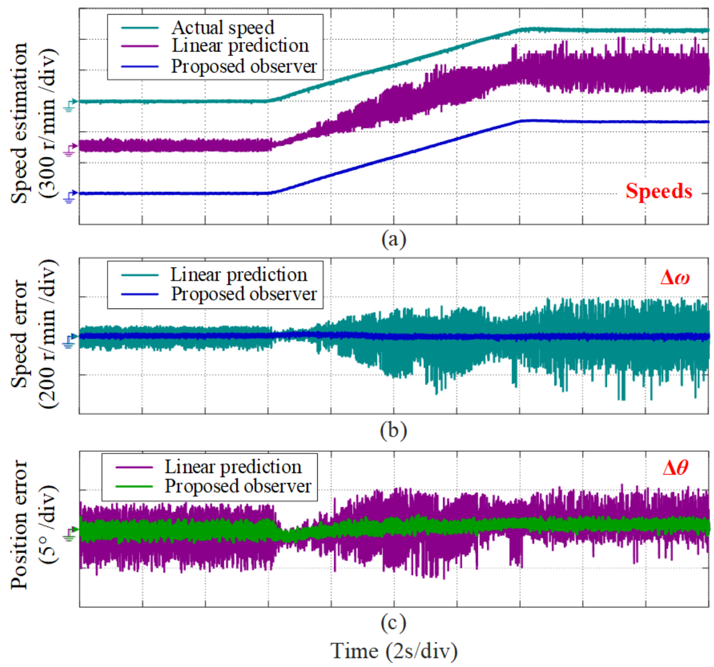

Figure 5.15 Estimation errors under ramp speed change from 300 r/min to 1000 r/min (rated speed). (a) Actual and estimated speeds. (b) Speed estimation errors. (c) Position estimation errors.

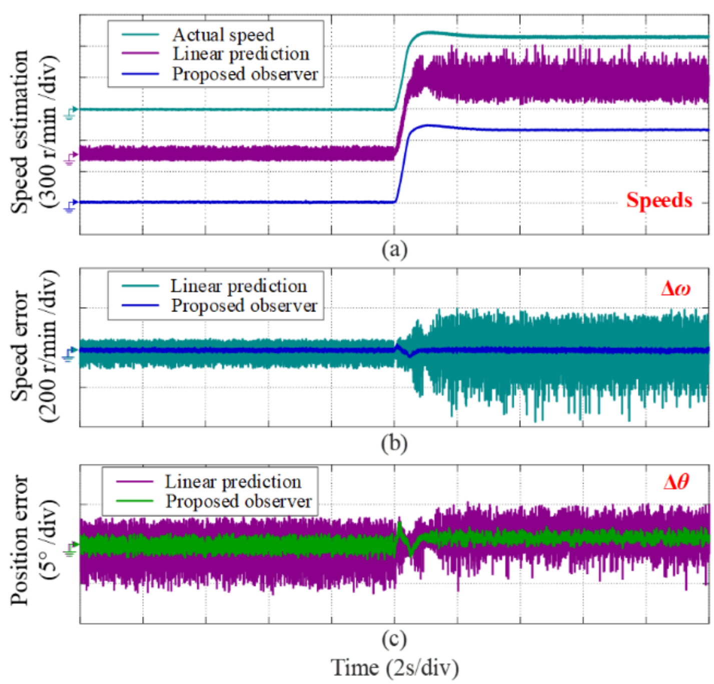

Figure 5.16 Estimation errors under step speed change from 300 r/min to 1000 r/min (rated speed). (a) Actual and estimated speeds. (b) Speed estimation errors. (c) Position estimation errors.

the rotor speed drops/increases by around 180 r/min but can stably converge to the reference speed. By summarizing the results in Figure 5.17(b) and Figure 5.17(c), the transient speed and position estimation errors of the proposed NSO are much smaller than the linear prediction method. Notably, the position estimation error of the linear prediction method reaches about 8° when the load is removed, which would make the conventional method unstable under such heavy load disturbance. In contrast, the proposed scheme can achieve higher estimation accuracy with the maximum transient position error within around 2°. Accordingly, the overall position-sensorless control performance of the SRM can be improved by the proposed observer.

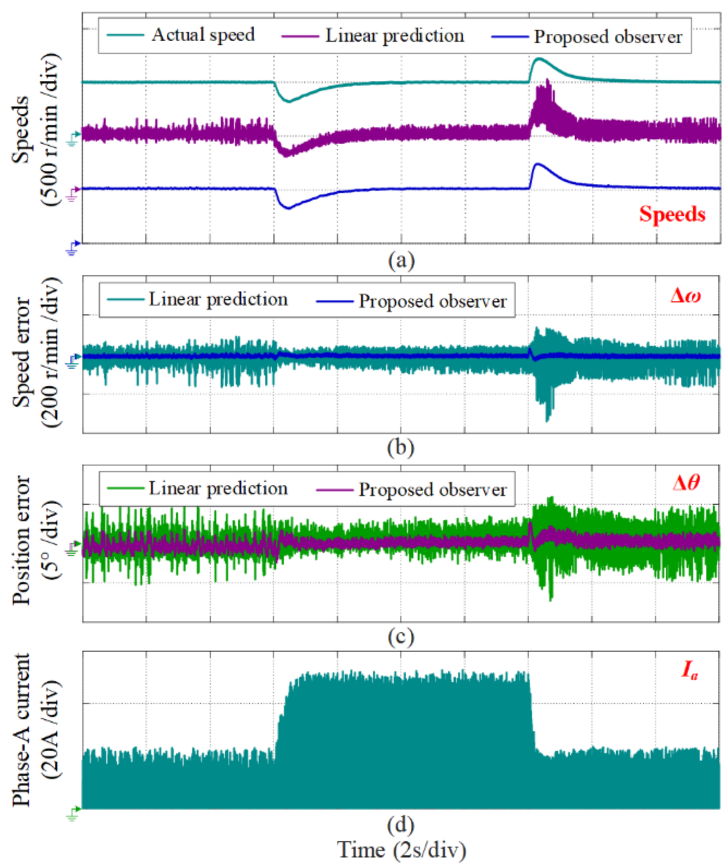

Figure 5.17 Comparative tests with the 15 N·m load disturbance at the half-rated speed.

Another comparative test with the linear prediction method is implemented, but the augmented state estimator proposed in this chapter is used as an in-loop filter for the convention linear prediction method, as illustrated in Figure 5.18(a). Compared to the proposed observer, the nonlinear Fourier estimators are replaced by the linear prediction method, while the augmented state estimators have the same bandwidth. This comparative test is used to verify the improvement of the proposed nonlinear Fourier estimator over the conventional linear prediction method. To validate it, a large flux linkage error is suddenly added in the estimation process when motor is operating, and the position estimation errors are measured. As can be found in Figure 5.18(b), before adding the additional flux linkage error, both the proposed observer and the in-loop-filter-based linear fitting method have much smaller estimation errors compared to the conventional linear fitting method. The accuracy improvement of the in-loop-filter-based linear fitting method is due to the lowpass characteristic of the proposed augmented state estimator. When a large flux linkage error is added, the conventional linear fitting method has a large position error to 10 degrees due to its high sensitivity to flux linkage errors. Although the combination of an in-loop filter may reduce the estimation error of the linear fitting method, the estimation error is still large and around 3 degrees in this instant. In contrast, the proposed observer utilizes the harmonic decoupling method, instead of a linear fitting method, to offer a smoother and ripple-free position signal, which has been proved in Figure 5.11. Most harmonics in the feature position can be eliminated by the harmonic decoupling, and thus having better robustness against the flux linkage error. As a result, the proposed observer shows better estimation accuracy compared to the conventional linear fitting method, even with a large flux linkage error.

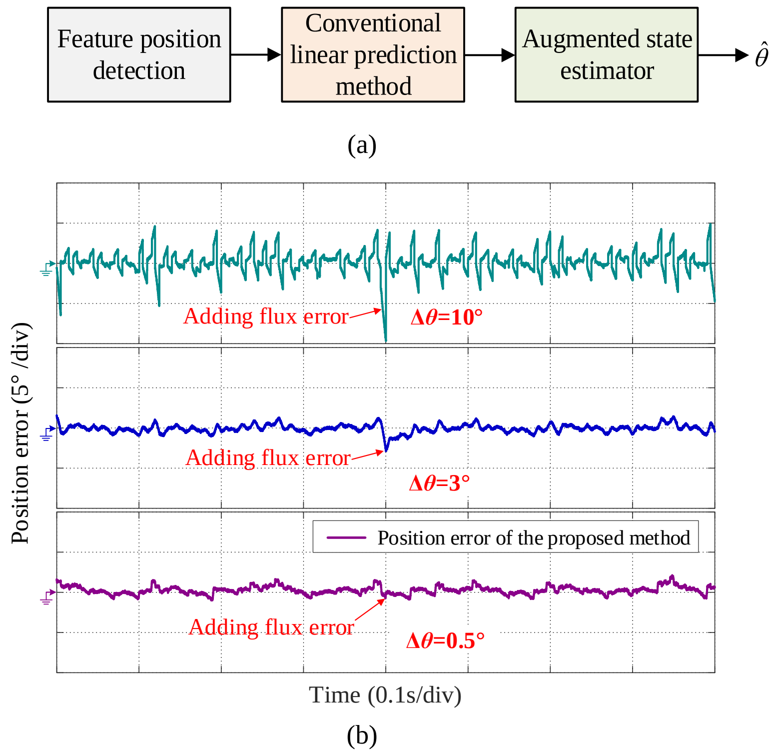

Figure 5.18 Comparative experimental validation of the conventional linear prediction method, an in-loop-filter-based linear prediction method, and the proposed observer at 500 r/min, with a suddenly added large flux linkage error. (a) Block diagram of the in-loop-filter-based linear prediction method. (b) Position estimation results.

5.6 Conclusion

The chapter proposes a new observer, NSO, to improve the position estimation accuracy of SRMs. The feature position is detected by monitoring the intersection of the calculated flux linkage and the reference flux linkage at 15° to estimate the rotor position without using three-dimensional magnetizing characteristics. Since most of the position information is lost when detecting the feature position, an online Fourier-series-based NSO is proposed to capture the inherent frequency characteristic of the feature position. On the basis, two non-linear estimators are designed to eliminate the primary position harmonics and reconstruct a more accurate rotor position. To improve the robustness against flux-linkage errors, a small-signal approximation model of the proposed observer is built to investigate the adverse impact on estimation. An augmented state observer is then proposed to improve the estimation accuracy in steady and transient states. Experimental validation on a 12/8 SRM setup was carried out by testing the performance under both speed and load step responses. The results show that the proposed scheme has lower position and speed estimation errors compared with the conventional linear prediction method. The SRM can run in the sensorless mode with the rapid speed variation and even a heavy load disturbance.

Chapter 6

Magnetic-Characteristic-Free Position Observer for High-Speed Position-Sensorless Control

6.1 Introduction

As mentioned in Chapter 5, the conventional medium- and high-speed sensorless control method relies on three-dimensional magnetic characteristics, which have to be measured offline. The designed NSO can avoid the usage of full magnetic characteristics and only adopt a feature flux-linkage curve. This method does not need the offline measurement and just requires a self-commissioning process. One drawback of the self-commissioning process is that the rotor needs to rotate at designed position. Although the process is automatic, the rotor rotation at the initial stage may be unacceptable in some applications.

To further simplify the position estimation algorithm of SRM drives, a novel magnetic-characteristic-free position-sensorless control strategy based on quadrature flux estimators (QFEs) is proposed in the chapter. This is a new perspective in SRM position estimation, which estimates the rotor position from a bias-free and harmonic-free flux linkage. To this end, the proposed QFE is designed as a speed-adaptive bandpass observer that can eliminate the harmonics and DC bias in the calculated flux linkage. Thus, the high nonlinearity in the SRM flux linkage can be reduced, and a simple orthogonal sine-cos position signal can be derived under both unsaturated and saturated conditions. After using a three-phase PLL, rotor position and speed can be easily estimated. Compared to existing approaches, the proposed method achieves several advantages *simultaneously*:

1) It does not use any magnetic characteristics for position estimation. Thus, either offline measurement or online self-commissioning process is not needed, which simplifies the implementation and also avoids parameter insensitivity issue.
2) Adverse impacts of flux harmonics and offsets can be eliminated, ensuring accurate rotor position estimation in case of magnetic saturation.
3) It is robust to current ripples and noises due to the bandpass filtering capability.
4) Full-cycle rotor position can be estimated continuously, instead of the discontinuous feature position estimation.

Moreover, a logic scheme is designed in this chapter to improve the convergence rate of the QFE. The speed adaptation capability is able to guarantee accurate estimation under variable-speed conditions. Finally, the effectiveness of the proposed scheme and comparative experimental tests of the conventional method are verified on a 5.5 kW 12/8 three-phase SRM setup.

6.2 Investigation of Flux Linkage-Based Position Estimation

6.2.1 Flux Linkage Analysis

Flux linkage of the SRM is a function of the rotor position and phase current, so the rotor position can be estimated by calculating the real-time flux linkage. The SRM model based on the flux linkage is repeated here for readability:

$$u = Ri + \frac{d\lambda(\theta, i)}{dt}. \tag{6.1}$$

The maximum flux linkage occurs at the aligned position 22.5°, and the minimum flux linkage is at the unaligned position 0°. The flux linkage, at a current i=i_c, can be therefore expressed by its Fourier series as a function of the rotor position θ:

$$\lambda(\theta, i_c) = \underbrace{\lambda_0(i_c)}_{\text{Flux bias}} - \underbrace{\lambda_1(i_c)\cos(N_r\theta)}_{\text{Fundamental flux}} - \underbrace{\sum\nolimits_{k=2}^{\infty}\lambda_k(i_c)\cos(kN_r\theta)}_{\text{Flux harmonics}} \tag{6.2}$$

where $\lambda_k(i_c)$ is the amplitude of the k-th flux harmonic, which is a constant at a current i=i_c.

At different current levels, the flux harmonic amplitude $\lambda_k(i_c)$ varies. The accuracy of this Fourier series-based model is validated here at different positions and current levels for the tested 12/8 machine, as shown in Figure 6.1. The Fourier series model can well capture the flux linkage characteristic.

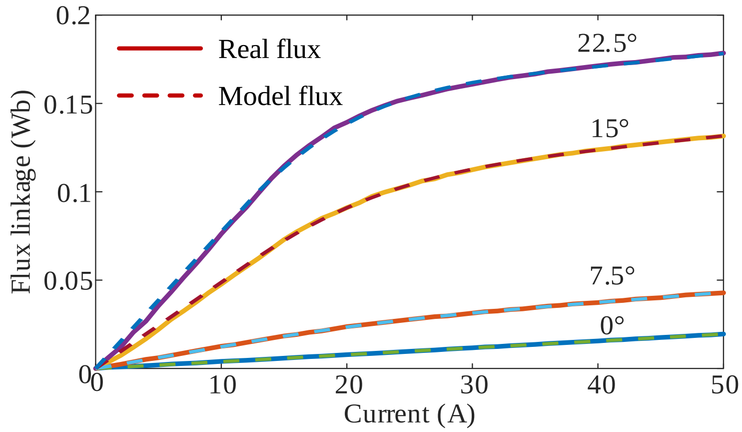

Figure 6.1 Flux linkage of a three-phase 12/8 SRM at different rotor positions, including real flux linkage and its model results from (6.2).

In (6.2), the first term is the bias of the flux linkage, the second represents the fundamental flux that is a cosine function of the rotor position, and the rest are flux harmonics. This nonlinear flux-position-current relationship makes the position estimation difficult, unless the flux characteristic is offline measured and prestored as a lookup table. However, using prestored characteristics leads to parameter sensitivity issues and requires extra offline measurement for each SRM. The request of additional manual work for parameter acquisitions is not attractive for commercial applications.

To solve the issues, the proposed method aims to estimate the rotor position without using flux linkage characteristics.

6.2.2 Basic Principle of the Proposed Scheme

As aforementioned in (6.2), the fundamental flux is a simple cosine function of the rotor position when the phase current is constant. If all flux bias and flux harmonics can be removed from the flux linkage λ, the position estimation will be simplified. Therefore, the flux linkage is calculated based on the voltage equation (6.1) in a constant current region, as illustrated in (6.3):

$$\lambda(\theta,i)=\begin{cases}\int\left(u-Ri\right)dt,\ (\theta\in\left[\theta_{\mathrm{on}},\theta_{\mathrm{off}}\right]) \\ 0,\ (\theta\in\mathrm{else})\end{cases}. \tag{6.3}$$

Here, the flux calculation (6.3) is a piecewise function. For the motoring operation, the turn-on instant often occurs in a low-inductance region (i.e, around the unaligned position), in which the phase current can be fast established. Hence, the phase current is approximated as a constant value around its reference during the excitation period [θ_{on}, θ_{off}]. For simplicity, the discussion of the proposed scheme will be focused on the motoring mode at positive speed in the rest of the chapter. For the generating and negative operation, the flux calculation needs a minor modification, which will be introduced separately.

After obtaining the flux linkage λ, the purpose of the proposed method is to extract the fundamental flux λ_{f} based on (6.2):

$$\lambda_{\mathrm{f}}=-\lambda_{\mathrm{mag}}\cos(N_{\mathrm{r}}\theta) \tag{6.4}$$

where λ_{mag}=$\lambda_1(i_{\mathrm{c}})$ is the magnitude of fundamental flux.

Compared to the original stator flux in (6.2), the rotor position only exists in the phase of the fundamental flux. However, the magnitude λ_{mag} is still an unknown function of the phase current and varies with magnetic saturation levels. To estimate the rotor position from the phase of the fundamental flux λ_{f}, another orthogonal signal is needed to remove the magnitude, expressed as

$$\lambda_{\mathrm{fq}}=-\lambda_{\mathrm{mag}}\sin(N_{\mathrm{r}}\theta) \tag{6.5}$$

where the λ_{fq} denotes the quadrature of the fundamental flux λ_{f}.

The magnitude of the fundamental flux can then be derived from (6.4) and (6.5):

$$\lambda_{\mathrm{mag}} = \sqrt{\lambda_{\mathrm{f}}^{2} + \lambda_{\mathrm{fq}}^{2}} \tag{6.6}$$

Afterward, the rotor position and speed can be estimated from (6.4)-(6.6) by adopting a PLL, as shown in Figure 6.2.

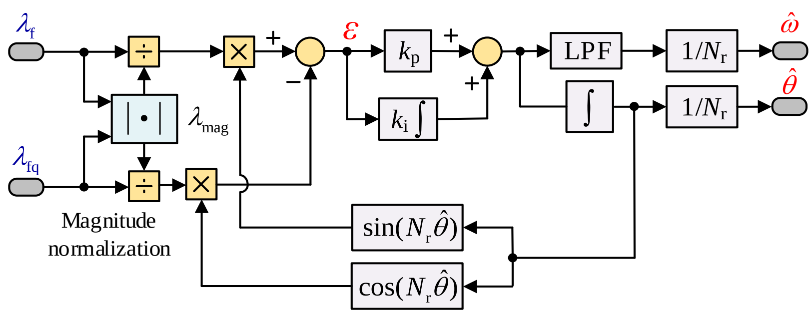

Figure 6.2 The structure of the PLL for position estimation.

According to Figure 6.2, a position-tracking error signal ε can be obtained by using a trigonometric heterodyne method, which is expressed as:

$$\varepsilon = \frac{-\lambda_{\mathrm{fq}}\cos(N_{\mathrm{r}}\hat{\theta}) + \lambda_{\mathrm{f}}\sin(N_{\mathrm{r}}\hat{\theta})}{\lambda_{\mathrm{mag}}} = \sin(N_{\mathrm{r}}\theta - N_{\mathrm{r}}\hat{\theta}) \approx N_{\mathrm{r}}(\theta - \hat{\theta})\,. \tag{6.7}$$

When the position-tracking error ε converges to zero by a PI controller in the PLL, the rotor position can be estimated due to $\hat{\theta} = \theta$. Meanwhile, the rotor speed $\hat{\omega}$ can also be obtained after using a lowpass filter.

As observed from the above signal processing, the position estimation does not require magnetic characteristics of the SRM since all the nonlinear and unknown parameters in the flux linkage are eliminated.

To realize the proposed position estimation procedure, the rest of the chapter will discuss the following two critical problems, which are: (a) how to eliminate the flux bias and flux harmonics in the calculated stator flux, as expressed in (6.4), and (b) how to generate a quadrature signal λ_{fq} of (6.5) from the fundamental flux λ_f .

6.3 Design of the Proposed Position Estimation Scheme Based on QFEs

6.3.1 Second-Order Generalized Integrator With A Highpass Filter

To solve the previous critical issues in flux estimation, the chapter adopts and upgrades a second-order generalized integrator with a highpass filter (SOGI-HPF) for position estimation. The SOGI-HPF has been proved to be a good quadrature signal generator with the capability to eliminate DC components and harmonics, which is widely adopted in grid-connected converters [110]–[112]. The structure of the SOGI-HPF is shown in Figure 6.3 [111], where $u(t)$ is the input signal, and $y_d(t)$ and $y_q(t)$ are the direct-axis output and the quadrature-axis output, respectively. An HPF is embedded in the feedforward path as an in-loop filter. If k_0=0, the SOGI-HPF will be a standard SOGI [111].

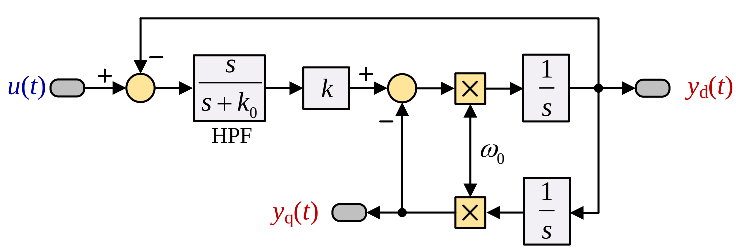

Figure 6.3 The structure of the SOGI-HPF.

From Figure 6.3, the transfer functions of the SOGI-HPF can be expressed as:

$$G_{\mathrm{d}}(s)=\frac{y_{\mathrm{d}}(s)}{u(s)}=\frac{k\omega_0 s^2}{\Delta(s)},\ G_{\mathrm{q}}(s)=\frac{y_{\mathrm{q}}(s)}{u(s)}=\frac{k\omega_0^2 s}{\Delta(s)} \tag{6.8}$$

where k and k_0 are the constant parameters, ω_0 is the resonance frequency, s is the Laplace operator, and the denominator is:

$$\Delta(s)=s^3+(k\omega_0+k_0)s^2+\omega_0^2 s+k_0\omega_0^2 \tag{6.9}$$

k, k_0, and ω_0 are positive.

To illustrate the characteristic of the SOGI-HPF, the Bode diagrams of the two transfer functions in (6.8) are depicted in Figure 6.4. The parameters of k=1.414, k_0=500, and ω_o=500 rad/s are used as an example. It can be seen that both the $G_d(s)$ and $G_q(s)$ are presented as bandpass filters around the resonance frequency ω_o and have the frequency-selection capability. When s=0 in the two transfer functions, their gains are both zero. Hence, the DC component in the input signal $u(t)$ does not exist in the output signals $y_d(t)$ and $y_q(t)$. At high frequency, the magnitude frequency responses of $G_d(s)$ and $G_q(s)$ decay with the slope of more than -20 dB/dec to reduce the high-frequency noises in $u(t)$. If the resonance frequency ω_0 of the SOGI-HPF is set to be the fundamental frequency of the input $u(t)$, the harmonics existing in $u(t)$ can be attenuated due to the bandpass characteristic.

Then, substituting $s=j\omega_0$ into the transfer functions $G_d(s)$ and $G_q(s)$ derives the amplitude- and phase-frequency responses, which are

$$\begin{cases} \left|G_{\mathrm{d}}(s{=}j\omega_0)\right|=1,\ \angle G_{\mathrm{d}}(s{=}j\omega_0)=0 \\ \left|G_{\mathrm{q}}(s{=}j\omega_0)\right|=1,\ \angle G_{\mathrm{q}}(s{=}j\omega_0)=-90^\circ \end{cases}. \tag{6.10}$$

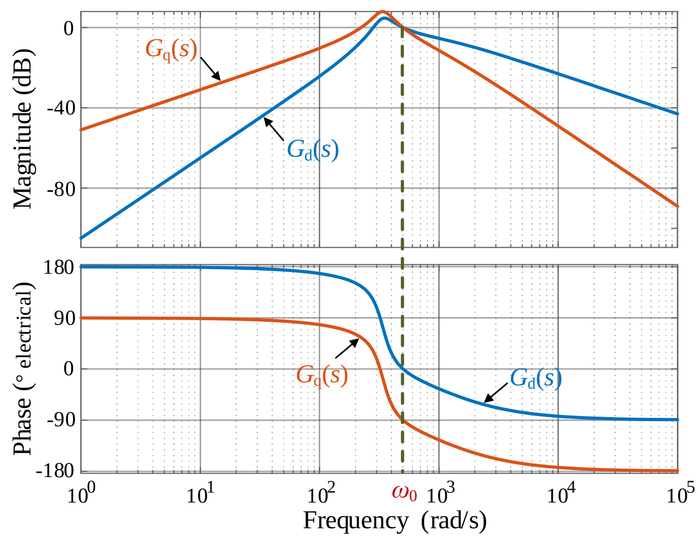

Figure 6.4 Bode diagram of the SOGI-HPF.

In (6.10), both of the output signals keep the same magnitude of $u(t)$ at the resonance frequency ω_0. The direct-axis output $y_d(t)$ has the same phase of the input $u(t)$ at ω_0, while a quadrature signal $y_q(t)$ with a -90° (in electrical) phase shift is generated by $G_q(s)$.

As observed, the SOGI-HPF can extract a frequency-selected signal at ω_0 with its quadrature form, while suppressing the DC offset and harmonics by the bandpass filtering capability. Therefore, the SOGI-HPF satisfies the requirements of the proposed flux estimator design and can be used to solve the previous two critical issues analyzed in Section 6.2.2.

6.3.2 Overall Design of the Proposed Position Estimator

The proposed position estimation method based on QFEs (quadrature flux estimators) is upgraded from the classic SOGI-HPF. The overall signal processing is shown in Figure 6.5, where a three-phase 12/8 SRM is studied as an example to illustrate the proposed scheme.

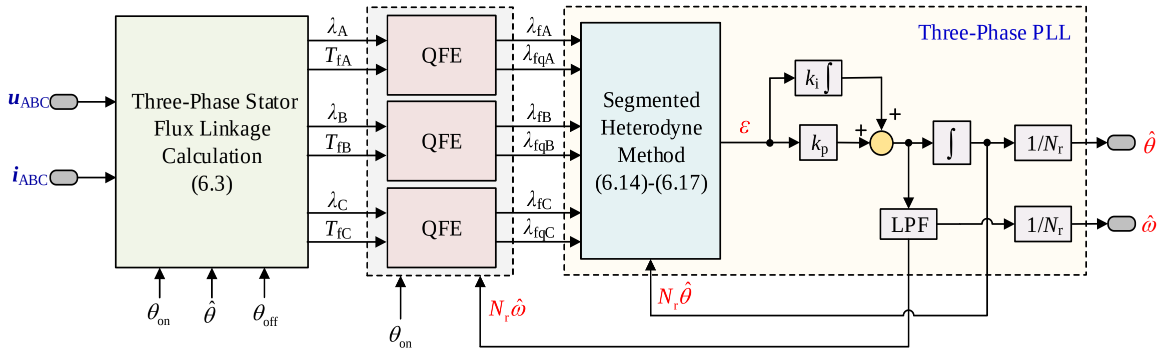

Figure 6.5 Signal processing of the proposed position estimation method based on QFEs.

The stator flux linkage $\lambda_{A,B,C}$ are calculated by the voltage equation in (6.3) in the three phases. Triger signals are enabled when the flux linkage is calculated in the phase conduction period [θ_{on}, θ_{off}], which will be used for the QFE design. Three QFEs developed from the classic SOGI-HPF work together to eliminate the DC offset and harmonics in the real-time flux linkage and generate orthogonal flux signals $\lambda_{fA,B,C}$ and $\lambda_{fqA,B,C}$. Afterward, a segmented heterodyne method in a three-phase PLL is proposed to obtain the position tracking error signal ε. The rotor position and speed can be estimated when the position tracking error ε converges to zero via the PI controller. To adapt the speed variation when the SRM operates, the estimated electrical speed $N_r\hat{\omega}$ is used as the feedback to the three QFEs for adaptive flux estimation.

6.3.3 Design of the QFE

The design of the QFE used for flux estimation is illustrated in Figure 6.6. Since the QFE is adopted for all phases, the variable subscript A, B, or C is omitted when introducing the QFE's design. As shown from Figure 6.6, the calculated flux linkage λ in one phase is set as the input of the QFE, and the outputs are the fundamental flux λ_f and its quadrature λ_{fq}.

The conventional SOGI-HPF is used for a continuous input signal, but it is not suitable for SRM position estimation since the calculated flux linkage is discontinuous, as expressed in (6.3). As an upgrade, the proposed QFE has a specific logic design. Two integrators in the QFE are modified with a reset and a rising-edge trigger according to the trigger signal T_f and initial states λ_{f0} and λ_{fq0}. This modification is made to enable the QFE only when the calculated flux linkage is non-zero. Besides, a magnitude latch with a falling-edge trigger is employed in the QFE to obtain the initial states of the integrators.

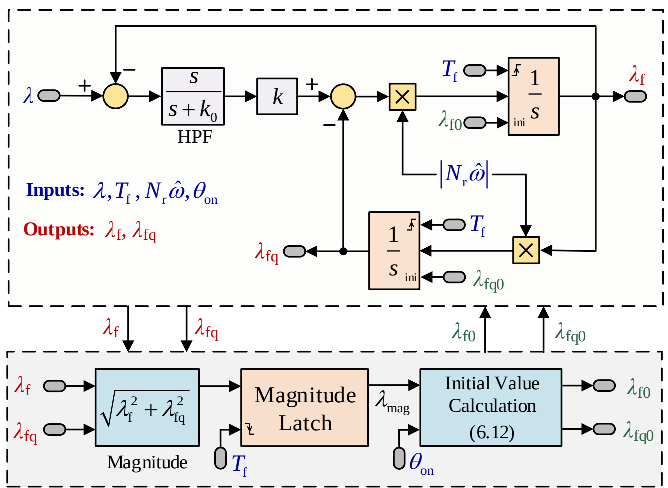

Figure 6.6 Design of the proposed QFE.

According to the Bode diagram shown in Figure 6.4, the proposed QFE is a bandpass estimator for both λ_f and λ_{fq}. To extract the fundamental flux without DC offset and high-order harmonics, the resonance frequency ω_0 of the QFE should be equal to the estimated rotor frequency $|N_r\hat{\omega}|$ of the SRM. The absolute value of the speed ensures position estimation in both speed directions. This subsection discusses the positive speed case first, and the negative speed operation needs minor modification and will be discussed later.

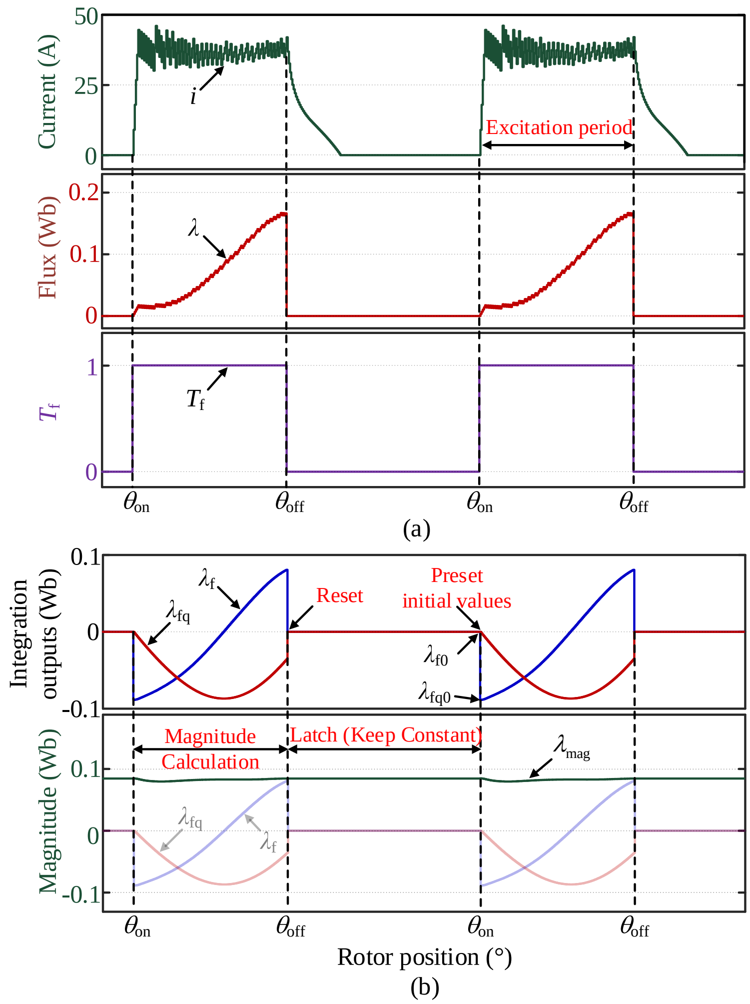

Figure 6.7 Illustration of the logic design of the proposed QFE.

To better illustrate the proposed logic design, the phase current, the trigger signal T_f, and the calculated flux linkage of the SRM with a 15 N·m load are depicted in Figure 6.7. The turn-on and turn-off angles of the SRM are set to 0° and 20°, respectively, as an example. As shown in Figure 6.7(a), the phase is excited between the position [θ_{on}, θ_{off}], and a trigger signal T_f is generated during the excitation period and then reset to zero when the position is out of the range [θ_{on}, θ_{off}]. The calculated flux linkage λ in one phase is discontinuous over an electrical cycle as it will be set to zero when the trigger T_f is null. After the phase is excited again, the flux linkage can be reobtained. Therefore, to estimate the rotor position from the flux linkage, the proposed QFE needs to be enabled only during the phase excitation period (i.e., when the trigger T_f=1), while being disabled when the phase is turned off (i.e., T_f=0).

The logic control in the QFE is realized by modifying the two integrators for the outputs λ_f and λ_{fq}. As illustrated in Figure 6.7(b), the flux integrators are trigged when T_f has a rising edge, namely when the phase is turned on at the position of θ_{on}. The QFE will start estimating the fundamental flux λ_f and quadrature flux λ_{fq} according to its input flux λ. Due to the suppression capability to the DC offset and flux harmonics, the estimated flux λ_f and λ_{fq} shown in the figure are purely cosine and sine functions of the rotor position. The expression of the estimated flux is repeatedly here for readability:

$$\begin{cases} \lambda_{\mathrm{f}} = -\lambda_{\mathrm{mag}} \cos(N_{\mathrm{r}}\theta) \\ \lambda_{\mathrm{fq}} = -\lambda_{\mathrm{mag}} \sin(N_{\mathrm{r}}\theta) \end{cases}. \tag{6.11}$$

According to (6.11), the initial values of the λ_f and λ_{fq} around the turn-on position θ_{on}, can be calculated as

$$\begin{cases} \lambda_{\mathrm{f0}} = -\lambda_{\mathrm{mag}} \cos(N_{\mathrm{r}}\theta_{\mathrm{on}}) \\ \lambda_{\mathrm{fq0}} = -\lambda_{\mathrm{mag}} \sin(N_{\mathrm{r}}\theta_{\mathrm{on}}) \end{cases}. \tag{6.12}$$

From (6.12), the initial values of the two integrators at θ_{on} would be non-zero. To accelerate the convergence rate of the QFE, the initial states of the two integrators should be preset to λ_{f0} and λ_{fq0} when the T_f has the rising edge.

As given in the initial flux values (6.12), the magnitude λ_{mag} of the fundamental flux should be first known. The magnitude can be calculated by the square-root of the λ_f and λ_{fq}, as expressed in (6.13). However, due to the discontinuous flux calculation, the magnitude estimation is also interrupted. Therefore, another logic design is needed to obtain a smooth magnitude, as illustrated in Figure 6.7(b). The magnitude calculation is enabled during the excitation period (T_f =1), while its value is latched when T_f =0 (i.e, at θ_{off}). The latched magnitude will be used to calculate (6.12) and preset the initial flux integrator's values when the next rising edge of T_f is detected.

$$\begin{cases} \lambda_{mag} = \sqrt{\lambda_f^{\,2} + \lambda_{fq}^{\,2}},\ (T_f = 1) \\ \lambda_{mag}\ \text{keeps constant},\ (T_f = 0) \end{cases} \tag{6.13}$$

After the phase execution ends, the stator flux λ is set to zero, and the QFE needs to be disabled. It can be achieved by resetting the two integrators to zero when T_f =0, as illustrated in Figure 6.7(b).

To illustrate clearly, the overall logic design of the proposed QFE in one electrical is concluded as a flow chart shown in Figure 6.8. First, the trigger T_f is generated when the phase turns on at θ_{on} and reset to zero after θ_{off}. By monitoring a rising edge of T_f, initial values λ_{f0} and λ_{fq0} of the two integrators in the QFE are calculated and preset to avoid unnecessary convergence time in flux estimation. After T_f =1, the stator flux λ is calculated by the voltage equation, and the QFE starts estimating the fundamental flux λ_f and its quadrature λ_{fq}. Meanwhile, the magnitude of the fundamental flux is obtained by the square-root calculation. When the phase excitation is over (T_f =0), all the flux calculation λ, λ_f, and λ_{fq} are reset to zero. Only the magnitude calculation is stored in a latch as a constant value for initial value calculation of the integrators when the next rising edge of T_f comes.

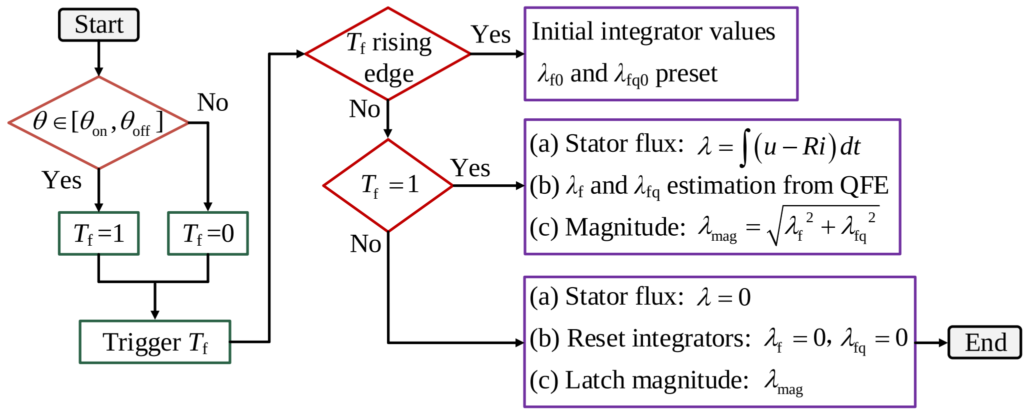

Figure 6.8 Flow chart of the logic design of the QFE in one electrical cycle.

In summary, the proposed logical design is able to guarantee that the QFE is only enabled during the phase excitation period, in which the position information can be extracted from the non-zero flux linkage. While the magnitude latch and initial integrator preset can link the flux estimation in the excitation cycles before and after, ensuring good transient estimation accuracy during SRM operation.

6.3.4 Design of the Three-Phase PLL

The fundamental flux λ_f and its quadrature λ_{fq} obtained from the QFE can then be used to estimate the rotor position and speed through a three-phase PLL.

Since at least one phase is turned on during SRM operation, combining all-phase flux estimation from the QFEs can obtain the full-cycle rotor position, as depicted in Figure 6.9. In this section, a segmented heterodyne method is proposed to extract the rotor position information from the three-phase estimated flux linkage.

According to the phase conduction sequence, three areas are divided for the proposed segmented design. When the phase-A is excited, shown as Area-A in Figure 6.9(b), a pair

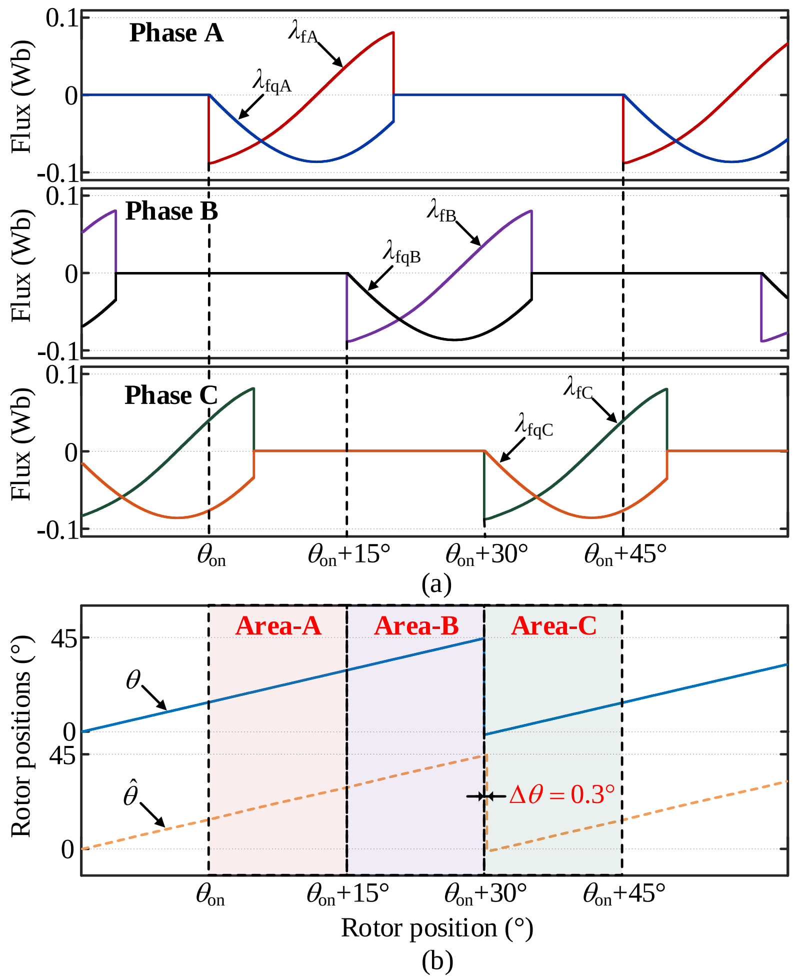

Figure 6.9 Full-cycle position estimation by combining the three-phase QFE's outputs.

of orthogonal flux signals λ_{fA} and λ_{fqA} can be used to obtain the phase-A position tracking error ε_A. Same as the conventional PLL analyzed in (6.7), the magnitude amplitude is adopted here, which derives:

$$\varepsilon_A = \frac{-\lambda_{fqA}\cos(N_r\hat{\theta}) + \lambda_{fA}\sin(N_r\hat{\theta})}{\sqrt{\lambda_{fA}{}^2 + \lambda_{fqA}{}^2}} \tag{6.14}$$

When the phase-B is turned on, as shown in Area-B, the calculation of the position tracking error ε_B can be done on the phase-B flux estimation by considering a $2\pi/3$ phase shift to phase A, as

$$\varepsilon_{\mathrm{B}} = \frac{-\lambda_{\mathrm{fqB}} \cos(N_{\mathrm{r}}\hat{\theta} - 2\pi/3) + \lambda_{\mathrm{fB}} \sin(N_{\mathrm{r}}\hat{\theta} - 2\pi/3)}{\sqrt{\lambda_{\mathrm{fB}}^{2} + \lambda_{\mathrm{fqB}}^{2}}} \tag{6.15}$$

Similarly, the calculation in Area-C can be done by the phase-C flux estimation:

$$\varepsilon_{\mathrm{C}} = \frac{-\lambda_{\mathrm{fqC}} \cos(N_{\mathrm{r}}\hat{\theta} + 2\pi/3) + \lambda_{\mathrm{fC}} \sin(N_{\mathrm{r}}\hat{\theta} + 2\pi/3)}{\sqrt{\lambda_{\mathrm{fC}}^{2} + \lambda_{\mathrm{fqC}}^{2}}} \tag{6.16}$$

Then, the position tracking error ε used for the PLL can be obtained by combining the above three tracking errors according, as:

$$\begin{cases} \varepsilon = \varepsilon_{\mathrm{A}},\ \hat{\theta} \in \left[\theta_{\mathrm{on}}, \theta_{\mathrm{on}} + 15°\right] \\ \varepsilon = \varepsilon_{\mathrm{B}},\ \hat{\theta} \in \left[\theta_{\mathrm{on}} + 15°, \theta_{\mathrm{on}} + 30°\right] \\ \varepsilon = \varepsilon_{\mathrm{C}},\ \hat{\theta} \in \left[\theta_{\mathrm{on}} + 30°, \theta_{\mathrm{on}} + 45°\right] \end{cases} \tag{6.17}$$

It is notable that when two phases overlap, the flux linkage of both phases can be used for position estimation. The calculation in (6.17) is given as an option.

Afterward, a PLL is used to converge the position tracking error ε to estimate the rotor position and speed, as shown previously in Figure 6.5. The simulation result of the position estimation under the 15 N·m load is given in Figure 6.9(b). Even though no magnet characteristics are used, the estimated rotor position obtained from the proposed scheme can match the actual position, with only 0.3° position errors.

6.3.5 Design for Generating Sensorless Operation

The chapter introduces the proposed approach in a view of SRM motoring operation, while the method can also work for generating operation with minor modifications.

According to the analysis in (6.2) and (6.3), the flux linkage needs to be calculated around a constant current level. For the motoring operation, the constant current region overlaps to the phase excitation period [θ_{on}, θ_{off}] approximately, as shown in Figure 6.7(a), since the phase current can be fast established at the turn-on instant θ_{on} (θ_{on} is around the low-inductance region depicted in Figure 6.10. However, the case is different for the generating mode.

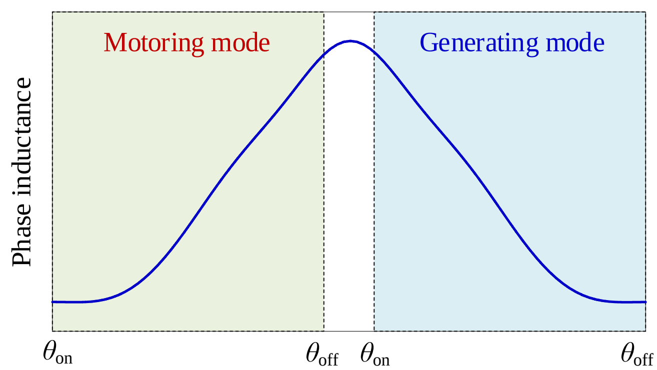

Figure 6.10 Commutation angle settings of the motoring mode and generating mode.

To generate a negative torque, the turn-on and turn-off instants should be lagged, and the phase often turns on in a large-inductance region, as presented in Figure 6.10. Therefore, the phase current increases slowly compared to the motoring mode, and the constant current region does not overlap to the phase excitation period [θ_{on}, θ_{off}], as shown in Figure 6.11. To avoid position estimation errors of the proposed scheme, the flux linkage calculation in the generating mode should be modified in a constant region as well. The flux linkage can be calculated by (6.18) in [θ_{ref}, θ_{off}], and the trigger signal T_f is set accordingly to enable the proposed QFE.

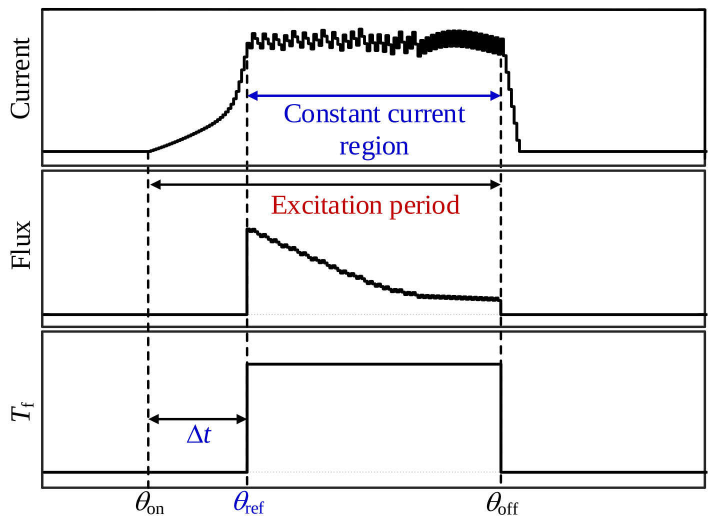

Figure 6.11 Illustration of the proposed method in the generating mode.

$$\lambda(\theta,i)=\begin{cases}\int(u-Ri)\,dt, & (\theta\in[\theta_{ref},\theta_{off}])\\ 0, & (\theta\in\text{else})\end{cases}. \tag{6.18}$$

The angle θ_{ref} can be calculated by counting the time interval Δt from the turn-on instant θ_{on} to the instant when the current reaches the constant value (such as reference):

$$\theta_{ref}=\theta_{on}+\hat{\omega}\Delta t\,. \tag{6.19}$$

Then, the initial values of the λ_f and λ_{fq} used in the proposed QFE, as expressed in (6.12) are changed accordingly in the generating mode, as

$$\begin{cases}\lambda_{f0}=-\lambda_{mag}\cos(N_r\theta_{ref})\\ \lambda_{fq0}=-\lambda_{mag}\sin(N_r\theta_{ref})\end{cases}. \tag{6.20}$$

Other signal processing keeps the same for both the motoring and generating modes.

6.3.6 Design for Negative-Speed Sensorless Operation

The previous analyses on position observer design focuses on positive-speed operation. At negative speed, minor changes are needed.

First, the negative speed changes the sign of the initial flux linkage calculation (6.12) and the PLL design (6.14)-(6.16) in the quadrant axis, which can be modified as

$$\begin{cases} \lambda_{\text{f0}} = -\lambda_{\text{mag}} \cos(N_{\text{r}}\theta_{\text{off}}) \\ \lambda_{\text{fq0}} = \lambda_{\text{mag}} \sin(N_{\text{r}}\theta_{\text{off}}) \end{cases} \tag{6.21}$$

$$\varepsilon_{\text{A}} = \frac{\lambda_{\text{fqA}} \cos(N_{\text{r}}\hat{\theta}) + \lambda_{\text{fA}} \sin(N_{\text{r}}\hat{\theta})}{\sqrt{\lambda_{\text{fA}}{}^2 + \lambda_{\text{fqA}}{}^2}} \tag{6.22}$$

$$\varepsilon_{\text{B}} = \frac{\lambda_{\text{fqB}} \cos(N_{\text{r}}\hat{\theta} - 2\pi/3) + \lambda_{\text{fB}} \sin(N_{\text{r}}\hat{\theta} - 2\pi/3)}{\sqrt{\lambda_{\text{fB}}{}^2 + \lambda_{\text{fqB}}{}^2}} \tag{6.23}$$

$$\varepsilon_{\text{C}} = \frac{\lambda_{\text{fqC}} \cos(N_{\text{r}}\hat{\theta} + 2\pi/3) + \lambda_{\text{fC}} \sin(N_{\text{r}}\hat{\theta} + 2\pi/3)}{\sqrt{\lambda_{\text{fC}}{}^2 + \lambda_{\text{fqC}}{}^2}}. \tag{6.24}$$

Second, when the speed is negative, the position decreases, and the phase conducts at the turn-off angle θ_{off} designed in the motoring mode and idles at the previous turn-on angle θ_{on}. Therefore, the initial flux linkage calculation in (6.21) utilizes the turn-off angle θ_{off}.

Besides, when the motor runs at motoring mode and negative speed, the phase is excited in the large inductance region and ended in the low inductance region. The same phenomenon as the generating mode with positive speed occurs, as shown in Figure 6.11. Hence, the initial angle needs modification as (6.19). Other quadrant cases can be analyzed in the same way.

6.3.7 Selection of Discretization Methods

To implement the proposed observer in the digital system, discretization is needed. Four typical discretization methods are compared, as summarized in Table 6.1.

Table 6.1 Four Discretization Methods

Methods	Implementation	Methods	Implementation
Forward Euler	$s=\frac{z-1}{T_s}$	Tustin	$s=\frac{2}{T_s}\frac{z-1}{z+1}$
Backward Euler	$s=\frac{z-1}{zT_s}$	Pre-warping Tustin	$s=\frac{\omega_0}{\tan\left(0.5\omega_0 T_s\right)}\frac{z-1}{z+1}$

According to the Bode diagram of the SOGI-HPF shown in Figure 6.7, the phases of the fundamental and quadrature flux estimators at the central frequency ω_0 should be 0° and -90°, respectively, for accurate position estimation. Hence, the discretization method can be determined by selecting the one having the lowest phase error in the discrete system.

Figure 6.12 shows the phases of the two flux estimators at the central frequency ω_0 when using different control frequencies. ω_0 is set as 837.76 rad/s (i.e., 133.3 Hz, rated speed). As can be observed, both the Forward Euler and Backward Euler methods have large phase errors of the flux estimator. The phases of the fundamental estimator and the quadrature estimator at ω_0 deviates from 0° and 90° respectively when the control frequency is lower, thereby resulting in position estimation errors. For the Tustin method, also known as Bilinear method, the phase deviation can be reduced a lot at low control frequencies, and the phase errors are almost zero when the control frequency is larger than 6 kHz for both the two flux estimators. Typically, the industrial SRM drive adopts more than 10 kHz control frequency for better current control performance. Therefore, the Tustin method can ensure accurate position estimation of the proposed observer in most cases. Moreover, for an ultra-high-speed SRM drive, the ratio between the control frequency and the electrical rotor frequency is reduced, so an advanced discretization method called pre-warping

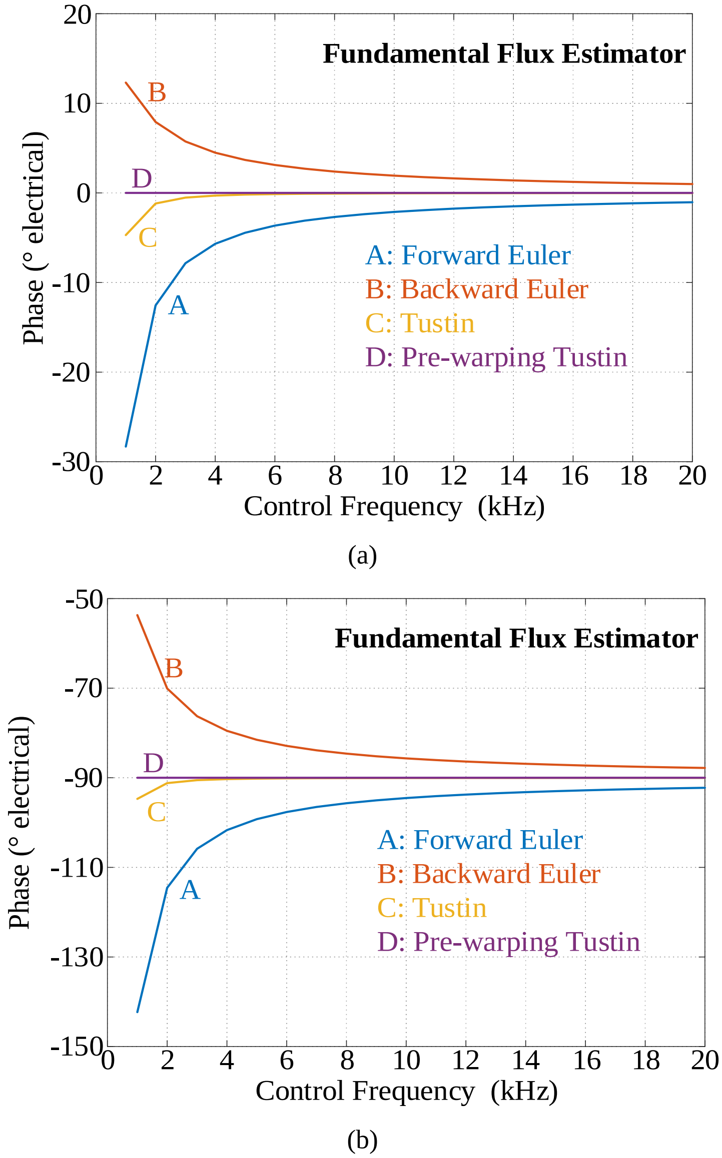

Figure 6.12 Flux estimators' phases at ω_0 with different control frequencies when using four discretization schemes (ω_0 =837.76 rad/s, i.e., 133.3 Hz and rated speed). (a) Fundamental flux estimator. (b) Quadrature flux estimator.

Tustin can be used for exact discretization implementation. As shown from the results, even with a low control frequency, the proposed observer has no phase errors in flux linkage estimation, which provides accurate position estimation regardless of the control frequency. Similarly, the pre-warping Tustin method can also be used for a high-power SRM drive of which control frequency is often low for switching loss reduction. Note that the ω_0 used in the pre-warping Tustin method can be set as the estimated rotor frequency $N_{\mathrm{r}}\hat{\omega}$ from the proposed observer.

In consequence, the control frequency would have limited influence on the proposed observer by using a Tustin method or pre-warping Tustin method for digital implementation. This chapter adopts a Tustin method for simplicity. For better universality, pre-warping Tustin method would be suggested.

6.4 Experimental Validation

The proposed position estimation scheme is validated experimentally on a 5.5 kW three-phase 12/8 SRM setup. The overall control diagram of the proposed position-sensorless control scheme is shown in Figure 6.13. The speed and current controller are the same as before. The rotor position and speed are estimated from the proposed QFE-based position estimator. Notably, the DSP shadow register causes one control period delay between the command gate signal and the actual gate signal. Hence, the estimated rotor position used l is advanced by one control period, i.e., $\hat{\theta}+T_{\mathrm{s}}\hat{\omega}$. This scheme can also be added in the NSO-based position estimation. Without specific mention, the phase commutation angles are set to be constants of 0° and 20° for simplicity. To implement the proposed method in the digital system, the Tustin method $s=2(z-1)/[T_{\mathrm{s}}(z+1)]$ is used to discretize the observer due to its high discretization accuracy. All experimental results are measured in the position-sensorless control mode.

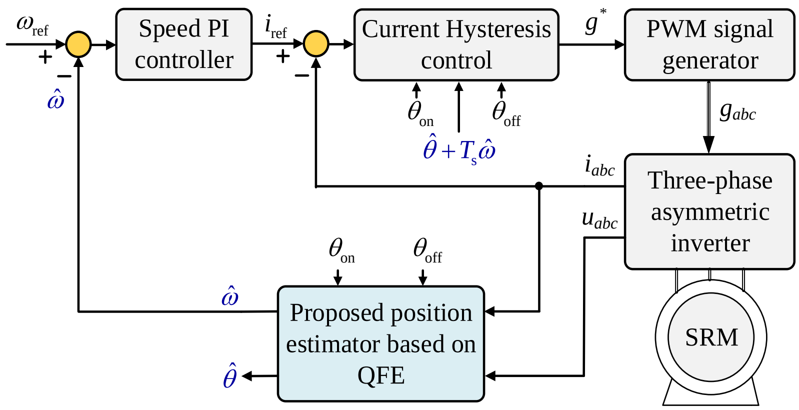

Figure 6.13 The overall control diagram of the proposed position-sensorless control.

Regarding the parameter selection, the tunable parameter k in the QFE relates to the bandwidth of the bandpass characteristic. A suggested value in literature is k=1.414 that gives good trade-off between the response rate and harmonic rejection capability [111]. The cutoff frequency k_0 of the HPF in the QFE can be set higher to avoid dynamic degradation, and k_0=500 rad/s is selected in this method. The PI parameters of the three-phase PLL can be tuned by adjusting the PLL's bandwidth ω_{PLL}, where $k_p=2\omega_{PLL}$ and $k_i=\omega_{PLL}^2$. The parameter design is based on pole placement of the PLL's transfer function, and the details can be found in [61]. In this method, the ω_{PLL} is chosen as 250 rad/s.

Figure 6.14 shows the experimental results of the three-phase current, calculated stator flux, and trigger signals, at 500 r/min with the 15 N·m load. The stator flux $\lambda_{A,B,C}$ are obtained from the voltage equation during the phase excitation period and then set to zero when the phase goes to the freewheeling. Meanwhile, trigger signals $T_{fA,B,C}$ in the three phases are generated when the stator flux is obtained, which will be used for the proposed QFE for flux estimation.

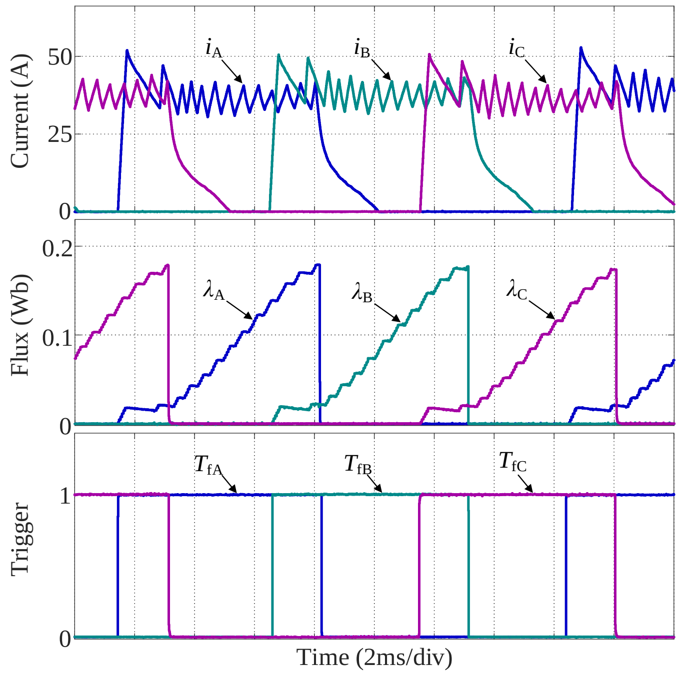

Figure 6.14 Experimental results of three-phase phase current, calculated stator flux, and trigger signals at 500 r/min.

As analyzed before, the QFEs in three phases will start estimating the fundamental flux $\lambda_{fA,B,C}$ and its quadrature $\lambda_{fqA,B,C}$ from the calculated stator flux when $T_{fA,B,C}$=1. Experimental results of the estimated fundamental flux at 500 r/min and the 15 N·m load are shown in Figure 6.15. As observed, experimental estimation results have a good agreement with the simulation shown in Figure 6.9. The DC component in the stator flux is eliminated, and the $\lambda_{fA,B,C}$ and $\lambda_{fqA,B,C}$ are smooth cosine and sine functions, respectively, which proves good harmonic reduction capability of the proposed QFE. A 90° phase shift can also be found in the quadrature flux $\lambda_{fqA,B,C}$ compared to the fundamental flux $\lambda_{fA,B,C}$. Moreover, the magnitude $\lambda_{magA,B,C}$ of the flux estimation is calculated through the square-root calculation given in (6.13) during the phase excitation period. When the flux estimation is disabled, both the estimated fundamental flux and its quadrature are reset to zero.

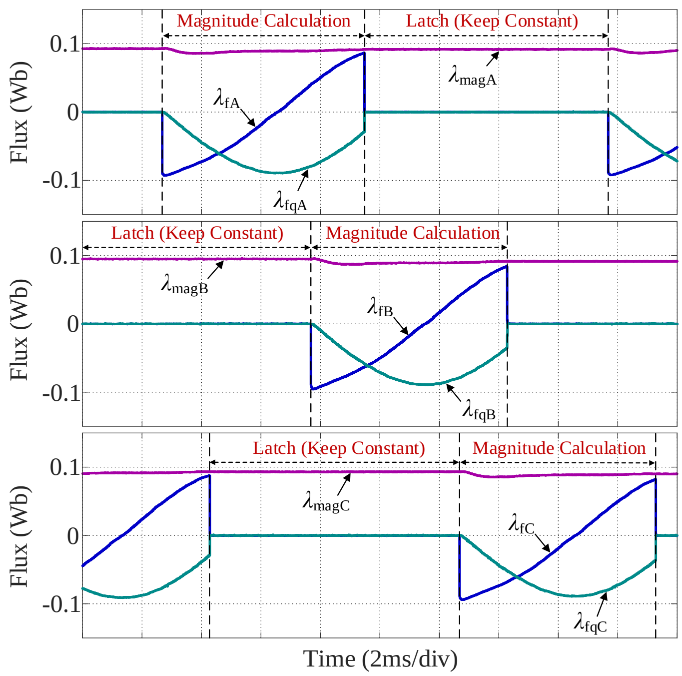

Figure 6.15 Experimental results of proposed Flux estimation from QFEs at 500 r/min.

Meanwhile, the calculated flux magnitude $\lambda_{magA,B,C}$ is latched and keeps constant, which will be used to calculate the initial values of the QFE integrators, as expressed in (6.12).

Afterward, the rotor position can be estimated from the three-phase fundamental flux using the three-phase PLL. The position estimation results of the proposed scheme under a 15 N·m load at 500 r/min are depicted in Figure 6.16(a). It can be seen that the estimated rotor position can well match the actual position measured by a resolver. The position error of the proposed scheme is around 1.4°. The experimental position error slightly differs from the simulation result since the simulation model is ideal. Some nonideal factors, such as SRM geometric asymmetric, magnetic parameter mismatch between the simulation model and the tested machine, and measurement noises, would cause additional estimation errors. Furthermore, to baseline the performance of the proposed scheme, a conventional magnetic

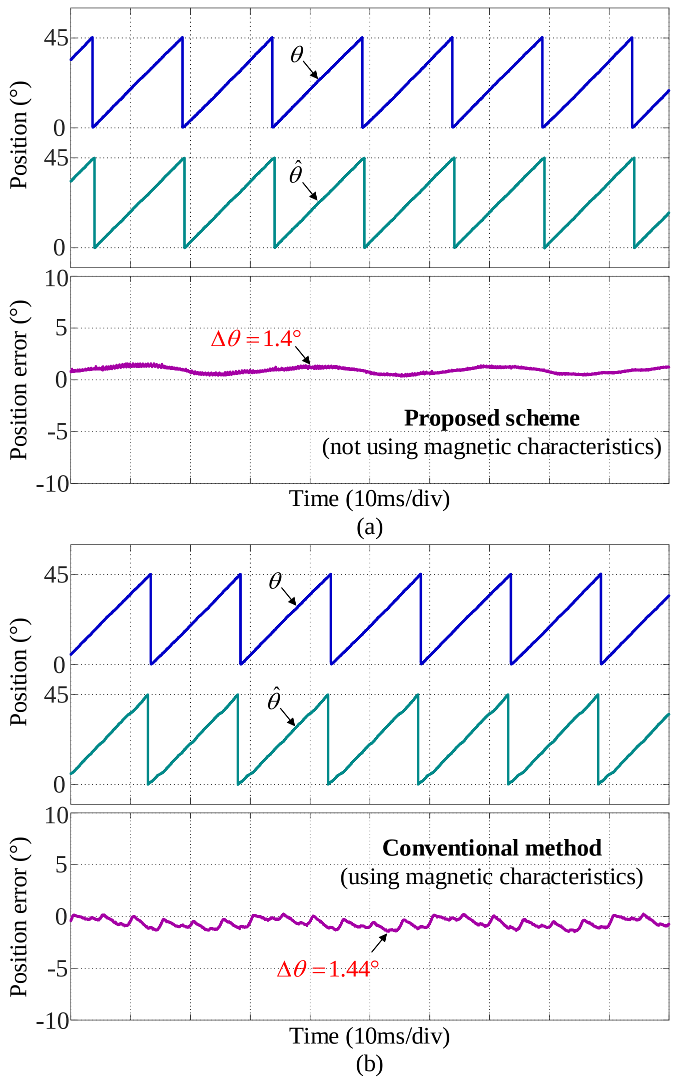

Figure 6.16 Comparative position estimation control results at 500 r/min. (a) Proposed scheme not using magnetic characteristics. (b) Conventional method using magnetic characteristics.

characteristic-based position estimation method proposed in [82] is used for comparison. This traditional scheme adopts a numerical observer based on flux linkage lookup tables and using a PLL for position estimation. The bandwidths of the PLLs used in both the proposed approach and the comparative method are set the same for fair comparisons. As observed from Figure 6.16(b), the maximum absolute position error of the conventional

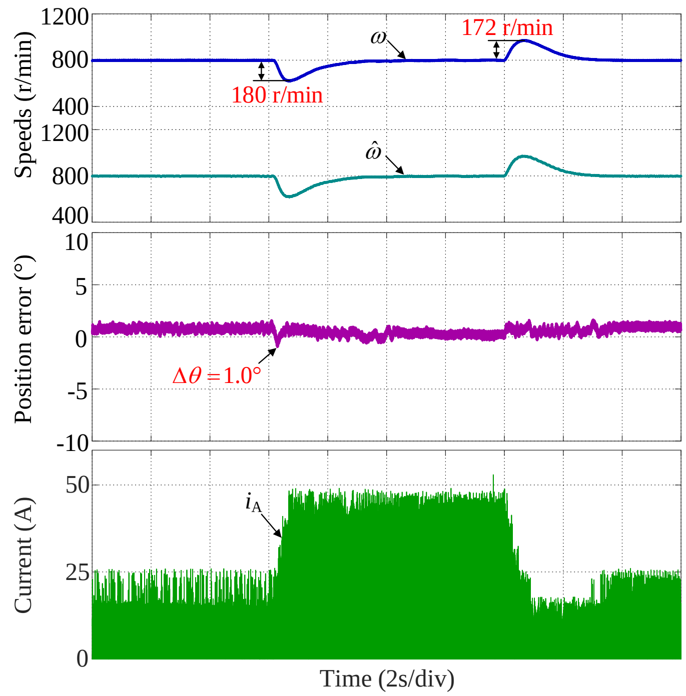

Figure 6.17 Position-sensorless control performance of the proposed scheme under 15 N·m load change at 800 r/min.

scheme at 500 r/min is 1.44°, which is almost the same as the proposed scheme. In summary, the proposed scheme can achieve the same estimation accuracy compared to the conventional method, while no magnetic characteristics are required for position estimation. This improvement avoids time-consuming offline parameter measurement and improves the generality of the sensorless control algorithms.

Figure 6.17 depicts the estimation accuracy of the proposed scheme under a 15 N·m load disturbance. The speed estimation, the position estimation error, and the phase-A current are shown. The SRM is first run at 800 r/min without load, and then a 15 N·m load generated by the IM are added to the shaft. At this instant, the rotor speed decreases by 180 r/min but can converge to its reference value due to the speed regulator. The position estimation has good accuracy as the transient position error is 1° at the load increasing instant. The rotor speed can be well estimated and track the speed variation. Afterward, the 15 N·m load is removed, and the speed increases by 172 r/min and then comes back to 800 r/min. The experimental result also proves that the magnetic saturation effect, which becomes deeper at heavier load conditions, has no effects on the proposed position estimation scheme. It is due to the DC component and harmonic rejection capability of the QFE. Accordingly, robust sensorless control under load variable can be guaranteed by the proposed sensorless control algorithm even though no magnetic characteristics of the SRM are used.

The position-sensorless control performance under speed transient conditions is also validated, as shown in Figure 6.18. Figure 6.18(a) validates the position and speed estimation results when a slope reference speed from 500 r/min to 1000 r/min is given. During the speed variation, the estimated speed can track the actual speed measured by a resolver, and the overall position estimation error is less than 1.8°. To validate the sensorless control performance with faster speed changes, a step speed command is given, and the estimation results are presented in Figure 6.18(b). As can be observed, the estimated speed can still well track the actual rotor speed in such fast speed transient state. The maximum rotor position estimation error increases temporarily to 2.3° at the rapid speed transition instant, while the sensorless SRM drive can work stably and track the fast speed response.

The previous validation tests use simply fixed commutation angles, θ_{on}=0° and θ_{off}=20°, for current hysteresis control, while the commutation angles and current references can be adjusted to achieve better control performance. To prove the flexibility of the proposed position estimation scheme, a comparative experimental test between the

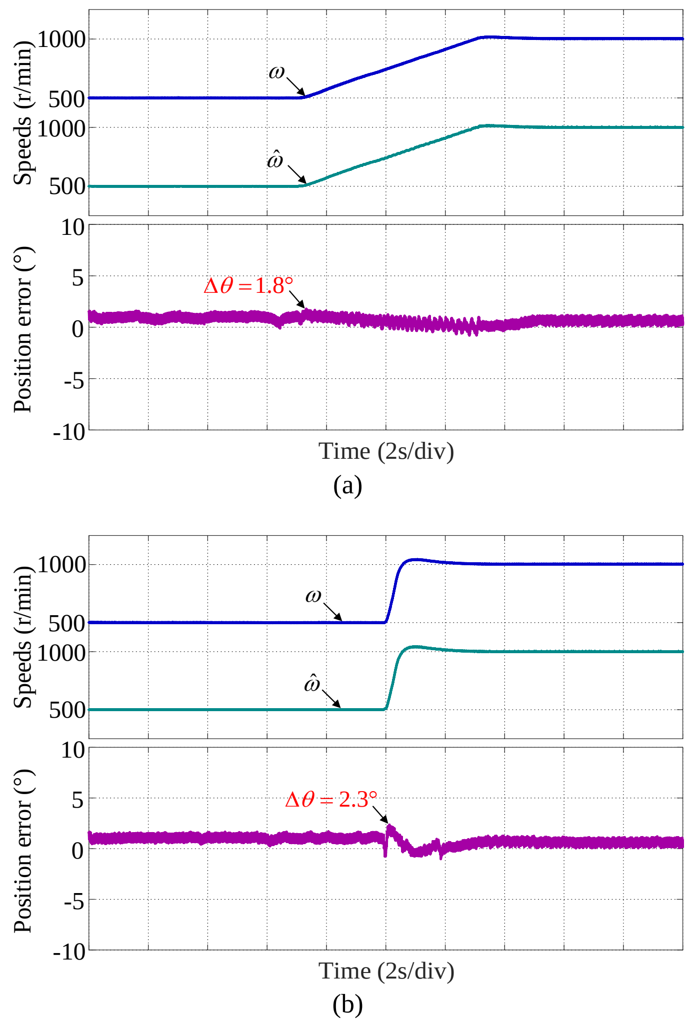

Figure 6.18 Position-sensorless control performance of the proposed scheme under speed changes from 500 r/min to 1000 r/min: (a) Slope speed command. (b) Step speed command.

conventional current control method and an advanced offline torque sharing function method [113] is given, as presented in Figure 6.19. Figure 6.19(a) shows the three-phase current, total torque, and position estimation results of the proposed position estimation method, when using the fixed commutation angles for current control. The SRM runs around 500 r/min with a 15 N·m load. The torque is calculated using the torque characteristic for better accuracy, instead of torque transducer measurement.

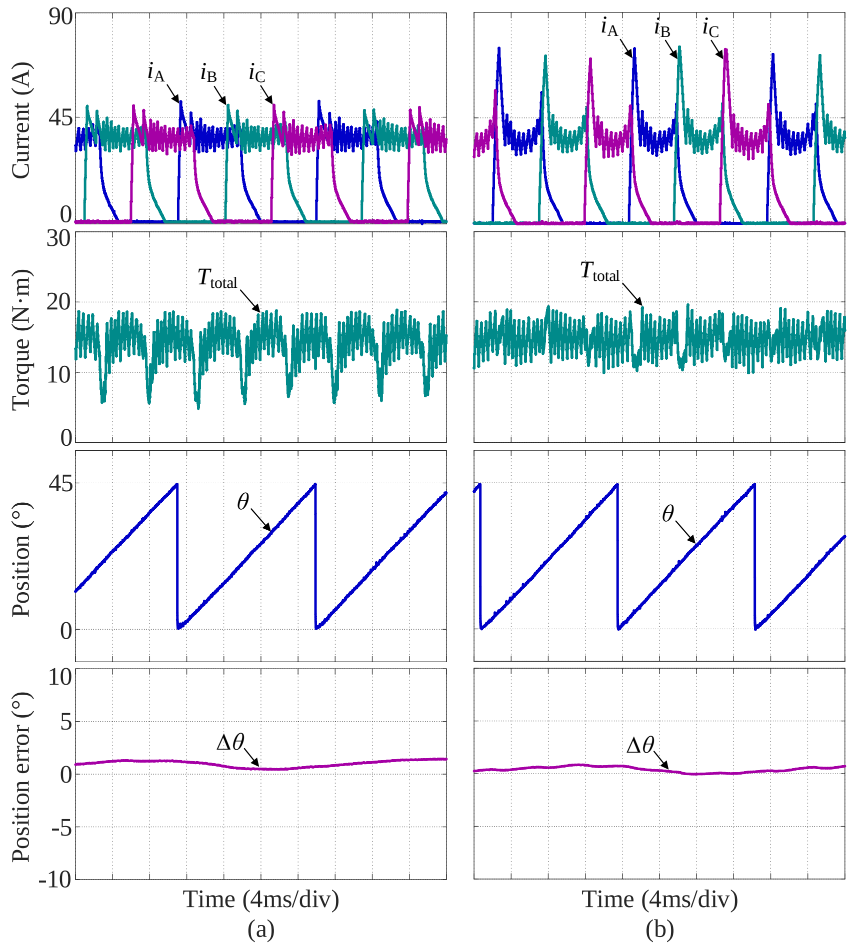

Figure 6.19 Position-sensorless control performance at 500 r/min with 15 N·m load. (a) Using fixed commutation angles (θ_{on}=0° and θ_{off}=20°). (b) Using optimized torque sharing function method.

As can be seen, the rotor position is accurately sensed, but large torque ripples occur when the two phase commutates. To reduce the torque ripple, the advanced offline sharing function scheme can be combined with the proposed sensorless control method, and the result is shown in Figure 6.19(b). In this case, the current reference trajectory is optimized, and the commutation angles are θ_{on}=3.625° and θ_{off}=19.49°. It can be observed that the phase current is larger during phase commutation, and the torque ripples can be reduced a

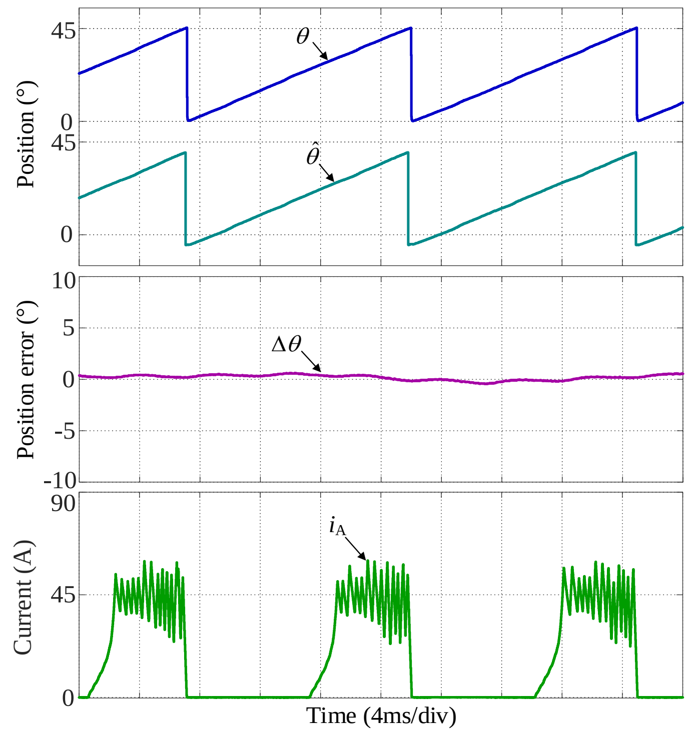

Figure 6.20 Position-sensorless control result in the generating mode at 500 r/min with -15 N·m load.

lot compared to the fixed-angle method, which demonstrates the better control performance. Meanwhile, the position estimation is still accurate, and the sensorless SRM drive can operate stably when the torque sharing function is adopted. There are some torque ripples caused by the current hysteresis control. It can be further reduced by enhanced PWM control [114]. Notably, this offline sharing function needs magnetic characteristics. This test mainly validates the adaption capability of the sensorless control to different current/torque control schemes. Magnetic-characteristic-free torque sharing function design is promising but out of the scope of the thesis.

Besides the position-sensorless control performance in the motoring mode, the proposed scheme is also validated in the generating mode. Figure 6.20 shows the position estimation results when the rotor speed is around 500 r/min and the torque is -15 N·m. Since the torque direction of the SRM depends on the rotor position, the negative torque can be generated by setting the commutation angles to θ_{on}=25° and θ_{off}=45° (in the negative torque region). From the experimental result, the estimated rotor position can track the actual position, and the position estimation error is almost around zero in the generating-mode sensorless operation. Therefore, the proposed position-sensorless SRM can operate as a generator for energy regeneration.

The position estimation accuracy when using the actual voltage and the reconstructed voltage for flux linkage calculation is validated, as presented in Figure 6.21. For cost reduction, phase voltage sensors are often not used in the commercial SRM drive, and the voltage feedback can be reconstructed by reference gate signals. Since the SRM drive contains large DC-link voltage ripples, the reconstructed phase voltage deviates from the actual one, as shown in Figure 6.21(a), which would result in DC and harmonic errors in the flux linkage calculation. However, due to the bandpass frequency characteristic of the proposed QFE, the flux distortions could be suppressed. Figure 6.21(b) shows the position estimation error when using the two voltages in the proposed scheme. As can be seen, the estimation accuracy is almost the same, so either the measured voltage or the reconstructed voltage can be adopted in the proposed sensorless control scheme.

The position estimation results when the current measurement is inaccurate are also validated, as presented in Figure 6.22. The SRM also runs around 500 r/min with a 15 N·m load. Figure 6.22(a) shows the position estimation error, the actual one-phase current i_{actual}, and the current feedback used for flux linkage calculation i_{used}. Three conditions are tested

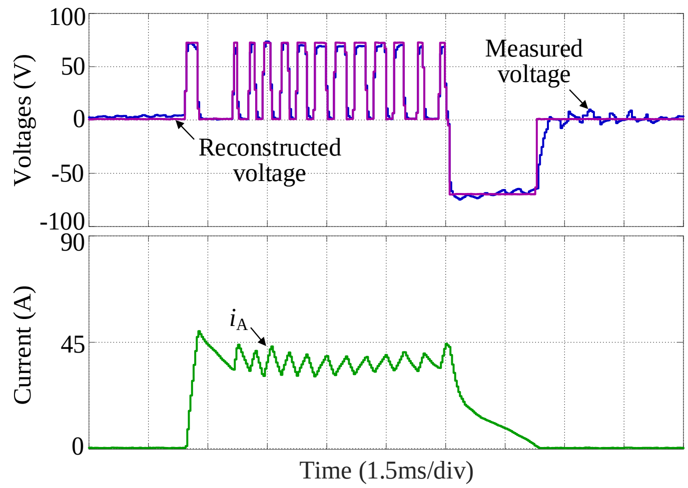

(a)

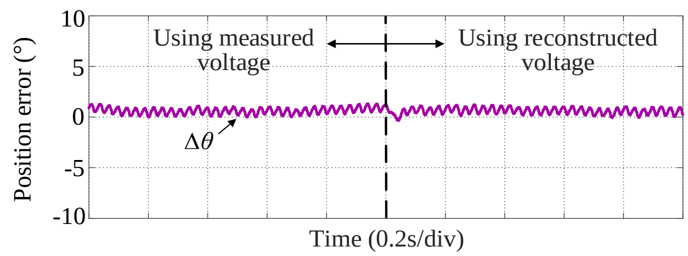

(b)

Figure 6.21 Position estimation results when using different voltages for flux linkage calculation at 500 r/min with 15 N·m load. (a) Voltage comparison. (b) Position estimation error comparison.

to verify the position estimation accuracy: Condition-I: accurate current feedback for flux linkage calculation, i.e., $i_{used}= i_{actual}$; Condition-II: current feedback for flux linkage calculation contains a 10% gain error, i.e., $i_{used}=0.9i_{actual}$; Condition-III: current feedback for flux linkage calculation contains a 10% gain error and a 2 A offset, i.e., $i_{used}=0.9i_{actual}+2$. The zoom-in current waveforms are presented in Figure 6.22(b). As observed, Due to the frequency-selection capability of the QFE, the current errors have limited effects on flux estimation, and the position estimation error keeps the same in the three conditions.

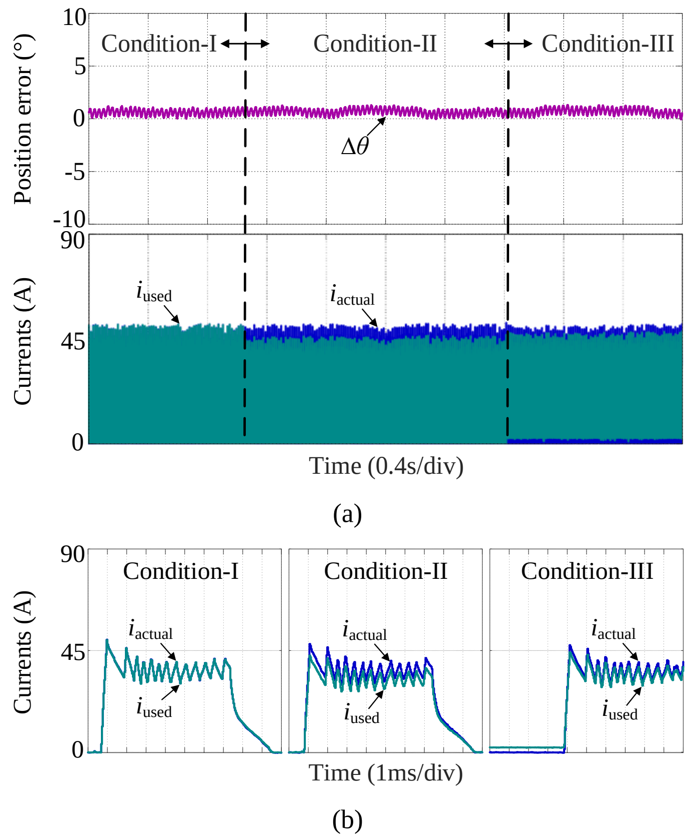

Figure 6.22 Position estimation results with current measurement errors around 500 r/min with 15 N·m load. (Condition-I: accurate current measurement, condition-II: 90% gain error, and condition-III: 90% gain error and 2 A offset). (a) Position estimation error and currents. (b) Zoom-in currents.

6.5 Conclusion

This chapter proposes a new high-speed position-sensorless method for SRM drives without using any magnetic characteristics. A QFE-based position estimator is built to extract position information from the flux linkage while suppressing all DC components and flux harmonics that are highly nonlinear to the rotor position and phase current. A logic design of the QFE is also analyzed in detail. The proposed scheme makes the SRM position estimation simpler as it does not require time-consuming offline measurement or selfcommission process for characteristic calibration. The sensorless control algorithm has better generality over the state-of-art method and is feasible for a general-purpose SRM drive. Experimental validation shows that the proposed scheme can achieve the same estimation accuracy level compared to the conventional magnetic characteristic-based method. Dynamic validation under a variable speed command and load disturbance is also provided to further verify the transient position and speed estimation accuracy.

Chapter 7

Wide-Speed Range Position-Sensorless Control

7.1 Introduction

In this chapter, a wide-speed range position-sensorless control strategy of the SRM drive is introduced. Chapter 3 and 4 discuss the low-speed position estimation methods, and Chapter 5 and 6 analyze the high-speed position estimation schemes. To realize the wide-speed range position-sensorless control, the combination of the low-speed method and the high-speed method is needed. This chapter proposes a simple linear switching function based on the estimated rotor speed to determine the operation range of the two types of position estimation methods. The algorithm switching logic can guarantee smooth transition performance from the low speed to high speed sensorless control. Experimental validations on the 5.5 kW 12/8 SRM test bench is carried out to prove the wide-speed range sensorless operation capability.

7.2 Wide-Speed Range Sensorless Control Algorithm

Position-sensorless control methods of SRMs are divided into two categories, low-speed methods and high-speed methods. The low-speed position estimation is based on high-frequency pulse injection in idle phases. The high-speed position estimation is often based on flux linkage/inductance calculation in conduction phases.

The two position estimation schemes only work well in a specific speed range. For example, the pulse-injection method needs to inject pulse voltages into the idle phase, and the rotor position can be estimated from the induced current. However, the phase current in freewheeling region decreases to zero slowly than the low-speed case. It results in that the width of the idle phase becomes narrower at higher speed due to the increasing back-EMF. In consequence, the pulse injection in three phases cannot cover a complete electrical cycle, thereby not able to estimate the full-cycle rotor position accurately. Moreover, high-frequency voltage pulses cause additional copper losses and torque ripples. Although the proposed TSMC-based injection method can reduce the adverse impact significantly, the model-based approaches not requiring injection is still more attractive for the SRM drive.

For the high-speed method, the flux linkage calculation utilizes a pure integrator and is accurate at high speed due to the larger SNR of the voltage acquisition. The noises in current or voltage feedbacks are considered to be much lower than the back-EMF, which makes the flux linkage calculation easier. Whereas, when the rotor speed decreases to a low value, the phase voltage reduces as well due to the lower back electromotive force. Any current and voltage acquisition offsets and harmonics can cause significant errors in the flux linkage integration at a low speed. These nonideal distortions often come from the current sensors, DC-link voltage ripples, and temperature variation.

In consequence, in order to realize the wide-speed range sensorless control of the SRM, it should combine both the pulse-injection method (for low-speed operation) and the flux-linkage method (for high-speed operation).

To start the motor from standstill to high speeds, the transition between the flux-linage based position observer and the pulse injection method is required. The transition region is designed as shown in Figure 7.1. Two speed bounds are set to determine the position estimation logic. When the absolute speed is larger than the upper bound, the flux-linkage-based method is used for high-speed sensorless control. Between the upper bound and the lower bound, there is a linear switching region in which both the flux-linkage-based method and the injection-based method are used for sensorless control. If the speed is below to the lower bound, only the position estimated by the injection-based estimator is used for sensorless control. The speed bounds can be selected around the medium speed of the SRM, in which both the injection and flux linkage-based methods have good estimation accuracy. Typical selection in literature is around 30% of the rated speed.

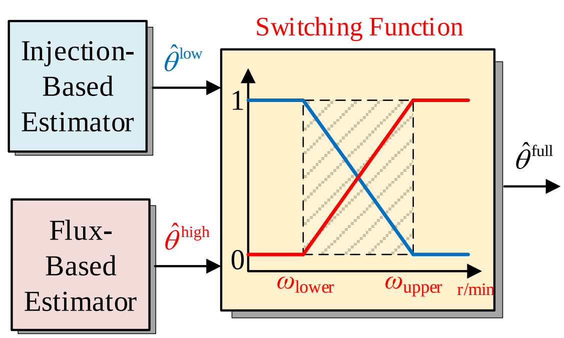

Figure 7.1 Wide-speed range position-sensorless control scheme by combining the flux-linkage-based method at high speed and the injection-based estimator at low speed.

According to Figure 7.1, the switching function is defined as:

$$\hat{\theta}^{\text{full}} = \left[1 - f\left(\hat{\omega}\right)\right]\hat{\theta}^{\text{low}} + f\left(\hat{\omega}\right)\hat{\theta}^{\text{high}} \tag{7.1}$$

where

$$f\left(\hat{\omega}\right) = \begin{cases} 0, & \left|\hat{\omega}\right| < \omega_{\text{lower}} \\ \dfrac{\left|\hat{\omega}\right| - \omega_{\text{lower}}}{\omega_{\text{upper}} - \omega_{\text{lower}}}, & \omega_{\text{lower}} \le \left|\hat{\omega}\right| \le \omega_{\text{upper}} \\ 1, & \left|\hat{\omega}\right| > \omega_{\text{upper}} \end{cases} \tag{7.2}$$

$f\left(\hat{\omega}\right)$ is the switching function, $\hat{\omega}$ is the estimated speed, and ω_{lower} and ω_{upper} are the lower and upper bounds of the switching function, respectively. $\hat{\theta}^{\text{low}}$ and $\hat{\theta}^{\text{high}}$ are the estimated position from the pulse injection method (at low speed) and the flux-linkage-based estimator (at high speed), respectively. $\hat{\theta}^{\text{full}}$ is the estimated position used for wide-speed range sensorless control by combining the two schemes.

7.3 Experimental Results

To validate the effectiveness of the wide-speed range sensorless control method, the starting-stage to the medium-speed operation performance is validated experimentally, as shown in Figure 7.2. The low-speed sensorless control method is selected as the RPLL-based estimator proposed in Chapter 3, and the high-speed sensorless control method is the QFE-based position estimator designed in Chapter 6. According to the wide-speed range sensorless control scheme in Figure 7.1, the starting-stage operation is based on the position estimated by the pulse-injection method.

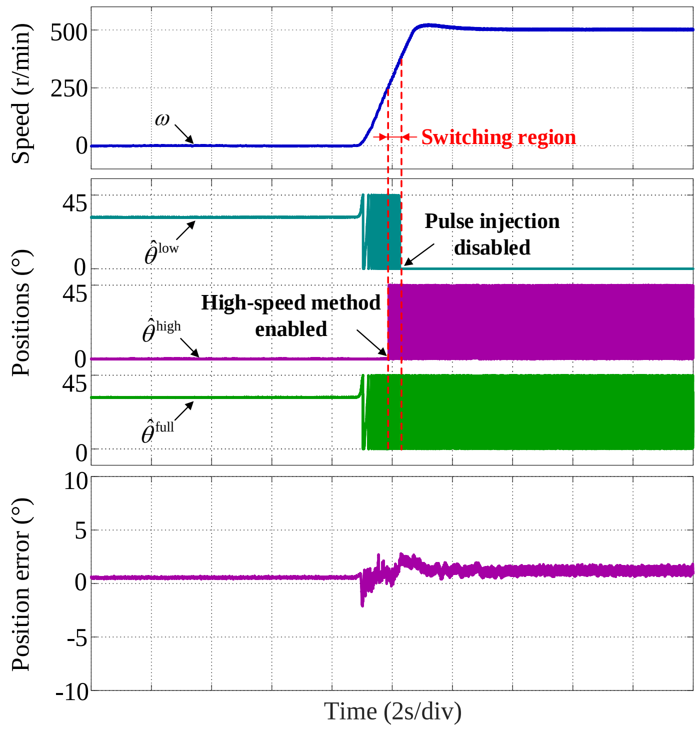

(a)

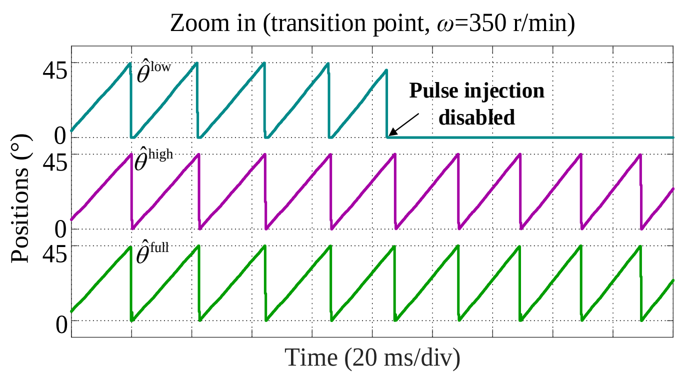

(b)

Figure 7.2 Wide-speed range SRM sensorless control by combining the proposed QFE and the pulse-injection-based method. (a) Overall performance. (b) Zoom in position estimation results at a transition point ω=350 r/min.

For this SRM test bench, the switching speed is selected around 300 r/min, which is 30% of the rated speed. The lower speed bound is 250 r/min, and the upper speed bound is 350 r/min. Below the lower speed bound (250 r/min), only the injection method is enabled.

When the estimated speed enters the transition region (250 r/min – 350 r/min), both the injection method and the proposed QFE are enabled simultaneously, and the estimated position is calculated from both methods according to the linear switching function expressed in (7.1). After the rotor speed is higher than the upper bound (350 r/min), the estimated position is only contributed by the proposed QFE.

As can be observed from the experimental result, the SRM starts smoothly and can support stable sensorless control at low speed. During the speed transition region, both the pulse-injection-based method and QFE-based scheme can estimate the rotor position well. The SRM sensorless control can then switch to the high-speed position estimation method when the rotor speed is higher than the upper bound. In consequence, by the simple linear switching function, the stable wide-speed range sensorless control can be realized without much additional calculation effort.

7.4 Conclusion

In this chapter, a wide-speed range position-sensorless control method is proposed for the SRM drive. The wide-speed range operation is realized by combining a low-speed position estimator and a high-speed position observer. A linear switching function is designed for smooth transition between the two schemes. Experimental validation using the RPLL-based position estimation method for low-speed operation and the QFE-based position observer for high-speed operation is conducted to prove the effectiveness. The results show that the transition between the two methods is smooth, and the wide-speed range position-sensorless control can be simply achieved without adding much calculation effort and complicated algorithm design.

Chapter 8

Conclusions and Future Work

8.1 Conclusions

This thesis presents a universal position-sensorless control scheme for SRM drives. The universality includes two aspects: (1) wide-speed range position-sensorless control and (2) independence on offline measured magnetic characteristics. Both the low-speed and the high-speed position observer designs are presented, which estimate the rotor position and speed with a simple online parameter self-commissioning processor or without any prestored magnetic characteristics. The work aims to improve the SRM position-sensorless control as a universal solution for industrial applications and capable of a general-purpose SRM converter.

The fundamentals of the SRM drive and a literature review of existing position-sensorless control methods are presented. The design of the three-phase asymmetric power converter and calibration of the commercial 12/8 SRM is introduced. A comprehensive survey of conventional pulse injection-based methods for low-speed position estimation and model-based methods for high-speed position estimation is given. As summarized from the literature, magnetic characteristics are necessary for accurate position estimation in existing techniques. Still, the offline measurement of the magnetic parameters limits the broad application of sensorless control in industries. At last, the significance and necessity of developing new position estimation methods without offline measurement effort are discussed.

Chapter 2 discusses a new position estimation method based on an RPLL for low-speed sensorless control. This approach utilizes the high-frequency pulse voltages injected into idle phases for inductance calculation. A self-commissioning process is designed to obtain some feature inductance characteristics of the SRM without involving manual work. Through the heterodyne design in the RPLL, the full-cycle rotor position can be estimated from the discontinuous idle-phase inductance. Compared to conventional pulse injection methods, the RPLL-based position estimation can achieve accurate position estimation at both no-load and load conditions. The RPLL also realizes speed reversal capability without additional quadrant determination. Experimental validation on the 5.5 kW 12/8 SRM test bench proves the effectiveness of the low-speed position-sensorless control in both steady and transient states. This study can simplify the low-speed sensorless control with reliable four-quadrant operation capability and without offline testing work. Therefore, it can be used in a general-purpose SRM drive that is appliable for various SRMs.

Following the low-speed position observer design in Chapter 2, Chapter 3 addresses the common drawbacks of conventional pulse injection methods, copper loss and torque ripple. Pulse voltages injected into the idle phase often induce large high-frequency currents around the unaligned position due to the low stator inductance. However, the significant copper loss and negative torque have limited the application of this method. The problems are solved by using a new TSMC-based injection voltage regulator. The designed nonlinear control law can control the amplitude of the high-frequency induced current to a minimal level over the idle-phase period. The robustness to parameter uncertainties can be guaranteed by adequately selecting the control parameters of the TSMC according to the convergence analysis and Lyapunov stability proof. Experimental results on the test bench show that the copper loss and the negative torque ripple in idle phases can be reduced by 95.9% and 92.3%, respectively. The adverse impacts of the pulse injection method on the SRM drive can be mitigated significantly.

Besides the low-speed sensorless control, high-speed position observer design is emphasized in the thesis. Conventional high-speed position estimation often searches a prestored flux linkage lookup table, but it needs time-consuming offline measurement and causes parameter sensitivity issues. In Chapter 4, a feature-position-based estimation scheme using an NSO is proposed. This scheme can estimate the feature position at 15° through an online acquired two-dimensional flux linkage curve at the feature position. No manual measurement is needed, thus improving the generality of the sensorless control algorithm. Furthermore, the effect of flux linkage errors on position estimation is analyzed, and an enhanced NSO based on the online Fourier series is designed to improve the position estimation accuracy. Comparative experimental results prove that the proposed scheme can accurately estimate the rotor position and speed compared to existing feature-position-based solutions.

In Chapter 6, a novel solution to estimate the rotor position at high speed is proposed, which does not use any magnetic characteristics. This approach is more straightforward than the idea presented in Chapter 5 since the position estimation requires neither offline measurement nor self-commissioning. This advantage is realized by analyzing the frequency characteristics of the SRM flux linkage. It finds that the flux linkage consists of a fundamental signal, DC offset, and harmonics. Through a QFE eliminating all the DC offset and harmonics in the calculated flux linkage, a pure sinusoidal orthogonal position signals can be extracted for position estimation. This study makes the SRM position estimation as simple as AC motor position estimation, which has been successfully applied in various commercial products. Experimental results on the SRM test bench validate the effectiveness under various operating conditions.

Overall, both the proposed low-speed position estimation method and the high-speed position observers are combined for wide-speed range position-sensorless control. The research work could facilitate the broad application of the SRM sensorless control in low-cost products or electric vehicles with robust position-sensor fault-tolerance capability.

8.2 Future Work

This thesis presents a universal position-sensorless control scheme for SRM drives. Still, the SRM sensorless control can be further investigated and improved in serval aspects. The future work of this topic is summarized as follows:

1) A magnetic-characteristic-free position estimation method for low-speed operation is attractive for general-purpose SRM drives. The thesis makes some research work on

high-speed position-sensorless control without using any magnetic characteristics, but the same way cannot be adopted for low-speed operation. The DC bias and harmonics in flux linkage cannot be eliminated at a low-speed case due to the closer frequencies to the fundamental flux linkage used for position estimation. The magnetic-characteristic-free low-speed position estimation will make the SRM position-sensorless fully independent of the knowledge of the machine.

2) A single-observer-based full-speed position sensorless control method will benefit easier implementation in the SRM drives. The thesis achieves the full-speed sensorless control by combining two observers at different speed regions. Although the reliable full-speed operation is performed, the two observers require more computational resources and design effort. Therefore, a single-observer-based method capable of both the low-speed operation and the high-speed operation will be more attractive for industrial applications.

3) Higher dynamic performance is always crucial for high-performance SRM drives. High current and speed control bandwidth need precise position and speed estimation in steady and transient states. The main challenge to improving estimation accuracy is eliminating nonideal distortions in the estimation, such as measurement errors, DC-link voltage ripples, and mutual coupling effects. Besides, the high-bandwidth observer design is also necessary to improve the overall sensorless control performance.

4) Ultra-high-speed position-sensorless control will bring challenges in discrete observer design. More focuses could be given to analyze the discrete frequency characteristic of the position observer and propose solutions to enhance the position-sensorless control

stability at an ultra-high speed.

5) The other future work is to combine the position-sensorless control with developed torque control schemes that require less or no magnetic characteristics. In existing research on SRM torque control, flux linkage and torque characteristics are necessary, increasing the complexity in control algorithms. The proposed approaches for characteristic-free position-sensorless control proposed in the thesis could be examples to develop new torque control techniques with less independence on magnetic characteristics.

8.3 Publications

8.3.1 Accepted Papers

[1] **(Thesis)** **D. Xiao**, J. Ye, G. Fang, Z. Xia, and A. Emadi, "Magnetic-Characteristic-Free High-Speed Position-Sensorless Control of Switched Reluctance Motor Drives With Quadrature Flux Estimators," *IEEE Journal of Emerging and Selected Topics in Power Electronics*, accepted.

[2] **(Thesis)** **D. Xiao**, J. Ye, G. Fang, Z. Xia, X. Wang, and A. Emadi, "Improved Feature-Position-Based Sensorless Control Scheme for SRM Drives Based on Nonlinear State Observer at Medium and High Speeds," *IEEE Transactions on Power Electronics*, vol. 36, no. 5, pp. 5711-5723, May, 2021.

[3] **D. Xiao**, S. Nalakath, Y. Sun, J. Wiseman, A. Emadi, "Complex-Coefficient Adaptive Disturbance Observer for Position Estimation of IPMSMs With Robustness to

DC Errors," *IEEE Transactions on Industrial Electronics*, vol. 67, no. 7, pp. 5924-5935, July 2020.

[4] **D. Xiao**, G. Fang, S. Liu, S. Yuan, R. Ahmed, S. Habibi, and A. Emadi, "Reduced-Coupling Co-Estimation of SOC and SOH for Lithium-Ion Batteries Based on Convex Optimization," *IEEE Transactions on Power Electronics*, vol. 35, no. 11, pp. 12332-12346, Nov. 2020.

[5] **D. Xiao**, S. Nalakath, Z. Xia, G. Fang, Y. Sun, J. Wiseman, and A. Emadi, "Computation-Efficient Position Estimation Algorithm for Permanent Magnet Synchronous Motor Drives Under Distorted Conditions," *IEEE Journal of Emerging and Selected Topics in Power Electronics*, vol. 9, no. 3, pp. 2759-2773, June. 2021.

[6] **D. Xiao**, S. Nalakath, S. R. Fiho, G. Fang, Y. Sun, J. Wiseman, and A. Emadi, "Universal Full-Speed Sensorless Control Scheme for Interior Permanent Magnet Synchronous Motors," *IEEE Transactions on Power Electronics*, vol. 36, no. 4, pp. 4723-4737, April, 2021.

[7] C. J. V. Filho, **D. Xiao***, R. P. Vieira and A. Emadi, "Observers for High-Speed Sensorless PMSM Drives: Design Methods, Tuning Challenges and Future Trends," *IEEE Access*, vol. 9, pp. 56397-56415, 2021. (Corresponding author)

[8] **D. Xiao** and M. Narimani, "Current Control of a New Five-Level Nested T-type Converter with Model Predictive Control," *2019 IEEE Energy Conversion Congress and Exposition (ECCE)*, Baltimore, MD, USA, 2019, pp. 6352-6356.

[9] **D. Xiao**, S. Ouni and M. Narimani, "A New Five-Level T-Type Converter with SPWM for Medium-Voltage Applications," *2019 IEEE 28th International*

Symposium on Industrial Electronics (ISIE), Vancouver, BC, Canada, 2019, pp. 2015-2020.

[10] **D. Xiao**, and J. Bauman, "Power Loss Comparison Between Three-Level T-type and NPC Converters with SVPWM and MPCC Modulation Schemes in Electric Vehicles," *2020 IEEE Transportation Electrification Conference and Expo (ITEC)*, Chicago, USA, 2020, pp. 308-313.

[11] G. Fang, J. Ye, **D. Xiao**, Z. Xia, and A. Emadi, "Computational-efficient Model Predictive Torque Control for Switched Reluctance Machines with Linear-Space-based Equivalent Transformations," *IEEE Transactions on Industrial Electronics*, accepted, 2021.

[12] G. Fang, F. P. Scalcon, **D. Xiao**, R. P. Vieira, H. A. Gründling and A. Emadi, "Advanced Control of Switched Reluctance Motors (SRMs): A Review on Current Regulation, Torque Control and Vibration Suppression," *IEEE Open Journal of the Industrial Electronics Society*, vol. 2, pp. 280-301, 2021.

[13] G. Fang, J. Ye, **D. Xiao**, Z. Xia, X. Wang, X. Guo and A. Emadi, "An Intersection-Method Based Current Controller for Switched Reluctance Machines with Robust Tracking Performance," *IEEE Transactions on Transportation Electrification*, accepted.

[14] Z. Xia, S. Filho, **D. Xiao**, G. Fang, Y. Sun, J. Wiseman and A. Emadi, “Computation-Efficient Online Optimal Tracking Method for Permanent Magnet Synchronous Machine Drives for MTPA and Flux-Weakening Operations,” *IEEE Journal of Emerging and Selected Topics in Power Electronics*, accepted.

[15] G. Fang, J. Ye, **D. Xiao**, Z. Xia, X. Wang and A. Emadi, "Time-Efficient Torque Shaping for Switched Reluctance Machines from Linear Space," *IEEE Transactions on Power Electronic*s, accepted.

[16] X. Wang, Z. Wang, M. Gu, **D. Xiao**, J. He and A. Emadi, "Diagnosis-Free Self-Healing Scheme for Open-Circuit Faults in Dual Three-Phase PMSM Drives," *IEEE Transactions on Power Electronics*, vol. 35, no. 11, pp. 12053-12071, Nov. 2020.

8.3.2 Submitted Papers

[1] **(Thesis) D. Xiao**, J. Ye, G. Fang, Z. Xia, X. Wang, and A. Emadi, "A Regional Phase-Locked Loop Based Low-Speed Position-Sensorless Control Scheme for General-Purpose Switched Reluctance Motor Drives," *IEEE Transactions on Power Electronics*, under third-round review, conditionally accepted.

[2] **(Thesis) D. Xiao**, S. R. Fiho, G. Fang, J. Ye, and A. Emadi, "Position-Sensorless Control of Switched Reluctance Motors - A review,“ *IEEE Transactions on Transportation Electrification*, under review.

8.3.3 To Be Submitted Papers

[1] **(Thesis) D. Xiao**, J. Ye, G. Fang, Z. Xia, and A. Emadi, "Induced Current Reduction in Pulse Injection-Based Low-Speed Position Sensorless Control of Switched Reluctance Motor Drives."

References

[1] B. Bilgin *et al.*, “Making the Case for Switched Reluctance Motors for Propulsion Applications,” *IEEE Transactions on Vehicular Technology*, vol. 69, no. 7, pp. 7172–7186, 2020.

[2] G. Fang, F. Pinarello Scalcon, D. Xiao, R. Vieira, H. Grundling, and A. Emadi, “Advanced Control of Switched Reluctance Motors (SRMs): A Review on Current Regulation, Torque Control and Vibration Suppression,” *IEEE Open Journal of the Industrial Electronics Society*, vol. 2, no. May, pp. 280–301, 2021.

[3] M. Ehsani and B. Fahimi, “Elimination of position sensors in switched reluctance motor drives: State of the art and future trends,” *IEEE Transactions on Industrial Electronics*, vol. 49, no. 1, pp. 40–47, 2002.

[4] S. Song, L. Ge, S. Ma, M. Zhang, and L. Wang, “Accurate measurement and detailed evaluation of static electromagnetic characteristics of switched reluctance machines,” *IEEE Transactions on Instrumentation and Measurement*, vol. 64, no. 3, pp. 704–714, 2015.

[5] P. Azer, B. Bilgin, and A. Emadi, “Mutually Coupled Switched Reluctance Motor:

Fundamentals, Control, Modeling, State of the Art Review and Future Trends," *IEEE Access*, vol. 7, pp. 100099–100112, 2019.

[6] S. Song, G. Fang, Z. Zhang, R. Ma, and W. Liu, "Unsaturated-Inductance-Based Instantaneous Torque Online Estimation of Switched Reluctance Machine with Locally Linearized Energy Conversion Loop," *IEEE Transactions on Industrial Electronics*, vol. 65, no. 8, pp. 6109–6119, 2018.

[7] H. Gao, F. R. Salmasi, and M. Ehsani, "Sensorless control of SRM at standstill," *Conference Proceedings - IEEE Applied Power Electronics Conference and Exposition - APEC*, vol. 2, pp. 850–856, 2001.

[8] G. Pasquesoone, R. Mikail, and I. Husain, "Position estimation at starting and lower speed in three-phase switched reluctance machines using pulse injection and two thresholds," *IEEE Transactions on Industry Applications*, vol. 47, no. 4, pp. 1724–1731, 2011.

[9] K. W. Hu, Y. Y. Chen, and C. M. Liaw, "A reversible position sensorless controlled switched-reluctance motor drive with adaptive and intuitive commutation tunings," *IEEE Transactions on Power Electronics*, vol. 30, no. 7, pp. 3781–3793, 2015.

[10] W. Wang and B. Fahimi, "Fault Resilient Strategies for Position Sensorless Methods of Switched Reluctance Motors Under Single and Multiphase Fault," *IEEE Journal of Emerging and Selected Topics in Power Electronics*, vol. 2, no. 2, pp. 190–200, 2014.

[11] Y. T. Chang and K. W. E. Cheng, "Sensorless position estimation of switched reluctance motor at startup using quadratic polynomial regression," *IET Electric*

Power Applications, vol. 7, no. 7, pp. 618–626, 2013.

[12] Y. T. Chang, K. W. E. Cheng, and S. L. Ho, “Type-V exponential regression for online sensorless position estimation of switched reluctance motor,” *IEEE/ASME Transactions on Mechatronics*, vol. 20, no. 3, pp. 1351–1359, 2015.

[13] L. Shen, J. Wu, and S. Yang, “Initial position estimation in SRM using bootstrap circuit without predefined inductance parameters,” *IEEE Transactions on Power Electronics*, vol. 26, no. 9, pp. 2449–2456, 2011.

[14] L. Zhang, Y. Yu, and Z. Xin, “A position estimation for switched reluctance motor using full cycle envelope,” *Proceedings of 2017 IEEE 3rd Information Technology and Mechatronics Engineering Conference, ITOEC 2017*, vol. 2017-Janua, pp. 909–913, 2017.

[15] J. Kim, J. M. Choe, S. Moon, and J. S. Lai, “Position Sensorless Control of Switched Reluctance Motor Drives Without Pre-stored Magnetic Characteristics,” in *2018 IEEE Energy Conversion Congress and Exposition, ECCE 2018*, 2018, pp. 1755–1761.

[16] T. Bamba, A. Komatsuzaki, and I. Miki, “Estimation of rotor position for switched reluctance motor at standstill,” *Fourth Power Conversion Conference-NAGOYA, PCC-NAGOYA 2007 - Conference Proceedings*, pp. 259–263, 2007.

[17] J. Cai and Z. Deng, “Sensorless control of switched reluctance motor based on phase inductance vectors,” *IEEE Transactions on Power Electronics*, vol. 27, no. 7, pp. 3410–3423, 2012.

[18] J. Cai and Z. Deng, “Initial Rotor Position Estimation and Sensorless Control of

SRM Based on Coordinate Transformation," *IEEE Transactions on Instrumentation and Measurement*, vol. 64, no. 4, pp. 1004–1018, 2015.

[19] J. Bu, "Eliminating starting hesitation for reliable sensorless control of switched reluctance motors," *IEEE Transactions on Industry Applications*, vol. 37, no. 1, pp. 59–66, 2001.

[20] A. Sarr, I. Bahri, D. Diallo, and E. Berthelot, "Sensorless control of Switched Reluctance Machine," *IECON Proceedings (Industrial Electronics Conference)*, pp. 6693–6698, 2016.

[21] I. Ralev, S. Max, and R. W. De Doncker, "Accurate Rotor Position Detection for Low-Speed Operation of Switched Reluctance Drives," *Proceedings - 2018 IEEE 18th International Conference on Power Electronics and Motion Control, PEMC 2018*, pp. 483–490, 2018.

[22] L. Ge, H. Xu, Z. Guo, S. Song, and R. W. De Doncker, "An Optimization-based Initial Position Estimation Method for Switched Reluctance Machines," *IEEE Transactions on Power Electronics*, vol. 8993, no. c, pp. 1–1, 2021.

[23] A. Khalil *et al.*, "Four-quadrant pulse injection and sliding-mode-observer-based sensorless operation of a switched reluctance machine over entire speed range including zero speed," *IEEE Transactions on Industry Applications*, vol. 43, no. 3, pp. 714–723, 2007.

[24] E. Kayikci and R. D. Lorenz, "Self-sensing control of a four phase switched reluctance drive using high frequency signal injection including saturation effects," *2009 IEEE International Electric Machines and Drives Conference, IEMDC '09*,

pp. 611–618, 2009.

[25] A. Khalil and I. Husain, "Four quadrant sensorless operation of a switched reluctance machine using fourier model," *PESC Record - IEEE Annual Power Electronics Specialists Conference*, 2006.

[26] X. Zhang, F. Wang, and X. Wu, "Low-speed direct-driven sensorless control including zero-speed for switched reluctance motor based on dynamic inductance model," *2014 17th International Conference on Electrical Machines and Systems, ICEMS 2014*, pp. 763–767, 2014.

[27] D. Zhou and H. Chen, "Four-Quadrant Position Sensorless Operation of Switched Reluctance Machine for Electric Vehicles over a Wide Speed Range," *IEEE Transactions on Transportation Electrification*, vol. 7782, no. c, pp. 1–13, 2021.

[28] M. Krishnamurthy, C. S. Edrington, and B. Fahimi, "Prediction of rotor position at standstill and rotating shaft conditions in switched reluctance machines," *IEEE Transactions on Power Electronics*, vol. 21, no. 1, pp. 225–233, 2006.

[29] J. Cai and Z. Deng, "Unbalanced phase inductance adaptable rotor position sensorless scheme for switched reluctance motor," *IEEE Transactions on Power Electronics*, vol. 33, no. 5, pp. 4285–4292, 2018.

[30] A. Xu, J. Chen, P. Ren, and J. Zhu, "Position sensorless control of switched reluctance motor based on a linear inductance model with variable coefficients," *IET Energy Systems Integration*, vol. 1, no. 3, pp. 210–217, 2019.

[31] J. Cai and Z. Liu, "An Unsaturated Inductance Reconstruction Based Universal Sensorless Starting Control Scheme for SRM Drives," *IEEE Transactions on*

Industrial Electronics, vol. 67, no. 11, pp. 9083–9092, 2020.

[32] J. Cai, Y. Yan, W. Zhang, and X. Zhao, "A Reliable Sensorless Starting Scheme for SRM with Lowered Pulse Injection Current Influences," *IEEE Transactions on Instrumentation and Measurement*, vol. 70, no. c, 2021.

[33] H. J. Guo, M. Takahashi, T. Watanabe, and O. Ichinokura, "A new sensorless drive method of switched reluctance motors based on motor's magnetic characteristics," *IEEE Transactions on Magnetics*, vol. 37, no. 4 I, pp. 2831–2833, 2001.

[34] E. Ofori, T. Husain, Y. Sozer, and I. Husain, "A Pulse-Injection-Based Sensorless Position Estimation Method for a Switched Reluctance Machine Over a Wide Speed Range," *IEEE Transactions on Industry Applications*, vol. 51, no. 5, pp. 3867–3876, 2015.

[35] J. Shao, Z. Deng, and Y. Gu, "Fault-Tolerant Control of Position Signals for Switched Reluctance Motor Drives," *IEEE Transactions on Industry Applications*, vol. 53, no. 3, pp. 2959–2966, 2017.

[36] Y. Maita and I. Miki, "Sensorless Control in Low-speed Region for Switched Reluctance Motor," *23rd International Conference on Electrical Machines and Systems, ICEMS 2020*, no. 2, pp. 1173–1177, 2020.

[37] H. Cheng, H. Chen, S. Xu, and S. Yang, "Four-quadrant sensorless control in switched reluctance machine drive using pulse injection based on special flux linkage curves," *IET Electric Power Applications*, vol. 11, no. 9, pp. 1566–1574, 2017.

[38] G. Gallegos-López, P. C. Kjaer, and T. J. E. Miller, "A new sensorless method for

switched reluctance motor drives," *IEEE Transactions on Industry Applications*, vol. 34, no. 4, pp. 832–840, 1998.

[39] J. H. Kim and R. Y. Kim, "Online sensorless position estimation for switched reluctance motors using characteristics of overlap position based on inductance profile," *IET Electric Power Applications*, vol. 13, no. 4, pp. 456–462, 2019.

[40] C. Gan, J. Wu, Y. Hu, S. Yang, W. Cao, and J. L. Kirtley, "Online Sensorless Position Estimation for Switched Reluctance Motors Using One Current Sensor," *IEEE Transactions on Power Electronics*, vol. 31, no. 10, pp. 7248–7263, 2016.

[41] C. J. Bateman, B. C. Mecrow, A. C. Clothier, P. P. Acarnley, and N. D. Tuftnell, "Sensorless operation of an ultra-high-speed witched reluctance machine," *IEEE Transactions on Industry Applications*, vol. 46, no. 6, pp. 2329–2337, 2010.

[42] W. Shao, R. Zhong, X. Guo, and W. Sun, "Analysis of the null current gradient position for sensorless control of SRM," *Proceedings IECON 2017 - 43rd Annual Conference of the IEEE Industrial Electronics Society*, vol. 2017-Janua, no. 2, pp. 1816–1821, 2017.

[43] I. Miki, H. Noda, and R. Moriyama, "A sensorless drive method for switched reluctance motor based on gradient of phase inductance," *ICEMS 2003 - Proceedings of the 6th International Conference on Electrical Machines and Systems*, vol. 2, pp. 615–618, 2003.

[44] J. Cai and Z. Deng, "A position sensorless control of switched reluctance motors based on phase inductance slope," *Journal of Power Electronics*, vol. 13, no. 2, pp. 264–274, 2013.

[45] J. Cai and Z. Deng, “A Joint Feature Position Detection-Based Sensorless Position Estimation Scheme for Switched Reluctance Motors,” *IEEE Transactions on Industrial Electronics*, vol. 64, no. 6, pp. 4352–4360, 2017.

[46] J. Cai, Z. Liu, and Y. Zeng, “Aligned Position Estimation Based Fault-Tolerant Sensorless Control Strategy for SRM Drives,” *IEEE Transactions on Power Electronics*, vol. 34, no. 8, pp. 7754–7762, 2019.

[47] J. H. Kim and R. Y. Kim, “Sensorless direct torque control using the inductance inflection point for a switched reluctance motor,” *IEEE Transactions on Industrial Electronics*, vol. 65, no. 12, pp. 9336–9345, 2018.

[48] P. Ren, A. Xu, S. Wang, and W. Zhang, “Sensorless control of switched reluctance motor based on the logical relationship of three-phase inductance,” *Chinese Control Conference, CCC*, vol. 2018-July, pp. 5035–5040, 2018.

[49] C. Gan, F. Meng, Z. Yu, R. Qu, Z. Liu, and J. Si, “Online Calibration of Sensorless Position Estimation for Switched Reluctance Motors with Parametric Uncertainties,” *IEEE Transactions on Power Electronics*, vol. 35, no. 11, pp. 12307–12320, 2020.

[50] D. Panda and V. Ramanarayanan, “Reduced acoustic noise variable DC-bus-voltage-based sensorless switched reluctance motor drive for HVAC applications,” *IEEE Transactions on Industrial Electronics*, vol. 54, no. 4, pp. 2065–2078, 2007.

[51] S. Wang, Z. Hu, and X. P. Cui, “High-precision Sensorless Control Based on Magnetic Flux/Current Method for SRM Starting/Generating System,” *IECON Proceedings (Industrial Electronics Conference)*, vol. 2020-Octob, pp. 251–258,

2020.

[52] K. Ha, R. Y. Kim, and R. Ramu, "Position estimation in switched reluctance motor drives using the first switching harmonics through fourier series," *IEEE Transactions on Industrial Electronics*, vol. 58, no. 12, pp. 5352–5360, 2011.

[53] H. Gao, F. R. Salmasi, and M. Ehsani, "Inductance model-based sensorless control of the switched reluctance motor drive at low speed," *IEEE Transactions on Power Electronics*, vol. 19, no. 6, pp. 1568–1573, 2004.

[54] C. Gan, Y. Chen, Q. Sun, J. Si, J. Wu, and Y. Hu, "A Position Sensorless Torque Control Strategy for Switched Reluctance Machines with Fewer Current Sensors," *IEEE/ASME Transactions on Mechatronics*, vol. 26, no. 2, pp. 1118–1128, 2021.

[55] D. Panda and V. Ramanarayanan, "Accurate position estimation in switched reluctance motor with smooth starting," *Proceedings of the IEEE International Conference on Industrial Technology*, vol. 1, pp. 388–393, 2000.

[56] D. Panda and V. Ramanarayanan, "Mutual coupling and its effect on steady-state performance and position estimation of even and odd number phase switched reluctance motor drive," *IEEE Transactions on Magnetics*, vol. 43, no. 8, pp. 3445–3456, 2007.

[57] H. P. Chi, T. J. Liang, C. L. Chu, J. F. Chen, and M. T. Chang, "Improved mutual voltage technique of indirect rotor position sensing in switched reluctance motor," *PESC Record - IEEE Annual Power Electronics Specialists Conference*, vol. 1, pp. 271–275, 2002.

[58] J. Ye, B. Bilgin, and A. Emadi, "Elimination of mutual flux effect on rotor position

estimation of switched reluctance motor drives," *IEEE Transactions on Power Electronics*, vol. 30, no. 3, pp. 1499–1512, 2015.

[59] J. Ye, B. Bilgin, and A. Emadi, "Elimination of mutual flux effect on rotor position estimation of switched reluctance motor drives considering magnetic saturation," *IEEE Transactions on Power Electronics*, vol. 30, no. 2, pp. 532–536, 2015.

[60] S. Y. Kuai, S. Zhao, F. P. Heng, and X. Cui, "Position sensorless technology of switched reluctance motor drives including mutual inductance," *IET Electric Power Applications*, vol. 11, no. 6, pp. 1085–1094, 2017.

[61] D. Xiao *et al.*, "Universal Full-Speed Sensorless Control Scheme for Interior Permanent Magnet Synchronous Motors," *IEEE Transactions on Power Electronics*, vol. 36, no. 4, pp. 4723–4737, 2021.

[62] D. Xiao, S. Nalakath, Y. Sun, J. Wiseman, and A. Emadi, "Complex-coefficient adaptive disturbance observer for position estimation of IPMSMs with robustness to DC Errors," *IEEE Transactions on Industrial Electronics*, vol. 67, no. 7, pp. 5924–5935, 2020.

[63] D. Xiao *et al.*, "Computation-Efficient Position Estimation Algorithm for Permanent Magnet Synchronous Motor Drives Under Distorted Conditions," *IEEE Journal of Emerging and Selected Topics in Power Electronics*, vol. 9, no. 3, pp. 2759–2773, 2020.

[64] G. Zhang *et al.*, "Pseudorandom-Frequency Sinusoidal Injection for Position Sensorless IPMSM Drives Considering Sample and Hold Effect," *IEEE Transactions on Power Electronics*, vol. 34, no. 10, pp. 9929–9941, 2019.

[65] G. Zhang, G. Wang, B. Yuan, R. Liu, and D. Xu, “Active Disturbance Rejection Control Strategy for Signal Injection-Based Sensorless IPMSM Drives,” *IEEE Transactions on Transportation Electrification*, vol. 4, no. 1, pp. 330–339, 2017.

[66] W. Sun, D. Xu, and D. Jiang, “Observability analysis for speed sensorless induction motor drives with and without virtual voltage injection,” *IEEE Transactions on Power Electronics*, vol. 34, no. 9, pp. 9236–9246, 2019.

[67] B. Wang, Z. Huo, Y. Yu, C. Luo, W. Sun, and D. Xu, “Stability and Dynamic Performance Improvement of Speed Adaptive Full-Order Observer for Sensorless Induction Motor Ultralow Speed Operation,” *IEEE Transactions on Power Electronics*, vol. 35, no. 11, pp. 12522–12532, 2020.

[68] B. Wang, Y. Shao, Y. Yu, Q. Dong, Z. Yun, and D. G. Xu, “High-Order Terminal Sliding-Mode Observer for Chattering Suppression and Finite-Time Convergence in Sensorless SPMSM Drives,” *IEEE Transactions on Power Electronics*, vol. 8993, no. c, 2021.

[69] L. Sun, X. Li, and L. Chen, “Motor Speed Control with Convex Optimization-based Position Estimation in the Current Loop,” *IEEE Transactions on Power Electronics*, vol. 8993, no. 1, 2021.

[70] X. Wang, Z. Wang, M. Gu, D. Xiao, J. He, and A. Emadi, “Diagnosis-Free Self-Healing Scheme for Open-Circuit Faults in Dual Three-Phase PMSM Drives,” *IEEE Transactions on Power Electronics*, vol. 35, no. 11, pp. 12053–12071, 2020.

[71] Y. J. Zhan, “A novel sliding-mode observer for indirect position sensing of switched reluctance motor drives,” *IEEE Transactions on Industrial Electronics*, vol. 46, no.

2. pp. 390–397, 1999.

[72] X. Zhang, G. Tan, S. Kuai, and Q. Wang, “Position sensorless control of switched reluctance generator for wind energy conversion,” *Asia-Pacific Power and Energy Engineering Conference, APPEEC*, 2010.

[73] A. Yalavarthi and B. Singh, “SMO-Based Position Sensorless SRM Drive for Battery Supported PV Submersible Pumps,” *IEEE Journal of Emerging and Selected Topics in Power Electronics*, vol. 6777, no. c, 2021.

[74] M. Ilic’-Spong, R. Marino, S. M. Peresada, and D. G. Taylor, “Feedback Linearizing Control of Switched Reluctance Motors,” *IEEE Transactions on Automatic Control*, vol. 32, no. 5, pp. 371–379, 1987.

[75] M. S. Islam and I. Husain, “Torque-ripple minimization with indirect position and speed sensing for switched reluctance motors,” *IEEE Transactions on Industrial Electronics*, vol. 47, no. 5, pp. 1126–1133, 2000.

[76] M. S. Islam, I. Husain, R. J. Veillette, and C. Batur, “Design and performance analysis of sliding-mode observers for sensorless operation of switched reluctance motors,” *IEEE Transactions on Control Systems Technology*, vol. 11, no. 3, pp. 383–389, 2003.

[77] P. Brandstetter and P. Krna, “Sensorless control of switched reluctance motor using sliding mode observer,” *International Conference on Applied Electronics*, pp. 1–4, 2013.

[78] M. Divandari, B. Rezaie, and A. R. Noei, “Sensorless drive for switched reluctance motor by adaptive hybrid sliding mode observer without chattering,” *Proceedings of*

the 2018 IEEE Conference of Russian Young Researchers in Electrical and Electronic Engineering, ElConRus 2018, vol. 2018-Janua, pp. 1714–1722, 2018.

[79] S. A. Hossain, I. Husain, H. Klode, B. Lequesne, A. M. Omekanda, and S. Gopalakrishnan, “Four-quadrant and zero-speed sensorless control of a switched reluctance motor,” *IEEE Transactions on Industry Applications*, vol. 39, no. 5, pp. 1343–1349, 2003.

[80] Y. Nakazawa and S. Matsunaga, “Position Sensorless Control of Switched Reluctance Motor Using State Observer,” *2019 22nd International Conference on Electrical Machines and Systems, ICEMS 2019*, no. 4, pp. 2019–2022, 2019.

[81] G. Gallegos-Löpez, P. C. Kjaer, and T. J. E. Miller, “High-grade position estimation for SRM drives using flux linkage/current correction model,” *IEEE Transactions on Industry Applications*, vol. 35, no. 4, pp. 859–869, 1999.

[82] F. Peng, J. Ye, A. Emadi, and Y. Huang, “Position Sensorless Control of Switched Reluctance Motor Drives Based on Numerical Method,” *IEEE Transactions on Industry Applications*, vol. 53, no. 3, pp. 2159–2168, 2017.

[83] Y. A. Khan and V. Verma, “Investigation of Pn and F-MRAS based Speed Estimators for Vector Controlled Switched Reluctance Motor Drive,” *Proceedings of 2018 IEEE International Conference on Power Electronics, Drives and Energy Systems, PEDES 2018*, pp. 4–9, 2018.

[84] Y. A. Khan and V. Verma, “Novel speed estimation technique for vector-controlled switched reluctance motor drive,” *IET Electric Power Applications*, vol. 13, no. 8, pp. 1193–1203, 2019.

[85] D. Pinto, J. Pelletier, W. Peng, and J. Gyselinck, "Combined Signal-Injection and Flux-Linkage Approach for Sensorless Control of Switched Reluctance Machines," *2016 IEEE Vehicle Power and Propulsion Conference, VPPC 2016 - Proceedings*, 2016.

[86] Y. Z. Li and K. G. Zhao, "Sensorless speed control of the switched reluctance motor using extended Kalman filter," *2nd International Conference on Information Science and Engineering, ICISE2010 - Proceedings*, vol. 1, pp. 2375–2378, 2010.

[87] N. Ouddah, N. Loukkas, A. Chaibet, M. Boukhnifer, and E. Monmasson, "Experimental evaluation of second sliding modes observer and Extended Kalman Filter in a sensorless robust control of Switched Reluctance Motor for EV application," *2015 23rd Mediterranean Conference on Control and Automation, MED 2015 - Conference Proceedings*, pp. 986–992, 2015.

[88] N. Ertugrul and A. D. Cheok, "Indirect angle estimation in switched reluctance motor drives using fuzzy logic based motor model," *IEEE Transactions on Power Electronics*, vol. 15, no. 6, pp. 1029–1044, 2000.

[89] L. Xu and C. Wang, "Accurate rotor position detection and sensorless control of SRM for super-high speed operation," *IEEE Transactions on Power Electronics*, vol. 17, no. 5, pp. 757–763, 2002.

[90] A. D. Cheok and N. Ertugrul, "High robustness and reliability of fuzzy logic based position estimation for sensorless switched reluctance motor drives," *IEEE Transactions on Power Electronics*, vol. 15, no. 2, pp. 319–334, 2000.

[91] E. Mese and D. A. Torrey, "An approach for sensorless position estimation for

switched reluctance motors using artificial neural networks," *IEEE Transactions on Power Electronics*, vol. 17, no. 1, pp. 66–75, 2002.

[92] L. O. De Araujo Porto Henriques, L. G. B. Rolim, W. I. Suemitsu, J. A. Dente, and P. J. Costa Branco, "Development and experimental tests of a simple neurofuzzy learning sensorless approach for switched reluctance motors," *IEEE Transactions on Power Electronics*, vol. 26, no. 11, pp. 3330–3344, 2011.

[93] S. Paramasivam, S. Vijayan, M. Vasudevan, R. Arumugam, and R. Krishnan, "Real-time verification of AI based rotor position estimation techniques for a 6/4 pole switched reluctance motor drive," *IEEE Transactions on Magnetics*, vol. 43, no. 7, pp. 3209–3222, 2007.

[94] E. Echenique, J. Dixon, R. Cárdenas, and R. Peña, "Sensorless control for a switched reluctance wind generator, based on current slopes and neural networks," *IEEE Transactions on Industrial Electronics*, vol. 56, no. 3, pp. 817–825, 2009.

[95] C. A. Hudson, N. S. Lobo, and R. Krishnan, "Sensorless control of single switch-based switched reluctance motor drive using neural network," *IEEE Transactions on Industrial Electronics*, vol. 55, no. 1, pp. 321–329, 2008.

[96] Y. Cai, Y. Wang, H. Xu, S. Sun, C. Wang, and L. Sun, "Research on Rotor Position Model for Switched Reluctance Motor Using Neural Network," *IEEE/ASME Transactions on Mechatronics*, vol. 23, no. 6, pp. 2762–2773, 2018.

[97] R. Zhong, Y. B. Wang, and Y. Z. Xu, "Position sensorless control of switched reluctance motors based on improved neural network," *IET Electric Power Applications*, vol. 6, no. 2, pp. 111–121, 2012.

[98] J. P. Lyons, S. R. MacMinn, and M. A. Preston, “Flux-current methods for SRM rotor position estimation.” pp. 482–487, 1992.

[99] I. H. Al-Bahadly, “Examination of a sensorless rotor-position-measurement method for switched reluctance drive,” *IEEE Transactions on Industrial Electronics*, vol. 55, no. 1, pp. 288–295, 2008.

[100] T. Wang, W. Ding, Y. Hu, S. Yang, and S. Li, “Sensorless control of switched reluctance motor drive using an improved simplified flux linkage model method,” *Conference Proceedings - IEEE Applied Power Electronics Conference and Exposition - APEC*, vol. 2018-March, pp. 2992–2998, 2018.

[101] W. Ding and K. Song, “Position Sensorless Control of Switched Reluctance Motors Using Reference and Virtual Flux Linkage with One-Phase Current Sensor in Medium and High Speed,” *IEEE Transactions on Industrial Electronics*, vol. 67, no. 4, pp. 2595–2606, 2020.

[102] S. Song, M. Zhang, and L. Ge, “A new fast method for obtaining flux-linkage characteristics of SRM,” *IEEE Transactions on Industrial Electronics*, vol. 62, no. 7, pp. 4105–4117, 2015.

[103] H. Chen, R. Nie, J. Gu, S. Yan, and R. Zhao, “Efficiency Optimization Strategy for Switched Reluctance Generator System with Position Sensorless Control,” *IEEE/ASME Transactions on Mechatronics*, vol. 26, no. 1, pp. 469–479, 2021.

[104] S. Song, L. Ge, and Z. Zhang, “Accurate Position Estimation of SRM Based on Optimal Interval Selection and Linear Regression Analysis,” *IEEE Transactions on Industrial Electronics*, vol. 63, no. 6, pp. 3467–3478, 2016.

[105] B. Fahimi, A. Emadi, and R. B. Sepe, “Four-quadrant position sensorless control in SRM drives over the entire speed range,” *IEEE Transactions on Power Electronics*, vol. 20, no. 1, pp. 154–163, 2005.

[106] P. Kanjiya, V. Khadkikar, and M. S. El Moursi, “Obtaining Performance of Type-3 Phase-Locked Loop Without Compromising the Benefits of Type-2 Control System,” *IEEE Transactions on Power Electronics*, vol. 33, no. 2, pp. 1788–1796, 2018.

[107] Y. Feng, F. Han, and X. Yu, “Chattering free full-order sliding-mode control,” *Automatica*, vol. 50, no. 4, pp. 1310–1314, 2014.

[108] T. R. Tesch and R. D. Lorenz, “Disturbance torque and motion state estimation with low-resolution position interfaces using heterodyning observers,” *IEEE Transactions on Industry Applications*, vol. 44, no. 1, pp. 124–134, 2008.

[109] G. Wang, R. Liu, N. Zhao, D. Ding, and D. Xu, “Enhanced Linear ADRC Strategy for HF Pulse Voltage Signal Injection-Based Sensorless IPMSM Drives,” *IEEE Transactions on Power Electronics*, vol. 34, no. 1, pp. 514–525, 2019.

[110] M. Karimi-Ghartemani, S. A. Khajehoddin, P. K. Jain, A. Bakhshai, and M. Mojiri, “Addressing DC component in pll and notch filter algorithms,” *IEEE Transactions on Power Electronics*, vol. 27, no. 1, pp. 78–86, 2012.

[111] S. Golestan, J. M. Guerrero, F. Musavi, and J. C. Vasquez, “Single-phase frequency-locked loops: A comprehensive review,” *IEEE Transactions on Power Electronics*, vol. 34, no. 12, pp. 11791–11812, 2019.

[112] M. Xie, H. Wen, C. Zhu, and Y. Yang, “DC Offset Rejection Improvement in Single-

Phase SOGI-PLL Algorithms: Methods Review and Experimental Evaluation," *IEEE Access*, vol. 5, pp. 12810–12819, 2017.

[113] Z. Xia, B. Bilgin, S. Nalakath, and A. Emadi, "A New Torque Sharing Function Method For Switched Reluctance Machines With Lower Current Tracking Error," *IEEE Transactions on Industrial Electronics*, 2020.

[114] F. Peng, J. Ye, and A. Emadi, "A Digital PWM Current Controller for Switched Reluctance Motor Drives," *IEEE Transactions on Power Electronics*, vol. 31, no. 10, pp. 7087–7098, 2016.